Blade Loading and Near-Wake Analysis of a Floating Wind Turbine Under Imposed Roll Motion

Master Thesis Aerospace Engineering

Berke Pakbeşe

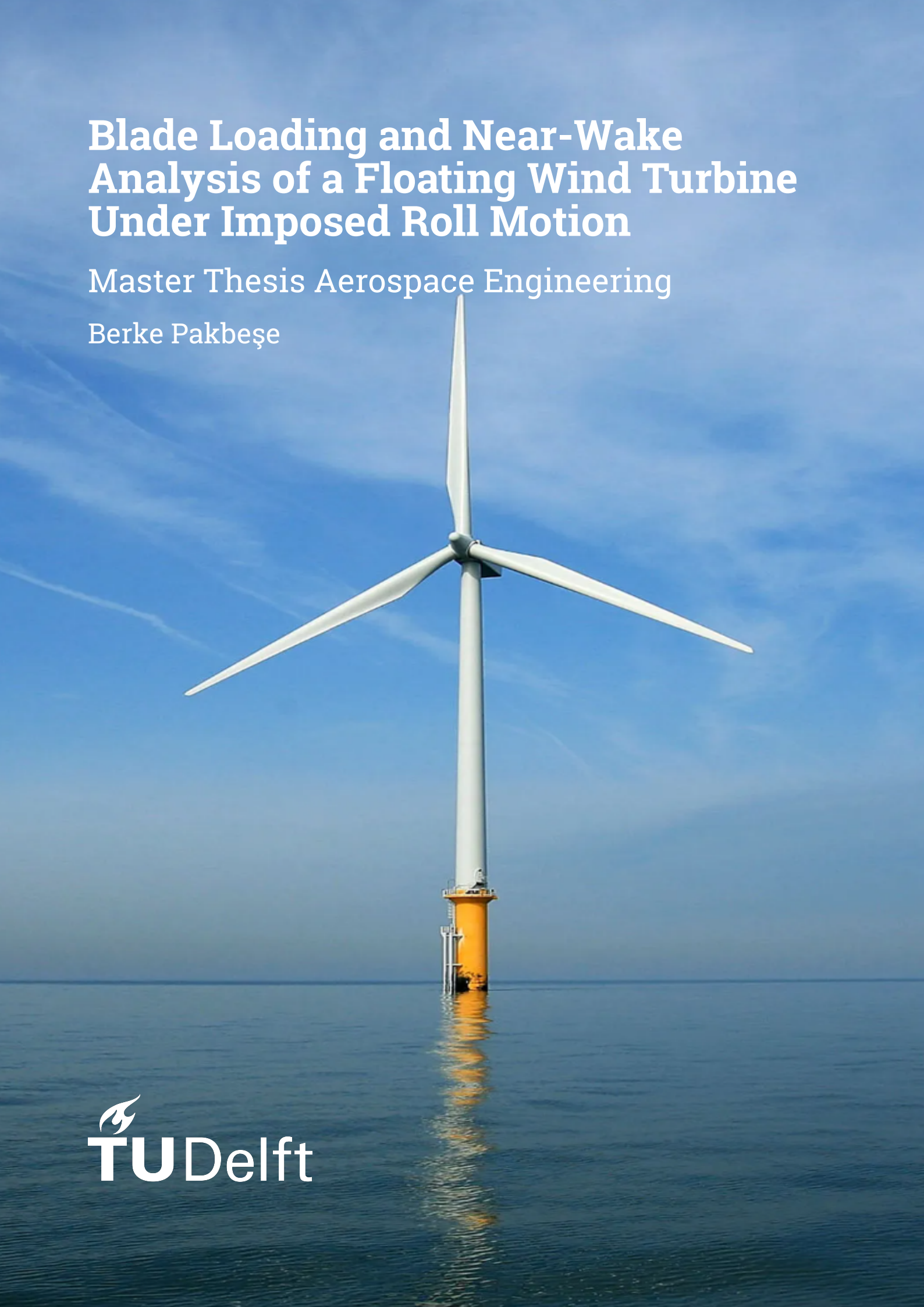

TU Delft

Blade Loading and Near-Wake Analysis of a Floating Wind Turbine Under Imposed Roll Motion

by

Berke Pakbeşe

Student number: 5215072

Supervisors:	Axelle Viré
	Evert Wiegant
	Delphine De Tavernier
Project Duration:	December, 2024 - August, 2025
Faculty:	Faculty of Aerospace Engineering

Preface

The completion of this thesis marks the culmination of a long, challenging, yet rewarding academic journey in engineering and the field of aerodynamics. I was drawn to wind energy research because the floating offshore wind industry is still in its early stages and remains a relatively under-researched field. This presented an inspiring opportunity to contribute to understanding the effects of platform motion on turbine aerodynamics which is a key step toward optimizing this promising renewable technology. It is my hope that this study will prove to be a useful contribution to the field.

I am grateful to the individuals who supported this process. I extend my sincerest thanks to my supervisor, Evert Wiegant, for his guidance and for always being available to answer my questions, especially as I learned to use Linux and the GRASP LES code. We have had very insightful discussions during our weekly meetings. I am also grateful to my supervisors, Delphine De Tavernier and Axelle Viré, for their valuable time, feedback, and mentorship. Furthermore, I would like to thank the team behind the DelftBlue supercomputer, whose work ensures its efficient and effective operation, and this research would not have been possible without this supercomputer. Finally, I am incredibly thankful to my family for their constant encouragement, patience, and funding for my education.

Berke Pakbeşe
Delft, August 2025

Abstract

Floating offshore wind turbines enable renewable energy expansion into deep-water regions with stronger, more consistent winds. However, they are subject to continuous platform motion from wind and waves, which complicates blade loading and wake aerodynamics. While surge and pitch effects have been extensively studied, the aerodynamic influence of roll motion remains underexplored. Roll motion uniquely induces a non-uniform tangential velocity field across the rotor, which would have implications on the blade loading, structure fatigue and the wake aerodynamics.

This thesis presents a baseline analysis of blade loading and near-wake aerodynamics for a FOWT under prescribed roll motions. A coupled high-fidelity GPU-based Large-Eddy Simulation code GRASP resolved turbulent wake dynamics, while OpenFAST calculated blade loads. Coupling was achieved via the Filtered Actuator Line Method and the AspFAST application programming interface. The IEA 15MW reference turbine was modeled under steady, uniform inflow, with variations in roll amplitude (5° and 10°), roll frequency (0.03Hz and 0.05Hz), and tip-speed ratio (TSR 7 and TSR 9) in a full factorial test set.

Results show that roll motion leads to asymmetric fluctuations across the rotor plane. Normal forces display strong vertical asymmetry, with greater variations in the upper side of the rotor due to its larger distance from the roll center. A kinematic analysis deriving the variation of tangential velocity both azimuthally and over time supported this finding. Tangential forces exhibit lateral variation, with a left-right asymmetry across the rotor plane, though the magnitude of variation is similar on both sides. Both roll amplitude and frequency increase the magnitude of loading fluctuations, while TSR influences their blade spanwise distribution.

Power Spectral Density analysis reveals that roll introduces spectral content at the roll frequency and at 1P sideband frequencies, the latter arising from modulation of the 1P frequency by roll. Higher roll amplitudes, frequencies, and TSRs amplify these load fluctuations. While the prominence of the 1P frequency is negligible at the blade, it is strong in the near wake along with the roll frequency, 3P frequency, and 3P sidebands.

The unsteady blade loads directly shape the near wake. The stable helical vortex system of a bottom-fixed turbine is replaced by an oscillatory corkscrew structure that breaks down earlier and more chaotically. Increased roll amplitude causes stronger lateral oscillations and fragmented vortices, while higher roll frequency produces shorter wavelength perturbations, accelerating vortex pairing. Higher TSR strengthens the initial vortices and accelerates breakdown. Standard deviation of velocity fields in the wake confirms larger fluctuations at the top of the rotor due to its greater distance from the roll axis.

This study establishes a direct link between roll-induced blade loads and near-wake dynamics, providing a foundation for improved FOWT design, control, and wake modeling. Future work should assess far-wake impacts, the persistence of lateral velocities induced by rotational motion, and inertial effects under highly unsteady roll conditions.

Contents

List of Figures

List of Tables

Nomenclature

List of Abbreviations

Abbreviation	Definition
ABL	Atmospheric Boundary Layer
ALM	Actuator Line Method
AMD	Anisotropic Minimum-Dissipation (SGS model)
API	Application Programming Interface
BEMT	Blade Element Momentum Theory
BET	Blade Element Theory
BR	Blockage Ratio
CFD	Computational Fluid Dynamics
CFL	Courant-Friedrichs-Lewy
CPU	Central Processing Unit
DALES	Dutch Atmospheric Large-Eddy Simulation
DOF	Degree(s) of Freedom
DSM	Dynamic Smagorinsky Model
FALM	Filtered Actuator Line Method
FOWT	Floating Offshore Wind Turbine
GCM	General Circulation Model
GPU	Graphics Processing Unit
GRASP	GPU-Resident Atmospheric Simulation Platform
IEA	International Energy Agency
IPCC	Intergovernmental Panel on Climate Change
IRENA	International Renewable Energy Agency
LES	Large-Eddy Simulation
NREL	National Renewable Energy Laboratory
PSD	Power Spectral Density
RANS	Reynolds-Averaged Navier-Stokes
SDEV	Standard Deviation
SFS	Sub-Filter Scale
SGS	Sub-Grid Scale
TKE	Turbulence Kinetic Energy
TSR	Tip-Speed Ratio
UNFCCC	United Nations Framework Convention on Climate Change
URANS	Unsteady Reynolds-Averaged Navier-Stokes

List of Symbols

Symbol	Definition	Unit
A	Floating motion amplitude	[m or $^\circ$]
B	Number of blades	[-]
b	Buoyancy term in LES code GRASP	[N/kg]
c	Chord length	[m]
C_D	Drag coefficient	[-]
C_L	Lift coefficient	[-]
C_n	Normal force coefficient	[-]
C_P	Power coefficient	[-]
C_S	Smagorinsky constant	[-]
C_T	Thrust coefficient	[-]
C_t	Tangential force coefficient	[-]
c_p	Specific isobaric heat capacity	[J/kg K]
D	Rotor diameter	[m]
f	Forcing term in LES code GRASP	[N/kg]
f_i	Natural frequency of a DOF	[Hz]
H	Hub height	[m]
k	Index for force point in OpenFAST	[-]
K_m	Eddy viscosity term in LES	[m^2/s]
K_{ii}	Diagonal stiffness matrix	[N/m]
M_{ii}	Diagonal mass matrix	[kg]
N	Number of actuator points per blade	[-]
N_F	Number of force actuator points	[-]
N_V	Number of velocity actuator points	[-]
n	Index for time step in OpenFAST	[-]
P	Power of rotor	[W]
p	Pressure	[Pa]
p_o	Reference pressure	[Pa]
q	Index for velocity point in OpenFAST	[-]
R	Rotor radius	[m]
r	Radial position along the blade	[m]
$\tilde{S}_{ij}$	Resolved velocity gradient tensor	[1/s]
St	Strouhal number	[-]
T	Thrust of rotor	[N]
t	Time	[s]
U or U_∞	Inflow velocity	[m/s]
u_i	Flow velocity component	[m/s]
$\tilde{u}_i$	Filtered (resolved) velocity in LES	[m/s]
$\bar{u}_i$	Mean velocity in RANS	[m/s]
u_i'	Turbulence velocity component	[m/s]

Symbol	Definition	Unit
α	Angle of attack	[°]
β	Blade pitch angle	[°]
γ	Geometric blade angle	[°]
Δ	Subfilter scale	[m]
ΔG^{n-1}	Gradient of lift force along the span in FALM	[N/m]
ΔN	Actuator point spacing	[m]
Δr	Blade element span in BET	[m]
ϵ	Gaussian kernel width (smearing parameter)	[m]
ζ	Damping ratio	[-]
η_ϵ	Gaussian kernel	[-]
λ	Tip-speed ratio (TSR)	[-]
ν_{sgs}	Subgrid-scale eddy viscosity	[m^2/s]
ρ	Density	[kg/m^3]
τ_{ij}	Subgrid-scale stress tensor in LES	[N/m^2]
ϕ	Inflow angle / Roll angle	[° or rad]
ϕ_o	Roll amplitude	[rad]
φ	Floating motion phase	[rad]
ψ	Azimuthal angle of the blade	[° or rad]
Ω	Rotational rate of rotor	[rad/s]
ω	Floating motion frequency	[rad/s]
ω_{roll}	Roll motion frequency	[rad/s]

1

Introduction

1.1 The Rise of Floating Offshore Wind Energy

As the effects of climate change become more evident, policymakers face mounting pressure to implement measures that align with the climate neutrality goals outlined in the Paris Agreement by United Nations Framework Convention on Climate Change (UNFCCC) (2025)[86]. A major challenge lies in energy production, as the global energy sector remains the largest contributor to CO_2 emissions as explained by The Intergovernmental Panel on Climate Change (IPCC) (2022)[81]. To address this, research and development and investment on renewable technologies, of which wind turbines is one of them, has significantly increased in the past decade. Estimates by the International Renewable Energy Agency (IRENA) (2022)[36] show that wind energy is expected to be one of the largest generation sources by 2030, accounting for 24% of total electricity needs.

Wind energy has proven its technical and economic potential onshore. However, its implementation has revealed certain limitations, including inconsistent wind conditions, space constraints, and challenges related to social acceptance and noise in populated areas. These drawbacks have prompted researchers and engineers to explore alternative locations for wind energy deployment. This search led to offshore wind farms, which, despite higher construction and operational costs and harsher environmental conditions, offer significant potential that outweighs these challenges.

Offshore wind turbines are only installed as a bottom-fixed turbine up to ocean depths of 50-60 meters. Depths larger than this make a bottom-fixed structure economically unviable. Major part of the ocean and coastal waters are deeper than 60 meters, and according to the Global Wind Energy Council (GWEC) (2022)[23]; 80% of the world's offshore wind resource potential lies in waters deeper than 60 meters. Therefore there is an incentive to push offshore wind projects farther from the shore and in deeper waters due to their tremendous energy potential (International Renewable Energy Agency (IRENA), 2024)[37]. This has led to the development and implementation of floating technologies for wind turbines.

Denmark deployed the first operational offshore wind farm with bottom-fixed turbines in 1991. In 2009, Norway installed the world's first floating offshore wind turbine (FOWT) with a capacity of 2.3 MW (International Renewable Energy Agency (IRENA), 2024)[37]. As of 2023, according to en:former (2023)[15] the global floating offshore wind capacity is estimated at 277 MW, with an additional 244 GW of floating offshore projects currently in the pipeline. This reflects an almost exponential growth in the installed offshore wind capacity worldwide. Furthermore, International Renewable Energy Agency (IRENA) (2021)[35] estimates that the global offshore wind potential in deep waters is approximately 13 TW, further highlighting the vast potential of offshore wind energy to meet the ever-increasing

global energy demand and replace existing non-renewable sources.

As shown in Figure 1.1, Europe is expected to ramp up its annual wind power installations between 2024 and 2030, averaging a total capacity of 29 GW per year. However, this remains insufficient to meet the 2030 climate and energy targets, which require an average annual installation of 33 GW (WindEurope, 2024)[96]. The projections also indicate a growing share of offshore wind in total new installations, with offshore capacity surpassing onshore by 2030.

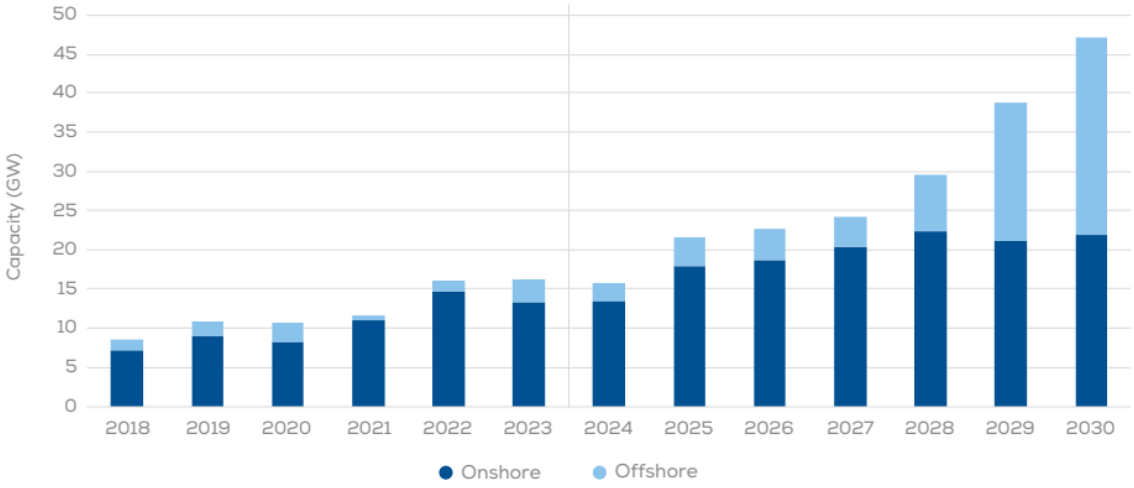

Figure 1.1: Outlook of annual onshore and offshore wind power installations in the European Union (WindEurope, 2024)[96].

Climate goals and growing consumer demand present an opportunity to develop and deploy this emerging yet promising technology. However, floating turbines operate in a vastly different environment and are not stationary, requiring a reassessment of existing technology in this new domain. Gaining a deeper understanding of turbine physics under these conditions is crucial for optimizing operation, improving design, and extending lifespan, ultimately reducing it's electricity costs and enhancing economic viability. Over the past decade, researchers have focused on floating motion and its impact on turbine physics to adapt designs and improve simulation models.

1.2 Thesis Structure

While significant progress has been made in understanding the effects of dominant motions like surge and pitch, the impact of platform roll on the near-wake region remains a less-explored but critical area of study. Roll motion, in particular, introduces complex asymmetric aerodynamic loading on the rotor blades, which directly influences the initial formation and evolution of the wake structures. A detailed understanding of these phenomena in the near-wake is important, as this region dictates the downstream, far-wake recovery and the loading experienced by subsequent turbines in a wind farm.

This thesis therefore aims to provide a baseline analysis of blade loading and near-wake aerodynamics for a floating offshore wind turbine subjected to prescribed, steady and unsteady roll motions. The study will utilize the aero-servo-hydro-elastic tool OpenFAST for blade loading analysis and the high-fidelity large eddy simulation code GRASP for a detailed investigation of the wake dynamics.

To address the research objectives, this thesis is organized into several key chapters. Chapter 2 begins by establishing the necessary theoretical foundation, covering the fundamentals of wind turbine wake aerodynamics, the principles of floating platform motion, and the numerical theories regarding the simulation tools used. Following this, Chapter 3 outlines the methodology, introducing the test cases and detailing the numerical setup of both OpenFAST and the GRASP CFD solver. To ensure the credibility of the simulations, a verification of the numerical setup is presented in Chapter 4. Finally, Chapter 5 presents the results and analysis, providing insights into the effects of the imposed motion on blade loads and near-wake behavior, followed by the main conclusions and recommendations for future research in Chapter 6.

2

Background Theory

This chapter provides background information on wind turbine wakes, and the effects of inflow conditions and floating motion on the wakes of floating offshore wind turbines. It also reviews relevant ongoing and completed research. Additionally, the chapter introduces and explains the theory of numerical methods, including the large-eddy simulation code GRASP, OpenFAST, and their coupling. Finally, the chapter ends with the introduction of the reference floating turbine used for this study, namely the IEA 15 MW turbine.

2.1 Wake of Bottom-Fixed Wind Turbines

Wind turbines extract kinetic energy from the incoming wind to generate electricity. This reduces the flow speed downstream. This region, characterized by the velocity deficit, is called the wake. Not only is there a velocity deficit, but also an increase in the turbulence intensity of the flow. Both of these effects have consequences for any turbine placed downstream of a farm. The velocity deficit results in lower power production, and the increased turbulence leads to additional fatigue on the structure. The extent to which these consequences are felt depends largely on the downstream distance of subsequent turbines and the rate of wake recovery.

The wake can be categorized into the near-wake and the far-wake (Vermeer et al., 2003)[90]. The characteristics of the wake differ between these regions, which are explained individually in detail in Subsection 2.1.1 and Subsection 2.1.2, respectively. The effects of the inflow conditions on the wake are explained in Subsection 2.1.3.

2.1.1 Near-Wake

The near-wake, as shown in Figure 2.1, refers to the region immediately downstream of the rotor, where the influence of rotor properties is distinguishable. This area typically extends from $1D$ (one rotor diameter) to $5D$ downstream (McKay et al., 2012)[55], depending on the specific turbine and operating conditions. In this region, the effects of rotor characteristics, such as the number of blades, blade aerodynamics (including stalled flow and three-dimensional effects), and the formation of highly coherent tip and root vortices, dominate (Vermeer et al., 2003)[90]. The strong tip and root vortices form due to pressure differences along the blades, and these vortices follow helical paths due to the turbine's rotational velocity. As they propagate downstream, the strength of the vortices decreases resulting in less coherent vortical structures. This marks the transition from the near-wake to the far-wake. This transition region is shown in Figure 2.1.

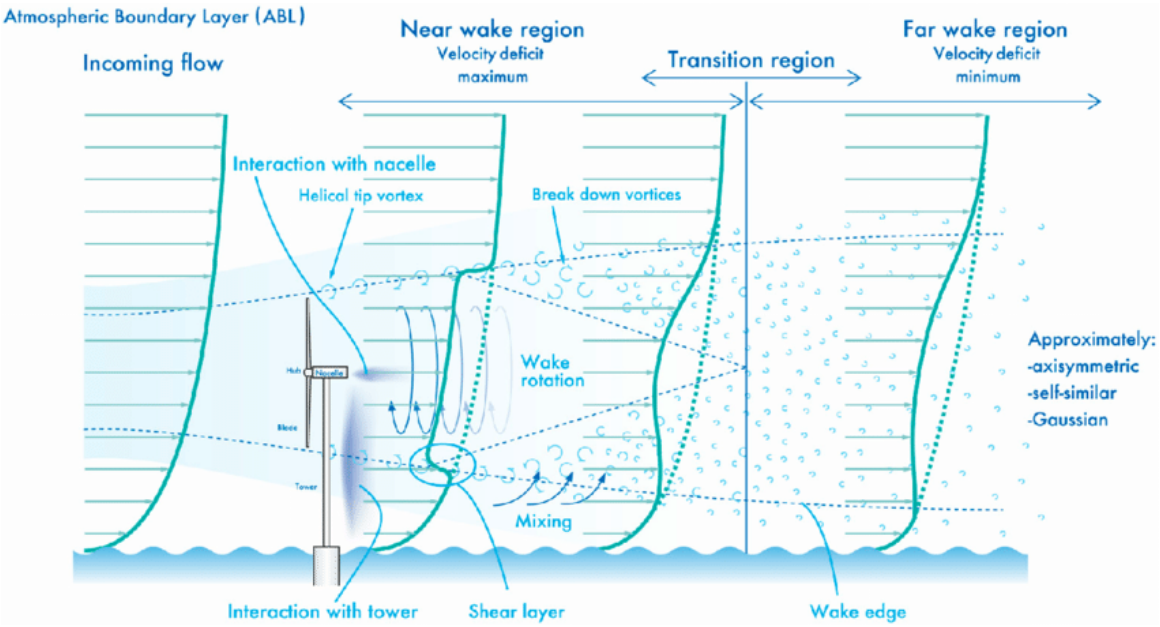

Figure 2.1: A schematic of bottom-fixed wind turbine wake imposed to shear inflow (Uchida, 2020)[85].

Within the near-wake, pressure recovery occurs after the initial drop at the turbine. This recovery causes the streamtube to expand until the pressure within the wake equalizes with the freestream pressure. The expansion of the streamtube's cross-sectional area leads to a reduction in velocity, as mass and momentum are conserved. At the same time, a shear layer forms at the interface between the wake velocity and the freestream velocity, which is highly unstable due to the large velocity differential between the two regions. This instability leads to turbulence that cascades into smaller scales and expands into the downstream wake region. The near-wake region is characterized by strong turbulence heterogeneity, predominantly due to tip and root vortices, and a high degree of unsteadiness (Vermeer et al., 2003)[90].

The near-wake is highly sensitive to turbine operating conditions, atmospheric conditions, and floating motions for floating turbines. Consequently, the near-wake is a critical area of research due to its relevance to rotor performance and the physical processes governing power extraction (Vermeer et al., 2003)[90]. Understanding the complex phenomena of unsteady flow, turbulence, and sensitivity to various operating and environmental conditions in this region is essential for improving turbine efficiency and accurately predicting wake behavior.

2.1.2 Far-Wake

A transition region, shown in Figure 2.1, exists between the near- and far-wake. In this region, the characteristics of the near-wake fade, and the wake becomes increasingly representative of the far-wake. This occurs as the coherent vortical structures break down and dissipate, and the wake becomes progressively more turbulent throughout. The shear layer created in the near-wake decreases in size as the velocity profile smooths, progressively adopting a Gaussian shape (Bastankhah and Porté-Agel, 2014)[3].

Studies of the far-wake region are more common in the context of wind farm analysis. The far-wake in extreme cases can extend up to $50D$ (McKay et al., 2012)[55] and is, therefore, the most influential

region for downstream turbines. The primary goal in most far-wake studies is to determine the influence of inflow or floating conditions on wake recovery. Unlike the near-wake, the influence of the rotor properties is not distinguishable; therefore, for numerical analysis of this region, the rotor does not need to be modeled as accurately (Vermeer et al., 2003)[90]. However, the far-wake is where most of the wake recovery takes place. The shear layer created in the near-wake breaks up and enhances mixing. This leads to high radial momentum transfer from the undisturbed flow into the wake, resulting in a reduction of the shear layer as the velocity deficit decreases and the velocity profiles approach a Gaussian distribution.

In the far-wake, the coherent vortical structures from the near-wake have already broken down into incoherent turbulence. As a result, unlike the near-wake, there is a high level of turbulence throughout the cross-section of the far-wake (Vermeer et al., 2003)[90]. Turbulence kinetic energy increases in the far-wake due to mixing and external flow entrainment.

Similar to the near-wake, the far-wake continues to expand, but linearly. This linear expansion is clearly visible after the transition line shown in Figure 2.1. This later followed by a constant size of wake when the pressure is equalized. Additionally, wake meandering is observed, a phenomenon specific to the far-wake. This involves the lateral and vertical movement of the wake driven by large-scale turbulence structures in the atmospheric boundary layer (ABL) (Stoevesandt et al., 2022)[77]. Stronger meandering is usually induced by specific types of floating motion.

2.1.3 Influence of Inflow Conditions on the Wake of a Wind Turbine

A wind turbine's wake is significantly influenced by its inflow conditions, an effect that can differ between the near-wake and far-wake regions due to their distinct aerodynamic characteristics. A review of the literature suggests that among all inflow parameters, turbulence is the most widely studied and influential contributor to the wake recovery of a bottom-fixed wind turbine.

According to Stull (1988)[78], two primary types of turbulence are generated within the ABL, classified by their generation process. The first is mechanical turbulence, which is produced by surface (terrain) roughness. In addition to turbulence this process causes due to obstacles on the terrain, the velocity profile results in sheared inflow which also generates turbulence. The second is buoyant convective turbulence, generated by convection of bodies of air due to atmospheric stratification.

This turbulence is described by two key properties: turbulence intensity and turbulence structure (Hodgson et al., 2023a)[32]. The former quantifies the magnitude of the turbulent fluctuations, while the latter concerns its composition, which is characterized by the distribution of turbulent eddy length scales (Davies, 1973)[12]. A thorough understanding of how these turbulence characteristics affect the wake shape, internal structure, and recovery rate is therefore crucial for the optimization of both individual wind turbine and overall wind farm performance.

The stability of the ABL is typically classified into three main categories: unstable, stable, and neutral. As described by Stull (1988)[78], an unstable ABL is caused by the vertical convection of heated, lower-density air rising through an overlying region of sinking cooler, denser air. This atmospheric

instability is driven by the buoyancy of the warmer air parcels and/or weight of the cooler air parcels. This vertical temperature distribution of the ABL is termed boundary layer stratification. Consequently, the enhanced vertical mixing characteristic of an unstable ABL leads to higher turbulence intensity compared to a neutral boundary layer. On the other hand, a stable ABL suppresses vertical mixing, thereby reducing turbulence. Additionally, as investigated by Gambuzza and Ganapathisubramani (2023)[20], ABL stability influences the size of turbulence scales. In an unstable ABL, larger integral length scales and smaller time scales are observed, which impact the wake recovery process. Xie and Archer (2017)[97] found that ABL stability also affects the wake shape. They concluded that a wake in a stable ABL expands more laterally, whereas in an unstable ABL, it expands more vertically. They also determined that in an unstable ABL, the background turbulence kinetic energy (TKE) is highest, leading to greater turbulence dissipation and a faster return to equilibrium with freestream conditions. Their findings support the consensus that an unstable ABL enhances wake recovery by increasing turbulence in the inflow.

In addition to turbulence induced by atmospheric instability, increased wind shear due to increased surface roughness, also lead to higher turbulence intensity. Bouhelal et al. (2024)[8] demonstrated that higher surface roughness results in an inflow kinetic energy deficit near the surface, thereby increasing wind shear. As explained by Porchetta et al. (2019)[61], in offshore environments, the primary source of surface roughness is the amplitude of sea waves. Even with the strongest waves, generally the surface roughness offshore is significantly less than onshore surface roughness (van Bussel and Bierbooms, 2004)[88] due to the absence of trees, buildings and hills. Consequently, onshore flow exhibits higher wind shear and inflow turbulence intensity. Gambuzza and Ganapathisubramani (2023)[20] demonstrated that higher turbulence intensity introduces instabilities in the tip vortices, leading to an earlier transition to the far-wake. Since wake recovery predominantly occurs in the far-wake, shortening the near-wake is beneficial as tip vortices in this region prevent high-momentum flow from the undisturbed region from mixing in. Consistent with this, Goit and Meyers (2015)[24] concluded that turbulence intensity benefits the near-wake by shortening it, while the far-wake is primarily influenced by Reynolds shear stress distribution at the wake centerline, which induces mixing. Ivanell et al. (2010)[38], using LES with harmonic perturbations near the blade tip, investigated tip vortex stability. They identified that certain excitation frequencies promote greater instability growth rates, accelerating wake breakdown. Their findings linked these instabilities to turbulence levels. Hodgkin et al. (2022)[30] expanded on Ivanell et al.'s stability analysis by incorporating inflow shear and stratification effects. Their study found that shear caused wake breakup to initiate earlier in the lower wake regions due to the closer spacing of tip vortices.

The benefits of higher turbulence intensity are well understood. However, Parinam et al. (2024)[60] explains that with higher shear inflow, near-wake tip vortices tilt with the shear and break down into smaller integral length scales. This is consistent with a stable ABL, which has the highest wind shear (Abkar et al., 2016)[1] and the smallest integral length scales. Vahidi and Porté-Agel (2024)[87] explains that smaller integral length scales are not beneficial for far-wake recovery because they carry less momentum into the wake from the undisturbed flow and penetrate only shallowly into the wake. Blackmore et al. (2014)[6] supports this conclusion by stating that larger integral scales lead to higher mixing in the far-wake but also cause a larger velocity deficit in the near-wake. Given this trade-off,

Stanislawski et al. (2023)[75] concludes that turbulence intensity is a far more influential factor in the overall wake recovery process than integral length scales.

Gambuzza and Ganapathisubramani (2023)[20] investigated the impact of inflow turbulence time scales on wake recovery and found that, for flows with a Kolmogorov-like turbulence spectrum, the wake recovery rate and the behavior of the turbine wake in high-integral time scale flows follow a linear function of freestream turbulence intensity. Hodgson et al.'s (2023b)[33] results align with this, as they concluded that shorter time scales are more amplified in the near-wake, causing tip vortices to break down earlier. Additionally, they found that longer time scales induce more wake meandering, similar to that induced by larger integral scales, as demonstrated by Larsen et al. (2008)[47], and delay the onset of energy entrainment due to slower tip vortex breakdown. They further observed that meandering can accelerate recovery by enhancing mixing and adding turbulence kinetic energy. Their study also explored how wake breakdown depends on inflow turbulence scales, identifying specific Strouhal numbers associated with enhanced wake breakdown. They found that when inflow turbulence energy is concentrated within St $\in$ [0.3, 0.7], both wake breakdown and recovery are intensified. Hodgson et al. (2022)[31] further added that smaller time scales enhance mixing due to faster energy transfer and quicker eddy breakup. The interplay between incoming turbulence and turbine-generated turbulence determines wake stability and recovery, influencing energy distribution in downstream regions.

Due to wind shear, wake mixing is uneven. Nanos et al. (2022)[58] investigated this effect and concluded that the upper part of the wake, which experiences higher velocities, transitions earlier and recovers faster than the lower part, resulting in wake deflection downward. Another occurrence of wake deflection, meandering, has been studied by Lee et al. (2013)[48], who found that a stable ABL leads to a lower frequency of meandering. The wake expansion rate increases linearly with the inflow turbulence intensity, and this linearity depends on the inflow speed (Liu et al., 2022)[51].

2.2 Theory of Floating Offshore Wind Turbines

Floating offshore wind turbines (FOWTs) are unlike bottom-fixed turbines, where they can undergo motion in 6 degrees of freedom (DOF). 3 of these are in translation, and 3 in rotation. In this section, these DOF along with the sources of these motions will be explained in Subsection 2.2.1. Then, a short explanation of the methodologies employed on floating offshore wind energy research and studies on the wind-wave coupling are introduced in Subsection 2.2.2. After this, Subsection 2.2.3 explains the theory of the state-space model which is utilized in this thesis to determine the excitation forces required to impose on the structure. Lastly, the researched effects of these motions on the wake are given in Subsection 2.2.4.

2.2.1 Types and Sources of Floating Motion

The DOF experienced by FOWTs are summarized in Table 2.1.

Degree of Freedom	Definition
Surge	Streamwise translation
Sway	Lateral translation
Heave	Vertical translation
Pitch	Rotation around the sway axis
Roll	Rotation around the surge axis
Yaw	Rotation around the heave axis

Table 2.1: The six degrees of motion of a floating offshore wind turbine.

These motions are clearly illustrated in Figure 2.2.

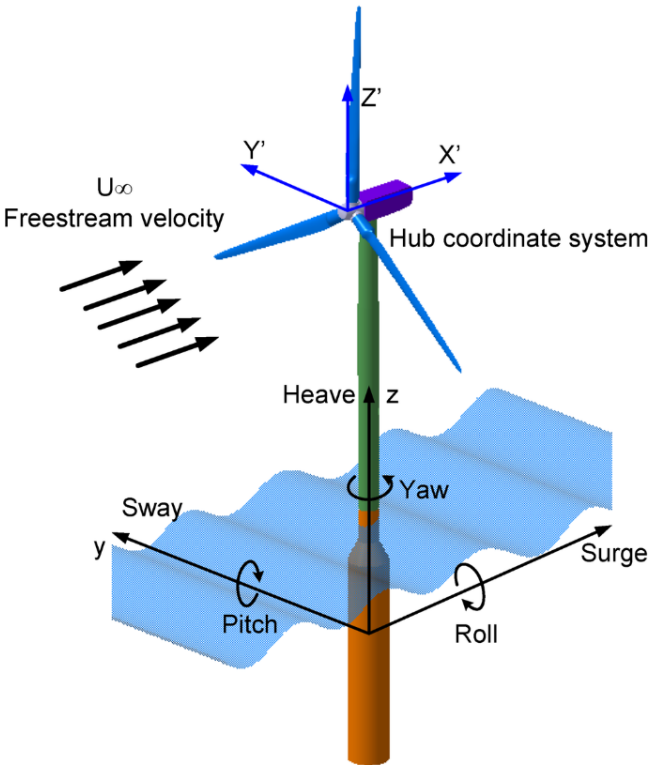

Figure 2.2: Degrees of freedom of the floating offshore wind turbine (Tran et al., 2014)[82].

The typical idealized behavior of a FOWT is often described by the amplitude and frequency of its sinusoidal motion across the six DOF. The formulation for one of DOF is shown in Equation 2.1.

$$x(t) = \mathrm{A}\cos\left(\omega t + \varphi\right) \tag{2.1}$$

Here, A is the amplitude [m / °], ω is the frequency [rad/s], φ is the phase shift [rad] of the DOF, and t is time [s]. x(t) is the parameter analyzed. If the surge position is described, $x(t)$ represents the turbine's position in the streamwise direction over time. The derivative of this equation represents the surge velocity, and the second derivative is the surge acceleration.

The motion of FOWTs is primarily driven by excitation forces resulting from wind, ocean currents, and waves. The system's response to these forces depends on a complex interplay of various parameters,

including the turbine's mass and inertia, the added mass due to the floater's displacement of water, aerodynamic and hydrodynamic damping influenced by the design of the rotor and floater, and the stiffness of the mooring system. Additionally, the turbine's operation, governed by its controller, plays a significant role in shaping the system's response. This makes the motion of FOWTs an aero-servo-hydro-elastic problem. To accurately capture their response, it is essential to use software that employs either a partially or fully coupled modeling approach. A widely used tool for this purpose is OpenFAST, which is further discussed in Subsection 2.4.4.

2.2.2 Studies on Floating Motion

To estimate the response of a FOWT to an excitation force, researchers have conducted extensive experiments and numerical simulations. By applying wave and wind conditions, often perpendicular to the rotor, they analyze the resulting motions and provide approximate magnitudes for the typical movements of specific platforms.

Yang et al. (2014)[99] demonstrates the coupling between wind and waves. Ocean waves are formed due to the interaction of the wind with the sea surface. If a sufficient amount of energy is transferred to the sea, a fully developed sea forms. This is a sea state in which wave height has reached its maximum potential for a given, constant wind speed. This occurs when the wind's fetch (distance) and duration are no longer limiting factors in wave development. For high-speed winds, these conditions are rare, as the required fetch can be exceptionally large. If the duration of energy transfer is too short, a fetch-limited sea forms.

Fully developed seas allow for larger power extraction due to lower surface resistance on the ABL, enabled by the faster propagation of sea waves. This also leads to more vertical momentum flux in the ABL (Yang et al., 2014)[99], meaning more recovery in the far-wake. In addition to this, Porchetta et al. (2019)[61] discusses the reverse coupling from waves to the wind. The velocity profile of wind depends on the alignment of the wind direction with the wave direction. The more alignment there is, the lower the surface roughness. This roughness parameter affects the turbulence intensity and vertical momentum flux of the flow from the sea surface to the atmosphere.

The coupled models are complex, and the use of high-fidelity models is limited by the computational power available. Thus, when the main subject of interest is the wake of a FOWT, a periodic motion in the form of Equation 2.1 is generally prescribed directly to the geometry. The amplitude and frequency of motion are typically obtained from tests in wave tanks on scaled models, literature available, or thorough numerical analysis, and largely depend on the design of floater considered.

2.2.3 The State-Space Model of Floating Motion

In both numerical and experimental analysis of a floating turbine, the state-space model is used to describe the motion response of the turbine to external loading. An equation for the i^{th} DOF, in the simplest form of the state-space representation for imposing motion, is shown in Equation 2.2. This equation disregards hydrodynamic effects, specifically by ignoring the added mass matrix and mooring stiffness. This is a necessary simplification because motion is imposed rather than being studied as a response to wave conditions.

$$M_{ii}\ddot{x}_i(t) + C_{ii}\dot{x}_i(t) + K_{ii}x_i(t) = F_{external,i}(t) \tag{2.2}$$

M_{ii} is the diagonal mass matrix, C_{ii} is the diagonal damping matrix, K_{ii} is the diagonal stiffness matrix, and $x_i(t)$ is the platform displacement or angle in time. The first and second derivatives of $x_i(t)$ are also present in the differential equation. $F_{external,i}(t)$ is the applied external loading over time causing the given i^{th} DOF. For numerical analysis using OpenFAST, the coefficients of these matrices are obtained from the input file of the ElastoDyn module which will be further elaborated upon in Subsection 2.4.4.

In the input file ElastoDyn.dat, the system mass for translational motion and moments of inertia for the three respective rotational degrees of freedom are defined. Therefore, the mass matrix M_{ii} is constructed by placing these terms diagonally. The system's stiffness matrix can be constructed from the mass matrix and the natural frequencies of each DOF (f_i). The formulation is given in Equation 2.3.

$$K_{ii} = M_{ii} \cdot (2\pi f_i)^2 \tag{2.3}$$

The natural frequency, f_i, is the frequency of prescribed motion for that DOF when motion is being imposed. Lastly, the damping matrix can be constructed using mass-proportional damping. The equation for this is given in Equation 2.4.

$$C_{ii} = 2\zeta\sqrt{K_{ii}M_{ii}} \tag{2.4}$$

The term ζ is the damping ratio that is selected based on the strength of damping needed to obtain the steady, sinusoidal motion.

Summarizing, the state-space approach is used in OpenFAST to obtain the desired motions' external forcing, $F_{external,i}(t)$ imposed on the turbine from a defined motion frequency and amplitude. Meaning, the code is able to calculate the external forcing required to obtain the desired periodic motion.

2.2.4 Influence of Floating Motion on the Wake of a Wind Turbine

Floating motion introduces unsteadiness, and its effect on the wake depends on the type of DOF excited. The extent of this difference due to the floating motion, compared to a bottom-fixed turbine, varies with the frequency and amplitude of the motion. Therefore, research in this section aims to understand these effects and potentially leverage them for optimizing power output per turbine or of a wind farm.

Raibaudo et al. (2022)[62] compared floating and bottom-fixed turbines, finding that floating turbines generated higher turbulence in the near-wake but lower turbulence in the far-wake. This aligns with Zhou et al. (2022)[100]'s research, which reported similar results. Using the same experimental setup, Garcia et al. (2022)[21] observed that surge motion had minimal impact on wake meandering. Messmer et al. (2024)[57] identified specific Strouhal number ranges for surge (St $\in$ [0.3, 0.9]) and sway (St $\in$ [0.2, 0.6]) motions that led to increased wake breakdown, partially overlapping with the inflow Strouhal numbers that promote recovery, as identified by Hodgson et al. (2023b)[33]. Messmer et al.'s findings also showed that sway induced significant meandering, while surge caused a pulsing effect

in the wake. The surging motion exhibited a complex quasi-periodic dynamic, a self-generated meandering mode that interacts nonlinearly with the imposed excitation frequency, leading to enhanced mixing.

Belvasi et al. (2022)[5] analyzed the effects of surge, pitch, and heave motions on a FOWT but found no significant evidence of improved wake recovery due to these motions. However, Kopperstad et al. (2020)[45] observed that motion-induced recovery improvements existed for both laminar and turbulent inflow conditions. Their study demonstrated greater recovery at higher motion amplitudes and frequencies. Similarly, Schliffke et al. (2020)[69] experimentally modeled surge motions in an ABL and found that while mean wake velocity remained unchanged, turbulence intensity and turbulent kinetic energy profiles shifted when extreme amplitudes and frequencies were applied.

Further experiments in an ABL flow representative of offshore conditions, conducted by Garcia et al. (2022)[21], indicated that surge motion had little effect on wake breakdown. However, the downstream signal retained the surge frequency, suggesting that a downstream turbine could experience a dynamic response. Angelou et al. (2023)[2] observed that wake recovery and expansion in real FOWTs are primarily driven by ambient turbulence, with FOWTs behaving similarly to bottom-fixed turbines. This highlights the importance of considering inflow turbulence in FOWT wake studies. Zhou et al. (2022)[100], using RANS simulations with blade-resolved models, found only minor differences in wake velocity distributions between floating and fixed turbines, with turbulence intensity reductions occurring more rapidly under ambient turbulence conditions. They also noted higher turbulence intensity levels directly behind the blades.

Xu et al. (2023)[98] conducted a fully coupled numerical analysis of a FOWT in an ABL, integrating FAST into their LES framework and using an actuator line method (ALM) for aerodynamics. Their findings revealed that pitching motion shifted the wake center, typically moving it to the left when viewed downstream. Static pitch generated an upward force, lifting the wake. They observed similar turbulence intensities in the wakes of both floating and bottom-fixed turbines, with only slight differences in wake deficits. Similarly, Nanos et al. (2022)[58] studied the effects of pitch and demonstrated that pitching could be used to deflect the wake toward the ocean surface, promoting wake dissipation and faster recovery.

Li et al. (2022)[49] studied the effects of sway motion of a FOWT on the wake dynamics using an LES simulation. They found that when the inflow turbulence intensity is low, certain Strouhal numbers of side-to-side turbine motion lead to wake meandering with amplitudes one order of magnitude larger than the FOWT motion. They demonstrated that this Strouhal number range, (St $\in$ [0.2, 0.6]), overlaps with the Strouhal numbers of wake meandering induced by shear layer instability. This suggests that turbine side-to-side motion can trigger the onset of the shear layer instability mechanism. At high turbulence intensities, the cause of wake meandering is dominated by the inflow turbulence rather than the floating motion. Schliffke et al. (2024)[70] conducted experiments on a model FOWT with surge, pitch, and heave motions in an ABL. They found that idealized DOF motions left no distinct signature in the energy spectra unless amplitudes and frequencies were extremely high and beyond typical FOWT operational ranges. Surge effects were evident up to $8D$ downstream for cer-

tain amplitude-frequency combinations, while heave and pitch had less pronounced effects, requiring higher amplitudes and frequencies to influence the wake. Their study also highlighted that surge and pitch motions had the greatest impact on the wake, with negligible differences when modeling pitch as surge motion.

Duan et al. (2022)[14] utilized LES simulations to analyze the wake of a FOWT under imposed surge with varying periods. Their findings showed that while short-period surge resulted in longer wake recovery compared to a fixed turbine, medium- and long-period surge improved recovery slightly and significantly, respectively, when the wind was unidirectional. However, for multidirectional wind, the wake elongated, reducing recovery effectiveness due to platform motions. Wei et al. (2024)[92]'s findings showed that surge destabilized the tip vortices, leading to a shorter near-wake and increased mixing in the far-wake. The cause of unstable tip vortices was explained by Thanh and Kim (2016)[80], who noted that as the platform surged toward the inflow, the tip vortices intersected with vortices from previous cycles, leading to interference. According to Farrugia et al. (2016)[16], the impact of surge motion on turbine performance and wake characteristics increased with tip speed ratio due to greater power and thrust fluctuations, resulting in larger flow unsteadiness. Janssen (2023)[39] examined the effect of surge amplitudes and found that at low amplitudes, the wake remained largely unchanged compared to a fixed turbine.

Fu et al. (2019)[18] performed wind tunnel experiments to analyze the impact of pitch and roll motions of a turbine on the wake. Their findings suggest that rolling induces a lower momentum deficit compared to pitching, which is detrimental for recovery. Both motions increase the mean power of the turbine under moderate oscillations. They state that this was due to an increase in velocity experienced at the rotor plane for both motions; specifically, with roll, momentum is replenished in the very near-wake, promoted by lateral motions. These effects can be studied further with a near-wake analysis. Fu et al. (2019)[18] also concluded that the effect of roll motion is only significant in the near-wake and becomes negligible at $7D$ downstream. This confirms that roll motion has a greater impact on the near-wake and is more important to study in this region.

A review of the literature indicates that roll motion has not been studied as thoroughly as other floating motions, such as surge and pitch. Research has often prioritized motions that influence the far-wake, as this region directly affects downstream turbines in a wind farm. The prioritization of research on floating motions other than roll may be partly due to findings, such as those of Fu et al. (2019)[18], which state that roll has limited significance far downstream. However, the resulting knowledge gap regarding roll motion, especially its effects on the blade loading and consequently the near-wake, imposes considerable limitations on current research.

A key research question arises from this gap. It was demonstrated by Gambuzza and Ganapathisubramani (2023)[20] that higher inflow turbulence intensity can shorten the near-wake by inducing tip vortex instability. It is not yet clear whether roll motion can produce a similar effect, which would have consequences for turbine interactions within a wind farm because even though roll doesn't influence the far-wake, expediting transition would be significant.

Furthermore, studies are emerging on coupled motions involving roll, which can lead to complex aero-hydro-servo-elastic behaviors. One such example is the roll-yaw lock phenomenon, a recently identified instability by Haslum et al. (2022)[26], resulting from a destabilizing aerodynamic coupling created by the turbine's thrust force. This coupling arises because a roll motion of the floater induces a yawing moment from the thrust acting at hub height, while a yaw motion, in turn, generates a rolling moment. This reciprocal action can couple the two motions, leading to instability. This phenomenon illustrates that roll motion can induce complex turbine dynamics that are not yet fully understood or characterized. Therefore, a baseline understanding of a turbine subjected to pure roll motion is essential to provide a foundation for research into these more complex, coupled behaviors.

2.3 Research Motivation & Objectives

As explained in Subsection 2.2.4, a key finding from the literature is that the influence of roll on the turbine wake remains underexplored. This oversight often stems from the conclusion of researchers, such as Fu et al. (2019)[18], that roll has a negligible impact on the far-wake and that its effects are confined to a short downstream distance. Consequently, studies focusing on roll motion are frequently neglected.

Unlike translational motions such as surge, sway, or heave which cause uniform velocity variations at the rotor, the rotational motions of roll, yaw, and pitch induce non-uniform velocities. This non-uniformity has significant influence on the loading distribution across the rotor-plane, which can cause fatigue and structural damage if left uncontrolled. Given that both pitch and yaw are extensively studied, and there is no evidence to suggest that roll is less likely to occur in nature, its investigation is equally warranted.

The distinguishing characteristic of roll is the additional rotation centered around the tower base, which results in induced velocities at the rotor of varying directions and magnitudes depending on the azimuthal location of each blade and the roll velocity/angle. This phenomenon has significant implications for load variation, not only within a roll cycle but also within a single blade cycle. Such variations can accelerate structural damage through fatigue. Therefore, this baseline study, and the further research that builds upon it, can inform the development of design or control schemes to mitigate fatigue damage. Furthermore, these loading variations are likely to produce a highly unsteady near-wake. This unsteadiness may manifest as complex vortical structures which also show meandering, while the velocity profiles may reflect the uneven blade loading at the rotor. Such complexity could shorten the near-wake and accelerate wake recovery, a potential benefit for downstream turbines in a wind farm. Therefore, this thesis aims to provide a fundamental understanding of the effects of roll motion, focusing on the blade loading and on the near-wake region where its influence is most significant. Ultimately, this report also seeks to bridge the gap between what is seen on the blade loading as a result of roll motion and the what is seen at the near-wake.

In addition to the motivations given for analysis of roll motion in this subsection, the study by Haslum et al. (2022)[26] also is a motivator, in the sense that, to be able to study and fully understand complex motions that involve roll, a baseline understand of roll motion should be available in literature. This thesis aims to provide this.

While Subsection 2.1 highlighted how a wind turbine's wake is influenced by many inflow characteristics, this study specifically aims to provide a baseline understanding of roll motion's effects. To achieve this, inflow conditions are kept simple, utilizing a uniform and steady flow. Instead, the research primarily focuses on the turbine's operational point, particularly through the rotor speed.

Following the objectives mentioned of the study, the research objectives can be formulated as two distinct main research questions:

1. **How does imposed roll motion on a floating wind turbine influence it's blade loading?**
   In order to answer this question on the blade loading, the following four sub-questions will be addressed:
   (a) How does the blade loading of a turbine subjected to roll motion differ from that of a bottom-fixed turbine?
   (b) How does the amplitude and frequency of the roll motion affect the blade loading and it's unsteady variation due to roll?
   (c) How does the rotor speed (defined by its tip-speed ratio at constant inflow wind speed) affect the blade loading variation due to roll?
2. **How does imposed roll motion of a floating wind turbine influence the flow characteristics in the near-wake directly behind the blade?**
   In order to answer this question on the wake characteristics, the following four sub-questions will be addressed:
   (a) How does the near-wake characteristics of a turbine subjected to roll motion differ from that of a bottom-fixed turbine?
   (b) How does the amplitude and frequency of the roll motion affect the near-wake characteristics and it's unsteady variation due to roll?
   (c) How does the rotor speed (defined by its tip-speed ratio at constant inflow wind speed) affect the influence of blade loading on the near-wake characteristics?

For the purpose of this study, the term 'wake characteristics' collectively refers to the velocity profiles, vortical structures, and fluctuation signals and their powers. The analysis is concentrated on these features within the near-wake region.

In order to answer these research objectives, various numerical tools that are coupled together to simulate the wake aerodynamics, model the turbine and compute the blade loading are used. The background theory of the numerical setup is given in Section 2.4.

2.4 Numerical Theory

This section begins with an introduction to the concept of turbulence and the turbulence closure problem in Subsection 2.4.1, given their fundamental importance in fluid flow and as a primary focus for most numerical modeling tools. Subsequently, a transition to numerical tools used in this thesis is established by introducing available tools for atmospheric simulations in Subsection 2.4.2. The numerical theory of GRASP, the computational fluid dynamics code utilized, is then extensively detailed in Subsection 2.4.3. This subsection integrates both the background theory of the code and relevant methodological aspects. Next, OpenFAST, the second numerical tool employed, is briefly explained in Subsection 2.4.4, succeeded by an explanation of the GRASP-OpenFAST coupling in Subsection 2.4.5. Subsection 2.4.6 explains the blade element theory (BET), a critical theoretical framework utilized by OpenFAST. Finally, the (filtered) actuator line method, which facilitates the coupling between GRASP and OpenFAST, is explained in Subsection 2.4.7.

2.4.1 The Turbulence Closure Problem

Turbulence is the random deviation from the mean flow velocity. These variations are almost always present in the flow and are promoted via physical phenomena introduced in Subsection 2.1.3.

The mathematical notation of turbulence is typically expressed in terms of deviations from the mean state of a given variable (Holtslag, 2016)[34]. The mean flow is represented with overbars, and fluctuations are denoted by primes. The sum of these yields the variation of a given parameter in time. The example of flow velocity is shown in Equation 2.5. This procedure, called Reynolds decomposition, splits the mean and turbulent parts of wind speeds.

$$u_i = \bar{u}_i + u_i' \tag{2.5}$$

As shown by Hintz (2016)[29], Reynolds decomposition is used in Reynolds-averaged Navier-Stokes (RANS) equations, commonly used in computational fluid dynamics (CFD). The RANS equations describe turbulent fluid flow by considering the time-averaged properties of the flow rather than directly solving for the turbulent fluctuations. In this approach, the mean flow is solved, while the effects of turbulence are modeled through additional terms known as Reynolds stresses. However, the introduction of these Reynolds stresses, which represent the fluctuating momentum transport, leads to a main challenge of modeling using CFD, that is the turbulence closure problem. This problem arises because the number of unknown variables exceeds the number of available equations in the RANS system. To close the system and make it solvable, these Reynolds stresses must be expressed or modeled in terms of the known mean flow properties. These stresses represent the momentum transport caused by turbulence and are typically modeled using turbulence models such as the k-ϵ or k-ω models.

RANS is a powerful tool for simulating turbulent flows because of its relatively low computational cost. However, its precision can be limited, particularly for complex or unstable flows and geometries. This limitation arises because RANS simplifies turbulence by representing it through time-averaged quantities, rather than solving for all turbulence scales. Although turbulence models attempt to capture the effects of turbulence, their accuracy is constrained by inherent simplifications. Enhancements such

as unsteady RANS (URANS) improve the treatment of unsteady flows, but for some cases, RANS provides insufficient accuracy. When higher fidelity is required, particularly for complex flows, large-eddy simulations (LES) are preferred, though they come at a higher computational cost. More on the LES and it's turbulence closure problem will be explained in Subsection 2.4.3.

2.4.2 Tools for Atmospheric Simulations

The GPU-Resident Atmospheric Simulation Platform (GRASP) is a numerical tool utilized in this thesis to simulate atmospheric flow using LES. The LES approach was first introduced by Smagorinsky (1963)[73] and later refined by Deardorff (1970)[13]. LES effectively resolves large-scale motions (large eddies), which contain the most kinetic energy, while smaller scales are parameterized using approximations. Similar to RANS, which uses Reynolds decomposition to obtain its mass and momentum conservation equations, LES utilizes spatial filtering where variables are separated into filtered (resolved) large-scale components and subgrid-scale (modeled) components. The notation for this separation is conceptually similar to Reynolds decomposition and is shown in terms of equation in Equation 2.5. For the instance of LES, $\bar{u}_i$ is the filtered (resolved) large-scale parameter and u_i' is the small-scale (subgrid-scale) parameter.

This method strikes a balance between accuracy and computational cost, allowing for a larger simulation domain without an excessive increase in computing requirements. However, large-scale atmospheric phenomena, such as pressure systems, cannot be fully resolved within the simulation, as expanding the domain to such sizes would be computationally prohibitive. To address this limitation, as demonstrated by Wiegant and Verzijlbergh (2019)[95] and Taschner et al. (2024)[79] using GRASP, LES domains are kept within a reasonable size, while general circulation models (GCMs) provide the initial and boundary conditions. GCMs simulate global weather patterns while parameterizing smaller-scale atmospheric variations, making them suitable for coupling with LES simulations. For this thesis, periodic boundary conditions will be set to model a uniform and steady inflow rather than obtaining real scenarios from GCMs. The use of realistic atmospheric inflow is outside the scope of this study.

GRASP originates from the Dutch Atmospheric Large-Eddy Simulation (DALES) code, described by Heus et al. (2010b)[28], but has been adapted for graphics processing units (GPUs), which significantly accelerate LES simulations compared to traditional central processing units (CPUs) (Jerôme et al., 2012)[40]. This GPU-based approach has drastically increased the efficiency of LES, making it a valuable tool for operational weather forecasting. Furthermore, the implementation of wind turbines in GRASP is highly accurate (Taschner et al., 2024)[79], enabling reliable power forecasting for offshore wind farms.

Some examples of using LES codes such as GRASP for weather hind-casting and operational forecasting are as follows. Gilbert et al. (2019)[22] demonstrated the proof of concept for using GRASP for operational forecasting at the Horns Rev I wind farm. Schepers et al. (2021)[68] presented a hind-casting application of GRASP, where they carried out a year-long LES simulation to study the effect of extreme events on the aero-elastic loads of a 10MW wind turbine. These studies utilized LES with periodic boundary conditions prescribed by large-scale weather models. As will be discussed

in Subsection 2.4.3, this approach requires additional source terms in Equation 2.7, which represent the large-scale subsidence, pressure gradients (expressed in terms of geostrophic wind), large-scale advective tendencies, and a relaxation term to avoid model drift. For further detail on model drift, see the article by Schalkwijk et al. (2015)[66].

GRASP allows for the parallel simulation of multiple nested LES domains, where the outer domain influences the inner domains, with only the innermost domain containing the wind turbines. This setup enables wind farm simulations with periodic boundary conditions and large-scale forcing while preventing turbine wake recirculation, which would otherwise occur in a single periodic domain (Vollmer et al., 2017)[91]. Alternative large-scale forcing methods in the literature bypass the assumption of horizontal homogeneity inherent to GRASP by avoiding periodic boundary conditions, but this comes at the cost of restricting the range of allowable wind directions (Santoni et al., 2020)[65].

2.4.3 Numerical Theory of GRASP

This subsection details the numerical theory underlying the GRASP LES code, incorporating relevant methodological aspects to enhance clarity. Initially, the governing equations of the GRASP LES code are presented, with a comprehensive explanation of each term. Subsequently, the subgrid-scale model section introduces subgrid theory and three selected turbulence closure approaches that utilize the eddy viscosity concept. These are the Smagorinsky model, the Dynamic Smagorinsky model, and Rozema's Minimum Dissipation Model. These specific models are detailed to facilitate the subgrid-scale model selection discussion in Subsection 3.4.5. Following this, the spatial discretization method implemented in GRASP is described, along with the theoretical underpinnings of its available momentum advection schemes. Finally, the temporal discretization scheme available in GRASP is explained, detailing the methodology for computing the necessary maximum domain velocity for a rolling wind turbine. Given that the GRASP theory introduced herein forms the basis for the methodology of this thesis, some overlap with Chapter 2.5 is inevitable.

Governing Equations

As mentioned in Subsection 2.4.2, GRASP is a code that utilizes LES. LES applies a filter to the grid of the control volumes in the domain. Turbulent eddies larger than the filter width are resolved, while those smaller, with less kinetic energy, are modeled by a subgrid-scale (SGS) model. Unlike RANS, which relies on time-averaged Reynolds decomposition, LES employs spatial filtering. This process separates physical variables into a filtered (resolved) part and a subgrid-scale (modeled) part. The notation for this, as introduced in Equation 2.5, uses $\bar{u}_i$ for the filtered (resolved) large-scale parameter and u_i' for the small-scale (subgrid-scale) parameter. Fluctuations are represented with $\tilde{u}_i$.

The GRASP model differs from DALES by implementing an anelastic approximation in its formulations (Böing et al., 2012)[10]. The governing equations for filtered mass and filtered momentum, are given in Equation 2.6 and Equation 2.7, respectively.

$$\frac{\partial \rho_b \bar{u}_j}{\partial x_j} = 0 \tag{2.6}$$

$$\rho_b \frac{\partial \bar{u}_i}{\partial t} + \frac{\partial \rho_b \bar{u}_i \bar{u}_j}{\partial x_j} = -\frac{\partial \bar{p}'}{\partial x_i} + \rho_b b \delta_{i3} - \frac{\partial \tau_{ij}}{\partial x_j} + \epsilon_{ij3} f_c (\bar{u}_j - u_j^g) + f_i^{WT} + f_i^{Fringe} \tag{2.7}$$

Here, $i \in$ 1,2,3 according to the Einstein summation convention (Taschner et al., 2024)[79]. $\rho_b = \rho_b(x_3)$ is the specified reference density profile, $\bar{u}_i$ is the filtered velocity, b is the buoyancy term $b = -g(\rho'/\rho_b)$, where g is the gravitational constant and $\rho' = \rho - \rho_b$ is the density fluctuation. $\bar{p}'$ is the filtered pressure fluctuation, where $\bar{p}' = \bar{p} - \langle \bar{p} \rangle$, and $\langle ... \rangle$ denotes the horizontal mean. τ_{ij} is the subgrid-scale stress tensor, a term that will be further discussed. f_c is the Coriolis forcing parameter, u_j^g is the geostrophic wind velocity, f_i^{WT} is the body force generated by the wind turbine, the procedure for obtaining which will be explained in further detail in Subsection 2.4.7. f_i^{Fringe} represents additional forcing terms applied to the flow to impose large-scale tendencies. These large-scale tendencies include large-scale subsidence, pressure gradients (expressed in terms of geostrophic wind), large-scale advective tendencies, and a relaxation term to avoid model drift (Taschner et al., 2024)[79]. It is necessary to include these large-scale tendencies as an additional forcing term because studies using LES to solve flow in large farms have limitations on the domain size due to computational costs. As large-scale effects are felt at the scale of farms, they are accounted for by an additional forcing term that essentially represents these effects. These terms are however turned off for the current study on a single turbine.

Time integration can be performed with either a fixed or variable time step using a third-order Runge–Kutta method (Wicker and Skamarock, 2002)[94]. Given the periodic boundary conditions in the streamwise and lateral directions, a pressure solver based on the fast Fourier transform is used to enforce the continuity equation. This solver operates on the periodic pressure fluctuation field ($\bar{p}'$), ensuring that the computed pressure fluctuations satisfy continuity (Taschner et al., 2024)[79].

Subgrid-Scale Model

LES does not resolve all scales of motion. Instead, it employs a filter to partition the domain into resolved and unresolved subgrid-scales. Motions larger than this filter are computed by Equation 2.7. To account for scales smaller than the filter, the SGS stress tensor, denoted as τ_{ij}, is incorporated into the momentum equation.

The subgrid-scale stress tensor is defined by Equation 2.8.

$$\tau_{ij} = \overline{u_i u_j} - \bar{u}_i \bar{u}_j \tag{2.8}$$

This formulation quantifies the influence of the unresolved scales on the resolved scales. However, this formulation is unclosed, presenting an analogous closure problem to that encountered in Reynolds-averaged Navier-Stokes (RANS) equations. In both cases, the process of averaging or filtering the governing equations introduces new, unknown terms that represent the effects of unresolved motions. SGS models are employed to provide closure for this term.

The Smagorinsky model, proposed by Smagorinsky (1963)[73], is widely recognized for its simplicity and is one of the most common SGS models. This eddy viscosity model establishes an analogy between the action of small eddies and molecular viscosity. It postulates that the anisotropic component of the SGS stress tensor is proportional to the resolved strain rate tensor (Blazek, 2015)[7]. This is namely the Boussinesq hypothesis (Schmitt, 2007)[71] which is given in Equation 2.9.

$$\tau_{ij} - \frac{1}{3}\tau_{kk}\delta_{ij} = -2\nu_{sgs}\bar{S}_{ij} \tag{2.9}$$

The isotropic component of the SGS stress tensor, $\frac{1}{3}\tau_{kk}\delta_{ij}$, is typically absorbed into the modified pressure term within the momentum equation. As it is a diagonal term, it does not directly influence the flow dynamics. Consequently, this term is generally omitted from the SGS stress tensor equation (Meneveau, 2016)[56]. δ_{ij} is the Kronecker delta. ν_{sgs} is the eddy viscosity, a scalar representing the effective viscosity due to subgrid-scale turbulence. Lastly, $\bar{S}_{ij}$ is the resolved strain rate tensor, calculated from the filtered velocity gradients.

$$\bar{S}_{ij} = \frac{1}{2}\left(\frac{\partial \bar{u}_i}{\partial x_j} + \frac{\partial \bar{u}_j}{\partial x_i}\right) \tag{2.10}$$

Variations among eddy viscosity models primarily stem from their respective formulations for the eddy viscosity. This represents an approximation-based modeling of the unresolved scales, with the accuracy of this approximation differing across models. For the Smagorinsky model, the eddy viscosity is defined as in Equation 2.11.

$$\nu_{sgs} = (C_S\Delta)^2|\bar{S}| \tag{2.11}$$

C_S is the Smagorinsky constant, which requires calibration based on the specific numerical configuration and flow characteristics. Typically, its value ranges from 0.08 to 0.23. Common values cited for isotropic turbulence are $C_S \approx 0.17$, and for anisotropic turbulence, $C_S \approx 0.1$. Nevertheless, the optimal value can vary with the particular application. This constant significantly influences the magnitude of SGS dissipation. A higher C_S results in greater dissipation, thereby preventing the modeling of smaller, lower-energy eddies. Conversely, a lower C_S leads to reduced dissipation (Blazek, 2015)[7].

Δ is the filter width. It is defined as the characteristic length scale filtering the resolved and unresolved eddies and is typically related to the grid size. For uniform grids, it can be approximated as the cube-root of the cell volume. $|\bar{S}|$ is the magnitude of the resolved strain rate tensor, given in Equation 2.12.

$$|\bar{S}| = \sqrt{2\bar{S}_{ij}\bar{S}_{ij}} \tag{2.12}$$

Physically, the eddy viscosity aims to emulate the dissipation of kinetic energy and its transfer from large, resolved scales to small, unresolved scales. In the Smagorinsky eddy viscosity equation, the term $(C_S\Delta)^2$ serves as a scaling factor. The magnitude of the resolved strain rate tensor, $|\bar{S}|$, quantifies the local intensity of turbulence. Consequently, regions exhibiting high strain rates result in a large eddy viscosity and increased dissipation, accurately reflecting enhanced turbulent transfer (Blazek, 2015)[7].

Given the limitations of the Smagorinsky model, which are elaborated upon in Subsection 3.4.5, alter-

native approaches to SGS modeling have been proposed. Dynamic eddy viscosity models represent one such alternative.

The Dynamic Smagorinsky Model (DSM) is a type of dynamic eddy viscosity model which uses the same relation as the Smagorinsky model for the evaluation of the eddy viscosity, but offers a dynamic way to compute the scaling coefficient that varies in space and time. A significant drawback of the Smagorinsky model is its assumption of a universal Smagorinsky constant, C_S. In reality, this constant exhibits variability with local flow conditions, necessitating careful calibration for each distinct flow. To mitigate this limitation, dynamic eddy viscosity models compute this coefficient locally and dynamically during the simulation. This is achieved by introducing a test filter, denoted by a hat over the parameter, which is a coarser filter applied to the already filtered velocity field (Meneveau, 2016)[56]. The mathematical formulation of this model is beyond the scope of this work and therefore will be excluded.

The coefficient employed for the eddy viscosity in the DSM model is considerably more intricate than that in the Smagorinsky model. However, this complexity is justified by its ability to address the limitations of the Smagorinsky model through the dynamic derivation of the constant from the magnitude of the strain rate tensor, rather than its manual prescription.

Another approach to subgrid-scale modeling is the Rozema's Anisotropic Minimum Dissipation (AMD) model that employs a modified version of Poincaré's inequality (Rozema et al., 2015)[64] to bound the energy of the subgrid-scale. This inequality establishes that the subgrid energy is bounded by the resolved velocity gradient energy. From this, an equation for the eddy viscosity is derived based on the minimum eddy dissipation condition, which requires sufficient dissipation to counteract the production of scaled velocity gradient energy. A significant feature of this formulation is its direct use of velocity gradients, rather than invariants of the rate of strain tensor, making it particularly advantageous for anisotropic grids.

Rozema's model adheres to fundamental physical principles, such as energy conservation, and is designed to be minimally dissipative while retaining essential properties of the subgrid-scale stress tensor. It accurately predicts zero subgrid-scale dissipation for a wide range of resolved flows, including laminar regimes, eliminating the need for manual tuning or complex dynamic procedures (Rozema et al., 2015)[64].

Spatial Discretization

GRASP employs an Arakawa C-grid for spatial discretization, utilizing a staggered arrangement where cell centers and faces correspond to full and half levels, respectively (Taschner et al., 2024)[79]. This is visualized in Figure 2.3. All prognostic variables are positioned at the cell center, except for the three velocity components. For instance, in the x-direction (i = 1), the velocity component in x-direction (u) is located at the half level along the x-axis denoted by subscript h, while it resides at full levels in the y- and z-directions denoted by subscript f in the coordinates.

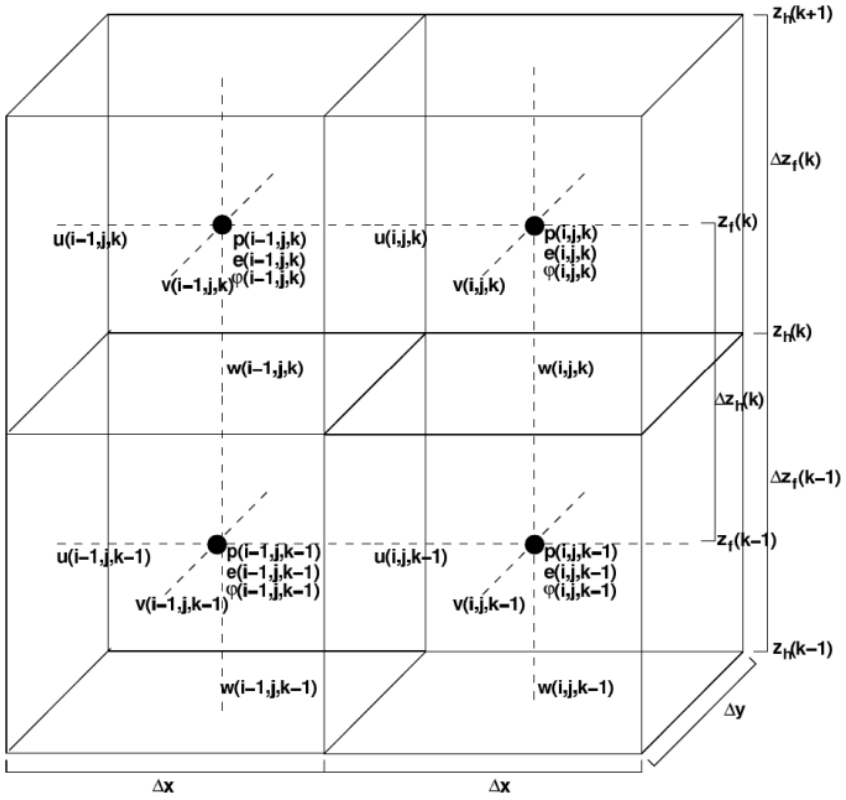

Figure 2.3: The Arakawa C-grid used in GRASP (Lundquist et al., 2010)[52].

Momentum Advection Scheme

The advection schemes available for vector prognostic variables are the second and fifth-order central difference schemes. The choice of the numerical scheme is crucial in order to accurately simulate the flow and maintain stability.

Advection is discretized using the flux form which has the following form in the x-direction given in Equation 2.13.

$$\frac{\partial(u\phi)}{\partial x} \approx \frac{u_{i+\frac{1}{2}}\phi_{i+\frac{1}{2}} - u_{i-\frac{1}{2}}\phi_{i-\frac{1}{2}}}{\Delta x} = \frac{F_{i+\frac{1}{2}} - F_{i-\frac{1}{2}}}{\Delta x} \tag{2.13}$$

$F_{i-\frac{1}{2}}$ represents the convective flux of the an arbitrary prognostic variable ϕ through the $i-\frac{1}{2}$ plane. ϕ is given by Equation 2.14.

$$\phi_{i+\frac{1}{2}} = \frac{\phi_i + \phi_{i+1}}{2}, \qquad \phi_{i-\frac{1}{2}} = \frac{\phi_{i-1} + \phi_i}{2} \tag{2.14}$$

Documentation of DALES (Heus et al., 2010a)[27], from which GRASP is derived from, explains the formulation of the fifth-order scheme. In order to obtain a fifth-order scheme, a sixth-order scheme is first formulated. Adding a small artificial dissipation term to it results in a fifth-order scheme with near-monotonicity. Near-monotone means that the advection scheme has the ability to dampen the generation of artificial oscillations.

The sixth order scheme for $F_{i-\frac{1}{2}}$, derived by Heus et al. (2010a)[27], is given in Equation 2.15.

$$F_{i-\frac{1}{2}}^{6th} = \frac{u_{i-\frac{1}{2}}}{60}[37(\phi_i + \phi_{i-1}) - 8(\phi_{i+1} + \phi_{i-2}) + (\phi_{i+2} + \phi_{i-3})] \tag{2.15}$$

The fifth-order scheme is given as the sixth-order scheme minus the small artificial dissipation term, as shown in Equation 2.16.

$$F_{i-\frac{1}{2}}^{5th} = F_{i-\frac{1}{2}}^{6th} - \left|\frac{\tilde{u}_{i-\frac{1}{2}}}{60}\right|[10(\phi_i + \phi_{i-1}) - 5(\phi_{i+1} + \phi_{i-2}) + (\phi_{i+2} + \phi_{i-3})] \tag{2.16}$$

The dissipative term acts to dampen spurious oscillations, making the scheme more robust for flows with sharp gradients or discontinuities.

Temporal Discretization & Maximum Velocity Determination

The selection of the timestep for integrating the governing equations is based on the Courant-Friedrichs-Lewy (CFL) condition. This condition serves as a stability criterion for explicit time-marching schemes. GRASP utilizes a third-order explicit Runge-Kutta scheme (Whiffle, 2025)[93]. The CFL criterion ensures that the timestep (Δt [s]) is sufficiently small such that fluid elements do not propagate across more than a specified characteristic distance per timestep, relative to the spatial resolution. The equation for this criterion is given in Equation 2.17.

$$CFL = \frac{u_{max} \cdot \Delta t}{\Delta x} \tag{2.17}$$

To adequately resolve tip vortices, it is generally recommended that the blade tip does not traverse more than one grid cell per timestep. Given that regions near the rotor are typically refined and characterized by small grid cells, this often necessitates the use of a timestep corresponding to a CFL number less than unity (Krishnendu, 2025)[46].

Here, u_{max} [m/s] denotes the maximum velocity within the computational domain if a safe but conservative approach is followed, Δx [m] is the characteristic grid dimension, and CFL is the dimensionless Courant number. The aforementioned requirement to maintain the Courant number below unity is specifically applicable to explicit time-marching schemes to prevent numerical instabilities. In contrast, implicit schemes permit the use of CFL values greater than unity. For wind turbine CFD analyses, particularly when blades are geometrically resolved or represented by actuator lines, a reduced timestep is generally required due to the high velocities of the blades for accurate resolution of tip vortices (Jha et al., 2014a)[41], (Sheidani et al., 2022)[72].

The maximum velocity encountered within the domain is, in most scenarios, defined by the tip speed of the rotor. The effective tip speed can be computed by incorporating the influence of floating body motion.

Roll introduces an additional velocity component within the rotor plane. The largest velocity within a cycle is at the instant the blade is crossing the 12 o'clock position when the turbine is rolling at maximum velocity in the same direction. The maximum roll velocity occurs at 0° of roll angle.

The roll motion imposed is described by a sinusoidal function, as presented in Equation 2.18.

$$\phi(t) = \phi_0 \cos(2\pi f_\phi t) \tag{2.18}$$

Where ϕ_0 represents the amplitude [rad] and f_ϕ the frequency [Hz] of the roll motion. The linear velocity at the top of the turbine turbine is given by the product of the angular velocity of the roll motion and the total height from turbine base to blade tip at the vertical position. This relationship is formulated in Equation 2.19.

$$v_{roll} = \dot{\phi}(t) \times (H_{hub} + R) = 2\phi_0 \pi f_\phi \cos(2\pi f_\phi t) \times (H_{hub} + R) \tag{2.19}$$

The resultant velocity at the blade tips is the superposition of the velocity due to rotor rotation and the velocity induced by the roll motion. Vectoral summation is required for this. The rotational component can be derived from the tip-speed ratio (TSR) equation, presented in Equation 2.20.

$$\lambda = \frac{\Omega R}{U_\infty} \tag{2.20}$$

Where λ denotes the TSR, U_∞ [m/s] is the undisturbed inflow velocity, Ω [rad/s] is the angular rotational velocity of the rotor, and R [m] is the rotor radius. The rotor speed, Ω, is constant throughout the oscillatory motion.

The maximum velocity is the vectoral sum of the maximum roll velocity, $v_{roll\ max}$, and linear velocity due to rotor motion ΩR. The direction of vectors can be approximated at the top position of the blade such that a simple scalar summation can be applied instead. The maximum roll velocity, $v_{roll\ max}$, occurs when the cosine term is unity. The resulting equation for u_{max} due to roll is provided in Equation 2.21.

$$u_{max\ roll} = 2\phi_0 \pi f_\phi (H_{hub} + R) + \Omega R \tag{2.21}$$

It is noteworthy that in the computation of the maximum velocity due to roll, the axial inflow velocity is assumed to be significantly smaller than the in-plane velocities. Consequently, velocity triangles were not utilized to incorporate out-of-plane velocity components.

Finally, the $u_{maxroll}$ will be employed in the calculation of the timestep for their respective simulation cases. The specific Courant number will be determined in Subsection 3.4.4.

2.4.4 OpenFAST

Given the complex coupling between aerodynamics, hydrodynamics, control, and structural dynamics in a FOWT, the system becomes an aero-servo-hydro-elastic problem. Codes such as OpenFAST (National Renewable Energy Laboratory, 2024)[59], which accurately capture these interactions, are essential for reliable simulations.

OpenFAST consists of multiple modules where each module is used to compute a part of the turbine dynamics. The most relevant and important of these modules include AeroDyn, HydroDyn, Moordyn, ServoDyn and ElastoDyn which are further explained in detail below. The OpenFAST glue code orchestrates the coupling of various modules, enabling the integrated simulation of nonlinear aero-servo-hydro-elastic wind turbine dynamics. The user can also link OpenFAST to external programs

as it offers a C++ application programming interface (API) (Taschner et al., 2024)[79]. This feature is used to develop the model that will be used for this thesis which couples OpenFAST with the LES code GRASP.

The module AeroDyn is responsible for resolving the aerodynamics at the blade. This module works by discretizing the blades and the tower using nodes. These nodes are spread along the blade forming actuator lines. This essentially forms the basis of the ALM which will be further explained in Subsection 2.4.7. AeroDyn receives information from OpenFAST about the orientation, position and flow velocity at each node based on all turbine dynamics. Based on BET which relies on two-dimensional airfoil data, the local lift and drag forces and pitching moment are calculated. From these, loads are obtained over the entire span of the blade. More on the BET is given in Subsection 2.4.6.

The ElastoDyn module calculates the structural dynamics of the turbine. This module is necessary for use because the turbine's desired DOF for blades, tower, generator and nacelle are set in this module. ElastoDyn receives aerodynamic loads from the AeroDyn module and controller commands and determines the resultant displacements, structural velocities and accelerations and reaction loads. Note that the structural displacements are turned off during this study, assuming the turbine is rigid. Additionally, for imposed motion, this module's definition inputs are used to model the state-space formulation of the system as explained in Subsection 2.2.

The ServoDyn module is related to the control aspects of the turbine. These include the blade pitch, generator torque and nacelle yaw. ServoDyn also has an interface, namely DISCON, which allows for integration of external turbine controllers. This module is not used during this thesis. More on the explanation of this can be found in Subsection 3.2.

The HydroDyn module that computes the hydrodynamic loads and determines the systems response for FOWTs and the Moordyn module that computes the mooring loads will not be used because floating motion will be imposed. Therefore, there is no necessity to use this module and is simply turned off to simplify the simulations.

In order to impose roll motion, the ExtPtfm module is used. This external module allows for the definition of motion in terms of imposed loading in time on the platform of the turbine.

The aerodynamics determined at the blade by the module AeroDyn has an influence on the wake of the turbine. Since the LES code GRASP is used for out of rotor plane simulations of aerodynamics, as is the wake, there needs to be a coupling between the nodes in OpenFAST with the grid of the LES domain. This will be explained in Subsection 2.4.7. To allow for computations of the wake to be done by GRASP, the wake feature is turned off in AeroDyn.

2.4.5 The GRASP-OpenFAST Coupling

Taschner et al. (2024)[79] demonstrates the newly developed coupling between LES code GRASP with OpenFAST. Although the GRASP solver utilizes the GPU, through its application programming interface (API), called ASPIRE, OpenFAST plugin running on the CPU can be coupled. This coupling is possible via a new ASPIRE plugin coded in C++ which is called AspFAST. AspFAST works to synchronize the GRASP simulations with OpenFAST simulations, allows for exchange of information concerning forces, velocity, turbine blade position, and orientation.

A schematic provided by (Taschner et al., 2024)[79] of the interrelations of each modules of the code is provided in Figure 2.4.

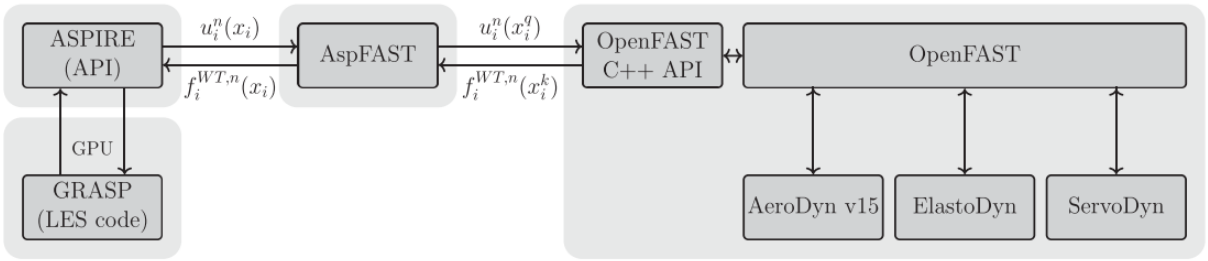

Figure 2.4: Schematic of the simulation environment showing the integration of AspFAST to allow coupling between GRASP and OpenFAST (Taschner et al., 2024)[79].

The ASPIRE plugin, AspFAST, facilitates communication between the LES solver and the OpenFAST C++ API at each time step t^n. Additionally, it handles the sampling of LES velocity at actuator points and the projection of point forces onto the LES grid.

It must be noted that there are two types of discrete points on the blades where different parameters are computed on. In OpenFAST, the blade is discretized with both force actuator points (N_F) and velocity actuator points (N_V). The number of these points are not equal therefore an interpolation is required to match them. The number of N_F points is a variable and specified in AspFAST but the number of N_V is determined by the number of blade sections along the blade which is set in the module AeroDyn. As a result, an increase in the velocity actuator points requires interpolation of the initial blade input data to the desired number of N_V points (Taschner et al., 2024)[79].

The notation shown in Figure 2.4 and that will be used from on here is as follows. The subscript, i, refers to the spatial direction following the Einstein summation convention. The superscripts, k, and q, represent the k^{th} force and q^{th} velocity actuator point respectively. The superscript n represents the time step placed as the superscript of t.

The simulation with the scheme shown in Figure 2.4 is initialized by the user input including information about the number of turbines, their position and N_F which are read by OpenFAST and communicated to OpenFAST via the OpenFAST C++ API. At each time step, AspFAST receives information of the complete LES velocity field $u_i^n(x_i)$ from GRASP and the current position of the points of the blades for the force and velocity points, x_i^k, and x_i^q respectively from OpenFAST. The LES velocity

at the current time step at the velocity actuator point $u_i^n(x_i^q)$ is sampled with linear interpolation from the nearest LES grid point x_i and then sent to OpenFAST. OpenFAST uses this input to advance the turbine model by one time step after calculating aerodynamic loads with AeroDyn and updating the actuator point locations.

This methodological approach to couple the flow physics occurring at the simulation domain using LES with turbine loading physics is proven to be an efficient and effective approach.

2.4.6 Blade Element Theory

AeroDyn calculates the spanwise distribution of aerodynamic forces acting on the blade using BET which uses two-dimensional blade element assumption to look up at airfoil lift and drag data to compute the load per element (Jonkman et al., 2017)[43]. The velocity locally at each blade element at each time step is computed with Equation 2.22.

$$U^n_{relative} = \sqrt{(u^n_{axial}(x_i^q))^2 + (\Omega^n r^q - u^n_\theta(x_i^q))^2} \tag{2.22}$$

Where $u^n_{axial}(x_i^q)$ is the axial, $u^n_\theta(x_i^q)$ is the tangential velocities sampled at each velocity point on the blade and $\Omega^n r^q$ is the linear velocity of the blade element at q^{th} $\mathsf{N_V}$. Ω denotes the angular velocity of the rotor. From Equation 2.22, the local inflow angle is given in Equation 2.23.

$$\phi^n(x_i^q) = \arctan\left(\frac{u^n_{axial}(x_i^q)}{\Omega^n r^q - u^n_\theta(x_i^q)}\right) \tag{2.23}$$

The velocities are expressed in blade-aligned coordinate system for simplicity, ($\mathsf{x}_1, \mathsf{x}_2, \mathsf{x}_3$) = ($r$, θ, x). The local angle of attack ($\alpha^n(x_i^q)$) is the difference between the inflow angle ($\phi^n(x_i^q)$) and the geometric blade angle ($\gamma^n(x_i^q)$). The geometric blade angle is the sum of the blade local twist and the collective blade pitch angles.

$$\alpha^n(x_i^q) = \phi^n(x_i^q) - \gamma^n(x_i^q) \tag{2.24}$$

As previously mentioned, the local lift and drag forces are obtained via look-up tables for lift and drag coefficients. These tables are a function of Reynold's number and the angle of attack. From the coefficients, the lift and drag forces per unit span at a blade element located at a point of $\mathsf{N_V}$ is calculated from Equation 2.25 and Equation 2.26 respectively.

$$\frac{F^n_L(x_i^q)}{\Delta r(x_i^q)} = \frac{1}{2}\rho(U^n_{relative}(x_i^q))^2 \mathsf{c}(x_i^q)\mathsf{C}^n_\mathsf{L}(x_i^q) \tag{2.25}$$

$$\frac{F^n_D(x_i^q)}{\Delta r(x_i^q)} = \frac{1}{2}\rho(U^n_{relative}(x_i^q))^2 \mathsf{c}(x_i^q)\mathsf{C}^n_\mathsf{D}(x_i^q) \tag{2.26}$$

where air density is ρ, $\Delta r(x_i^q)$ denotes the spanwise extent of the blade element that has been discretized which is associated to the actuator point and $\mathsf{c}(x_i^q)$ is the chord length at the blade element. The resultant force vector is transformed into the LES Cartesian coordinate system and communicated to AspFAST for the actuator points x_i^k (Taschner et al., 2024)[79].

In order to obtain the power and torque of the turbine, the normal and tangential forces need to

be obtained. Following the geometry shown in Figure 2.5, the normal and tangential forces can be derived from the lift and drag forces and are given in Equation 2.27 and Equation 2.28 respectively.

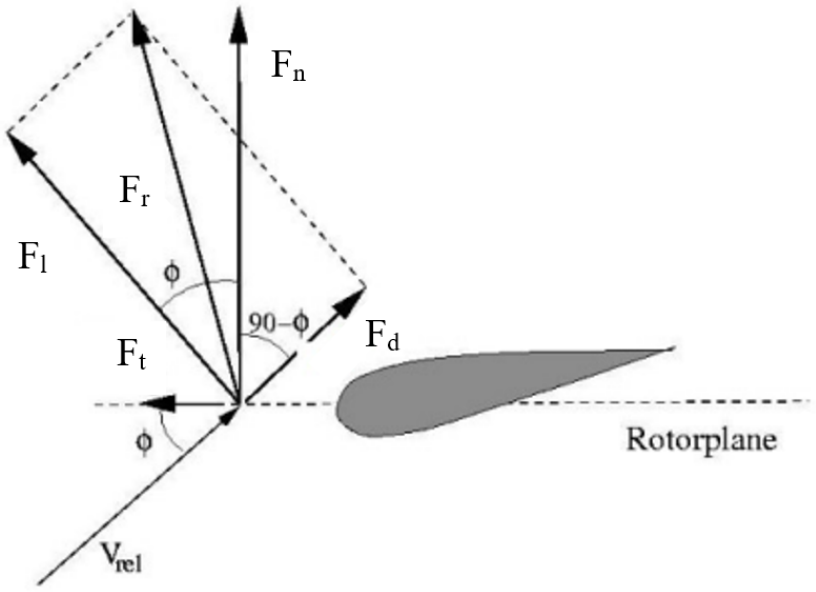

Figure 2.5: Loads on a blade element (Hansen, 2008)[25].

Where in the figure, F_l is the lift per unit element, equivalent to $\frac{F_L^n(x_i^q)}{\Delta r(x_i^q)}$ in Equation 2.25. Same logic applies to F_d, F_n and F_t.F_r is the resultant force per unit element.

$$\frac{F_N^n(x_i^q)}{\Delta r(x_i^q)} = \frac{F_L^n(x_i^q)}{\Delta r(x_i^q)} \cos\left(\phi^n(x_i^q)\right) + \frac{F_D^n(x_i^q)}{\Delta r(x_i^q)} \sin\left(\phi^n(x_i^q)\right) \tag{2.27}$$

$$\frac{F_T^n(x_i^q)}{\Delta r(x_i^q)} = \frac{F_L^n(x_i^q)}{\Delta r(x_i^q)} \sin\left(\phi^n(x_i^q)\right) - \frac{F_D^n(x_i^q)}{\Delta r(x_i^q)} \cos\left(\phi^n(x_i^q)\right) \tag{2.28}$$

The normal and tangential forces represent the blade loading and are indicators of the momentum deficit and the swirl added to the wake respectively. Due to their direct relation to the wake characteristics, these are the forces that are of interest when analyzing the influence of blade loading on the wake.

2.4.7 (Filtered) Actuator Line Method & Force Projection onto LES Grid

This subsection details both the methodology of the actuator line method (ALM) and the additional steps applied to enhance the accuracy of the model, resulting in the filtered actuator line Method (FALM). The ALM approach incorporates force smearing to project the loads computed on the nodes onto the LES grid which is thoroughly explained.

ALM is a tool commonly used in CFD for modeling the rotating blades of a wind turbine. Unlike full blade-resolved simulations, ALM represents blades as rotating lines of actuator points, significantly reducing computational cost while retaining key flow physics.

The points forces $f_i^{WT,n}(x_i^k)$ obtained on N_F points is spread across multiple LES grid points using a convolution with a constant Gaussian kernel, η_ϵ, with a prescribed kernel width, ϵ. ϵ is also known as

the smearing parameter. The purpose of smearing is to spread out the load from single points so that the load distribution is realistic. The equation of the Gaussian kernel and the convolution are given in Equation 2.29 and Equation 2.30 respectively.

$$\eta_\epsilon = \frac{1}{\epsilon^3 \pi^{3/2}} \cdot \exp\left(\frac{-(x_i - x_i^k)^2}{\epsilon^2}\right) \tag{2.29}$$

$$f_i^{WT,n}(x_i) = f_i^{WT,n}(x_i^k) \circledast \eta_\epsilon \tag{2.30}$$

Where $(x_i - x_i^k)$ is the distance between the LES grid point and the location of the force point N_F in OpenFAST. Following this convolution, the force that the LES domain feels from the set of points on the blade is ensured to be smooth and more representative of the actual distribution. The convolved resulting force defined on the LES domain, $f_i^{WT,n}$, is input into GRASP momentum equation, Equation 2.7.

The set of steps given in Equation 2.29 and Equation 2.30 outline the process of ALM explained by Sorensen and Shen (2002)[74]. The shortcomings of ALM lie in the over-prediction of blade loads which in turn impacts the power generation. When ϵ is too large, wider and weaker tip vortices are induced and smaller associated induced velocities resulting in wrong estimation of the angle of attack and an overestimation of the generated lift (Stanly et al., 2022)[76]. Martínez-Tossas et al. (2017)[53] concluded that this occurs when the Gaussian kernel width selected is larger than the value found to be optimal, ϵ^{opt} = 0.25c where c is the blade's chord length. However, an optimal Gaussian kernel width is difficult to work with due to its resulting highly refined grid which is infeasible to use for LES simulations on a large scale. Therefore, Martínez-Tossas and Meneveau (2019)[54] proposed a subfilter correction that applies to the sampled LES velocity. This leads to filtered-ALM (FALM) which fixes the main but not all shortcomings of ALM since the same modeling assumptions still persist.

Taschner et al.'s (2024)[79] work demonstrates the implementation of FALM to GRASP. FALM works by determining the resolved and the missing part of the induced velocity to be able to correct the sampled LES velocity. The sampled LES velocity which OpenFAST takes as an input, is determined on a grid which leads to a sub-optimal kernel size due to computational limitations of the grid refinement mentioned previously. The corrected velocity equation is shown in Equation 2.31.

$$\hat{u}_i^n(x_i^k) = u_i^n(x_i^k) + \Delta u_{i,induced}^n(x_i^k) \tag{2.31}$$

Where $u_i^n(x_i^k)$ is the sampled LES velocity and $\Delta u_{i,induced}^n(x_i^k)$ is the subfilter velocity correction accounting the difference in resolved and optimal-induced velocity at the k^{th} force actuator point N_F.

The derivation of the equation for induced velocity is outside of the scope of this thesis, but can be found in the paper by Taschner et al. (2024)[79].

After a thorough analysis on the difference of FALM and ALM, Stanly et al. (2022)[76] concluded that FALM predicts stronger induced velocities mainly at the root and the tip and as a result larger blade loads. FALM compared to experimental data, only over-predicts power by 1%, as opposed to 12.96% for ALM under the numerical conditions chosen. This is a significant difference. However, analyzing

the flow field in the wake, FALM did not show significant difference in the flow field compared to that of ALM. According to Stanly et al. (2022)[76], the increase in computational time due to FALM is only by 1%. Hence, it is strongly beneficial to implement FALM as the emphasis placed on blade loading is high for this study.

AspFAST receives the force vectors from OpenFAST always at the force actuator points N_F. This is the reason that the entire calculations of FALM, including the velocities defined on the k^{th} force actuator points, are carried out on these points. Only the final corrected LES velocities are translated onto the velocity actuator points N_V before they are sent to OpenFAST.

2.5 The Reference IEA 15 MW Turbine

The purpose of this thesis is to understand the relationship between turbine motion and the near-wake of any turbine regardless of its design. However, for a more relevant analysis, a 15 MW turbine has been selected which has a commonly seen power rating for turbines used in the offshore industry nowadays.

The key parameters of the IEA-15 MW offshore turbine relevant to the research in this paper are given in Table 2.2.

Table 2.2: Key parameters for the IEA-15 MW offshore turbine (Gaertner et al.,2020)[19].

Parameter	Value	Unit
Power rating (P_{rated})	15	MW
Cut-in wind speed (U_{cutin})	3	m/s
Rated wind speed (U_{rated})	10.59	m/s
Cut-out wind speed (U_{cutout})	25	m/s
Rotor diameter (D)	240	m
Hub height (H_{hub})	150	m
Design tip-speed ratio (λ_{design})	9	-
Minimum rotor speed (Ω_{min})	5.0	RPM
Maximum rotor speed (Ω_{max})	7.56	RPM
Design power coefficient ($C_{P,design}$)	0.489	-
Design thrust coefficient ($C_{T,design}$)	0.799	-

The operation of a turbine is distinctively split into two regions shown by Figure 2.6. These are the below rated region and the above rated region, which are split by the rated velocity, and end with the cut-in and the cut-out velocity respectively.

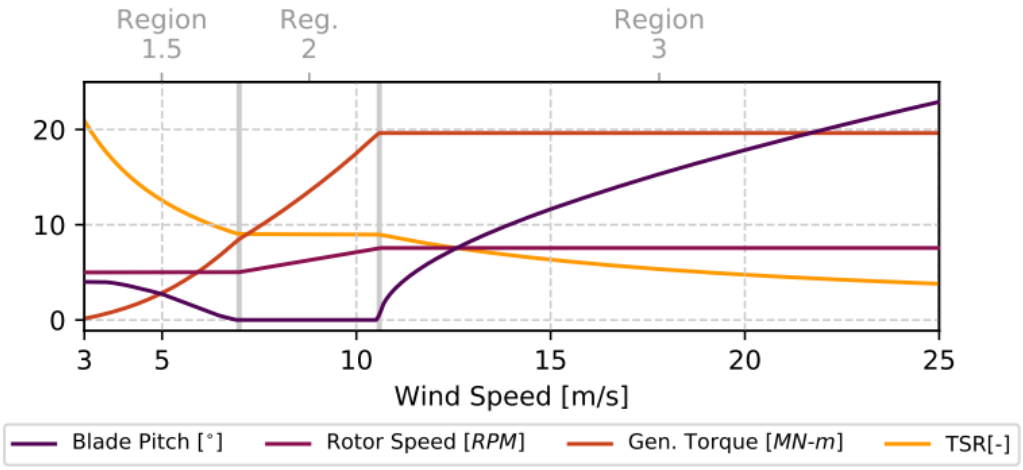

Figure 2.6: The idealized control curve of the IEA 15 MWW turbine showing the operational tip-speed ratios and blade pitch angles (Gaertner et al., 2020)[19].

Between cut-in and rated wind speeds, the turbine maximizes power output by optimizing the Tip Speed Ratio (TSR) to achieve the highest power coefficient (C_P). This is done by measuring rotor speed and adjusting generator torque, resulting in power increasing cubically with wind velocity. Above rated wind speed, the turbine's goal shifts to maintaining a constant rated power to prevent generator overload. This is primarily accomplished by adjusting the blade pitch angle, which reduces the angle of attack, thereby decreasing lift and drag. In this region, generator torque is typically held near its rated value.

Turbine controller is not a part of this study and is only introduced to support the explanations in the methodology, specifically in Subsection 3.2.

3

Numerical Set-Up

This chapter focuses on the presentation of the choices made for the numerical simulations. It begins with the presentation of test cases, along with the rationale for their selection to address the research questions in Subsection 3.1. Subsequently, Section 3.4 provides a thorough investigation of the effects of identified numerical input parameters and outlines their selection procedure. The chapter concludes with Section 3.5, which explains the input files necessary for properly running simulations and obtaining results.

3.1 Test Case Selection

Research on the effects of floating motion on turbine wake aerodynamics suggests that both the frequency and amplitude of floating platform motions, across all degrees of freedom, significantly influence the turbine's wake characteristics.

To systematically investigate the effect of these parameters on the near-wake, a set of cases has been formulated for numerical analysis. The selection of cases aims to cover a range of operational conditions. To comprehensively address the research questions given in Section 2.3, a range of magnitudes for these parameters is selected.

The selection of frequency and amplitude, detailed in Subsection 3.1.1, is not based on site-specific data, unlike much of the existing literature. Since the objective of this thesis is to analyze blade loading and its direct effects on the near-wake, the imposed motion is not necessarily based on realistic conditions. However, the conditions are maintained within realistic bounds, even though some selected cases will be highly unsteady to induce the unsteady loading and wake phenomena. While the selected motions classified as unsteady are still probable, their likelihood of occurrence within a turbine's lifetime is very low. Such conditions are most likely observed only during extreme events such as storms. Consequently, the low probability of these motions is not a concern, as the primary focus of this study is to understand the relationship between blade loading and the very near-wake.

3.1.1 Amplitude and Frequency Selection

For the selection of amplitude and frequency in roll, reduced quantities have not been utilized. Roll angles defining the amplitude are specified in degrees [°], which are dimensionless on itself. The resulting selection is provided below.

$$\phi_0 = [5^\circ, 10^\circ]$$

$$f_\phi = [0.03 \text{ Hz}, 0.05 \text{ Hz}]$$

The objective in selecting test cases was to impose roll motion such that its effects would be noticeable. This necessitated amplitudes large enough to produce significant displacement and frequencies high enough to induce substantial velocity due to roll, resulting in a significant variation of the resultant velocity on the blade. Although the kinematics is far more complex, the formulation for the TSR of the turbine can be used to simplify the problem. The absolute percentage variation of the TSR for each roll configuration is presented in Subsection 3.1.2 within Table 3.1.

3.1.2 Tip-Speed Ratio Selection

The TSR values are selected such that the rotor speed for a fixed inflow velocity of 10 m/s lies within the operational rotor speed range specified in Table 2.2.

The operational TSR, according to the control curve in Figure 2.6, is 9 at the selected inflow velocity. This value was chosen as one of the TSRs to enable simulation as close to real operational conditions as possible.

A second TSR value of 7 has been selected, which is below the operational TSR for this inflow velocity. Although the turbine operates sub-optimally in this configuration, it is essential for the study to investigate the effect of TSR on blade loading and near-wake aerodynamics. This value was chosen as the second TSR because it is neither too close to 9, which would risk negligibly differing results, nor too small, which would lead to unrealistic imposed control.

The final selected TSR values, denoted by λ, are summarized below.

$$\lambda = [7, 9]$$

The rotor speeds corresponding to these values, given an inflow velocity of 10 m/s and a rotor radius of 120 m, are 5.57 RPM and 7.16 RPM respectively. These speeds fall within the operational range of the turbine as provided in Table 2.2. These rotor speeds will be kept constant for their respective test cases by turning the controller off to simplify the analysis of the problem. More on the reasoning for this is explained in Subsection 3.2.

Although the rotor speed and the inflow velocity is kept constant, the TSR of the rotor varies due to roll motion which induces additional velocity at the blade. This velocity can be split into tangential and radial component, of which the former influences the TSR. More on this is explained in the kinematic study of the rolling wind turbine given in Section 5.1.

Resulting from the operational rotor speed computed from the set TSR per case and the roll configurations introduced in Subsection 3.1.1, Table 3.1 is generated. This table shows the percentage variation of TSR in a single cycle of roll and is crucial for quantifying the significance of roll in terms of its effect on TSR, which, in turn, leads to fluctuations in blade loading, performance coefficients, and wake characteristics, all of which will be examined in this thesis.

Table 3.1: Tip-speed ratio variation during a single cycle per roll configuration shown absolutely and in terms of percentage differece.

Roll Motion					
f_ϕ [Hz]	$f_{\phi,reduced}$ [-]	ϕ_0 [°]	λ_{fixed} [-]	$\lvert\Delta\lambda_{\text{max}}\rvert$ [-]	$\lvert\Delta\lambda_{\text{max}}\rvert$ [%]
0.03	0.72	5	7	0.44	6.3
0.03	0.72	10	7	0.89	12.7
0.05	1.2	5	7	0.74	10.57
0.05	1.2	10	7	1.48	21.1
0.03	0.72	5	9	0.44	6.3
0.03	0.72	10	9	0.89	12.7
0.05	1.2	5	9	0.74	10.57
0.05	1.2	10	9	1.48	21.1

Where $|\Delta\lambda_{\text{max}}|$ is the amplitude of TSR variation expressed in absolute and percentage terms. For example the first case has a TSR variation of $[\lambda_{\text{fixed}} - |\Delta\lambda_{\text{max}}|, \lambda_{\text{fixed}} + |\Delta\lambda_{\text{max}}|]$ = [6.56, 7.44]. $f_{\phi,reduced}$ is the non-dimensional form of the frequency obtained via the equation $f_{\phi,reduced} = \frac{f_\phi D}{U_\infty}$.

The oscillation amplitude has been computed by first determining the maximum tip speed only due to roll motion using the first part of Equation 2.21. In reality, the TSR of the turbine is not constant throughout the rotor in roll motion but instead depends on the location of the blade and how much of the roll induced linear velocity aligns with the tangential component of velocity at the blade tip. Further explanations of this is left for the kinematics study in Section 5.1.

The reason for Table 3.1 being plotted is that it indicates that a wide range of TSR are considered, which will result in a varying range of significance on the aforementioned parameters.

3.2 A Note on Wind Turbine Controller

To address the research questions listed in Section 2.3, the control scheme for the IEA 15 MW turbine, introduced in Section 2.5, was not implemented. Consequently, the rotor speed and blade pitch angle, the two controlled parameters, are maintained constant throughout the simulation. While this approach causes the simulations and subsequent results to deviate from realistic conditions, the simplification of the problem was considered important. This research serves as a baseline for future studies, thus reducing the number of untested variables is beneficial.

This approach has implications for the realism of the results; however, realism is not the primary objective. Instead, the focus is on identifying flow characteristics induced by roll motion that are not observed in fixed cases, and analyzing how these characteristics vary with differing roll motions. This comparative analysis reduces the significance of controller implementation.

The rotor speed is determined by the TSR selected for each respective case, as presented in Table 3.2. The blade pitch angle is fixed at 1°. These differences must be considered when referencing data in the verification section of Chapter 3.5.

3.3 Summary of Test Cases

A full factorial approach is employed in this study to capture all interaction effects and provide a comprehensive description of the influence of roll frequency, amplitude, and TSR on blade loading and near-wake characteristics.

The final set comprises 10 cases, including two baseline cases featuring fixed turbines at the specified TSR. A complete list of these cases, along with their respective IDs, is presented in Table 3.2.

Table 3.2: Test cases selected for analysis.

Roll Motion				
Case ID	f_ϕ [Hz]	$f_{\phi,reduced}$ [-]	Amplitude [°]	λ [-]
002	0.03	0.72	5	7
003	0.03	0.72	10	7
004	0.05	1.2	5	7
005	0.05	1.2	10	7
006	0.03	0.72	5	9
007	0.03	0.72	10	9
008	0.05	1.2	5	9
009	0.05	1.2	10	9
Bottom-Fixed				
Case ID	f [Hz]	$f_{reduced}$ [-]	Amplitude [°/m]	λ [-]
010	-	-	-	7
011	-	-	-	9

3.4 Numerical Set-up

The numerical setup methodology encompasses the selection of simulation-specific parameters. These include domain size, grid size, nudging configuration, momentum advection scheme, time-stepping scheme, subgrid-scale model, and (filtered) actuator line method-specific parameters, each of which is discussed in the following subsections.

While prior studies offer guidance on some of these parameters, the results obtained from the chosen numerical configuration must still be validated against other findings, as these are purely numerical inputs without direct physical significance, and their influence on the solution must be carefully assessed.

To simplify the numerical set-up, a bottom-fixed turbine is utilized for the comparison of various cases, for example when comparing the effects of domain size. This approach is adopted because a rolling turbine introduces additional parameters for the roll motion itself, such as roll amplitude. It also complicates comparisons, which would need to account for the phase of the roll motion.

3.4.1 Computational Domain and Grid Size Selection

This subsection details the steps taken for selecting the domain size, turbine positioning, and grid size. These numerical parameters demonstrably exert a significant impact on the accuracy and reliability of the numerical simulations. Ideally, the domain should be maximized in size while the grid size is minimized. However, computational time and cost limitations necessitate a compromise in numerical simulations, precluding this ideal setup.

Domain Size Selection

The initial step involved determining the domain size. The selection of the lateral (Y) and vertical (Z) domain dimensions is primarily driven by blockage effects. Blockage, resulting from the rotor's presence within the computational domain, leads to increased flow velocity around the rotor due to mass conservation, inaccurate pressure distributions, and consequently, incorrect modeling of the wake and, critically, the turbine's performance. The blockage ratio (BR) of a rotor is defined as the area ratio of the frontal rotor area to the domain plane area where inflow is prescribed.

According to Franke et al. (2004)[17], a BR of less than 3% is generally recommended for CFD simulations in urban environments with respect to the numerical domain, a guideline also applicable to wind turbines. Furthermore, a sensitivity analysis by Van Leeuwen (2025)[89] indicates that reducing the BR below 3% has minimal additional impact on the rotor performance coefficients.

Consequently, the domain's lateral and vertical dimensions were both set at 5.3D, yielding a BR of 2.8%, as demonstrated in subsubsection 3.4.1. This configuration was determined to be a sufficient compromise between accuracy and computational cost.

$$BR = \frac{\frac{\pi D^2}{4}}{L_y \times L_z} \cdot 100\% = \frac{\frac{\pi \cdot 240^2}{4}}{5.3 \cdot 240 \times 5.3 \cdot 240} \cdot 100\% \approx 2.80\%$$

The selection of the domain size in the roll direction, laterally (Y), is based only on the blockage ratio. The effects of blockage are widely understood, allowing an acceptable domain size in the plane of the rotor to be chosen reliably. The introduction of roll motion does not significantly influence this choice. Even with the largest roll angle of 10°, as given in Table 3.2, the rotor moves only $0.11D$ closer to the edge of the domain. This lateral displacement of the hub is computed from the tower height (150m) multiplied by the sine of the 10° roll amplitude. Normalizing this displacement by the rotor diameter provides the aforementioned result.

The determination of the streamwise length of the domain (X) remains and the greatest focus of the domain size selection is on this. To achieve an optimal size, with the study's objective of analyzing the wake immediately behind the rotor in mind, various configurations were investigated. These options are listed below in the form (L_x, L_y, Lz).

- $7.5D \times 5.3D \times 5.3D$
- $8.5D \times 5.3D \times 5.3D$
- $9.6D \times 5.3D \times 5.3D$
- $14.9D \times 5.3D \times 5.3D$

Given the focus on studying the wake in close proximity to the blades, L_x options typically considered

small for wind turbine domains were predominantly examined. A large domain behind the turbine is not strictly necessary for this purpose. The largest L_x option, 14.9D, was considered solely for comparative purposes. As the objective is to minimize domain size while mitigating numerical effects, comparing smaller domains with a larger one proves beneficial. However, this larger domain becomes infeasible when the grid refinement necessary for a proper near-wake study is applied, owing to GPU memory limitations.

The specific decimal values for the dimensions result from GRASP's requirement to round the number of nodes in the domain to a multiple of 32. This constraint is a memory requirement of the code.

Prior to analyzing the domain size, the turbine's positioning in the streamwise direction must be determined. To this end, the test cases were expanded beyond the aforementioned list by defining specific turbine locations.

1. $7.5D \times 5.3D \times 5.3D -$ turbine at $3D$
2. $7.5D \times 5.3D \times 5.3D -$ turbine at $5D$
3. $8.5D \times 5.3D \times 5.3D -$ turbine at $2D$
4. $8.5D \times 5.3D \times 5.3D -$ turbine at $3D$
5. $9.6D \times 5.3D \times 5.3D -$ turbine at $3D$
6. $9.6D \times 5.3D \times 5.3D -$ turbine at $5D$
7. $14.9D \times 5.3D \times 5.3D -$ turbine at $3D$
8. $14.9D \times 5.3D \times 5.3D -$ turbine at $5D$

Initially, the domain with an $8.5D$ dimension was not tested, meaning only turbine positions of $3D$ and $5D$ had been considered. In a later part of the study, the $8.5D$ case was investigated with $2D$ and $3D$ turbine positions, as $5D$ was concluded to be needlessly large. This information is provided at this step to prevent confusion. Further details will be presented during the comparison analysis.

For each domain, the spatial and temporal resolutions were selected coarsely, with a grid size $(\Delta x, \Delta y, \Delta z)$ = (8m $\times$ 8m $\times$ 8m) and the time-stepping set to a Courant number of 0.8. The selected nudging to the precursor simulation utilized a factor of 0.95 and an extent of 0.06 in the streamwise direction. In the lateral and vertical directions, the same factor is used but with an extent of 0.01. All analyses were conducted for a fixed turbine operating at a TSR of 7 with an inflow velocity of 10 m/s.

The time-averaged velocity profiles at varying downstream locations of the bottom-fixed turbine for cases where the turbine position is at $3D$ from the domain inlet are presented in Figure 3.1.

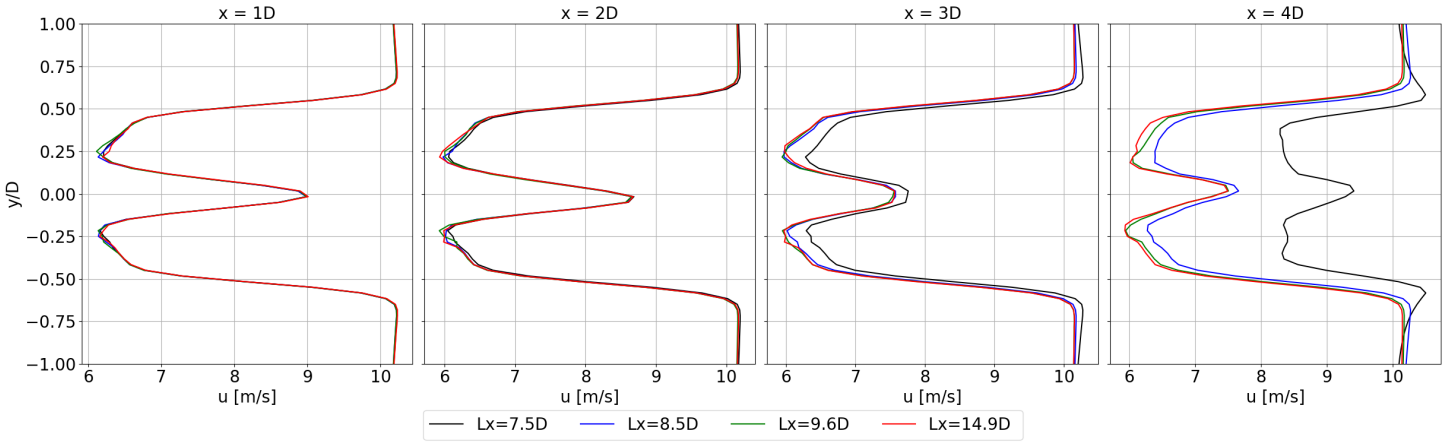

Figure 3.1: The effect of streamwise domain size (L_x), on the time-averaged velocity profile at various downstream locations of the turbine placed at $3D$ behind the domain inlet.

The objective is to minimize the domain size in the streamwise direction while preventing numerical effects from the downstream boundary propagating upstream. More specifically, effects caused by the nudging of the cursor simulation to the precursor simulation. The requirement for the unaffected area was set at $2D$ downstream of the turbine. While small for a general turbine wake study, this limited extent is advantageous for maximizing grid refinement given the focus on the near-wake just behind the turbine. Therefore, examining Figure 3.1, all test cases satisfy this requirement because they are representative of the largest test case with $L_x = 14.9D$ until at least $2D$. This largest test case serves as a reference due to the certainty that numerical effects around the tested region are insignificant with such an extensive domain size. As anticipated, the effects of nudging downstream become apparent first for the smallest domain, $L_x = 7.5D$, at approximately $3D$, and subsequently for the case with $L_x = 8.5D$ at around $4D$.

Another observation from these plots is that the velocity outside the wake is slightly higher than the inflow velocity of 10 m/s. This is attributable to blockage effects, as mass conservation necessitates flow acceleration when the turbine and its wake are present within the domain.

Concluding from Figure 3.1, the domain $7.5D \times 5.3D \times 5.3D$ has been selected. To this point, only a turbine position of $3D$ downstream of the inlet has been considered. However, other options for its position, including $2D$ and $5D$, have been tested and require evaluation. These are plotted in Figure 3.2.

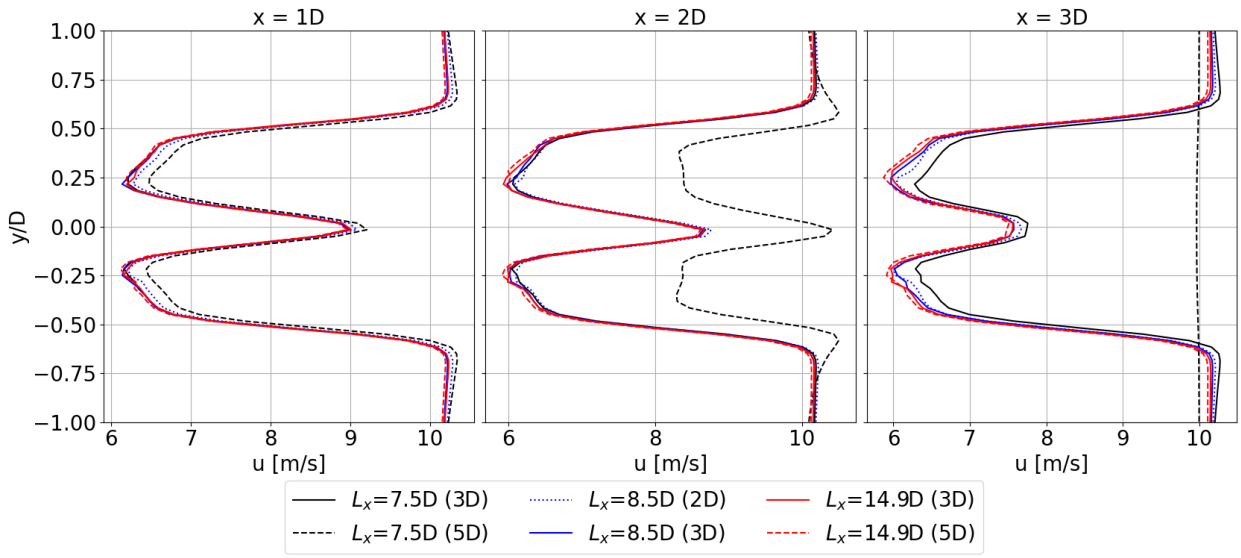

Figure 3.2: The effect of turbine position from the domain inlet and streamwise domain size (L_x), on the time-averaged velocity profile at various downstream locations of the turbine.

Analysis of Figure 3.2 indicates that a configuration with $L_x = 7.5D$ and a turbine position of $5D$ is not feasible due to the limited distance between the turbine and the downstream boundary. As demonstrated in Figure 3.1, the $L_x = 7.5D$ (turbine at $3D$) case presents a promising candidate, though further investigation is required to ascertain if positioning the turbine at $2D$ would constitute a more optimal configuration. For the $L_x = 8.5D$ domain, a turbine position of $2D$ was tested, revealing an even closer similarity to the $L_x = 14.9D$ reference case, particularly beyond $2D$ downstream. The objective in determining the optimal configuration can be summarized as maximizing the downstream unaffected distance while minimizing the overall domain size, which inherently translates to minimizing the distance between the upstream boundary and the turbine. However, the situation is more complex. While $L_x = 7.5D$ with the turbine at $2D$ appears optimal based on wake recovery, positioning the turbine excessively close to the inlet can induce interference between the rotor's induction field and the upstream boundary. Such interference may lead to incorrect interpretation of it's performance. Therefore, a definitive conclusion can only be drawn after these aspects are thoroughly evaluated. These coefficients are summarized for all test cases in Table 3.3.

Table 3.3: The effect of turbine position and streamwise domain size on the time-averaged thrust and power coefficients.

Test Case	C_T	C_P
$7.5D \times 5.3D \times 5.3D$ – turbine at $3D$	0.703	0.454
$7.5D \times 5.3D \times 5.3D$ – turbine at $5D$	0.704	0.457
$8.5D \times 5.3D \times 5.3D$ – turbine at $2D$	0.707	0.463
$8.5D \times 5.3D \times 5.3D$ – turbine at $3D$	0.703	0.455
$9.6D \times 5.3D \times 5.3D$ – turbine at $3D$	0.703	0.455
$9.6D \times 5.3D \times 5.3D$ – turbine at $5D$	0.702	0.452
$14.9D \times 5.3D \times 5.3D$ – turbine at $3D$	0.704	0.457
$14.9D \times 5.3D \times 5.3D$ – turbine at $5D$	0.702	0.453

According to Figure 4.1, for the current configuration with a TSR of 7 and a blade pitch angle set to 0°, the turbine should operate at approximately C_T = 0.650 and C_P = 0.44. Even though these coefficients are obtained from Blade Element Momentum Theory (BEMT), a lower-fidelity method, they are used for reference because they are documented in the official IEA 15 MW documentation by Gaertner et al. (2020)[19]. Differences in these coefficients from the current study are anticipated, primarily due to differing code fidelity, limited domain size in the lateral and vertical directions, and a coarse grid of 8 m in size in all directions. Blockage effects can lead to an overestimation of these coefficients due to flow acceleration near the wake. These reference values are utilized solely to ensure that the coefficients do not diverge significantly.

For all test cases shown in Table 3.3, a closer proximity of the turbine to the upstream boundary correlates with a greater overestimation of C_T and C_P. An exception is observed for the smallest domain size with L_x = $7.5D$, where moving the turbine downstream in such a small domain causes it to fall under the influence of nudging, thereby rendering the results unreliable. The highest coefficients are observed in the test case where the turbine is placed closest to the inlet boundary, at $2D$. This suggests that the turbine should not be positioned this close, potentially due to the aforementioned interference effects between the induction region and the inlet. Finally, examining the L_x = $7.5D$ $(3D)$ case, its coefficients are reasonably close to those of the test case that would experience the least numerical influences but be unfeasible for the required grid refinement, namely L_x = $14.9D$ $(5D)$.

As a conclusion, the test case $7.5D \times 5.3D \times 5.3D$ – turbine at $3D$ has been selected for this study due to its sufficiently aligned velocity profiles up to the desired location and its representative performance coefficients. The visualization of this domain with the turbine, including the coordinate system used, is shown in Figure 3.3.

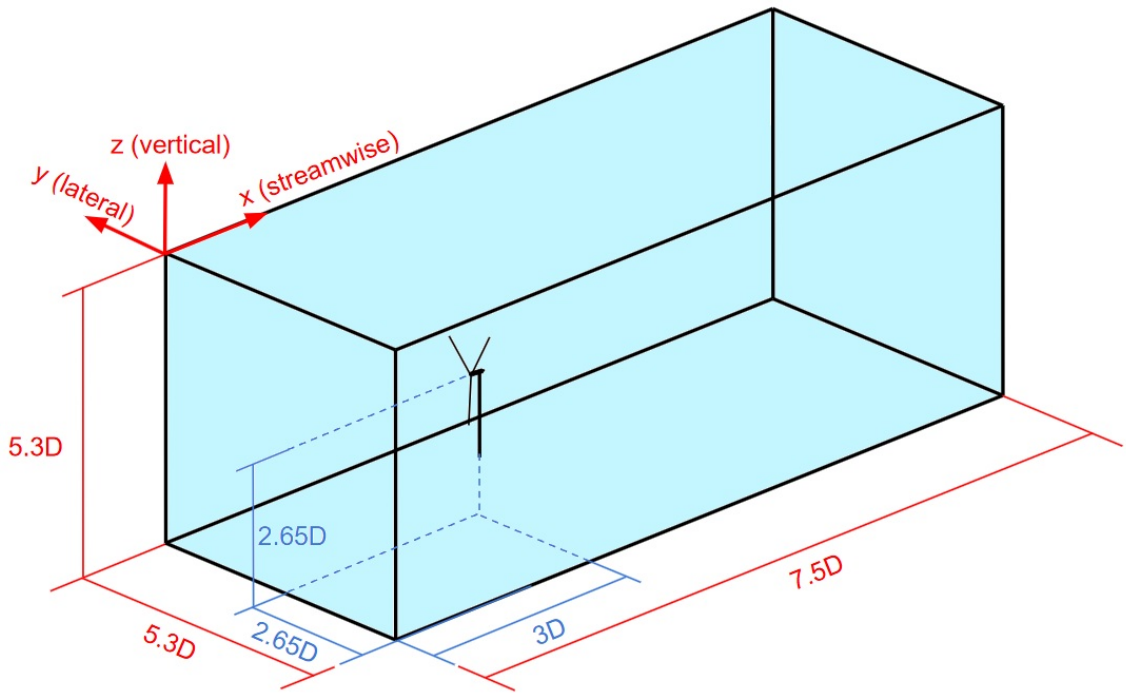

Figure 3.3: Numerical domain and the turbine position.

Grid Size Selection

GRASP does not permit local grid refinement, which would have been extremely beneficial for flow analysis at and immediately behind the blade. Consequently, the selected grid applies to the entire computational domain.

An isotropic grid with dimensions $\Delta x, \Delta y, \Delta z = 3.5\text{m}, 3.5\text{m}, 3.5\text{m}$ has been selected, resulting in a total of 63,438,848 nodes in the domain with the selected domain size. This choice aligns with the recommendations of Hodgson et al. (2023a)[32]. Hodgson et al. specifies that for proper resolution of tip vortices, which are crucial for near-wake studies, the grid size must be at least 32 times smaller than the rotor radius. With a rotor diameter of 240 m, this implies a maximum grid size of 3.75 m. A grid size of 3.5 m was chosen due to the available GPU memory on the DelftBlue supercomputer (TU Delft, 2025)[84], a benefit of the domain size optimizations performed in previous steps, and because 3.5 m is a convenient size for defining the domain dimensions.

This grid size was determined to be sufficient for analyzing the turbulence structures in the near-wake behind the rotor, although a smaller size would always offer greater benefits. However, the limits of GPU memory have been reached, and further refinement would necessitate a smaller domain, which would be too restrictive for obtaining reliable results.

3.4.2 Nudging Configuration Selection

Periodic boundary conditions are employed in GRASP for this study. This is a commonly utilized type of boundary condition in numerical wind turbine aerodynamics analysis due to its ability to facilitate smaller domains without compromising result reliability, simplify the application of boundary conditions, and provide a more efficient approach to modeling turbulent inflow. For these reasons, excluding the reasoning for turbulence generation, this type of boundary condition has been adopted.

Periodic boundary conditions operate by solving two simulations: the precursor and the cursor. The precursor simulation primarily serves as a boundary/initial condition for the domain in which the turbine is situated within the cursor simulation. Although periodic boundary conditions simplify the simulation setup, they introduce the concept of nudging. The downstream domain in the cursor simulation is 'nudged' towards the precursor simulation before this flow is recycled back into the cursor domain. The nudging must be configured appropriately to obtain representative results. As this is a purely numerical input for the simulation and challenging to select correctly, a thorough study is undertaken.

Nudging is characterized by the nudging factor and the nudging extent. The nudging factor is a dimensionless value that determines the strength of the nudging. This value can be set to any number except 1, due to potential numerical instabilities (Whiffle, 2025)[93]. The nudging extent defines the fraction of the domain size that is under the effect of nudging. This is a number between 0 and 1, but it is not recommended to assign a value close to 1, as this would result in most of the domain being influenced by nudging. Results obtained in regions under the influence of nudging are inaccurate because the flow in those regions, particularly within the wake, is accelerated to the prescribed inflow velocity. One approach is to minimize the extent and maximize the factor to reduce this affected region while still achieving effective nudging. While this seems like a solution, the risk of this is that

it can lead to artificial damping of oscillatory motion in the flow such as vorticity which is a crucial parameter of this study.

To be able to determine the ideal nudging configuration, a list of test cases has been prepared and is provided below.

1. Factor: 0.65, Extent: 0.06
2. Factor: 0.65, Extent: 0.12
3. Factor: 0.65, Extent: 0.24
4. Factor: 0.95, Extent: 0.01
5. Factor: 0.95, Extent: 0.06
6. Factor: 0.95, Extent: 0.12
7. Factor: 0.95, Extent: 0.24
8. Factor: 1.10, Extent: 0.01
9. Factor: 1.10, Extent: 0.06
10. Factor: 1.10, Extent: 0.12

These test cases only apply nudging extent to the streamwise direction. In the lateral and vertical directions, a default value of 0.01 is used and no further study is needed because the wake is only required to be nudged to ensure there is no deficit in the inflow which travels only in the streamwise direction. The nudging factor selected for the streamwise direction also applies to the lateral and vertical directions.

A nudging extent of 0.01 for a factor of 0.65, and an extent of 0.24 for a factor of 1.10 have not been used for analysis because the nudging effects would be too small and too large respectively. All of the testing runs have been done in the domain determined previously of configuration $7.5D \times 5.3D \times 5.3D -$ turbine at $3D$.

Before the velocity profiles are plotted, the convergence of the domain in time is studied by visualizing the spatial average of horizontal velocity on the xy-plane in time. This is shown in Figure 3.4.

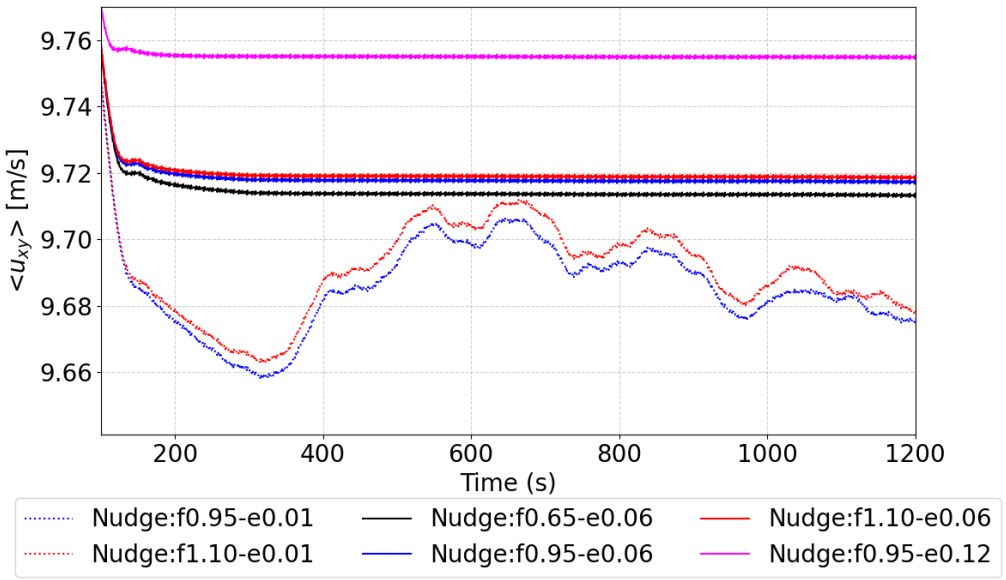

Figure 3.4: Spatial average of the horizontal velocity component, u, on the xy-plane plotted in time for all configurations of nudging factor and extent.

The initial conclusion drawn from Figure 3.4 is that cases with a nudging extent of 0.01 (dotted) do not achieve convergence to a specific constant value within the simulated time. This indicates that such a small extent is insufficient, thereby demonstrating the importance of nudging for convergence. This is due to the extent being too small to sufficiently nudge the outflow to the target inflow velocity, resulting in the effects of wake on the turbine's inflow.

As anticipated, a higher nudging extent results in a larger average velocity because a greater fraction of the wake in the streamwise direction is accelerated towards the prescribed inflow velocity of 10 m/s. Consequently, a higher inflow velocity, closer to 10 m/s, is achieved. Conversely, the nudging factor does not exert as much influence, as evidenced by the three central lines. While a higher factor will marginally increase the average velocity, the nudging effect is not significant.

Based solely on Figure 3.4, the optimal combination of nudging factor and extent for the simulation cannot be accurately deduced. This plot is only useful to understand the effects of both nudging parameters on the streamwise velocity distribution in the domain. To determine whether the nudging configuration selected is acceptable, the velocity distributions at various downstream locations must be verified with references that do not utilize periodic boundary conditions. This is done in Subsection 4.2 and Subsection 4.3. However, before verifying the results, these parameters are roughly determined in this subsection by plotting the velocity profile in the inflow and simultaneously studying the velocity profile in the wake. All such time-averaged velocity profiles are presented in Figure 3.5.

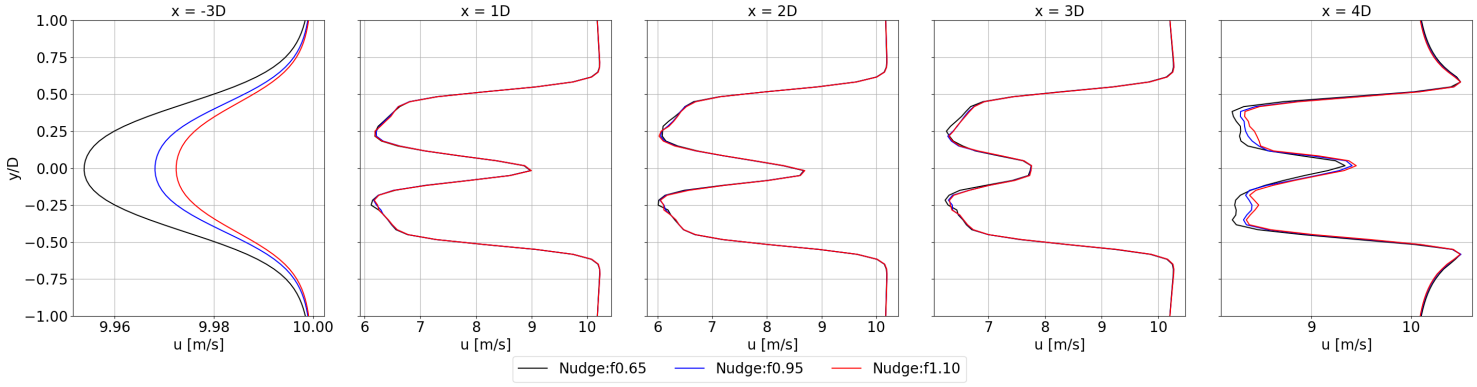

(a) The effect of nudging factor on the time-averaged velocity profile at various locations of the domain for nudging extent of 0.06.

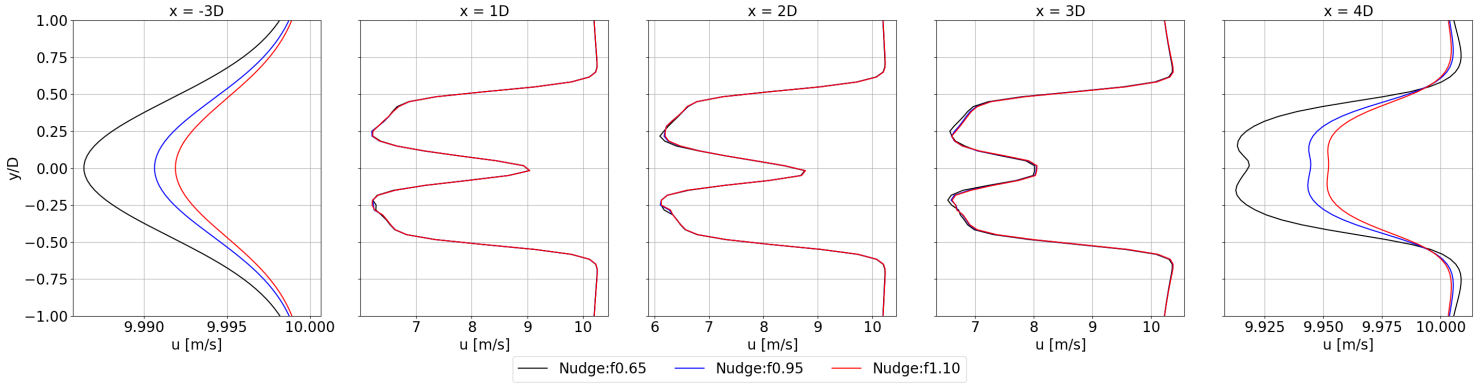

(b) The effect of nudging factor on the time-averaged velocity profile at various locations of the domain for nudging extent of 0.12.

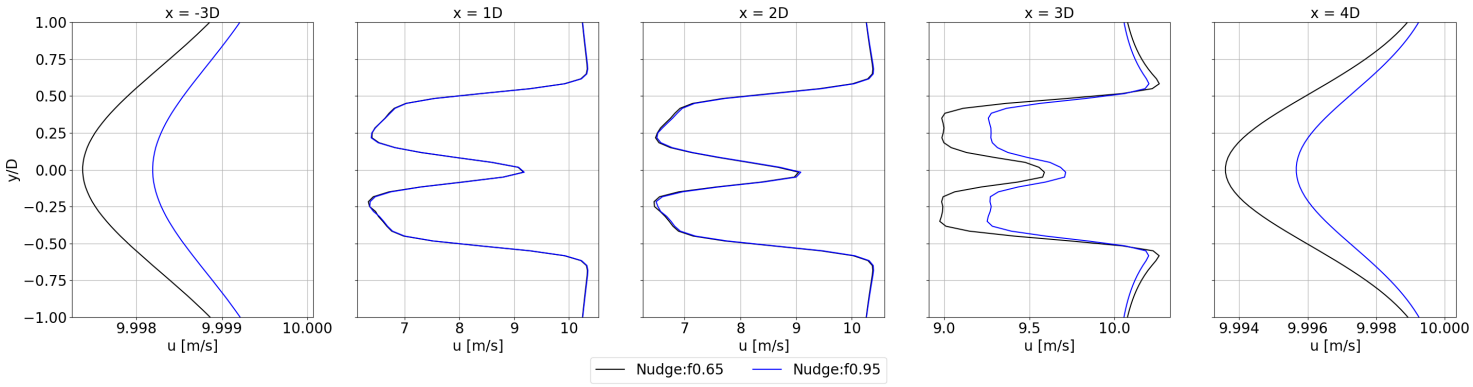

(c) The effect of nudging factor on the time-averaged velocity profile at various locations of the domain for nudging extent of 0.24.

Figure 3.5: The effect of nudging factor and extent on the time-averaged velocity profiles at various locations of the domain.

Observation of Figure 3.5a reveals that the nudging factors do not induce a significant difference in the velocity profile within the wake up to $4D$ downstream. This is acceptable, as flow accuracy is only required up to $2D$ downstream, as specified during domain size selection. The general trend across all plots in Figure 3.5 indicates that the impact of the chosen nudging factor is only visible in regions directly influenced by nudging, as determined by its extent. This explains why significant differences are primarily observed in the profiles at $-3D$ and $4D$, near the domain boundaries. Only in Figure 3.5c does the velocity profile diverge at $3D$ downstream for factors of 0.65 and 0.95, because the extent of 0.24 is large enough for this effect to be seen closer to the turbine.

Analyzing the inlet velocity profiles at $-3D$ from the turbine, the nudging extent demonstrates an influence on the inflow velocity deficit, caused by wake recirculation, by a factor of 10. From these plots, it was determined that the inflow velocity deficit for a nudging extent of 0.06 in Figure 3.5a is excessively large for any of the selected nudging factors. Ideally, no deficit should be present, but this is challenging to achieve without compromising downstream simulation accuracy, especially given the minimized domain size.

The other two options, nudging extents of 0.12 and 0.24, are considered good candidates. It was subsequently decided that, although it does not impact the minimal analysis region ($2D$ downstream of the turbine), a nudging extent of 0.24 represents a large fraction of the domain and would restrict analysis to within $2D$. In the event that an interesting finding emerges between $2D$ and $3D$ in future analyses, a smaller extent such as 0.12 would still allow for reliable study. A nudging factor of 0.95 was selected from the velocity profile at $-3D$ in Figure 3.5b because a factor of 0.65 exhibits an excessively large inflow deficit while not significantly differing from other downstream profiles until much further ($4D$) for this analysis. A nudging factor of 1.10 was avoided, as it could cause velocity overshoots or over-dampening. Since the nudging factor applies to all boundaries, including lateral and vertical directions, there was also concern that velocities near these boundaries would be amplified over time with a nudging factor above 1.

Summarizing, the selected configuration of nudging factor of 0.95 with an extent of 0.12, is deter-

mined to be satisfactory of the requirements set for the representativeness of the domain for the given domain size and rotor position. Given that there is negligible deficit at the inlet, as is the case shown in Figure 3.5b, the last step remains to verify the configuration in Chapter 3.5. However before this, the remaining numerical parameters need to be chosen.

3.4.3 Momentum Advection Scheme Selection

For this study, following established literature, it is essential to utilize the fifth-order central difference scheme for momentum to fully leverage the grid refinement. A second-order scheme would yield lower errors for a coarse grid, but with the current levels of refinement, it tends to produce unrealistic oscillations, excessive dispersion, and can become unstable.

For this study, the grid was semi-refined to $(\Delta x, \Delta y, \Delta z)$ = $(5\text{m} \times 5\text{m} \times 5\text{m})$ to mitigate the likelihood of increased errors that can arise from using coarse grids with higher-order schemes while keeping the simulations computationally cheap.

The difference between the inflow of the two identical cases is observable in Figure 3.6. At $2D$ upstream of the turbine, where the inflow consists of recirculated flow due to the employment of periodic boundary conditions, the second-order scheme shows a highly oscillatory inflow compared to the steady inflow of the fifth-order scheme.

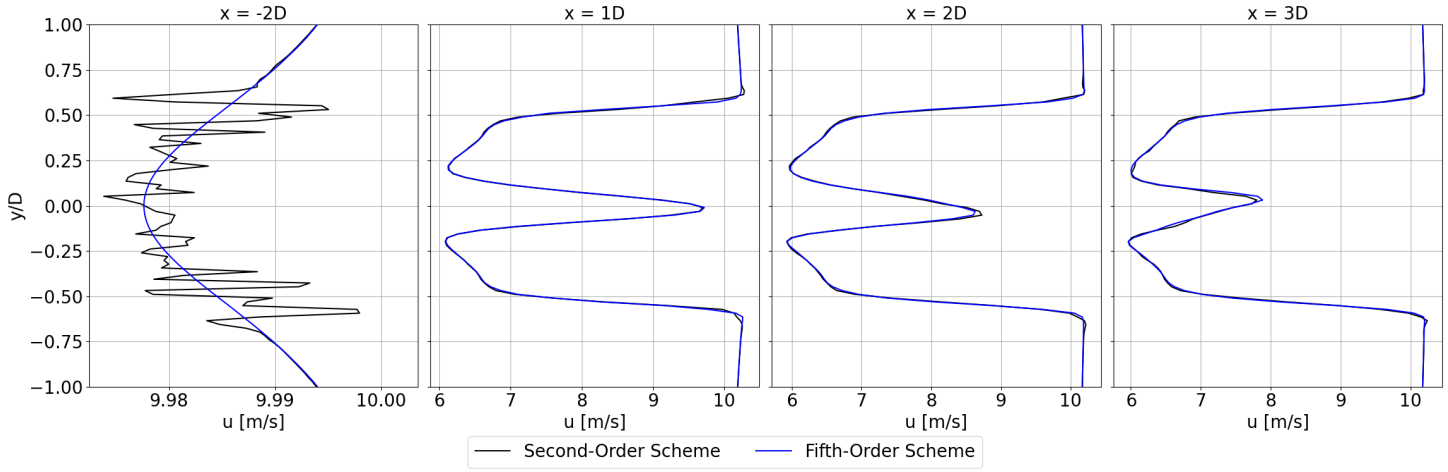

Figure 3.6: The effect of advection scheme on the time-averaged velocity profiles at various locations of the domain.

Additionally, a fifth-order scheme better captures high pressure and velocity gradients by dampening artificial oscillations at sharp gradients. This is seen at the end of the shear layer of the wake at $1D$ downstream of the turbine. The results for this steady case do not appear significant and exhibit negligible impact on the turbine's performance. However, as the flow becomes more unsteady, with unsteady roll, the benefit of the fifth-order scheme can become more pronounced.

The selection of the advection scheme is also evident in the vorticity magnitude contour map. This is given in Figure 3.7.

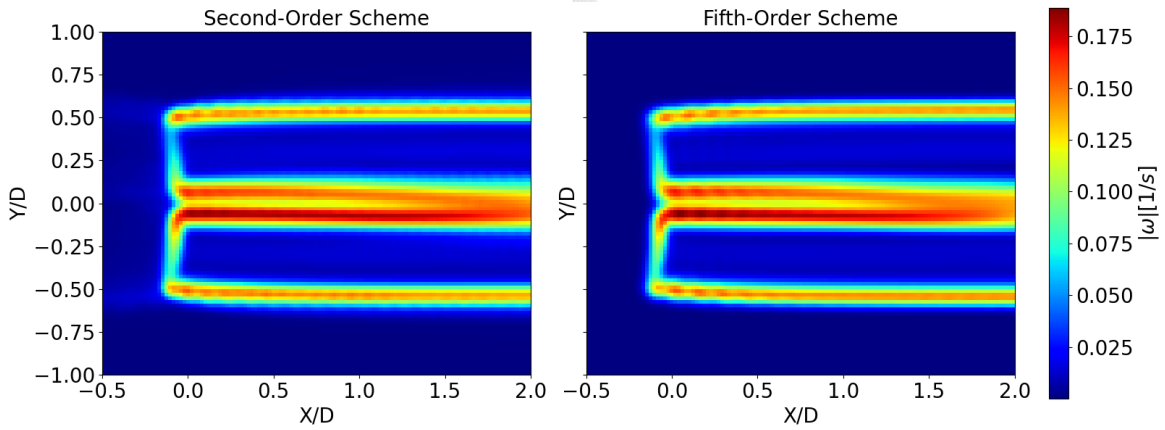

Figure 3.7: The effect of advection scheme on the time-averaged vorticity magnitude in the domain.

Observation of Figure 3.7 indicates that the fifth-order scheme more distinctly resolves the vortex cores emerging from both the blade roots and tips. The second-order scheme exhibits noise at the vortex edges, particularly visible at the blade root at $1.75D$, whereas these are smooth with the fifth-order scheme. This noise will intensify with further grid refinement.

Lastly, a vorticity of approximately 0.050 [1/s] is observed in the inflow directly at the turbine only for the second-order scheme. This is solely attributable to numerical errors, likely induced by noise in the inflow, as observed in Figure 3.6.

3.4.4 Time-Stepping Criterion

The time-steps for each test case were determined according to the Courant-Friedrichs-Lewy (CFL) condition, as presented in Equation 2.17. Consequently, each test case maintained a specific constant time-step, which was dependent on the maximum velocity calculated within the domain using the formulas provided in Subsection 2.4.3, specifically in the 'Temporal Discretization' part. Therefore, the sole selection parameter within the numerical setup concerning time-stepping was the Courant number (CFL). For analysis, Courant numbers of 0.4, 0.65, 0.8, and 1.0 were selected.

The results for average velocity, turbulence kinetic energy, and vorticity profiles for a turbine undergoing surge are plotted in Figure 3.8. These results indicate that the Courant number does not exert a significant influence on the wake properties. Similar findings were reported by Combette (2023)[11]. This insensitivity is also observed at the blade tips, where the domain velocity is maximal.

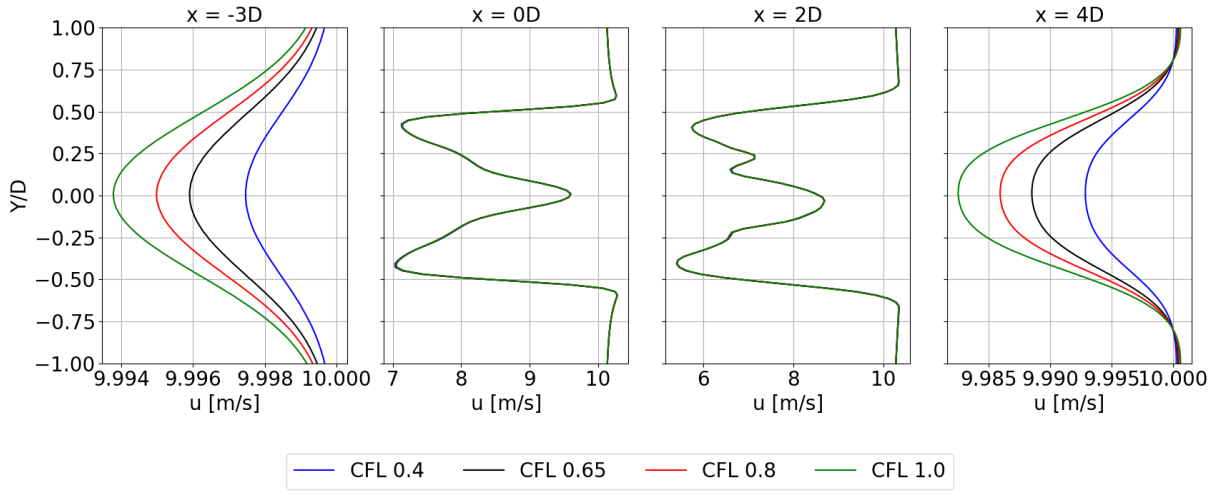

(a) The effect of Courant number on the time-averaged velocity profile at various streamwise locations.

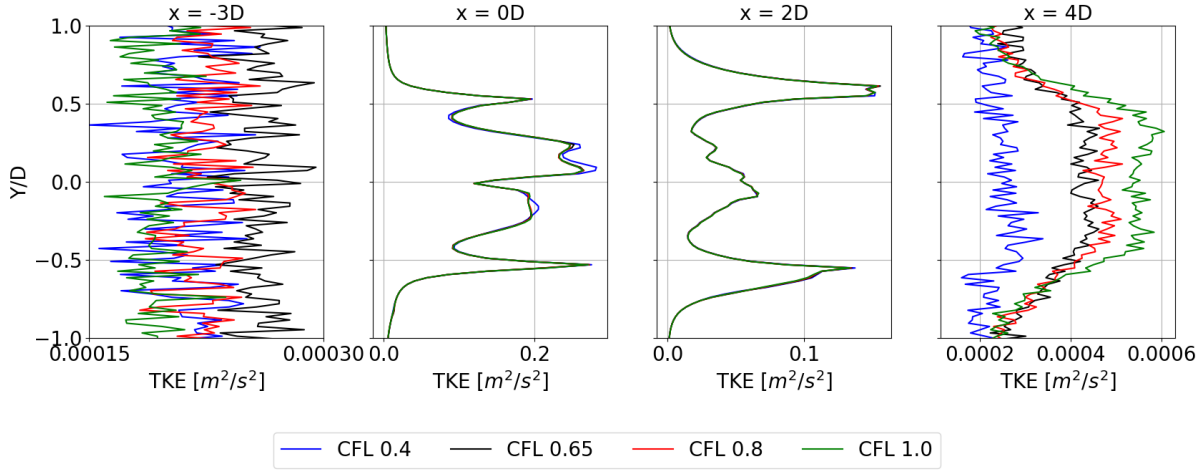

(b) The effect of Courant number on the time-averaged turbulence kinetic energy profile at various streamwise locations.

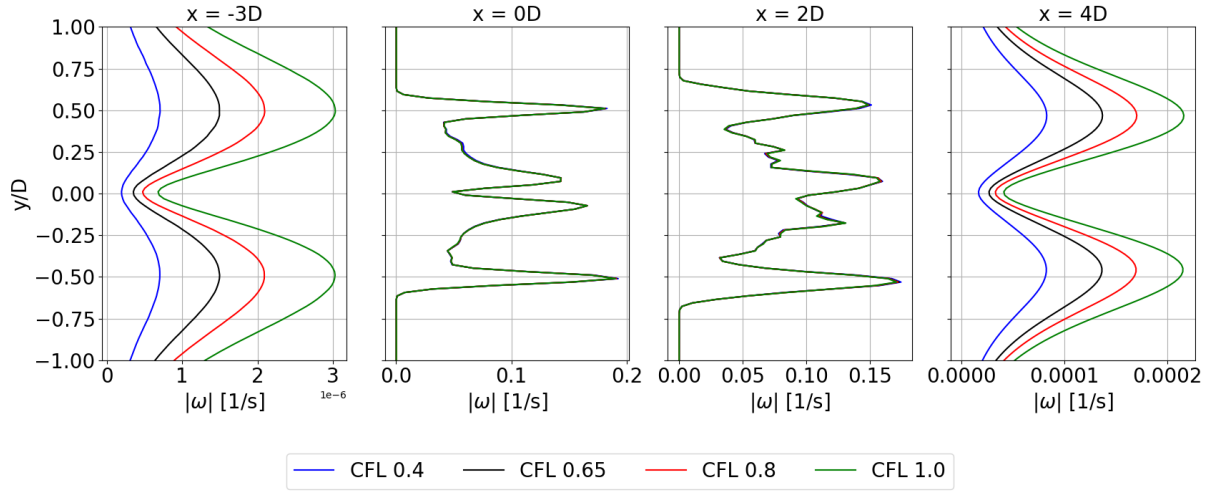

(c) The effect of Courant number on the time-averaged vorticity magnitude profile at various streamwise locations.

Figure 3.8: The effect of Courant number on the time-averaged profiles at various streamwise locations.

In agreement with the results of Combette (2023)[11], the Courant number exhibits only a very small effect on the turbine's blade loading. Minor variations in blade loading cumulatively contribute to incremental changes in the total thrust and power of the turbine. This relationship manifests as significantly varying thrust and power coefficients, which are plotted in Figure 3.9.

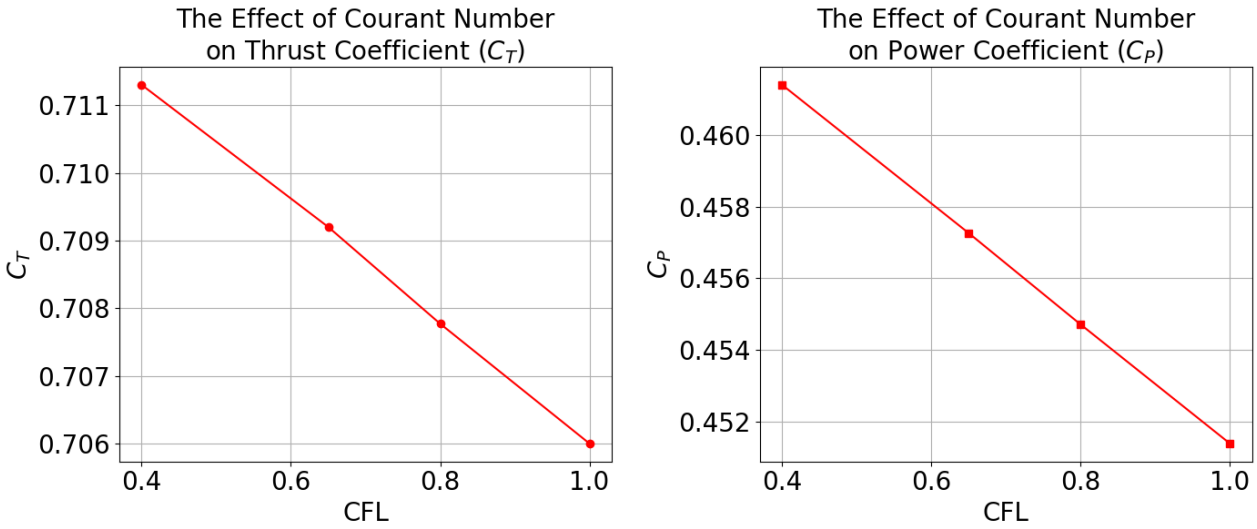

Figure 3.9: The effect of Courant number on the time-averaged thrust and power coefficients.

Considering the high sensitivity of the thrust and power coefficients to the Courant number, the selection of the Courant number is primarily based on the conclusion that it does not significantly impact blade loading.

Comparing these coefficients to those tabulated in Table 3.3, the present values are slightly larger for the same Courant number of 0.8. As this chapter follows a chronological order of the methodology, the discrepancy is likely attributable to nudging effects. Although the finer grid employed here would typically lead to reduced coefficients, the nudging effect appears to be more dominant. This confirms that even if the wake velocity differs near the turbine due to nudging, the inflow velocity is more sensitive to nudging because the turbine is positioned $3D$ behind the inlet, consequently affecting the performance coefficients.

Ultimately, a Courant number of 0.8 was selected, balancing temporal resolution with computational efficiency. Consequently, the relationship presented in Figure 3.9 serves as a constant reminder of the Courant number's effects when comparing with reference data during the verification process in Chapter 3.5.

Coarser Courant numbers were considered, but to mitigate risks of instability, particularly at the blade tips, 0.8 was established as the upper limit for selection. Although the setup is highly conservative with this Courant number, as the velocity at the blade tips determines the global time-step, tip velocities can still become unrealistic due to numerical errors when the Courant number approaches 1.

These time-steps are computed individually for each test case introduced in Table 3.2 using their respective maximum tip velocity influenced also by roll motion in the CFL equation.

3.4.5 Subgrid-Scale Model Selection

The accuracy of LES heavily relies on the selection of the SGS model, which parametrizes the influence of the unresolved, smaller turbulent eddies on the resolved flow field. The near-wake region of a wind turbine presents a particularly challenging environment for SGS modeling, characterized by strong shear layers at the blade tips with coherent vortex structures. The SGS model significantly influences the modeling of the formation and evolution of unresolved coherent tip and hub vortices, as well as rapid turbulence development and decay.

While the Smagorinsky model is simple and straightforward to implement, it has its shortcomings. It assumes that the Smagorinsky constant C_s is universal, which is not true because this constant can vary with the type of flow. This requires careful calibration for each flow, which is a drawback. The Smagorinsky model can also be overly dissipative in regions of weak turbulence, such as near walls, where it incorrectly predicts high SGS viscosity due to high mean shear (Blazek, 2015)[7]. This is due to its formulation of the eddy viscosity as given in Equation 2.11. Near walls, the velocity gradients are very large due to the no-slip condition, which is accounted for in the strain rate tensor $|\bar{S}|$. The failure of the Smagorinsky model in this context is its assumption that high strain rate always implies high turbulent activity at unresolved scales. However, near a wall, the high strain rate is primarily due to the mean shear of the resolved flow. Additionally, turbulence itself is damped closer to the wall, leading to a significant decrease in turbulence kinetic energy. This also implies that the Smagorinsky model lacks a wall damping mechanism, as there is no formulation for the flow to discern its proximity to a wall (Blazek, 2015)[7]. As previously mentioned, it causes excessive dissipation near the wall due to high strain rate, resulting in a large eddy viscosity. For these reasons, the Smagorinsky constant, which governs the scaling of the eddy viscosity, must be dynamically adjusted and re-evaluated to allow for proper damping near walls.

It is essential that the model performs accurately near walls because the flow directly behind the blades in the near-wake constitutes the focus of this thesis. The blades are essentially a wall. The Dynamic Smagorinsky Model (DSM) which addresses these problems, is thoroughly explained by Lilly (1992)[50]. adapts to local flow conditions without empirical constants, making it robust near walls by sensing the flow field directly. It accurately captures coherent vortex structures in the near-wake by reducing artificial dissipation when energy transfer is minimal, preserving vortex cores. Additionally, DSM can model backscatter—energy transfer from small to large scales—unlike the strictly dissipative Smagorinsky model, preventing excessive damping and maintaining physically accurate wake decay. This leads to a more energetic and realistic flow representation.

While DSM represents a significant improvement over the Smagorinsky model, it still exhibits limitations in anisotropic flow modeling due to its derivation from the Boussinesq hypothesis. DSM is an isotropic eddy viscosity model that assumes the SGS stress tensor, τ_{ij}, can be approximated as being proportional to the resolved strain-rate tensor $\bar{S}_{ij}$, as described by the Boussinesq hypothesis in Equation 2.9. This represents a key limitation of the model for any complex flow where anisotropy is crucial. Flows with swirl, strong streamline curvature, and separation, especially near bluff bodies, are highly anisotropic (Blazek, 2015)[7]. This constitutes a significant limitation, particularly for the analysis of flow near turbine blades.

Arising from the isotropic nature of the DSM, even with dynamic adjustment, the model can cause excessive dissipation of coherent structures, such as tip vortices in the near-wake, leading to their rapid decay and smearing. For these reasons, Rozema's Anisotropic Minimum Dissipation (AMD) model is considered the optimal SGS model for the simulation configuration and the area of interest in the wake. The advantages of this model, which informed its selection for use directly downstream of the blades, are listed below (Rozema et al., 2015)[64]:

- **Inherently anisotropic nature:** The model is not based on the Boussinesq hypothesis, which assumes isotropy. Instead, it is derived by considering the local rate of energy transfer between resolved and subgrid scales. This approach does not limit the model to correctly resolving isotropic flow, resulting in much more accurate modeling of turbulent structures in highly anisotropic regions. As it is also a minimum-dissipation model, it excels at preserving strong, coherent vortex structures, dissipating energy only when it is genuinely subgrid and turbulent, while allowing resolved rotational motion to persist. It is also accurate for shear layer modeling, dissipating energy across the shear layer while preserving tangential momentum.
- **Dynamically adaptive:** The coefficients are dynamically computed based on local flow gradients. The model is far more integrated with the flow physics compared to DSM.
- **Independence to a test filter:** The absence of a test filter in AMD simplifies its implementation, as the test filter is a numerical parameter that can be counter-intuitive to employ.

In conclusion, although DSM represents a significant improvement over the Smagorinsky model, it still exhibits limitations in anisotropic flow modeling due to its derivation from the Boussinesq hypothesis. A different approach to the closure problem is the AMD model, which is not based on this hypothesis. Since the flow in the vicinity of the blades is highly anisotropic, the inherently anisotropic ADM model is selected as the optimal SGS model for near-wake analysis.

3.4.6 Filtered Actuator Line Method Set-Up

The study of the near-wake, particularly directly behind the blades, is highly dependent on the blade load distribution and its variation due to unsteady effects. Although Stanly et al. (2022)[76] concluded that the use of FALM did not lead to differences in the flow compared to ALM, FALM is chosen for its improved prediction of blade loading with minimal computational trade-off. This enhances the modeling of the wind turbine; however, two important numerical parameters remain to be selected: the filter width, also known as projection or smearing width, ϵ, and the number of FALM nodes/points used to discretize the blade, N.

The latter is also referred to as N_F, the number of force actuator points utilized for the BET in OpenFAST and here simply referred to as the number of actuator nodes/points per blade, N.

For ALM or FALM coupled to a CFD with domain grid size Δx, Troldborg (2009)[83] found that the value of the projection width must satisfy the criterion $\epsilon \geq 2\Delta x$. If ϵ is lower than $2\Delta x$, the force computed per node, which is smeared over the span, becomes too concentrated, potentially leading to numerical oscillations and nonphysical sharp gradients. Conversely, if too large an ϵ is selected,

for example $\epsilon \geq 4\Delta x$, the forces are excessively smeared out. While this can enhance stability, it diffuses the wake structures excessively, particularly near the blade, thereby negating the benefits of CFD domain refinement. Thus, a widely used pre-factor of 2 from literature has been selected, resulting in $\epsilon = 7$ for a Δx of 3.5 m.

A variety of pre-factors have been tested by Jha et al. (2014b)[42]. The difference in power and thrust from experimental data decreases as the pre-factor reduces to 2, demonstrating that this value yields results closest to reality. Pre-factors below 2 are not investigated in this research due to the aforementioned risks of instabilities.

The selection criterion for the number of nodes on the blades arises from the necessity to properly smear the force points to achieve a continuous, smooth force distribution over the blade onto a CFD grid using a projection width of ϵ. If the spacing between the actuator nodes, Δ_N, is significantly larger than the smearing width ϵ, the projection of forcing onto the CFD grid results in a series of discrete force clouds rather than a continuous distribution. This leads to an unrealistic representation of the blade's influence. A smooth force distribution can only be achieved by satisfying the criterion $\Delta_N \leq \epsilon$.

The effect of actuator point spacing is studied by Jha et al. (2014b)[42]. The blade loading distribution and rotor power and thrust are compared with experimental data for actuator point spacing (Δ_N) to local grid size (Δx) ratios of 1, 1.5, and 1.8. The most refined ALM, with a ratio of 1.8, demonstrates the closest results for power and thrust. However, the distribution of loading shows very small differences. The greatest differences are observed near high force gradients at the tips and roots.

The number of actuator points significantly increases computational cost. Following the analysis of Jha et al. (2014b)[42], it was concluded that a blade discretization refinement of $\Delta_N/\Delta x$ of 0.7 is selected. For a grid size of 3.5 m, this results in $\Delta_N = 2.45$ m, which still satisfies the criterion regarding ϵ. The rotor radius, given in Table 2.2, is 120 m, meaning a total of 50 actuator points per blade are used when the intermediate number of nodes is rounded up.

3.4.7 Summary of Numerical Parameters

A summary of the final selections for the numerical parameters are given in Table 3.4.

Table 3.4: Summary of numerical parameters selected.

Parameter	Value	Unit
Domain Size (L_i)	(L_x, L_y, L_z) = ($7.5D$,$5.3D$,$5.3D$)	-
Turbine Position	($3D$,$\frac{5.3D}{2}$,$\frac{5.3D}{2}$)	-
Grid Size (Δ_i)	(Δ_x, Δ_y, Δ_z) = (3.5, 3.5, 3.5)	m
Nudging Factor (x,y,z)	(0.95, 0.95, 0.95)	-
Nudging Extent (x,y,z)	(0.12, 0.01, 0.01)	-
Momentum Advection Scheme	Fifth-order	-
Time-Stepping Courant Number (CFL)	0.8	-
Subgrid-Scale Model	Rozema	-
Smagorinsky Constant (C_s)	0.1	-
Filter/Projection Width (ϵ)	7 ($= 2\Delta x$)	-
Number of actuator points per blade (N)	50	-

3.5 Numerical Set-Up File Structure

Following the selection of numerical parameters, the necessary input files were generated. For simulation execution, three distinct programs, thoroughly explained in Subsection 2.4.3, were utilized. Their interaction is depicted in Figure 2.4. Each program necessitates a specific set of inputs, which are detailed in this subsection. Beyond the input files for simulation execution, additional files are required to utilize the DelftBlue supercomputer, which is managed by the Slurm Workload Manager (SCHEDMD, 2024)[67].

OpenFAST, primarily utilized for BET (Subsection 2.4.6), requires seven essential files, one for each module in use. For instance, as previously mentioned, the hydrodynamics module is deactivated because motion is imposed rather than simulated from sea waves. Consequently, HydroDyn.dat is not among the input files in Figure 3.10; instead, two input files related to motion imposition, ExtPtfm_XXX.dat and ExtPtfmInput_XXX.dat, are required. The former file is read by the main input file XXX.fst, and the latter, which contains information regarding external forcing on all six degrees of freedom of the turbine required to achieve the desired motion, is read by the former. The state-space theory employed in the creation of the ExtPtfmInput_XXX.dat file was presented in Subsection 2.2.

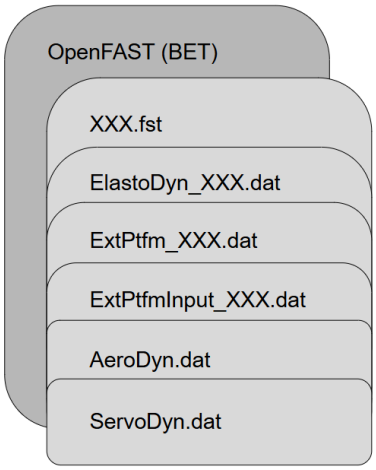

Figure 3.10: List of input files required for OpenFAST.

The remaining modules have been previously explained in Subsection 2.4.4. The 'XXX' in the naming convention denotes the case IDs assigned in Table 3.2.

AspFAST, which utilizes FALM to project smeared forces from the blade actuator points onto the CFD grid, requires two input files, as shown in Figure 3.11.

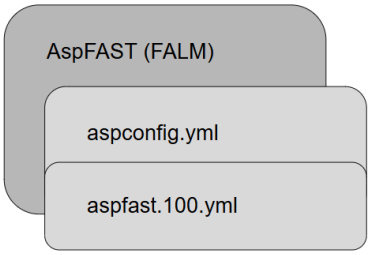

Figure 3.11: List of input files required for AspFAST.

The aspconfig.yml serves as the configuration file for properly setting up the main AspFAST input file, aspfast.100.yml. Within this file, previously investigated parameters such as the projection width ϵ and the number of actuator points per blade, N, are defined. Additionally, it specifies the turbine's position, turbine model, the choice between ALM and FALM, and velocity sampling locations. The option to enable or disable tower and nacelle forcing to the flow is also available and is set to off in this study.

The final set of input files required for running the simulations pertains to the LES code GRASP. GRASP requires two input files, grasp.001.nml and grasp.100.nml, as presented in Figure 3.12. The setup and configuration of these files have been documented in detail by Whiffle (2025)[93].

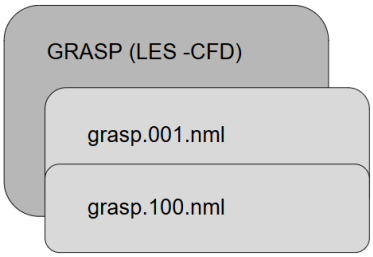

Figure 3.12: List of input files required for GRASP.

The '001' in the naming convention denotes the input file for the precursor simulation, and '100' for the cursor simulation. As briefly explained during the nudging configuration determination in Subsection 3.4.2, periodic boundary conditions are employed primarily to reduce the computational cost associated with domain size. For periodic boundary conditions, a precursor and a cursor simulation are run. The former provides the reference boundary flow towards which the outlet flow in the latter is nudged, as this flow is being recycled. The precursor simulation does not include the turbine within its domain; its sole purpose is to provide boundary conditions.

In both input files, nearly all previously investigated numerical parameters are defined, including the domain size, grid refinement, momentum advection scheme, time-stepping Courant number, subgrid-scale model, and Smagorinsky constant. Nudging parameters are defined exclusively in the cursor simulation, which is nudged towards the precursor. In addition, other non-numerical simulation-specific parameters are defined, such as run-time, surface roughness, inflow velocity, temperature, variations in height for atmospheric input variables, and flow perturbation-related terms. Finally, output variables can be requested in slices, following the guidelines of Whiffle (2025)[93].

All executable code, including the CFD code GRASP, the coupling code AspFAST, and the API ASPIRE, is contained within a .sif file. This is a Singularity Image Format (SIF) file, a specific type of container image commonly employed for high-performance computing programs, such as those on DelftBlue. This file, named aspkit-devel.sif, requires a license for its utilization.

As LES is computationally expensive for execution on an ordinary personal computer, TU Delft's DelftBlue supercomputer is utilized. DelftBlue operates with the Slurm Workload Manager (TU Delft, 2025)[84]. This manager is integrated into DelftBlue, allowing users to specify computational resource requirements at the login nodes via 'job' files. Based on hardware requests and other factors, including the type of share assigned to the user (which establishes hierarchy) and prior usage, the Slurm manager orchestrates the queuing of jobs alongside those of other users. Once a job's turn in the queue is complete, its simulations are executed on a compute node, utilizing the requested hardware for the duration specified in the job file. An example of this job file is provided in Figure 3.13.

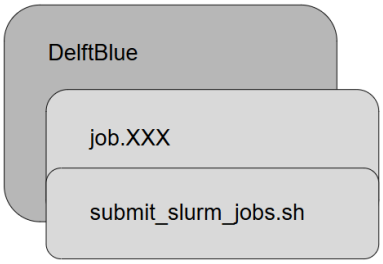

Figure 3.13: List of input files required for DelftBlue.

The job.XXX file (unique for each case ID) defines the user's requests, including run-time, number of GPUs, CPUs, memory, and required software modules. Additionally, a command requesting the execution of the aspkit-devel.sif file with the input files grasp.001.nml and grasp.100.nml is included after the line specifying the necessary license key. This job file is a shell script and must adhere to a specific format compatible with Slurm, which is configured for Linux systems. The second file, submit_slurm_jobs.sh, is utilized for submitting multiple simulation cases concurrently.

4

Verification Study

Before conducting simulations to address the research questions presented in Section 2.3, the numerical setup established in Chapter 2.5 must be verified against existing numerical simulations. Specifically, the numerical configuration summarized in Table 3.4 underwent testing using selected reference cases. Discrepancies observed in the available data were evaluated, considering the numerical setup and limitations inherent in the reference cases.

Three reference papers have been selected. To ensure comparability of results, it was confirmed that all selected reference studies were conducted on the IEA 15 MW turbine. The first reference is the official documentation by NREL (Gaertner et al., 2020)[19], which provides information solely on rotor performance obtained via the BEMT. The second reference is the paper by Parinam et al. (2024)[60], which investigates the effects of inflow shear on the blade loading and wake of a bottom-fixed turbine, utilizing the Actuator Line Method for turbine representation and Large-Eddy Simulation for inflow/wake modeling. Lastly, the study by Ramos-García et al. (2022)[63] is employed to verify results when floating motion is involved. While the current thesis studies the effects of roll, a direct verification of this motion with a reference is not possible due to the lack of research on roll for the identical IEA 15MW turbine. Therefore, the influence of motion on the turbine wake is instead verified using the more commonly studied surge motion, with the paper by Ramos-García et al. (2022)[63]. This reference paper examines the effects of surge amplitudes, frequencies, and TSR on the turbine's performance and wake, utilizing MIRAS, a vortex-solver code that employs a lifting line module, and is used to verify the response of the turbine's wake is as expected when motion is involved.

One important remark is that, while a fixed rotor speed was utilized for all verification studies, a 1° blade pitch angle was maintained specifically for the comparison with the NREL documentation in Section 4.1. This was necessitated by the availability of data at this particular blade pitch angle within the documentation. For the remaining verification studies, the standard fixed 0° blade pitch angle was employed.

4.1 Verification with NREL Turbine Documentation by Gaertner et al. (2020)[19]

The NREL documentation provides information on the turbine's performance. Figure 4.1 is a figure obtained from this reference where the thrust and power coefficient iso-curves against TSR and blade pitch angle are plotted, respectively

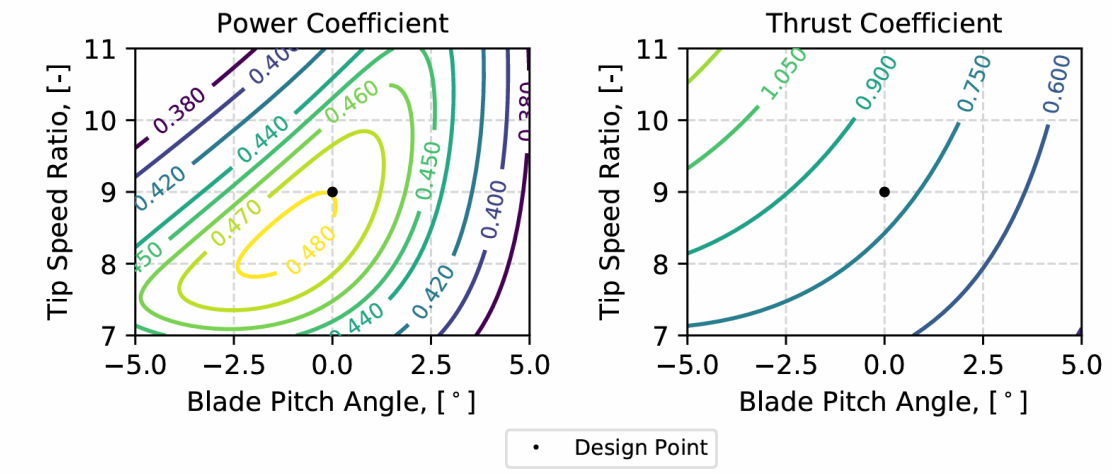

Figure 4.1: The thrust and power coefficient iso-curves obtained from blade element momentum analysis (Gaertner et al., 2020)[19].

Observing Figure 4.1, at a blade pitch angle of 1° and a TSR of 9, under rated inflow wind speed, the thrust and power coefficients are reported as 0.761 and 0.475, respectively. These values are provided for comparison with GRASP data in Table 4.1. For the identical setup case, the GRASP-OpenFAST configuration computes thrust and power coefficients of 0.856 and 0.505, respectively. This yields an error of 12.5% for the thrust coefficient and 6.3% for the power coefficient.

Table 4.1: Fixed turbine thrust and power coefficient comparison to the NREL documentation (Gaertner et al., 2020)[19] operating at rated wind speed of 10.59 m/s with TSR of 9 and pitch angle of 1°.

	Reference - NREL	GRASP setup	% difference
C_P	0.475	0.505	6.3
C_T	0.761	0.856	12.5

The reason for this difference can be attributed to limitations within the GRASP numerical setup and the low-fidelity nature of the reference data, which utilizes BEMT. The GRASP setup is likely the primary contributor to this discrepancy, particularly because a TSR of 9 does not typically induce extreme, unsteady, or three-dimensional flow effects, such as significant radial flow or flow separation, which BEMT is inherently incapable of modeling.

As explained in Subsection 3.4.1, blockage effects can influence both the thrust coefficient and the power coefficient. Although the selected domain cross-sectional area was determined to be sufficiently large, a non-infinitely large domain will still lead to increased thrust and power estimations. Additionally, computational limitations necessitated minimizing the domain in the streamwise direction, which introduces minor but present nudging effects. Even though minor, this potentially accelerates the flow at the turbine, leading to increased blade loading. Consequently, the performance

coefficients are significantly overestimated, as small gains in blade loading incrementally contribute to a substantial increase in total turbine performance.

Filtered actuator line discretization is not considered the cause of this overestimation; rather, it is more a result of the CFD domain's spatial and temporal discretizations, which were also significant contributors, as explained in Subsection 3.4.4.

The limitations of BEMT primarily arise near the blade tips and roots, where empirical corrections such as the Prandtl tip and root loss models are applied. Although these corrections should not cause significant discrepancies at this TSR given the turbine's stable operational conditions, they can still lead to deviations in loading distributions near the blade ends. Another limitation of BEMT is its inability to account for radial flow effects. For a bottom-fixed turbine operating at the current conditions, radial flow is likely negligible along the entire blade span. However, as rotor rotational velocity increases, radial flow may become more pronounced due to stronger centripetal forces and 3-dimensional flow effects, including root and tip vortices. The differences between the two models would be further amplified under roll motion, which induces additional radial flow. This radial flow alters blade loading distributions by modifying the pressure gradients along the blade.

Comparisons conducted by Bouhelal et al. (2017)[9] show similar conclusions regarding the under-prediction of turbine thrust and power at various TSRs. The discrepancy increases with lower TSRs because the angle of attack on the blade increases, leading to separating flow. Separation typically initiates near the blade roots due to the lowest in-plane velocity in that region.

In conclusion of the results presented in Table 4.1, the difference between the reference data and the GRASP-OpenFAST data was deemed sufficiently close, given the notorious difficulty in matching these coefficients due to their sensitivity to the numerical setup.

The NREL documentation also provides information on blade loading obtained from BEMT for an inflow velocity of 10 m/s, with the turbine operating at a TSR of 9 and a blade pitch angle of 0°. For comparison, the bottom-fixed TSR 9 case was utilized, which differs only in having a blade pitch angle of 1°. Plots of the time-averaged normal and tangential force distribution are presented in Figure 4.2.

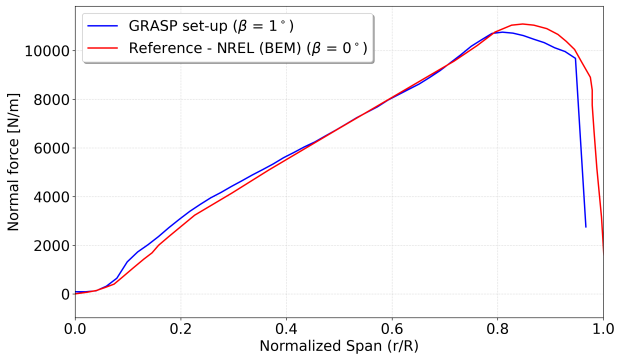

(a) Time-averaged normal force distribution comparison to reference data from NREL documentation (Gaertner et al., 2020)[19] for fixed turbine operating at inflow velocity of 10 m/s at TSR of 9.

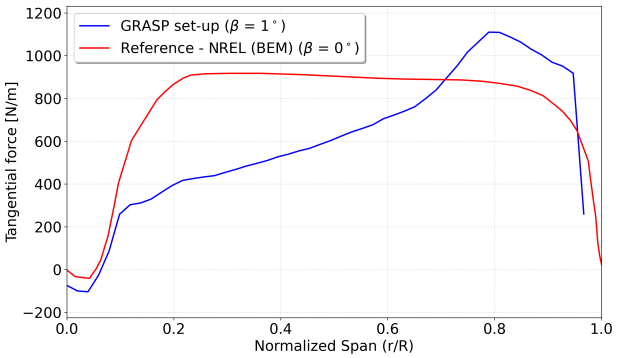

(b) Time-averaged tangential force distribution comparison to reference data from NREL documentation (Gaertner et al., 2020)[19] for fixed turbine operating at inflow velocity of 10 m/s at TSR of 9.

Figure 4.2: Time-averaged normal and tangential force distribution comparison to reference data from NREL documentation (Gaertner et al., 2020)[19] for fixed turbine operating at inflow velocity of 10 m/s at TSR of 9.

In Figure 4.2a, the loads exhibit a match, though it is crucial to highlight that this alignment is attributable to the pitch angle used in GRASP-OpenFAST bottom-fixed case. A small increase in blade pitch angle results in a downward shift of the normal force, with increasing deviation from the no-pitch load further away from the root. Accounting for this pitch, the blue curve should theoretically lie slightly above and parallel to the red curve. The current situation shows that the normal force is larger near the root since with a larger blade pitch angle, the angle of attack is reduced which reduces the stall. This explains the higher thrust coefficient, to which normal loading is a contributor. Even with the blade pitch present in the reference, Table 4.2 demonstrates that the thrust coefficient still differs by 8.5% compared to the NREL BEMT data. This discrepancy would be greater in the absence of the blade pitch angle. Lastly, near the blade root and tip, the GRASP data is expected to show a more plausible reduction in load compared to the empirically estimated reduction by the Prandtl correction, which indicates a smoother loss.

Greater deviations from the reference data are observed in the tangential load distribution, as shown in Figure 4.2b. The effect of blade pitch angle on the tangential load is similar to that on the normal load. Accounting for the pitch difference, the tangential load distribution would initially align with the blue curve up to a normalized span position of 0.1. Subsequently, it would reach a greater load before following a path parallel to the blue curve for the remainder of the normalized span locations. This implies that the tangential load is still over-predicted by BEMT in the inner half of the blade and under-predicted in the outer half. This leads to power overestimation, as power is the product of torque and rotor speed. Given that the tangential load, which contributes to torque, is more outboard loaded in the GRASP-OpenFAST simulation, the resulting torque is larger. This accounts for the larger power coefficients observed in the GRASP-OpenFAST data.

The observed differences in loading distribution shape can be attributed to the turbine's operational point. As shown in Figure 4.6, the tangential load distribution appears more similar to the BEMT distribution at 8 m/s and TSR 9 despite a 1° difference in blade pitch angles between the GRASP results in Figure 4.6 and Figure 4.2. The shift toward outboard loading may result from enhanced

3-dimensional effects under higher loading conditions, as evidenced by comparing Figure 4.2 and Figure 4.6.

At higher inflow velocities with the same TSR, the turbine operates at increased rotational speed, amplifying Coriolis effects on the blades. This inertial force, arising from blade rotation, enhances radial flow momentum toward the tip. The augmented momentum improves blade aerodynamics by stabilizing the boundary layer and delaying flow separation (Khedr and Castellani, 2025)[44]. Consequently, the tangential loading shifts outward—a phenomenon that BEMT with empirical corrections cannot capture and which doesn't exist significantly at lower rotor speeds as in Figure 4.6.

Table 4.2: Fixed turbine thrust and power coefficient comparison to the NREL documentation (Gaertner et al., 2020)[19] operating at wind speed of 10 m/s with TSR of 9.

	Reference - NREL (β = 0°)	GRASP setup (β = 1°)	% difference
C_P	0.489	0.513	4.9
C_T	0.804	0.872	8.5

Following the comparisons made with the NREL documentation, it can be concluded that the results obtained from the GRASP-OpenFAST data fall sufficiently within the range of the reference data. Deviations in blade loading are present but minor, leading to larger deviations in the performance coefficients. A certain margin of error relative to any reference is deemed acceptable, attributable to the different fidelities of the numerical methods employed.

4.2 Verification with Parinam et al. (2024)[60]

Parinam et al.'s (2024)[60] study concerning the impact of varying inflow shear and velocity profiles on the wake of the IEA 15 MW bottom-fixed turbine was selected for this verification study. Within this paper, uniform inflow is simulated as the baseline case for comparison in this verification study.

This reference paper employs the CFD code YALES2, a Large-Eddy Simulation tool, for simulating the inflow and the wake. Details on the numerical setup are summarized in Table 4.3. The blades of the IEA 15 MW turbine are modeled using ALM.

Table 4.3: Numerical setup description of reference research by Parinam et al. (2024)[60] employing YALES2 LES code.

Parameter	Value	Unit
Domain Size (L_i)	(L_x, L_y, L_z) = ($18D$,$10D$,$6D$)	-
Turbine Position	($3D$,$5D$,$3D$)	-
Grid Size (Δ_i)	(Δ_x, Δ_y, Δ_z) = (2, 2, 2) (locally at the wake)	m
Momentum Advection Scheme	Fourth-order	-
Time Step	40	ms
Subgrid-Scale Model	Smagorinsky	-
Smagorinsky Constant (C_s)	0.16	-
Filter/Projection Width (ϵ)	$= 2\Delta x$	-
Number of actuator points per blade (N)	64	-

The prescribed boundary conditions are also periodic, arising from a precursor and a cursor simulation. No information is available regarding the extent and factor of applied nudging, but its effects are assumed to be small in the region of interest due to the large streamwise domain size. Additionally, the presence of the nacelle is excluded from the study, similar to the approach taken in this thesis.

Prior to commencing the verification study, differences in the numerical setup, which are likely to lead to discrepancies in the results, should be discussed. The capability for local refinement in YALES2 offers numerous possibilities and benefits for the domain setup. Local refinement has enabled Parinam et al. to extend the domain significantly more in all directions compared to the GRASP setup. Additionally, local refinement permits a very small grid size in zones of interest, which was implemented by selecting a uniform grid size of 2 m within the wake. This approach generally yields more realistic and reliable results compared to the GRASP setup. Consequently, the drawback of periodic boundary conditions, specifically the nudging effects, is reduced in the region of interest.

The time step utilized herein is approximately equivalent to that obtained from the set Courant number of 0.8, as detailed in Subsection 3.4.4. The use of the Smagorinsky model is likely a main limitation of the reference study due to its inability to resolve anisotropies and its non-dynamic eddy viscosity constant, which introduces global limitations within the domain. This may impose limitations on the resolved scales of motion but is not expected to have a significant impact on the parameters investigated in this study. Lastly, the additional 14 actuator points per blade used in ALM do not significantly improve the results, as the domain grid size is generally a more critical parameter. It is noted that the GRASP setup employs FALM, which mitigates some of the limitations of standard ALM, as explained in Subsection 2.4.7.

The turbine operates at its optimal TSR of 9 under a uniform, steady inflow of 8 m/s. This configuration has also been simulated using the numerical setup derived from Chapter 2.5. The available data from the reference paper are compared with the results obtained from the current simulations.

The lift and drag coefficient plots in Figure 4.3 demonstrate good agreement.

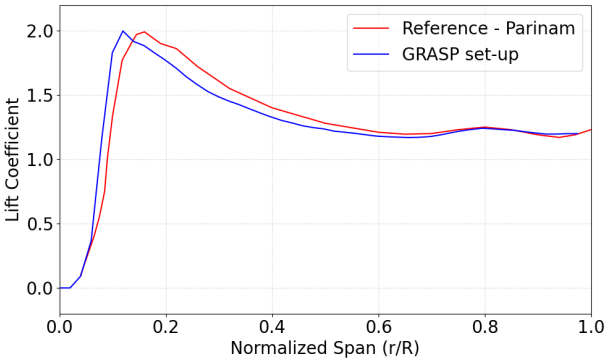

(a) Time-averaged lift coefficient distribution comparison to reference data by Parinam et al. (2024)[60] for fixed turbine operating at inflow velocity of 8 m/s at TSR of 9.

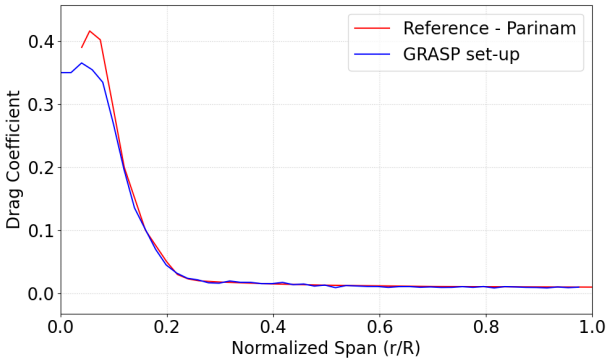

(b) Time-averaged drag coefficient distribution comparison to reference data by Parinam et al. (2024)[60] for fixed turbine operating at inflow velocity of 8 m/s at TSR of 9.

Figure 4.3: Time-averaged lift and drag coefficients distribution comparison to reference data by Parinam et al. (2024)[60] for fixed turbine operating at inflow velocity of 8 m/s at TSR of 9.

Larger differences are observed when comparing the standard deviation (SDEV) of the lift and drag coefficients, as presented in Figure 4.4. Near the root, the peak in the SDEV lift coefficient is similar; however, the reference data exhibits a second peak that is absent in the GRASP setup. Conversely, the SDEV drag coefficient distribution, as depicted in Figure 4.4b, exhibits a more similar profile.

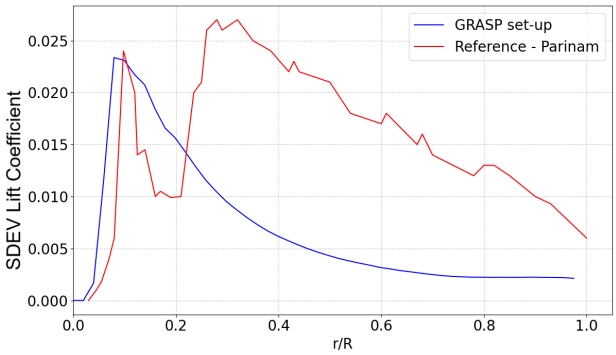

(a) Standard deviation of lift coefficient distribution comparison to reference data by Parinam et al. (2024)[60] for fixed turbine operating at inflow velocity of 8 m/s at TSR of 9.

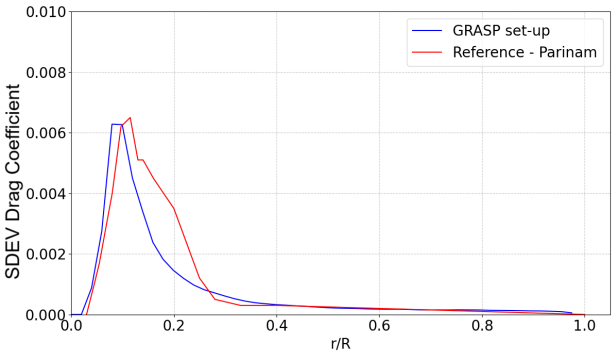

(b) Standard deviation of drag coefficient distribution comparison to reference data by Parinam et al. (2024)[60] for fixed turbine operating at inflow velocity of 8 m/s at TSR of 9.

Figure 4.4: Standard deviation of lift and drag coefficients distribution comparison to reference data by Parinam et al. (2024)[60] for fixed turbine operating at inflow velocity of 8 m/s at TSR of 9.

The normalized velocity profiles at various streamwise locations are presented in Figure 4.5. At the inflow, a small velocity deficit is observed in both simulations. At $0D$, the GRASP setup exhibits a slightly larger velocity deficit compared to the reference.

At $1D$, the profiles match very well, and both show a larger deficit compared to the $0D$ case, with the same trend persisting. However, at $3D$ downstream, the limitations of the GRASP setup, arising from its short streamwise domain and nudging effects, become apparent. The velocity profile displays a significantly lower velocity deficit compared to the reference, which persists due to artificial wake recovery caused by nudging. This confirms that the results are not reliable beyond $3D$, even if the profiles would have matched better without the blade pitch angle.

The difference in the velocity profiles cannot be attributed to the difference in blade force projection methods, as confirmed by the study of Taschner et al. (2024)[79].

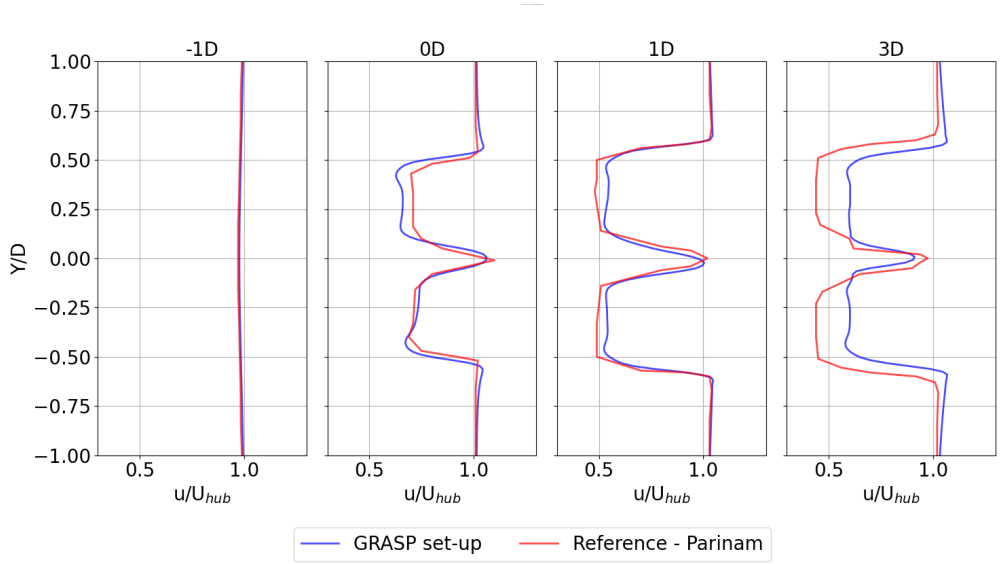

Figure 4.5: Time-averaged velocity profile comparison to reference data by Parinam et al. (2024)[60] for fixed turbine operating at inflow velocity of 8 m/s at TSR of 9.

4.3 Verification with Ramos-García et al. (2022)[63]

The final reference selected for verification is the paper by Ramos-García et al. (2022)[63]. This research utilizes MIRAS, a vortex solver code that employs a lifting line in combination with a hybrid-filament-particle-mesh method. The lifting line models rotor blades as discrete filaments, a distinct approach from the actuator line method. These filaments account for the bound vortex strength and release vorticity into the flow. Through the DTU coupling, a Python code, MIRAS is integrated with HAWC2, a multi-body finite element solver functioning as an aero-servo-hydro-elastic solver. Furthermore, the MIRAS flow solver can be deactivated to prevent blade loads from MIRAS from feeding into HAWC2, a feature utilized for studying BEMT as well. Further details on the numerical setup are available in the reference by Ramos-García et al. (2022)[63].

Blade loading results for the bottom-fixed turbine operating at an optimal TSR of 9 with an inflow velocity of 8 m/s are presented in Figure 4.6. The normal and tangential force distributions exhibit similar magnitudes near the blade center but diverge near the root and tip. While the GRASP-OpenFAST coupling continues to show increasing load, both reference datasets from Ramos-García et al. indicate a decreasing load in these regions. Although the limitations of BEMT have been previously discussed, the MIRAS-HAWC2 coupling exhibits a similar trend to the BEMT configuration. Both of these represent lower-fidelity tools compared to CFD, making fundamental assumptions to enhance computational efficiency rather than physically solving the flow as in large-eddy simulation CFD.

The lifting line theory employed by the reference addresses the blade root and tip by incorporating spanwise induced effects, recognizing that induced velocity varies along the span and circulation must approach zero at both the tip and the root. Models for induced velocity variation near the tip and root are often based on idealized concepts. Consequently, the complex flow at these extremities is oversimplified. While lifting line theory reduces lift towards the ends due to induced flow, the specific distribution and magnitude of this reduction may differ from reality. The analytical models might

impose a stronger or smoother reduction than the complex, non-linear induced field present in 3-dimensional turbulent flow, particularly when influenced by separation and concentrated vortices. In contrast, LES captures complex unsteady and turbulent effects, as well as radial flow, which accounts for the larger blade loading near the tips observed in CFD. Similar discrepancies in results have also been reported by Behrens de Luna et al. (2022)[4].

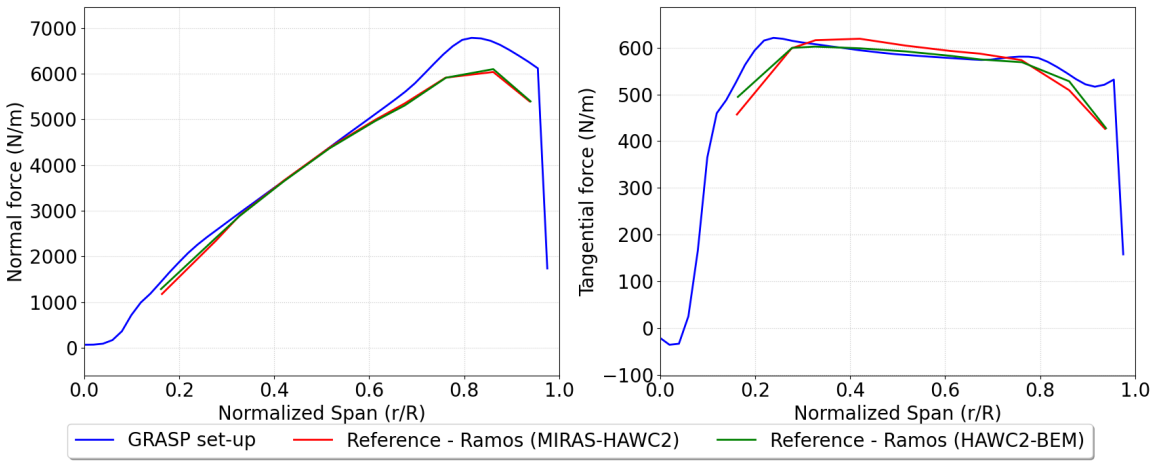

Figure 4.6: Time-averaged blade normal and tangential force distribution comparison to reference data by Ramos-García et al. (2022)[63] for fixed turbine operating at inflow velocity of 8 m/s at TSR of 9.

The influence of differences in blade loads, particularly the normal force, is evident in the turbine's performance, as characterized by its thrust. The same reasoning for the discrepancies observed in the comparison for the bottom-fixed turbine in Figure 4.6 applies to the thrust versus surge position plots in Figure 4.7, Figure 4.8, and Figure 4.9 for the surging turbine.

The normal force distribution across the blade is the primary contributor to the turbine's thrust. The significant decrease in load near the tips, resulting from the aforementioned approximations of lower-fidelity methods, leads to a lower average thrust within a cycle of surge motion. This explains the vertical shift of approximately 300 kN observed between the GRASP-OpenFAST data and the reference data in Figure 4.7, Figure 4.8, and Figure 4.9. This represents an error of 12% relative to the thrust at the rated wind speed of 2.6 MN, which is considered acceptable with due consideration.

In Figure 4.7, for any of the given surge cases, the turbine remains within the region of constant pitch angle at 0°. Given that the GRASP setup also does not employ any pitch angle, and for this verification study the blade pitch angle is also set to 0°, the curves exhibit a similar oval shape. During a surge motion, a clockwise path is followed, indicating that when the turbine surges into the inflow, defined by a positive surge position, the thrust increases due to an increased inflow velocity and a higher angle of attack. Immediately before the turbine reaches its maximum position, defined by the surge amplitude, the velocity reduces to zero while the thrust simultaneously decreases. The turbine then accelerates downstream, consequently reducing both the inflow velocity and the thrust.

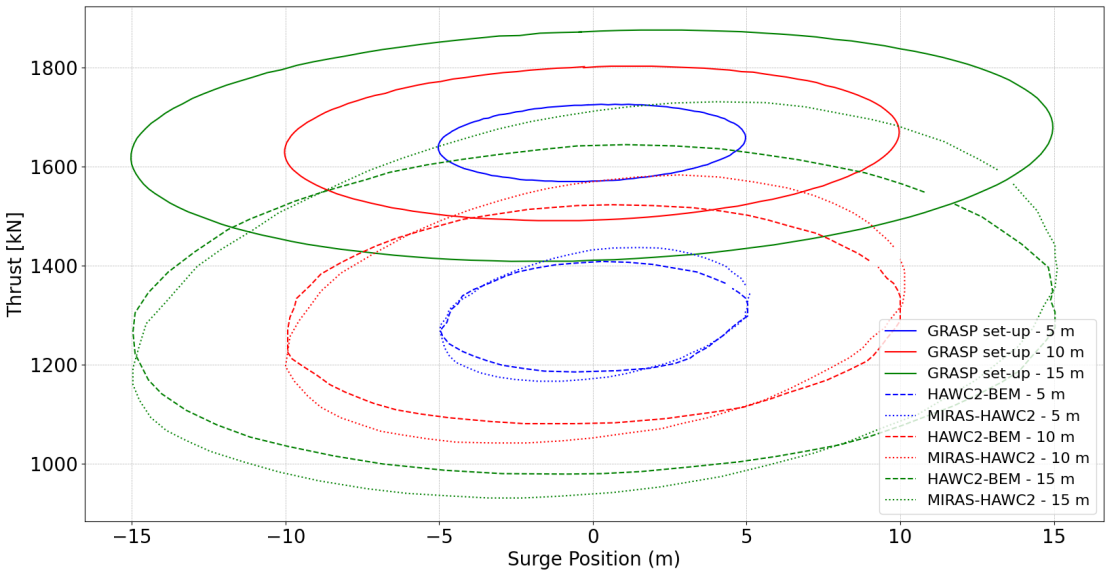

Figure 4.7: Comparison of the turbine thrust map against surge position with the reference data by Ramos-García et al. (2022)[63] for varying surge amplitudes at a frequency of 0.01419 Hz, inflow velocity of 8 m/s, and TSR of 9.

The thrust versus surge position curve in Figure 4.8 for a frequency of 0.01419 Hz again exhibits a shape similar to its respective reference data, as also observed in Figure 4.7. This is because, at this frequency, the rotor velocity does not cause the turbine to operate outside the zero blade pitch conditions. However, at a frequency of 0.05676 Hz and an amplitude of 15 m, the turbine's operation during a surge cycle exceeds its rated velocity and drops below the minimum velocity required for pitch actuation. The activation of blade pitch control in the reference data leads to a distinct curve shape, as depicted by the red dashed and dotted lines in Figure 4.8. Conversely, without the pitch controller, the solid red line maintains an oval shape, and higher thrust values are obtained during the surge motion towards the inflow. This contrasts with the pitch-controlled results, where load shedding occurs.

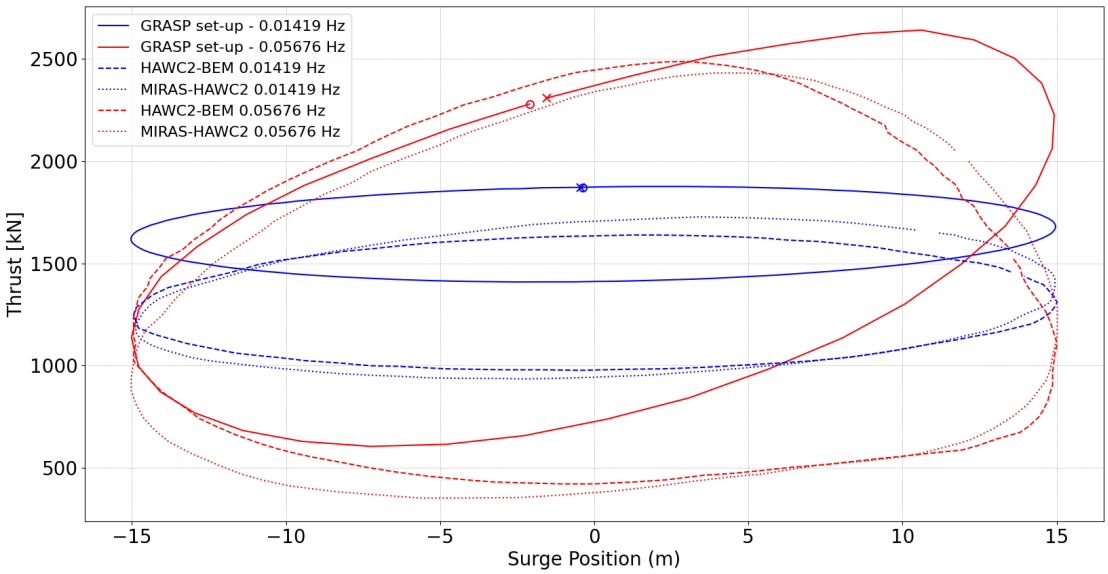

Figure 4.8: Comparison of the turbine thrust map against surge position with the reference data by Ramos-García et al. (2022)[63] for varying surge frequencies at an amplitude of 15 m, inflow velocity of 8 m/s, and TSR of 9.

In Figure 4.9, at an inflow velocity of 15 m/s, the turbine operates within the pitch-activated zones of its controller even when stationary. This results in significantly larger differences between the reference data and the GRASP setup, with deviations approaching 1550 kN. The shapes also differ considerably, as the pitch-actuated reference data exhibit a more complex thrust trajectory when the turbine surges downstream.

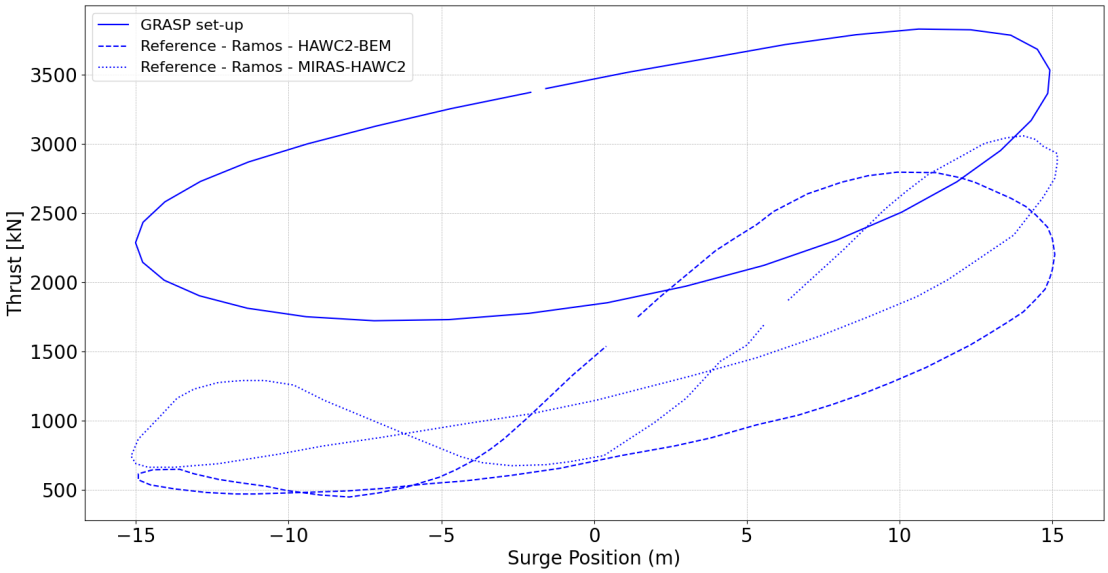

Figure 4.9: Comparison of the turbine thrust map against surge position with the reference data by Ramos-García et al. (2022)[63] for a surge amplitude and frequency of 15 m and 0.05676 Hz respectively, for an inflow velocity of 15 m/s, and TSR of 6.33.

The velocity profiles for the bottom-fixed turbine at various downstream locations of the horizontal mid-plane are presented in Figure 4.10. The velocity profiles from the GRASP setup, depicted in blue, are identical to those plotted in Figure 4.5 due to the identical configuration.

Comparing Figure 4.10 and Figure 4.5, the results from the lifting line theory by Ramos-García et al. exhibit greater discrepancies than the LES results by Parinam et al., as anticipated. Therefore, the most significant differences observed in Figure 4.10 are likely attributable to the lower fidelity of the lifting line theory.

The lifting line theory results predict a larger velocity deficit, a steeper gradient in the velocity profile behind the blades, and a smaller deficit behind the region where the hub would have been located. These first two discrepancies arise from the simplifications inherent in modeling the blade as a vortex filament, whereas CFD more accurately models complex, unsteady flow near the tips. The latter difference is due to the lack of viscosity in the lifting line theory. Due to viscosity, CFD smoothens out high velocity gradient regions, specifically smoothing the low deficit region downstream of the hub, which is otherwise situated within a high deficit region caused by the rotor wake.

The nudging effects, which constitute the main limitation of the GRASP setup, become significant beyond a downstream distance of $2D$. These effects will also be examined through streamwise average-velocity profiles following Figure 4.10.

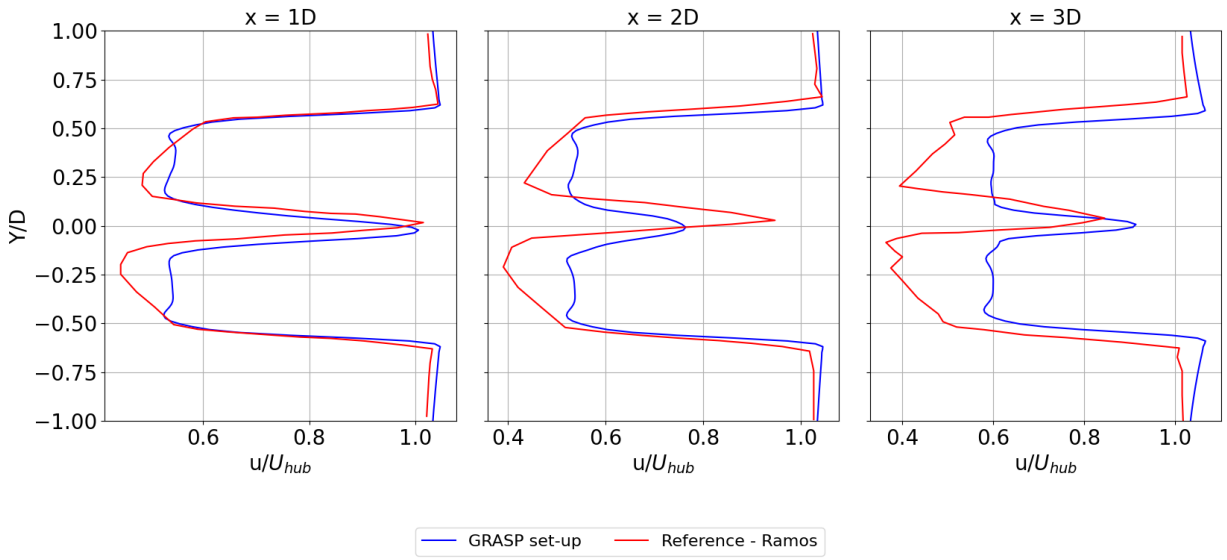

Figure 4.10: Time-averaged velocity profile comparison to reference data by Ramos-García et al. (2022)[63] for bottom-fixed turbine operating at inflow velocity of 8 m/s at TSR of 9 for various downstream locations.

The comparison of streamwise normalized time- and spatially averaged wake velocity for the bottom-fixed turbine is shown in Figure 4.11. The curves closely match near the turbine but diverge downstream due to nudging effects and the limited GRASP domain size. With a $14D$ streamwise domain and no outlet boundary conditions influencing upstream flow, this data serves as a reliable reference. At $2D$ downstream, the wake velocity is 10% higher than without nudging, with errors increasing significantly beyond this point.

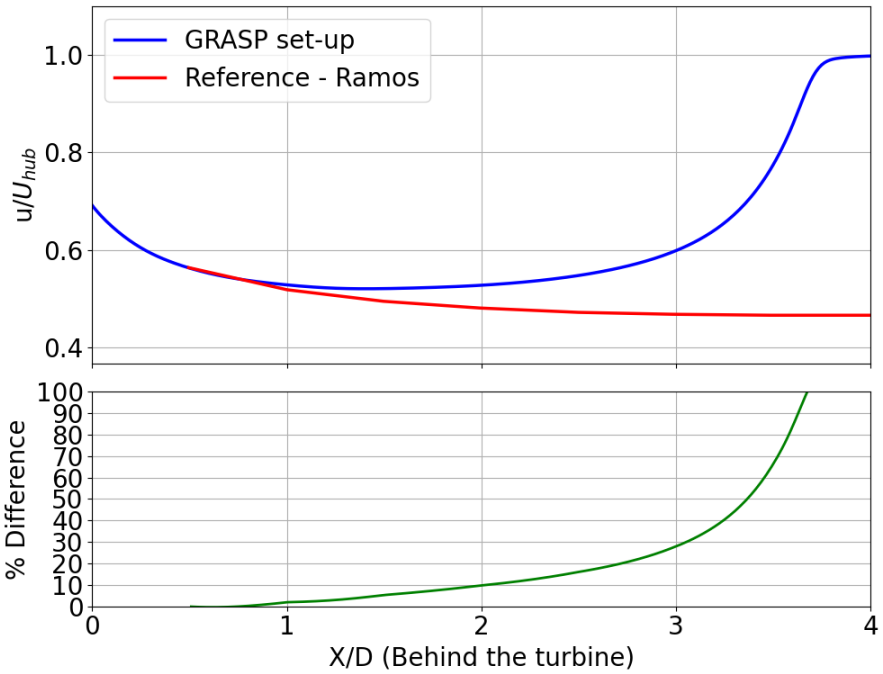

Figure 4.11: Comparison of time- and spatial-averaged normalized velocity in the wake along the streamwise direction to reference data by Ramos-García et al. (2022)[63] for fixed turbine operating at inflow velocity of 8 m/s, and TSR of 9.

Similar to the plot in Figure 4.11 for the bottom-fixed turbine, Figure 4.12 presents a comparison of wake velocities for a surging turbine at various amplitudes. The error at $2D$ downstream, which was the selected threshold downstream location for analysis, is at most 17%. While this error is high, several other factors are also present, such as differences in domain setup or numerical model fidelity. A high error does not necessarily imply that the GRASP setup is incorrect; it is also possible that the lifting line theory over-predicts the deficit. Furthermore, nudging effects are inevitable, given the very small streamwise domain size necessitated by memory limitations.

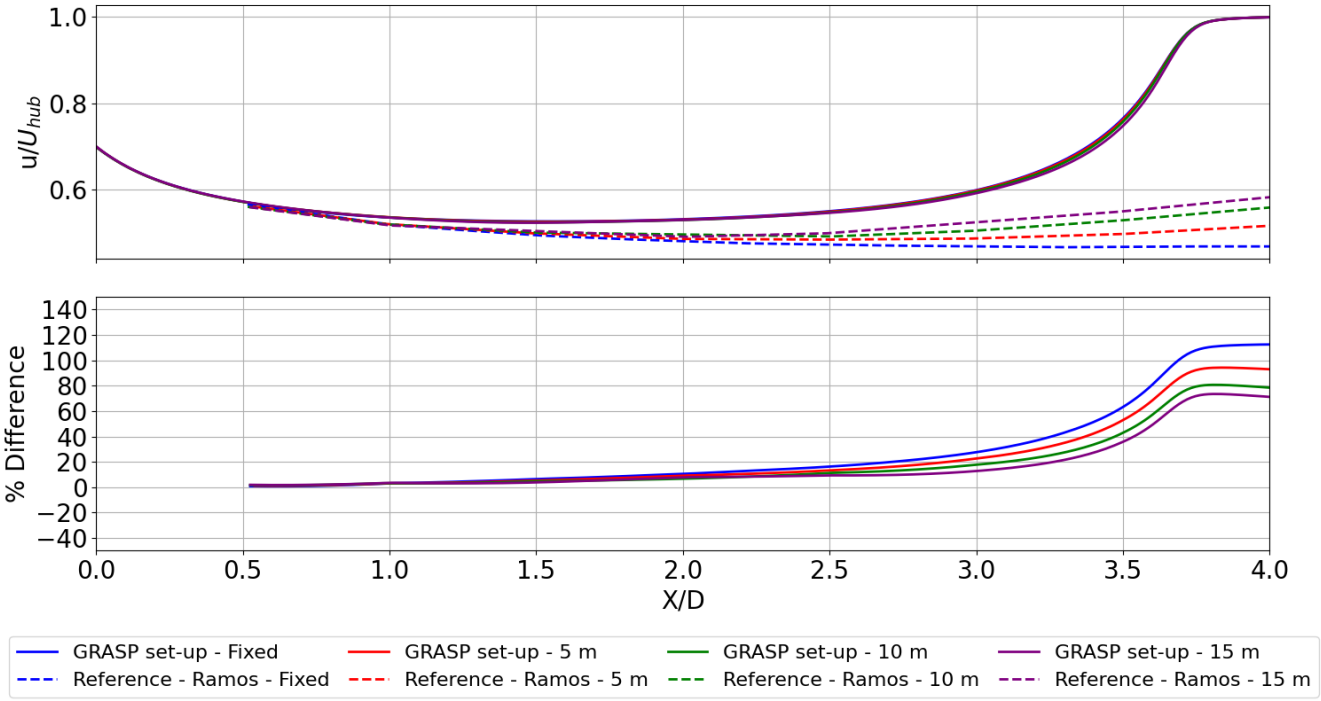

Figure 4.12: Comparison of time- and spatial-averaged normalized velocity in the wake along the streamwise direction to reference data by Ramos-García et al. (2022)[63] for surging turbines with varying amplitudes at a frequency of 0.01419 Hz, inflow velocity of 8 m/s, and TSR of 9.

Comparisons are also conducted for a constant amplitude of 15 m but varying frequencies. The difference in average velocities between various surge frequencies is larger in the reference data compared to the GRASP setup, particularly for the highest frequency of 0.05676 Hz. However, a similar trend is observed: a larger oscillation frequency corresponds to a smaller velocity deficit immediately behind the turbine.

Unlike other studies, the 0.05676 Hz case presented here exhibits a larger velocity deficit near the turbine before nudging effects reverse this trend, leading to an initial negative percentage difference. The maximum error, as previously noted for the fixed case, is approximately 10% at $2D$ downstream from the turbine.

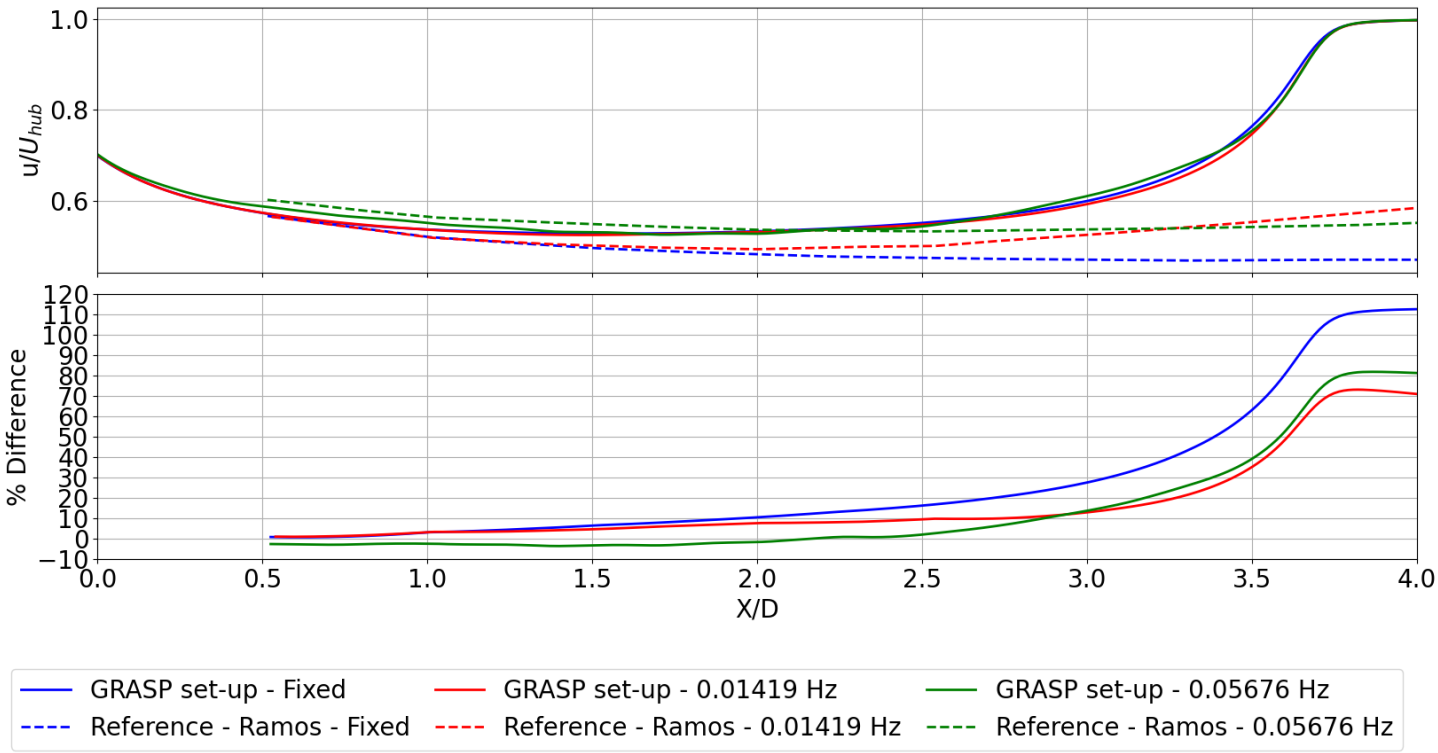

Figure 4.13: Comparison of time- and spatial-averaged normalized velocity in the wake along the streamwise direction to reference data by Ramos-García et al. (2022)[63] for surging turbines with varying frequencies at an amplitude of 15 m, inflow velocity of 8 m/s, and TSR of 9.

4.4 Verification Summary

Following the comparisons of blade loading, rotor performance, and wake velocity profiles with the selected references of varying fidelities, the GRASP setup, developed using the methodology outlined in Section 2.5, is concluded to yield results within acceptable limits. An exact match between the reference and the GRASP setup was not anticipated, even for tools of similar fidelity. This study has demonstrated that the obtained results fall within an acceptable range, defined by whether the observed differences can be explained through logical reasoning, with reference to the limitations of the numerical tool, numerical model, and the specific setup.

In comparisons with the NREL documentation, the GRASP-OpenFAST setup demonstrated a thrust coefficient difference of 12.5% and a power coefficient difference of 6.3% relative to BEMT data for a fixed turbine operating at rated conditions. Accounting for the 1° blade pitch angle used in the GRASP setup for this comparison, the thrust coefficient difference was 8.5%. These deviations are attributed to the low-fidelity nature of BEMT, which cannot model 3-dimensional flow effects such as radial flow or the Coriolis effect that leads to more outboard blade loading, unlike the GRASP-OpenFAST setup. Additionally, blockage and nudging effects in the GRASP computational domain contributed to higher performance coefficient estimations. Despite these differences, the results were deemed sufficiently close given the sensitivity of these coefficients to numerical setups and the fundamental differences in model fidelity.

The verification against the LES results by Parinam et al. showed good agreement in time-averaged lift and drag coefficients. Larger discrepancies were observed in the SDEV of lift outboard. Wake velocity profiles initially matched well, but the GRASP setup exhibited an artificial wake recovery beyond $1D$ to $2D$ downstream due to the limited streamwise domain size and nudging effects. This indicates that results from the GRASP setup are reliable within approximately $2D$ to $3D$ downstream of the turbine.

Further verification against the vortex solver code MIRAS by Ramos-García et al. revealed that blade loading near the root and tip regions differed, with GRASP showing increased load where MIRAS exhibited a decrease. These differences are primarily attributed to the lower fidelity and idealized concepts inherent in lifting line theory compared to LES, particularly regarding the modeling of complex flow near blade ends. For surging turbine conditions, a vertical shift of approximately 300 kN was observed in the thrust versus surge position plots, representing a 12% error relative to the rated thrust of 2.6 MN. This shift is consistent with the under-prediction of load by lower-fidelity methods near the blade tips. Furthermore, distinct differences in thrust map shapes were noted when the reference data included controller activation, a feature not active in the GRASP verification setup. In terms of wake velocity, the GRASP setup showed a 10% larger average normalized velocity at $2D$ downstream for the fixed turbine case compared to the MIRAS data, and up to 17% error for surging cases at the same downstream distance. These percentages, while notable, are considered acceptable given the lower fidelity of the reference's numerical model and the unavoidable nudging effects within the GRASP setup's computationally constrained domain.

5

Results and Discussion

This study aims to provide a baseline but thorough understanding of the effect of roll motion on a floating offshore wind turbine on the blade loading and the very near-wake aerodynamics. To achieve this, the results obtained from GRASP and OpenFAST coupling are presented through plots and graphics, and are discussed with explanations to the trends seen within and among simulation cases of roll.

The study starts off with kinematics analysis of a rolling turbine in Section 5.1 where the equations for tangential and radial velocities at the blade are derived and discussed. Then followed by blade loading analysis in Section 5.2 where the normal and tangential forces are thoroughly studied. Once the analysis on the loading is complete, the effects of the blade loading on the flow is analyzed in Section 5.3. To achieve this, key flow characteristics are examined at selected downstream locations within the near-wake. The analysis includes velocity distributions and their fluctuations, vorticity fields, vortical structures identified using the Q-criterion, and the spectral content of wake signals.

5.1 Introduction to Rolling Turbine Kinematics

The complexity of the kinematics of a wind turbine undergoing roll motion arises from the superposition of two distinct rotational motions: the rotor's own rotation about its hub and the entire turbine's roll about its base. Since these two motions have non-coincident centers of rotation, the roll motion induces an additional translational velocity component at the rotor plane. This component combines with the velocity generated by the rotor's spin, creating a complex resultant velocity.

Consequently, the resultant velocity vector at any point on a blade is a function of the instantaneous roll angle (ϕ) and roll velocity ($\dot{\phi}$), the blade's azimuthal position (ψ), and the rotor's angular velocity (Ω).

The objective of this section is to derive the governing equations for the tangential and radial velocity components induced in the rotor plane by this combined motion. This derivation provides a fundamental kinematic framework for interpreting the aerodynamic blade loading variations analyzed in Section 5.2. The section begins in Subsection 5.1.1 by establishing the coordinate systems and sign conventions used for the derivation. Following this, Subsection 5.1.2 details the derivation itself, beginning with velocities in a global reference frame and subsequently transforming them into the rotor's reference frame. Finally, in Subsection 5.1.3, these kinematic equations are applied to analyze the time-varying loads for a selected roll case, providing a discussion of the implications for blade loading.

5.1.1 Rolling Turbine Kinematics

The first step in the derivation is to define the coordinate system, the variables, and the two reference frames (global and rotor-frame). These are explained below.

- **Description of the physical system**: A tower of height H is pinned at the origin and has a roll angle ϕ from the vertical Z-axis. It rolls with an angular velocity $\dot{\phi}$. The top of the tower is the hub, from which a blade extends with a radius R. An arbitrary point P is located on the blade r away from the hub. The blade rotates with a constant angular velocity Ω.
- **Global frame**: A fixed frame used globally with it's origin at the tower base. The Z-axis is vertical (positive up), and the X-axis streamwise (positive downstream) directions. Following the right-hand rule, the Y-axis is lateral (positive to the left when viewed from upstream). This is shown in Figure 5.1a. The unit vectors are $\hat{k}$ and $\hat{j}$, respectively.
- **Rotor frame**: A moving frame with the rotor, with its origin at the hub. Defined by a radial and tangential vector which is positive away from the hub and in the counter-clockwise (CCW) direction respectively. Shown in Figure 5.1b.

  The Z-axis is vertical (positive up), and the Y-axis is horizontal (positive to the left) when viewed from upstream. The unit vectors are $\hat{k}$ and $\hat{j}$, respectively.
- **Angle definitions and sign conventions**:
  - ϕ: The roll angle of the tower, measured from the positive Z-axis. The roll angle that causes a positive Y displacement in the inertial frame is positive, meaning it's CCW positive from the Z-axis.
  - $\dot{\phi}$: The roll velocity of the tower, which is positive also in the CCW direction.
  - ψ: The azimuthal angle of the blade, measured clockwise (CW) from the top-dead-center position on the rotor. The top-dead-center position is always parallel to the inertial frame Z-axis.
  - Ω: The magnitude of the rotor's angular velocity and is positive CW.

The summary of the information given above is shown in Figure 5.1. The global reference frame and the rotor-frame are shown in Figure 5.1a and Figure 5.1b respectively.

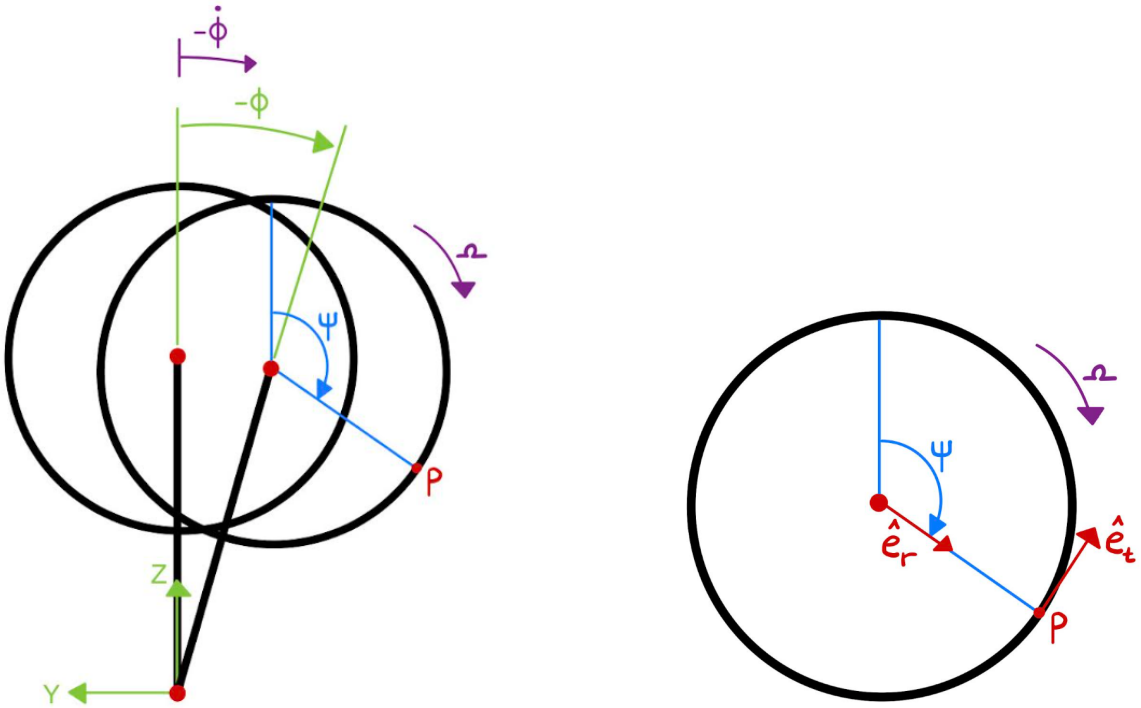

(a) Global-frame definition of the coordinate system and sign convention of a rolling wind turbine for the kinematic study.

(b) Rotor-frame definition of rotor's radial and tangential unit vectors useful for transformation of global velocities into rotor-frame velocities.

Figure 5.1: Description and sign convention of the parameters used in the kinematic analysis of a rolling turbine when viewed from upstream.

5.1.2 Derivation of the Velocity Equations

The absolute position of the point, $\vec{P}_{\text{point}}$, is the vector sum of the hub's position and the point's position relative to the hub. This is given in Equation 5.1.

$$\vec{P}_{\text{point}} = \vec{P}_{\text{hub}} + \vec{r}_{\text{point/hub}} \tag{5.1}$$

Where $\vec{r}_{\text{point/hub}}$ is the relative position of the point with respect to the hub.

The position of the hub can be expressed in terms of the roll angle based on the convention shown by the global frame in Figure 5.1a. Additionally, $\vec{r}_{\text{point/hub}}$ is obtained as a function of the azimuthal angle also as given in Figure 5.1a. The components are obtained as follows:

$$\vec{P}_{\text{hub}} = (H\sin(\phi))\hat{j} + (H\cos(\phi))\hat{k}$$
$$\vec{r}_{\text{point/hub}} = (-r\sin(\psi))\hat{j} + (r\cos(\psi))\hat{k}$$

Where for the $\vec{r}_{\text{point/hub}}$, the Y-component given by $\hat{j}$, is negative because a positive azimuthal angle causes a negative Y displacement in the global frame.

The components of the vectors are summed according to their direction and the following global absolute position of point P is obtained relative to the base of the turbine:

$$Y_{\text{point}} = H\sin(\phi) - r\sin(\psi) \tag{5.2}$$

$$Z_{\text{point}} = H\cos(\phi) + r\cos(\psi) \tag{5.3}$$

The absolute velocity $\vec{V}_{\text{point}}$ is the sum of the hub's velocity and the point's velocity relative to the hub.

$$\vec{V}_{\text{point}} = \vec{V}_{\text{hub}} + \vec{V}_{\text{point/hub}} \tag{5.4}$$

The velocity vectors for the hub (due to tower roll) and the point relative to the hub (due to rotor rotations) are:

$$\vec{V}_{\text{hub}} = \frac{d}{dt}(\vec{P}_{\text{hub}}) = (H\dot{\phi}\cos(\phi))\hat{j} - (H\dot{\phi}\sin(\phi))\hat{k}$$

$$\vec{V}_{\text{point/hub}} = (-r\Omega\cos(\psi))\hat{j} - (r\Omega\sin(\psi))\hat{k}$$

Noting that $\dot{\psi} = \Omega$.

Summing these vectors gives the final absolute velocity components in the global frame:

$$V_Y = H\dot{\phi}\cos(\phi) - r\Omega\cos(\psi) \tag{5.5}$$

$$V_Z = -H\dot{\phi}\sin(\phi) - r\Omega\sin(\psi) \tag{5.6}$$

The global-frame velocities in the Y and Z directions are useless for the blade loading because blades 'feel' only tangential and radial velocities. For this reason, these velocities are converted into the $V_{\text{tangential}}$ and V_{radial} components at the rotor-frame as given by the directions in Figure 5.1b.

These components are found by projecting the absolute velocity vector $\vec{V}_{\text{point}}$ onto the rotor's radial and tangential unit vectors. The unit vectors are defined based on the convention shown in Figure 5.1b in terms of the azimuthal angle:

$$\hat{e}_r = (-\sin(\psi))\hat{j} + (\cos(\psi))\hat{k} \tag{5.7}$$

$$\hat{e}_t = (\cos(\psi))\hat{j} + (\sin(\psi))\hat{k} \tag{5.8}$$

Multiplying the $\vec{V}_{\text{point}}$ with the unit vector $\hat{e}_r$ using dot product gives V_{radial}.

$$\begin{aligned}
V_{\text{radial}} &= \vec{V}_{\text{point}} \cdot \hat{e}_r = -V_Y\sin(\psi) + V_Z\cos(\psi) \\
&= -(H\dot{\phi}\cos\phi - r\Omega\cos\psi)\sin\psi + (-H\dot{\phi}\sin\phi - r\Omega\sin\psi)\cos\psi \\
&= -H\dot{\phi}\cos\phi\sin\psi + r\Omega\cos\psi\sin\psi - H\dot{\phi}\sin\phi\cos\psi - r\Omega\sin\psi\cos\psi \\
&= -H\dot{\phi}(\cos\phi\sin\psi + \sin\phi\cos\psi) \\
&= -H\dot{\phi}\sin(\phi + \psi)
\end{aligned}$$

The same is repeated for $V_{\text{tangential}}$ which instead utilizes the unit vector $\hat{e}_t$.

$$\begin{aligned} V_{\text{tangential}} &= \vec{V}_{\text{point}} \cdot \hat{e}_t = V_Y \cos(\psi) + V_Z \sin(\psi) \\ &= (H\dot{\phi}\cos\phi - r\Omega\cos\psi)\cos\psi + (-H\dot{\phi}\sin\phi - r\Omega\sin\psi)\sin\psi \\ &= H\dot{\phi}\cos\phi\cos\psi - r\Omega\cos^2\psi - H\dot{\phi}\sin\phi\sin\psi - r\Omega\sin^2\psi \\ &= H\dot{\phi}(\cos\phi\cos\psi - \sin\phi\sin\psi) - r\Omega(\cos^2\psi + \sin^2\psi) \\ &= H\dot{\phi}\cos(\phi+\psi) - r\Omega \end{aligned}$$

The radial and tangential velocities at the blade tip for various azimuthal locations are plotted for two points of the roll cycle. The case plotted for is roll of frequency 0.05Hz, amplitude of 10° and TSR of 7, corresponding to case 5. The sub-figure on the left of Figure 5.2 shows the instant of roll when the turbine is rolling with maximum velocity in the same direction of Ω at the vertical position, ϕ = 0. The net velocity (red) is a sum of the radial (blue) and tangential (green) velocity vectors. The sub-figure on the right shows the instant when the turbine comes to a stop at maximum negative roll angle. At this instant, the velocities look identical the fixed case but the acceleration is maximum which differentiates the problem from the fixed case because of the inertial effects.

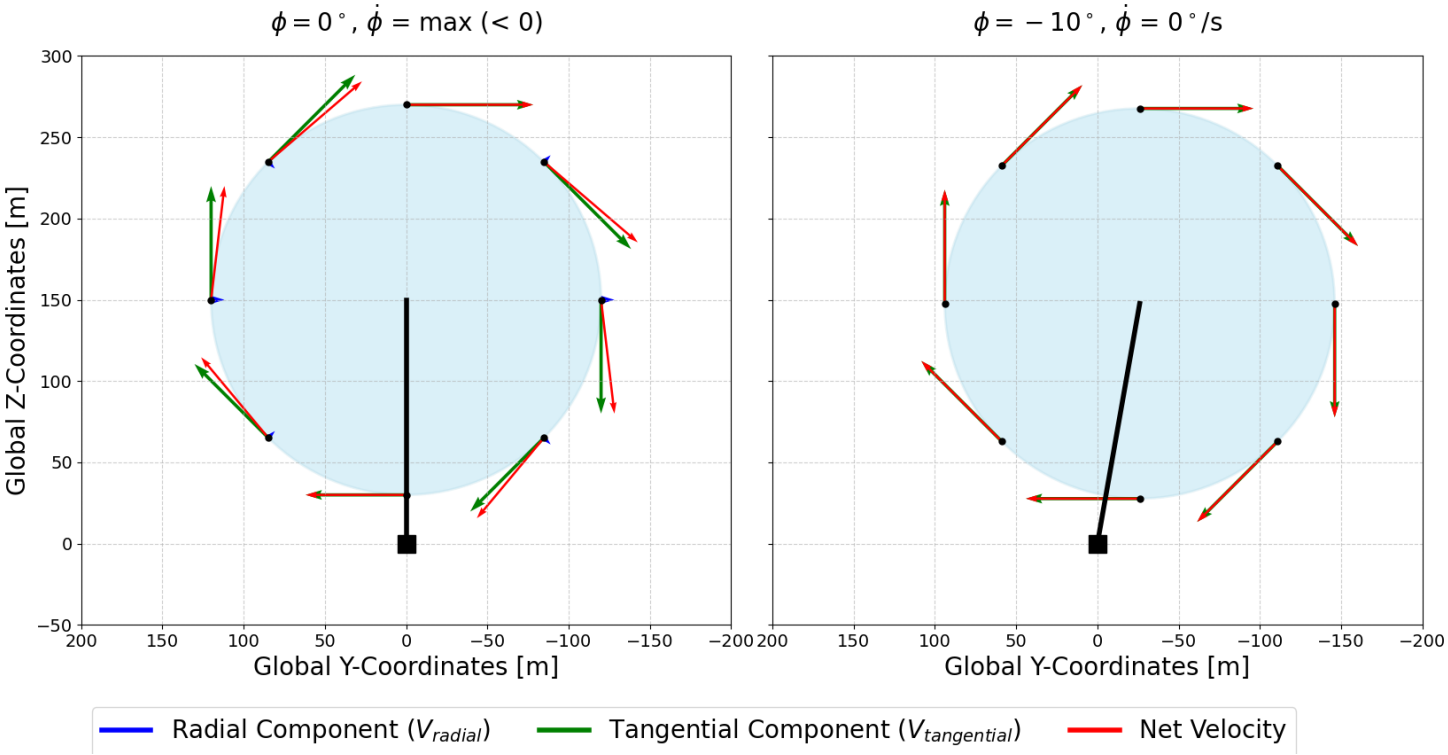

Figure 5.2: The variation of tangential, radial, and net velocities at various azimuthal angles for 2 phases of a rolling turbine with the characteristics of case 5 (0.05Hz, 10°, TSR 7).

The two phases of roll plotted do not give enough information on the variation of these velocities while the roll motion proceeds. These are the simplest cases where either the roll angle or the roll velocity is 0. To better understand the variation, these velocities are plotted in time for various roll cases selected in Subsection 5.1.3.

An important note on Figure 5.2 is that the view from this plot is from upstream. This means that the velocities represented show the velocity of the rotor in the air and not the velocity that the blades 'feel'. The velocities that the blades feel are in the opposite direction, therefore the tangential and radial velocity equations obtained are of opposite sign when the velocity at the blades are studied.

The velocity that the turbine feels in both of it's components are summarized by a color map in Figure 5.3 at the upright position with maximum velocity in the negative direction of roll (rolling CW when viewed from upstream) for case 5.

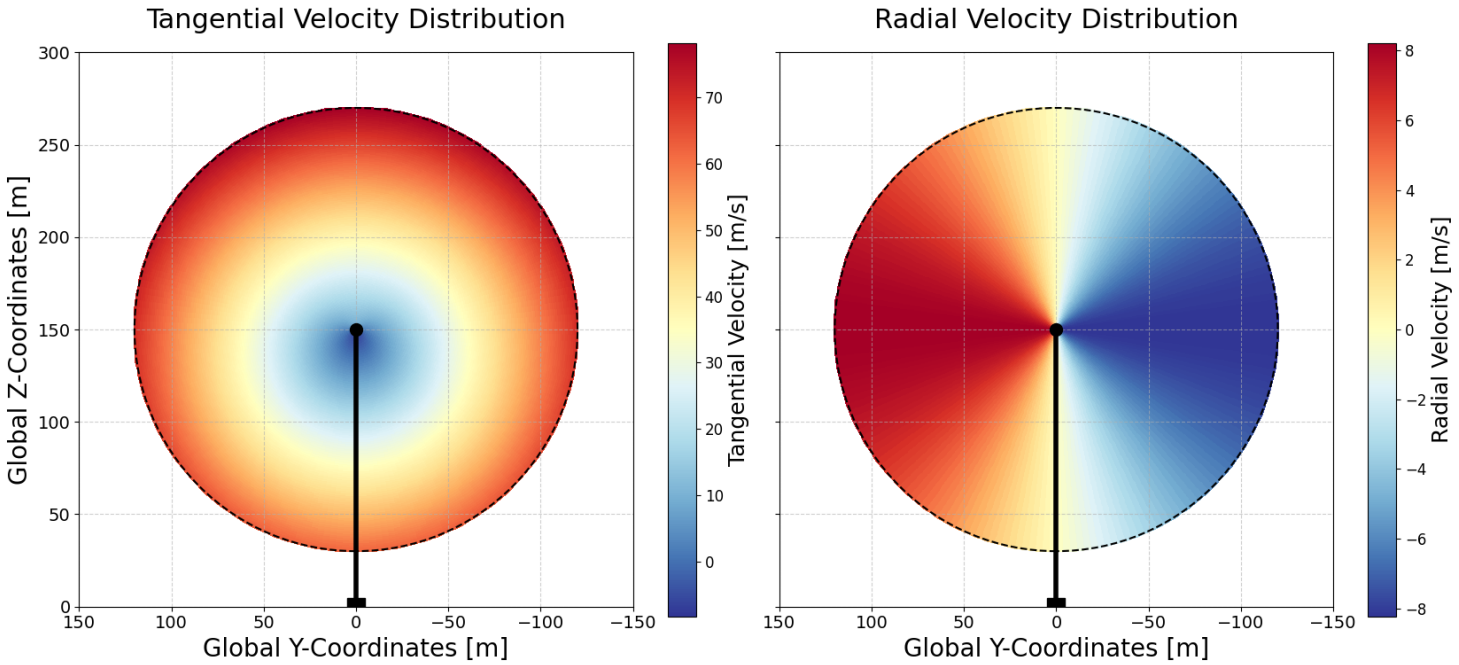

Figure 5.3: The distribution of tangential (left) and radial (right) velocities on the rotor at ϕ = 0°, $\dot{\phi}$ = max (< 0) for a rolling turbine with the characteristics of case 5 (0.05Hz, 10°, TSR 7).

The further away from the rotor, the larger the tangential velocity as expected due to the Ωr component. However, asymmetry in distribution is introduced because the roll axis is at the tower base. Since the rotor section above the hub is further from the roll axis compared to the lower section, the induced roll velocity is always higher in the upper section, leading to a load variation larger on the upper section compared to the lower. This can affect fatigue due to varied loading but also the wake, which can show shearing effects and must be studied. The consequence of this asymmetry will be studied on blade loading in Subsection 5.2.8 and on the wake in Section 5.3.

The radial velocity the blades feel is outwards (positive) on the outer side of the roll rotation and inwards (negative) on the inner side. The closer the blade is to the horizontal line crossing the hub, the larger the radial velocity magnitude as given by its equation. At azimuthal angles 0° and 180°, since the roll velocity and rotor velocity directly add up only to result in tangential velocity, the radial velocity there is null.

5.1.3 Temporal Study of Kinematic Velocities

Before the tangential and radial velocities are plotted in time, the parameters ϕ, $\dot{\phi}$, ψ, and Ω should be defined as a function of time.

First, the equations of tangential and radial velocities are rewritten in the convention that they represent the velocity that the blade 'feels'. These are given in Equation 5.9 and Equation 5.10 respectively.

$$V_{\text{tangential}} = -H\dot{\phi}\cos(\phi + \psi) + r\Omega \tag{5.9}$$

$$V_{\text{radial}} = H\dot{\phi}\sin(\phi + \psi) \tag{5.10}$$

The roll angle, ϕ, is defined as a function of time with a cosine function:

$$\phi(t) = \phi_0 \cdot \cos\left(\omega_{\text{roll}} t\right)$$

Where ω_{roll} is the roll frequency [rad/s] and ϕ_0 is the roll amplitude [rad]. The derivative of this in time is the roll velocity, $\dot{\phi}$:

$$\dot{\phi}(t) = -\phi_0 \omega_{\text{roll}} \cdot \sin\left(\omega_{\text{roll}} t\right)$$

While the rotor speed, Ω [rad/s] is constant, the azimuthal angle is the integral of this rate given by:

$$\psi(t) = \Omega t$$

This is assuming that the point of interest that will be plotted in time is at ψ = 0° initially.

Grouping all of these time-variant parameters gives the time-variant tangential and radial velocities in Equation 5.11 and Equation 5.12.

$$V_{\text{tangential}}(t) = H\phi_0\omega_{\text{roll}} \cdot \sin\left(\omega_{\text{roll}} t\right)\cos(\phi_0 \cdot \cos\left(\omega_{\text{roll}} t\right) + \Omega t) + r\Omega \tag{5.11}$$

$$V_{\text{radial}}(t) = -H\phi_0\omega_{\text{roll}} \cdot \sin\left(\omega_{\text{roll}} t\right)\sin(\phi_0 \cdot \cos\left(\omega_{\text{roll}} t\right) + \Omega t) \tag{5.12}$$

These time-dependent velocities have been plotted for case 5 for blade mid-span, for a turbine operating at TSR of 7 (Ω = 0.5833 rad/s) while rolling at a frequency of 0.05Hz (0.314 rad/s) and at an amplitude of 10° (0.175 rad) in Figure 5.4.

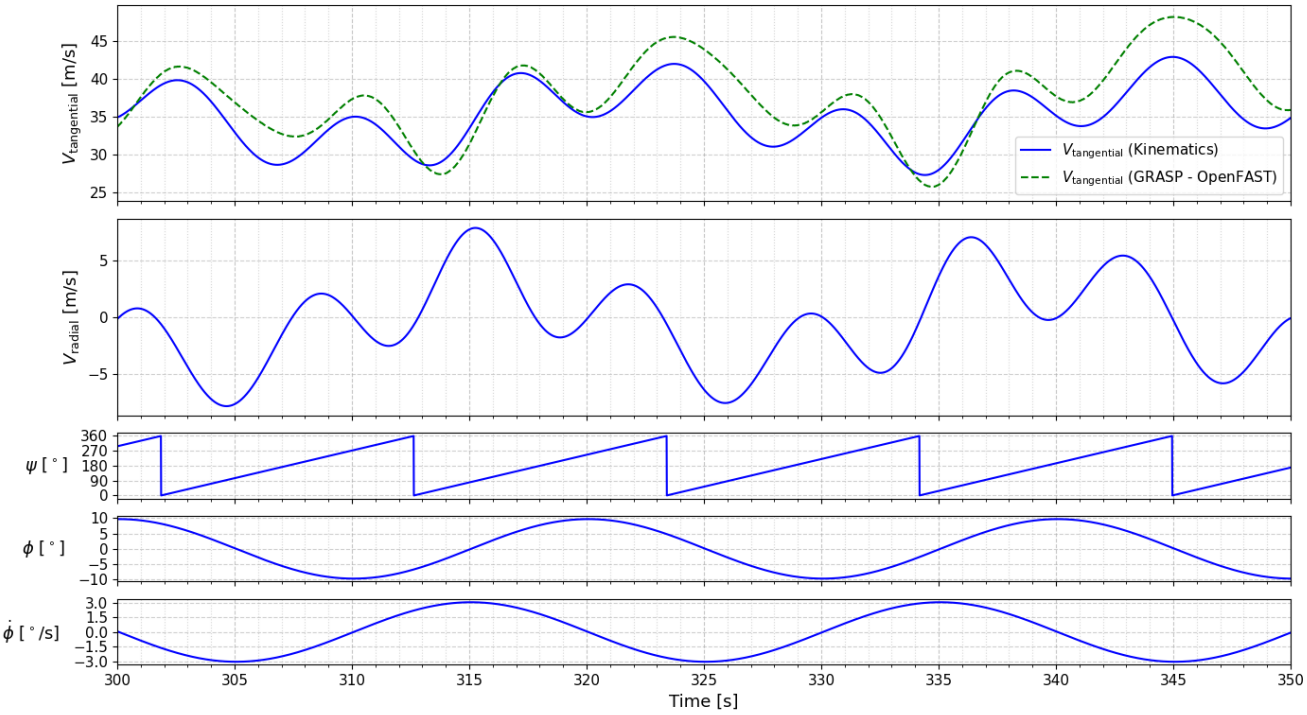

Figure 5.4: Plots of tangential and radial velocities, azimuthal and roll angle, and roll velocity in time for case 5 (0.05Hz, 10°, TSR 7).

In this figure, the top sub-plot showcases the tangential velocity. This plot was made for mid-span instead of the tip because it is also used for comparison to the result obtained from the numerical set-up shown in green. At the tip, complex flow dynamics such as tip vortices which only CFD would capture would not be a fair comparison to verify the formulation of the kinematics.

The kinematics show a similar trend to the numerical results, suggesting they are correct. Differences are expected, visible as slight offsets during certain times of the motion and mostly an underestimation of tangential velocity with kinematics. The former effect is because CFD flow is more complex and also shows inertial effects linked to flow acceleration. These are completely ignored by the velocity equations of kinematics. The radial velocity, as given by Equation 5.10, is directly influenced by the roll velocity since the average value increases with increasing roll velocity. This is logical because radial flow on a turbine does not exist if stationary, hence it is an artifact of roll. The smaller oscillations within the large-scale oscillation are caused by the roll angle and azimuthal angle influencing how the roll velocity contributes to the radial velocity.

A notable observation is that the tangential velocity during roll motion is predominantly higher than the bottom-fixed case baseline of Ωr, equal to 35 m/s for case 5. Since tangential velocity is the primary determinant of resultant velocity at the blade, this sustained increase in average tangential velocity suggests roll motion leads to an average increase in aerodynamic loading compared to a bottom-fixed turbine.

Having established the influence of roll motion on the velocity components at the blades, the analysis now proceeds to how these kinematic changes translate into aerodynamic loads. The effect of these induced velocities is particularly significant because the normal and tangential forces are proportional to the square of the resultant velocity. This quadratic relationship amplifies the impact of velocity fluctuations on blade loading.

Therefore, the subsequent section, Section 5.2, provides a detailed investigation of the blade loading under various roll motion scenarios.

5.2 Study of the Blade Loading

Kinematic analysis provides a fundamental understanding of roll motion by defining the velocities experienced by the turbine blades. This analysis reveals that the tangential velocity is the primary contributor to blade loading, while the effect of the radial flow velocity is negligible. The resulting velocities and their variations directly influence blade loading, which subsequently affects the turbine's wake.

This section examines the effect of roll motion on blade loading. The analysis commences in Subsection 5.2.1 with an introduction to the results of the steadiest roll case obtained from the numerical set-up and its Power Spectral Density (PSD) analysis, and a comparison with the results obtained with kinematics as was derived in Section 5.1. This is followed by an investigation into the phase-averaged blade-averaged normal force in Subsection 5.2.2 and the tangential force in Subsection 5.2.4. A brief explanation in Subsection 5.2.3 addresses the influence of a numerical error identified during the simulations. For verification purposes, the PSD of the normal loading is presented in Subsection 5.2.5. Subsequently, the emphasis shifts to load distribution, first examining the forces along a single blade in Subsection 5.2.6. The unsteady variations are then quantified through a standard deviation study in Subsection 5.2.7. The section concludes with a thorough analysis of the azimuthal loading distribution on the rotor in Subsection 5.2.8 at specific phases of the roll motion.

5.2.1 Introduction to Blade Loading Study

This subsection is divided into three parts. The first part presents the normal and tangential loading per blade for a rolling turbine, as obtained from the GRASP-OpenFAST coupling. The second part compares these results to the loading from the kinematic study, providing insight into the variation of loading and establishing a connection to subsection 5.1. Finally, the third part introduces the PSD analysis of a rolling turbine, based on data from the numerical set-up.

Introduction to Blade-Loading Computed by GRASP-OpenFAST

To introduce the analysis of blade loading, the steadiest roll condition, case 2, is examined first. This case, characterized by a TSR of 7, a roll frequency of 0.03Hz, and a roll amplitude of 5°, was selected to minimize unsteady effects that could introduce unnecessary complexity into the initial results.

The analysis begins with the study of the variation of normal and tangential forces obtained from OpenFAST over time for each blade at mid-span. This is plotted in Figure 5.5. This figure also indicates several key phases of the roll cycle with vertical red lines:

- Phase 0: The turbine crosses the vertical (zero roll angle) position while rotating clockwise (viewed from upstream). At this instant, the roll velocity is at its maximum and aligns with the direction of the rotor's rotation.
- Phase $\pi/2$: The turbine reaches its maximum clockwise roll angle and momentarily stops.
- Phase π: The turbine is again at the vertical position but is now rolling counter-clockwise, in the opposite direction of the rotor's rotation.
- Phase $3\pi/2$: The turbine reaches its maximum counter-clockwise roll angle and momentarily stops.

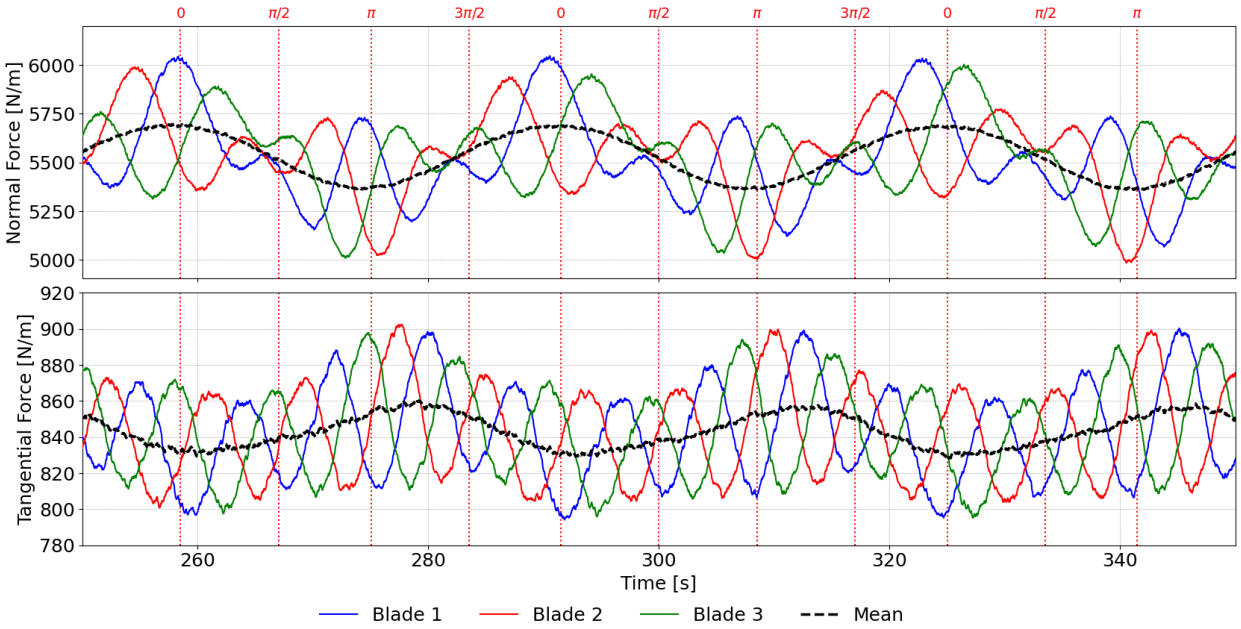

Figure 5.5: Normal and tangential force variation per blade in time at mid-span (0.5 r/R) for case 2 (5°, 0.03Hz, TSR 7).

The normal force variation in Figure 5.5 exhibits two distinct oscillatory components. The first is the high-frequency variation equivalent to the rotor rotational frequency (1P) caused by the blade's rotation, driven by the TSR. The second is the low-frequency variation of the blade-averaged load, which is driven by the roll motion itself and is indicated by the black dashed line.

The blade-averaged normal force varies sinusoidally with only trace of the roll frequency. The blade-averaged loading at phase 0 is larger than at phase π. Although the lower section of the rotor experiences higher velocities at phase π, the increase in velocity experienced by the upper section of the rotor is significantly larger at phase 0. This occurs because the distance from the turbine base (the roll center) to the top of the rotor is greater than to the bottom. This geometric asymmetry generates a loading bias, where the highest average rotor load is produced only when the roll motion and the rotational velocity of the upper rotor disk are aligned, as also illustrated by the tangential load distribution in Figure 5.3.

For a bottom-fixed turbine under idealized conditions, including uniform inflow, removed tower and nacelle, zero pre-cone and tilt, fixed blade pitch, both the blade-averaged forces and the load on each

blade is constant in time. The roll motion introduces fluctuations in both the blade-averaged load and the 1P-frequency load on individual blades. The normal force fluctuation per blade in Figure 5.5 is to an extent representative of the tangential velocity variation shown in Figure 5.4. However, a direct correlation is complex because the force is a function not only of the resultant velocity but also of the inflow angle and the aerodynamic lift and drag polars, as defined by Equation 2.27 and Equation 2.28. While a full explanation is not intuitive, several effects of the roll motion can be commented on.

The roll-induced velocity amplifies the amplitude of the 1P oscillations, as shown by the larger normal force variations for each blade in Figure 5.5. Near the slow-moving phases ($\pi/2$ and $3\pi/2$), the loads on each blade begin to converge toward the constant value expected for a bottom-fixed turbine. However, they do not have sufficient time to fully converge and the loading velocity effects on the blade loading is delayed due to inertial effects. Before convergence to a fixed case loading, the turbine accelerates in the opposite direction, inducing velocities of roll at the blade leading to a change in load. The response of the blade in terms of loading on the velocity depends on its azimuthal position and the direction of roll. The former parameter is the reason for diverging blade loads after the turbine comes to a stop at phases $\pi/2$ and $3\pi/2$.

The tangential load variation is different, following a more sinusoidal oscillation but again showing the same trend of increased amplitude near phases 0 and π. The tangential force appears less affected by the roll-induced variations, suggesting that changes in lift are the main driver of the unsteady oscillations seen in the normal force. Since the turbine operates near the maximum lift coefficient, the lift force is highly sensitive to small changes in the angle of attack in both directions of angle of attack. In contrast, the drag remains relatively constant. Given that the normal force is proportional to the product of lift and the cosine of the inflow angle (Equation 2.27), it is highly sensitive to lift changes given that the inflow angle is small at mid-span. This is less true for the tangential force, which is proportional to the product of lift and the sine of the small inflow angle (Equation 2.28).

In Figure 5.5, a key observation is the differing peak phases for blade-averaged tangential and normal forces: the tangential force peaks slightly after phase π, while the normal force peaks at phase 0. This stems from the time-varying angle of attack and its effect on lift and drag coefficients (from their polars), combined with the distinct formulations in Equation 2.27 and Equation 2.28. While tangential velocity variation, as shown in Figure 5.4, drives overall loading, the difference between normal and tangential load profiles is explained by their formulations. The tangential force is proportional to the difference of lift and drag; with the small inflow angle, drag contributes more to its variation, as it is paired with the cosine of the inflow angle, unlike lift's sine pairing which is small. Thus, when the blade-averaged tangential force is reduced, a larger angle of attack (not shown) increases the drag coefficient, lowering the tangential load. Angle of attack variation is complex, not simply $\arctan(V_{\text{inflow}}/V_{\text{tangential}})$, due to the fluctuating induction zone deficit, which varies in a feedback loop with rotor thrust and roll. The normal load, being a sum of lift and drag with the lift term paired with the cosine of the inflow angle, is less sensitive to the lift–drag ratio, and more influenced by tangential velocity in its time variation.

The normal and tangential forces are fundamental metrics for this investigation due to their direct

relationship with turbine performance and wake characteristics. The normal force corresponds to the rotor thrust, which extracts kinetic energy from the inflow to create the velocity deficit in the wake. In contrast, the tangential force generates the aerodynamic torque, which determines the turbine's power output and induces swirl in the wake.

Typically, the normal force is an order of magnitude larger than the tangential force. This is because the normal force is dominated by the large lift vector, while the tangential force is a function of the much smaller net force in the plane of rotation. Given that the objective of this study is to analyze the coupling between blade loading during roll and its effects on the wake, these two forces are the most relevant quantities for analysis. Therefore, the following sections will focus on blade-averaged loads to characterize the overall rotor response, rather than the time-varying loads on individual blades.

Comparison of Kinematic and Numerical Loads

Following the introduction of the blade loading variation obtained from the numerical set-up, a comparison with the phase-dependent loading analysis obtained via kinematics is essential. This step will help identify the underlying reasons for the observed trends and any discrepancies with the simplified kinematic model.

Figure 5.6 presents the variation of normal and tangential loads for case 2 at mid-span, comparing the results obtained from the OpenFAST-GRASP set-up (dashed lines) with those from the kinematic analysis (solid lines).

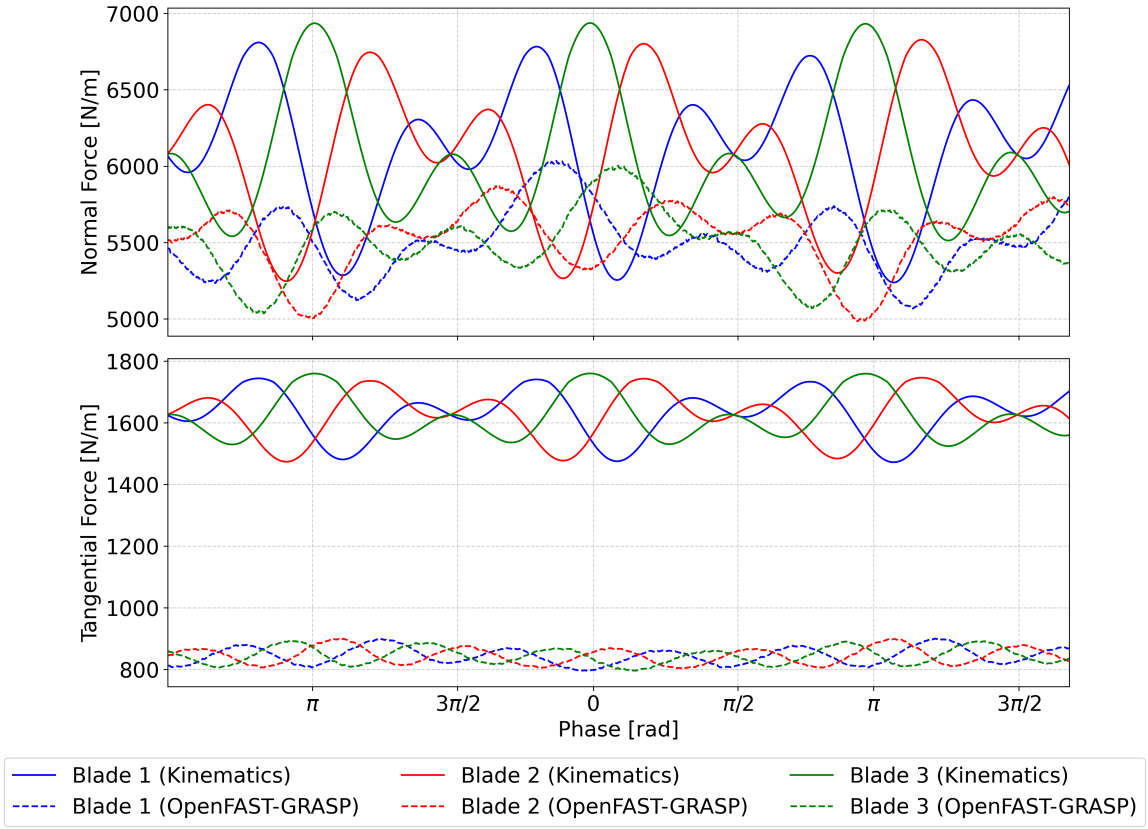

Figure 5.6: Normal and tangential force obtained from the numerical set-up and kinematics per blade at mid-span (0.5 r/R) for case 2 (5°, 0.03Hz, TSR 7).

The formulation of tangential velocity in Figure 5.4 has been used to plot the kinematic normal and tangential forces shown in Figure 5.6. BET has been applied for this derivation with a uniform axial inflow velocity of 10 m/s. The angle of attack, obtained from the velocity triangle at each blade section, is used to determine the local lift and drag coefficients. These coefficients are then combined with the local resultant velocity to compute the blade loading.

A key assumption in the derivation of the kinematic blade loading is the absence of the induction zone. Consequently, the axial inflow velocity is assumed to be 10 m/s. In reality, as represented in the numerical set-up, the flow decelerates ahead of the turbine in the induction zone. This results in a reduced axial velocity and consequently a lower angle of attack. Analysis of the numerical set-up shows that streamwise velocity deficits can reach up to 4 m/s at the turbine inflow, with a distribution resembling a Gaussian profile upstream and the maximum deficits occurring near the hub.

Another potential reason for differences between the kinematic and numerical loading is that, as shown in Figure 5.4, the tangential velocity formulation can overestimate the actual tangential velocity at certain times. Since the loading equations are proportional to the square of the velocity, even small deviations in the approximated velocity can lead to significant differences in loading.

Although the selected case is relatively steady and the analysis point is at mid-span, far from regions where 3-dimensional flow effects are prominent, small influences from 3-dimensional flow, including radial induced flow, are likely. The numerical set-up captures this radial induced flow, whereas the kinematic loading neglects it entirely, using only the tangential velocity from Equation 5.11 and ignoring the radial induced velocity in Equation 5.12.

With these differences in mind, a detailed comparison of the loadings in Figure 5.6 can be made. Considering the normal force first, both variations exhibit a similar pattern, resembling the variation of the tangential velocity in Figure 5.4. However, several distinctions are evident. Although both curves oscillate at the 1P frequency, the kinematic loading does not capture oscillations at the roll frequency. This was previously explained as the frequency of oscillation of the blade-averaged loading. For the kinematic loading of a rolling turbine, the blade-averaged loading remains constant. This is likely due to the constant axial inflow velocity assumption, whereas in reality, the induction zone's velocity deficit varies with the oscillating thrust of the rolling turbine, leading to loading variations. This oscillatory effect at the roll frequency is also visible in the resultant velocity and angle of attack in Figure A.1 in Appendix A.

The mean kinematic normal loading is larger than the mean numerical normal loading, mainly due to the higher angle of attack, which results in larger lift and drag coefficients at mid-span, as obtained from the lift and drag polars. The comparison of these coefficients is shown in Figure A.2 in Appendix A. While a higher axial inflow velocity of 10 m/s should theoretically produce a higher resultant velocity than the decelerated inflow in the induction zone, Figure A.1 shows the opposite. Interestingly, the variation in resultant velocity is very similar in both cases. A further explanation is provided in Appendix A.

The amplitude of the 1P oscillation in the kinematic normal loading is much larger than that in the numerical result. This can be attributed to two factors. First, the higher axial inflow velocity increases the inflow angle, causing the drag coefficient to contribute more to the normal loading than in the numerical case. This is consistent with Equation 2.27, which shows that drag's contribution to the normal force is proportional to the sine of the inflow angle. Second, as shown in Figure A.2, the drag coefficient varies more significantly in the kinematic case due to the shift in the airfoil's operational point at the higher angle of attack. This larger variation, combined with the increased contribution of the drag coefficient, results in larger 1P oscillations.

Examining the tangential loading in Figure 5.6 shows that the mean kinematic tangential load is nearly twice as large as the numerical result. This difference is driven mainly by the inflow angle and aerodynamic coefficients. Although a higher resultant velocity could contribute to the difference, Figure A.1 does not indicate a higher resultant velocity for the kinematic case. The higher inflow angle increases the angle of attack, which in turn produces larger lift and drag coefficients, as shown in Figure A.2. According to Equation 2.28, lift contributes more to the tangential force at higher inflow angles, while drag's contribution decreases, increasing the mean tangential force. The oscillation amplitude at 1P also increases, similar to the normal force, due to the increased sensitivity of the aerodynamic coefficients to changes in angle of attack during roll.

In the numerical tangential force, the amplitude of the 1P oscillation decreases during stationary phases at $\pi/2$ and $3\pi/2$, whereas in the kinematic results, the loading converges for each blade, similar to the normal loading. While the trend in the kinematic tangential load can be explained by the variation in angle of attack and resultant velocity in Figure A.1, the absence of convergence in the numerical tangential loading is less clear. This is likely due to the combination of the airfoil's operational point with angle of attack variation and inflow angle, and their combined effect as shown by the tangential force equation in Equation 2.28. It may also be influenced by inertial effects, which prevent the tangential load from stabilizing when the turbine is briefly stationary.

A general observation for both forces is that the time variation of loading for each blade does not perfectly match the shape of the numerical variation, thus the kinematic loading sometimes lags or leads the numerical loading. This has been explained for the tangential velocity in Figure 5.4 by the fact that the kinematic formulation does not consider inertial effects, whereas the numerical results do. The time required for the load to develop or decay with turbine motion introduces this discrepancy, which is expected to become larger under more unsteady roll conditions.

Introduction to Power Spectral Density of Blade-Loading Computed by GRASP-OpenFAST

Returning back to purely analyzing the results of the numerical set-up, the PSD analysis is plotted for the normal force at mid-span for case 2 in Figure 5.7a. This figure reveals several distinct frequency peaks directly or indirectly related to the roll and rotor frequencies. The primary peaks for a rolling wind turbine are the roll frequency ($f_{\text{roll}} = 0.03$Hz) and the rotor's rotational frequency (1P, $f_{\text{rotor}} = 0.093$Hz). While the roll frequency exhibits the highest power, the 1P peak is barely noticeable relative to its neighbors. This minimal 1P power is attributed to the uniform inflow velocity profile and the omission of tower and rotor geometric angles (rotor tilt and pre-cone) in this study, which leads to

little variation in blade angle of attack and loading within a single rotation. Note that this contradicts the analysis made for normal loading in Figure 5.5. Further explanation of this is given in two paragraphs below.

Other prominent peaks correspond to the first upper- and lower-sideband frequencies, which arise from the modulation of the rotor frequency by the roll motion and are defined by the relation $f_{\text{rotor}} \pm n \cdot f_{\text{roll}}$. Specifically, the first-order sidebands ($n = 1$), located at 0.063Hz and 0.123Hz, show considerably greater power than the rotor (1P) frequency. These frequencies stem from the temporal variation of tangential velocity at the blades, which in turn affects the angle of attack and loading. As supported by Figure 5.7b, which presents the PSD analysis of tangential velocity obtained via kinematics (as per Equation 5.11), the tangential velocity itself only exhibits these sideband frequencies.

Previously, in the study of Figure 5.5 it was mentioned that roll and 1P frequencies are observed. The correction to this statement would be that 1P frequencies are observed as sideband frequencies instead as given by Figure 5.7b. This is because the normal loading is largely driven by the tangential force. However, the 1P frequencies are more prominent in the tangential force plotted in time in Figure 5.5, possibly resulting in more powerful 1P peaks of tangential force PSD.

Interestingly, while the tangential velocity primarily varies at sideband frequencies due to the combined influence of rotor and roll velocities, the blade loading (as depicted in Figure 5.7a) also prominently features the roll frequency. A possible explanation for this lies in the induction zone-blade loading feedback loop briefly mentioned above. This occurs when the turbine rolls, the rotor's thrust coefficient varies with the roll frequency which consequently has affects the induction zone velocity deficit. This then alters the local inflow velocity and angle of attack at the blades. This change in inflow velocity and angle of attack directly influences blade loading. This continuous feedback between the thrust coefficient and the induction zone explains the high power observed at the roll frequency.

As anticipated, the second-order sidebands ($n = 2$), found at 0.032Hz and 0.153Hz, are present but carry significantly less power. Higher-order sidebands ($n \geq 2$) are too weak to be distinguished.

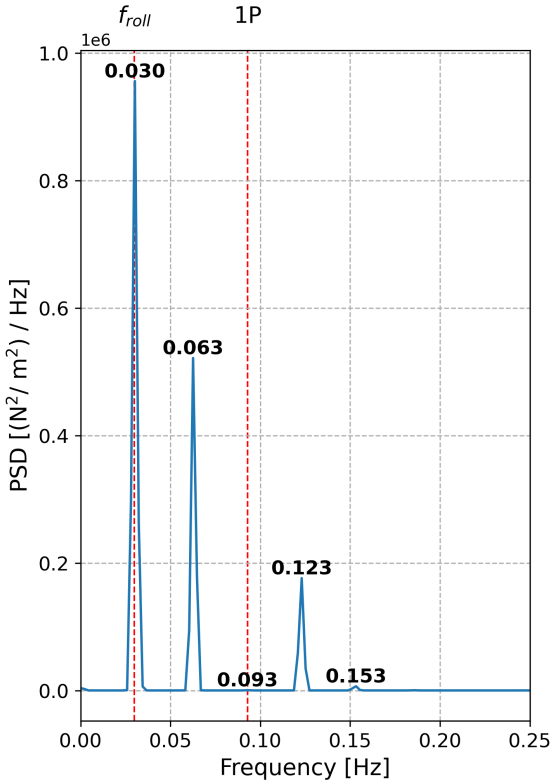

(a) Power Spectral Density of the normal force at mid-span (0.5 r/R) for case 2 (5°, 0.03Hz, TSR 7).

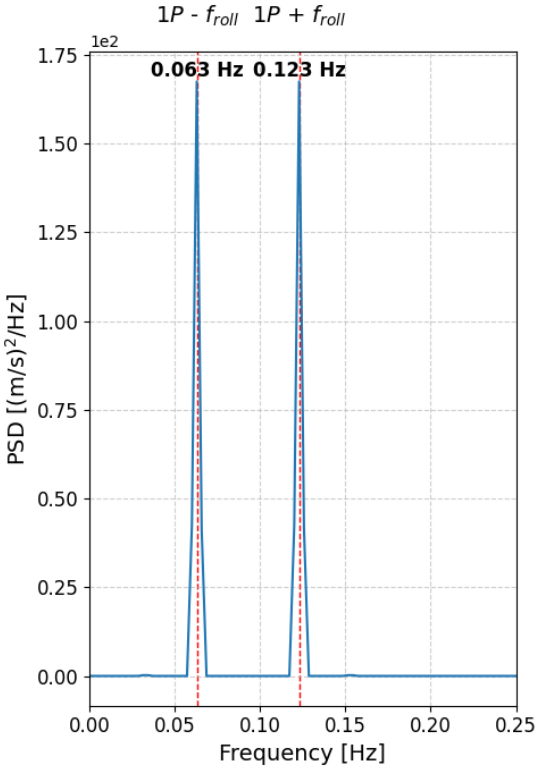

(b) Power Spectral Density of the tangential velocity obtained by kinematic analysis at mid-span (0.5 r/R) for case 2 (5°, 0.03Hz, TSR 7).

Figure 5.7: Power Spectral Density for case 2 (5°, 0.03Hz, TSR 7) normal force and tangential velocity obtained by kinematic analysis at at mid-span (0.5 r/R).

Concluding, the PSD analysis clearly demonstrates that the roll motion not only introduces roll frequencies to into the blade loading spectrum but also significant first-order sideband frequencies. These resulting harmonic load fluctuations are anticipated to propagate into the turbine's wake, subsequently inducing corresponding velocity fluctuations within the flow field.

5.2.2 Normal Force Analysis

Building upon the foundational analysis of case 2 presented in Subsection 5.2.1, this subsection extends the investigation to the blade-averaged normal force. The analysis here compares the blade-averaged load across all simulated roll cases, focusing on two representative spanwise locations: 0.75 r/R and 0.95 r/R. A comprehensive study of the complete spanwise load distribution is postponed to Subsection 5.2.6.

Figure 5.8 presents the phase-averaged blade-averaged normal force at the 0.75 r/R station for all cases, with the results organized by TSR. The motions of 0.03Hz and 0.05Hz roll frequencies have been adjusted to the same scale.

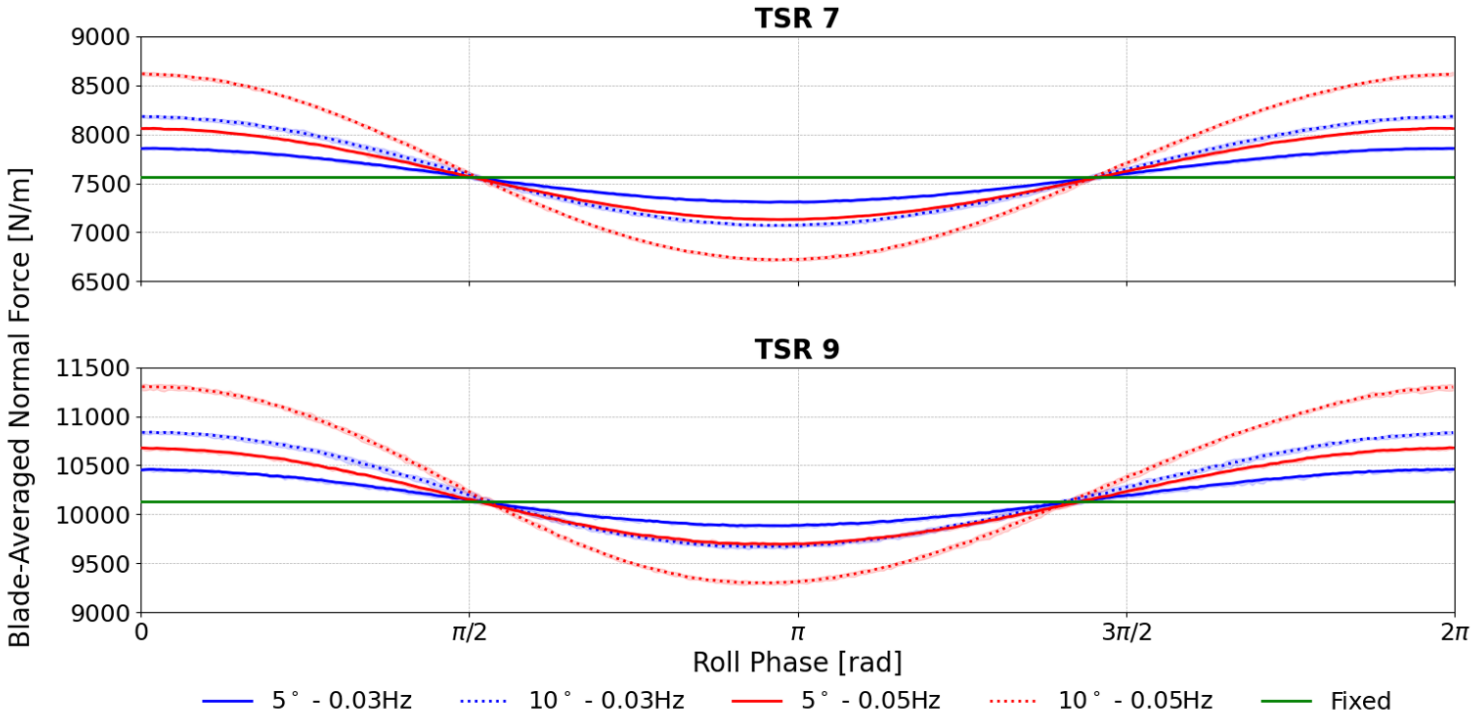

Figure 5.8: Phase-averaged blade-averaged normal force variation at 0.75 r/R for all cases.

Observing the results for both TSRs shows that an increase in roll amplitude, which can be compared by looking at the solid and dotted lines, leads to an increased amplitude of fluctuation, as expected.

The intersection points of the normal force curves for each case with the bottom-fixed (green) case do not align exactly with the stationary phases of roll. When the wind turbine rolls clockwise (as viewed from upstream) and comes to a stop, there is a slight delay before the loading matches the bottom-fixed case, as indicated by the intersection occurring shortly after phase $\pi/2$. The opposite trend is observed for counterclockwise roll. The intersection occurs slightly before phase $3\pi/2$. This asymmetry is also evident at phase π, where the minimum load is slightly skewed, where the drop in load approaching phase π is steeper than the subsequent recovery. Such behavior can be attributed to inertial aerodynamic effects, specifically the lag between the turbine's motion and the flow's ability to adapt, which delays the loading response. This effect becomes more pronounced under strongly unsteady roll conditions and is further amplified by the inherent geometric asymmetry of the system.

Increasing the TSR amplifies the loading asymmetry and increases the absolute fluctuation relative to the bottom-fixed case. However, in terms of percentage fluctuation, the difference compared to TSR 7 is not significant.

The effect of roll frequency can be assessed by comparing the blue and red curves. Increasing the roll frequency generates a higher roll-induced velocity, which has a similar effect to increasing the roll amplitude. In the time domain, a higher frequency would naturally result in more frequent loading fluctuations. A limitation of this comparison is that the roll frequency increase is not twice the baseline value, whereas the roll amplitude is doubled from $5°$ to $10°$. Consequently, it is difficult to isolate whether frequency or amplitude has the greater influence on the magnitude of load fluctua-

tions. Intuitively, the variation in loading is proportional to the variation in velocity, and the maximum roll-induced velocity is proportional to the product of roll amplitude and frequency.

To examine whether this skew is a localized effect, the results at 0.75 r/R in Figure 5.8 are compared with the near-tip results in Figure 5.9. Interestingly, the phase-averaged normal loading intersects the bottom-fixed loading at a phase very close to the stationary position, $\pi/2$. Although the minimum load region appears more symmetric around phase π, the intersection at the opposite stationary phase occurs, as in Figure 5.8, slightly before $3\pi/2$.

Figure 5.9 also shows that near the blade tip, the fluctuations are more unsteady, as indicated by the larger shaded regions around the phase-averaged curves. These shaded areas represent the maximum and minimum values observed at each phase over the full simulation. This unsteadiness becomes more pronounced with increasing TSR.

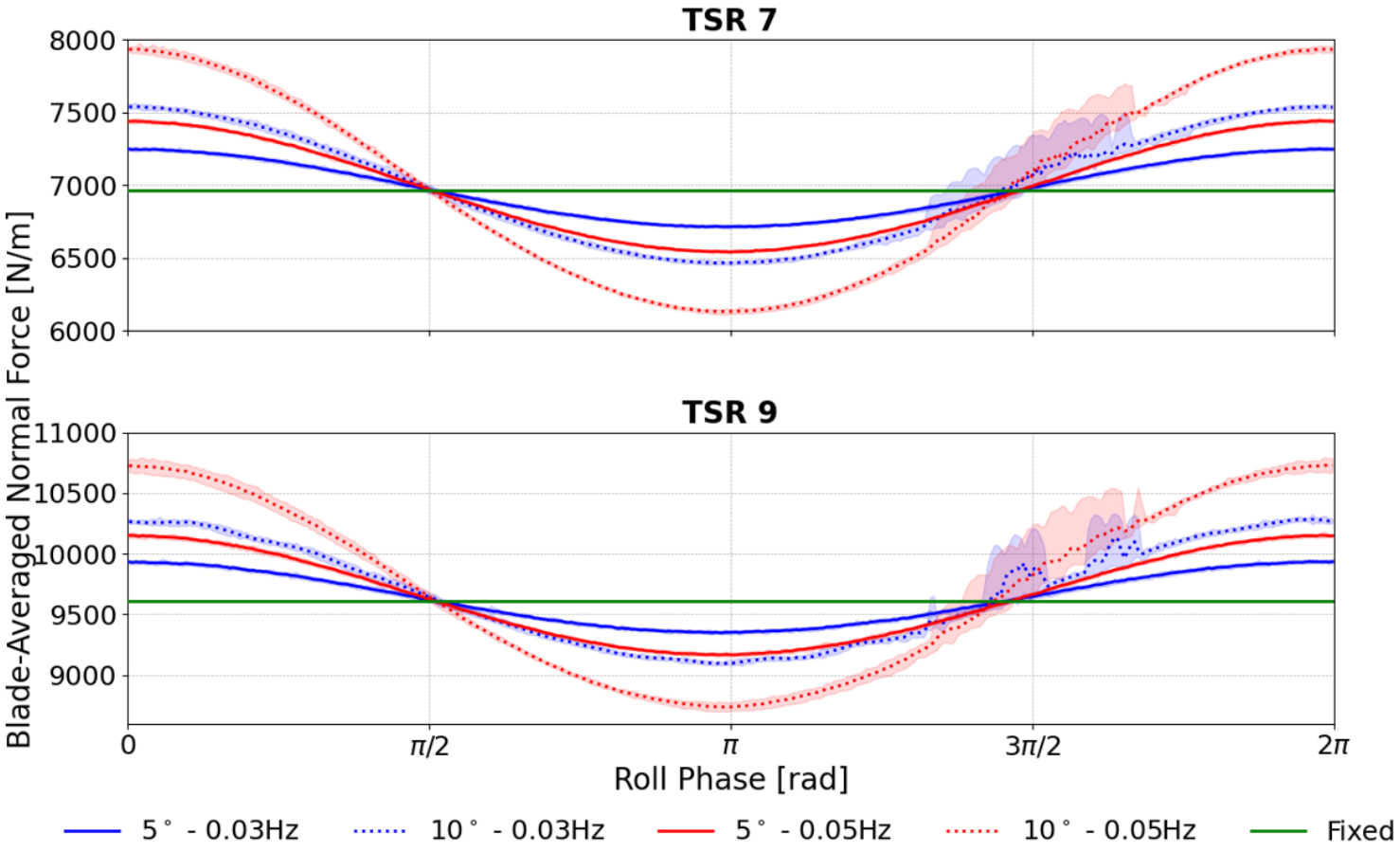

Figure 5.9: Phase-averaged blade-averaged normal force variation at 0.95 r/R for all cases.

Analysis of the normal force variation near the blade tip, as shown in Figure 5.9, reveals an anomalous sharp peak in the loading at and after phase $3\pi/2$, when the turbine is at maximum roll angle. This peak is exclusively observed in cases with high roll amplitude, and its magnitude becomes more pronounced at higher TSRs.

A high roll frequency is not a prerequisite for this phenomenon, as it appears in high-amplitude, low-frequency cases but is absent in low-amplitude, high-frequency cases, potentially eliminating the

possibility of unsteady/inertial effects. This effect cannot be attributed to the kinematic effects described in Section 5.1, since the roll velocity is minimal at this phase. Likewise, inertial effects are an unlikely cause for such a sudden increase in load.

Further investigation determined that this peak is an artifact resulting from a numerical error. Subsection 5.2.3 is dedicated to explaining this numerical error and showing its implications on the results.

5.2.3 Study of the Numerical Error

The cause of sudden increase in load as was shown by Figure 5.9 near the tip that occurs mainly at phase of $3\pi/2$ is explained in this subsection. To understand the cause of this, several plots have been made, from which one was them was useful to understand the problem. This was the iso-vorticity plot as shown by Figure 5.10.

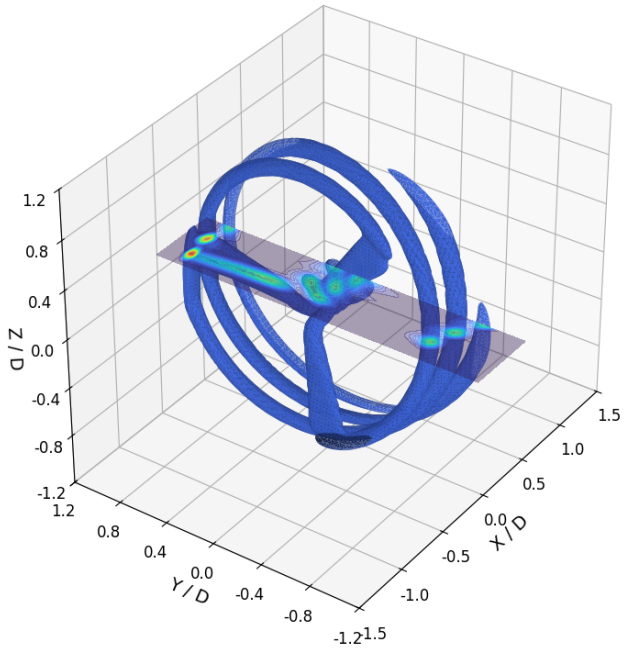

Figure 5.10: Iso-vorticity plot at phase $3\pi/2$ for case 7 (10°, 0.03Hz, TSR 9).

Visual inspection of the flow field in Figure 5.10 reveals a flattened region of iso-vorticity around the 9 o'clock blade position (when viewed from upstream). This distortion is corroborated by the XY-slice, which shows elliptical vortex cores being shed from the blade, in contrast to the more circular cores on the opposite side at the 3 o'clock position. Furthermore, the iso-vorticity contours appear abruptly truncated at this location, with artificially large magnitudes.

The conditions for this anomaly are specific as it occurs only at the largest roll amplitude (10°), precisely when the turbine reaches its maximum roll angle at phase $3\pi/2$ and at the instant a blade is passing through the 270° azimuthal position, achieving its maximum lateral displacement from the tower base. The sudden truncation of the iso-vorticity field suggests that the ALM is constrained to a finite computational domain.

This is indeed the case. For computational efficiency, the ALM is active only within a prescribed box. The model distributes loads via a Gaussian smearing function, and this bounding box prevents the

distribution from extending to infinity. While this method is effective when the turbine operates within the box, a numerical error arises when a blade tip touches or exceeds the boundary. At that point, one or more nodes of the ALM are found too close to, or outside of, the border, causing the Gaussian distribution to be prematurely truncated. The numerical solver interprets this sharp, artificial gradient as a region of extremely high circulation near the tip, which manifests as the false load peaks seen in Figure 5.9.

This mechanism explains why the error is dependent on roll amplitude but independent of roll frequency. The reason it occurs primarily at phase $3\pi/2$ (and to a much lesser extent at $\pi/2$) is likely due to a slight lateral offset in the placement of the ALM active zone relative to the hub. Such an offset would cause the blade to intrude the boundary more severely on one side of its roll cycle than the other, influencing the magnitude of the resulting numerical peak.

The implications of this numerical artifact shall be studied since it has non-negligible effects.The variation of angle of attack and dynamic pressure are first analyzed. These are plotted near the tip for case 7, the case in which this effect is seen consistently in every roll cycle given by it's presence in the phase-averaged results in Figure 5.9, in Figure 5.11.

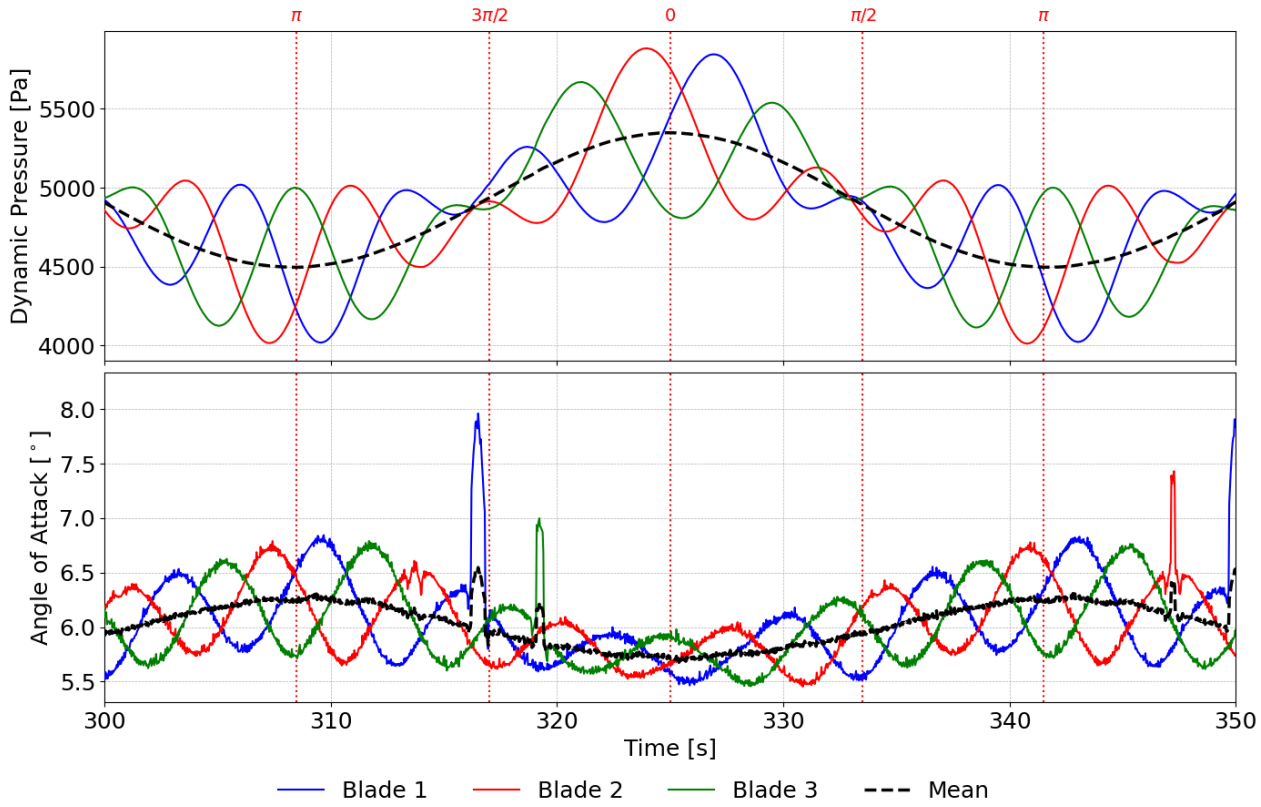

Figure 5.11: Dynamic pressure and angle of attack variation per blade in time at 0.95 r/R for case 7 (10°, 0.03Hz, TSR 9).

An analysis of the blade-averaged dynamic pressure reveals no evidence of this anomaly, confirming that its origin is not related to kinematic changes in the resultant velocity.

Instead, plotting the angle of attack over time shows that the force peaks are caused by a sudden,

nonphysical discontinuity in the calculated angle of attack, which results from the artificially high circulation induced by the numerical error. This discontinuity occurs for each blade in sequence as it passes through a critical azimuthal position. For instance, blade 1 reaches this position first, followed by blade 2, and then blade 3. The consistent recurrence of this numerical error in every roll cycle for all blades, as observed in case 7, is a direct consequence of the harmonic relationship between the roll frequency and the rotor's rotational frequency.

The spanwise distribution of normal and tangential forces, plotted in Figure 5.12 for blade 1 at instants before and during the load peak, confirms that the effect is highly localized to the blade tip. The tangential load is more severely affected by this numerical error. This is because the large, nonphysical increase in the angle of attack also substantially increases the inflow angle. According to Equation 2.28, this larger inflow angle causes the lift vector, which is the dominant aerodynamic force, to contribute more significantly to the tangential force component, in addition to increase lift coefficient due to higher angle of attack, resulting in a disproportionately large peak.

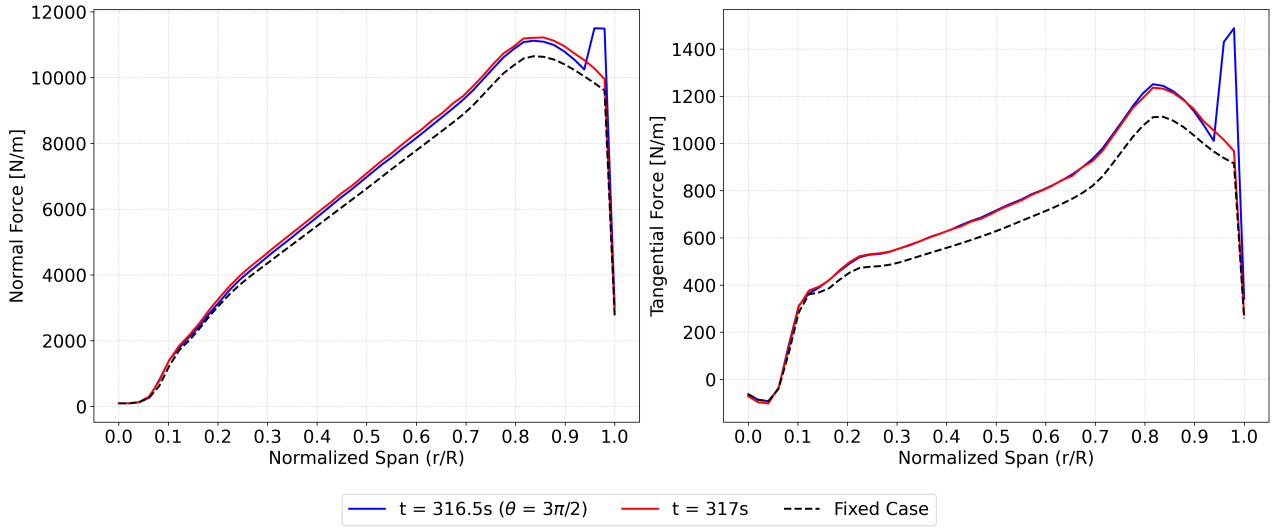

Figure 5.12: Normal and tangential force distribution over the span of blade 1 at the time of and after the load peak of case 7 (10°, 0.03Hz, TSR 9).

The normal and tangential load distributions are determined by the lift and drag coefficients, which are a direct function of the angle of attack. The left plot in Figure 5.13 presents the spanwise distribution of the angle of attack and the corresponding lift coefficient at instants just before and during the load peak.

The plot shows that the peak in the angle of attack near the tip leads to a sudden, proportional increase in the lift coefficient. This confirms that the airfoil section is operating below its stall angle. Since the blade operates on this linear portion of the lift polar, the increase in the angle of attack does not lead to a significant rise in the drag coefficient. This combination explains the large increase in the tangential load; the drag force, which theoretically hinders the tangential force, remains small and does not counteract the significant increase in the lift-induced component.

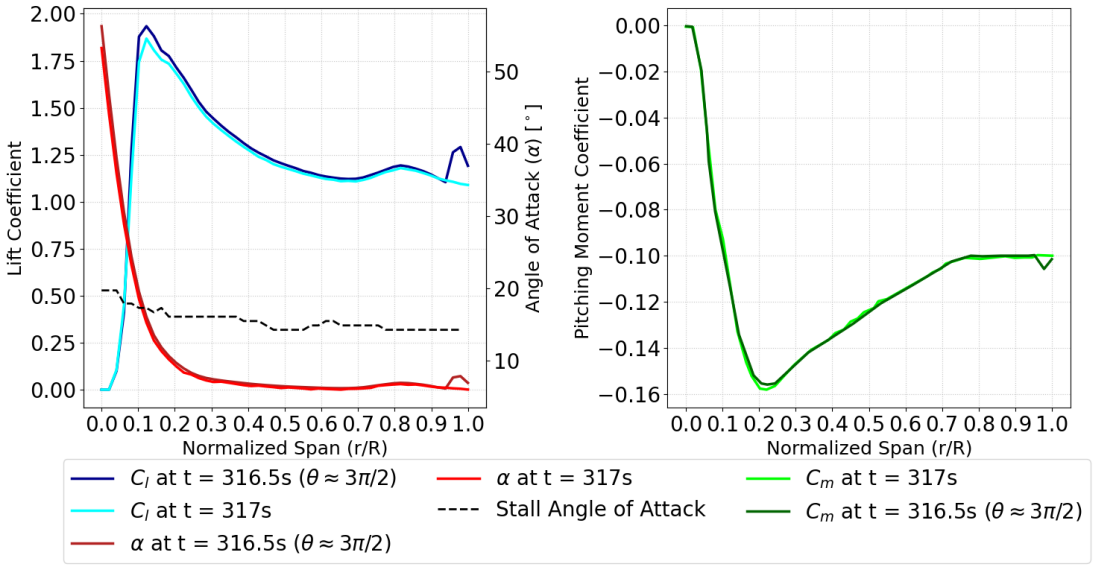

Figure 5.13: Lift coefficient and angle of attack (left), and pitching moment coefficient (right) over the span of blade 1 at time of and after the load peak of case 7 (10°, 0.03Hz, TSR 9).

The objective of this analysis was to document the implications of this numerical artifact on the results and to ensure that subsequent analyses are interpreted with this effect in mind. A detailed discussion was deemed essential because, due to time limitations, the causes of this numerical error was not corrected.

5.2.4 Tangential Force Analysis

The blade loading analysis continues with the study of the phase-averaged tangential load for various spanwise locations.

Figure 5.14 shows the variation of the tangential load at spanwise location of 0.75 r/R for all cases, grouped by TSR. At this location, the artifacts of numerical error is not present due to the distance from the blade tip.

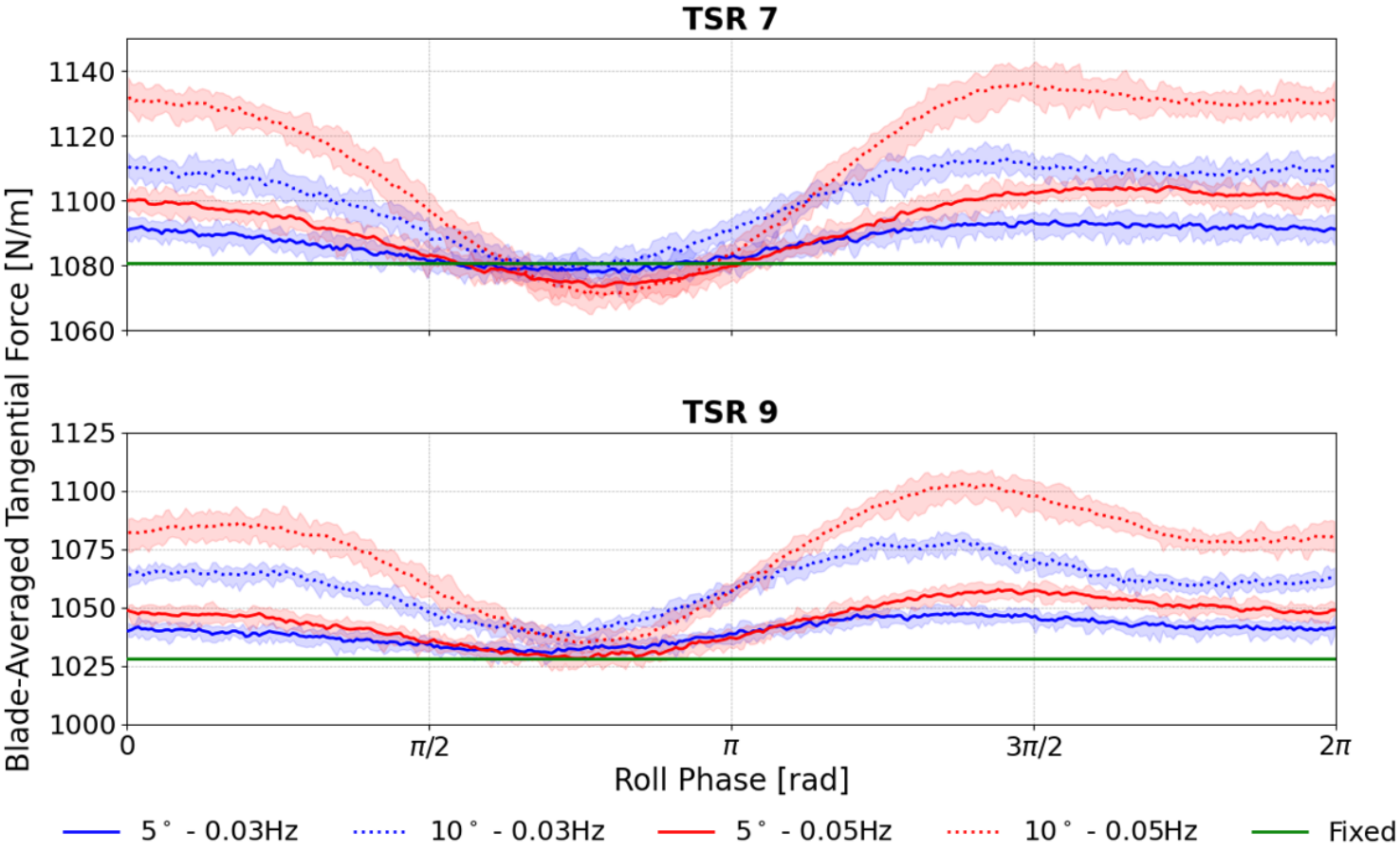

Figure 5.14: Phase-averaged blade-averaged tangential force variation at 0.75 r/R for all cases.

A notable characteristic of the tangential load variation with phase is its non-sinusoidal waveform, which contrasts with the more regular oscillations of the normal force shown in Figure 5.8. For the unsteadier cases, the tangential load reaches a maximum slightly before phase $3\pi/2$, whereas for the steadier cases the peak is less pronounced, resulting in a more uniform tangential loading distribution. The minimum tangential loading occurs between phases $\pi/2$ and π.

Both increasing roll amplitude and roll frequency predictably enhance the tangential load oscillations, similar to the normal force response. However, the difference between low-amplitude cases of differing frequencies is minimal. The influence of frequency is negligible at low roll amplitudes but becomes more pronounced when the amplitude is higher.

The shaded regions around the phase-averaged, blade-averaged curves represent the range be-

tween the maximum and minimum values observed during the full simulation. While the absolute tangential load unsteadiness is smaller than that of the normal load, due to the larger magnitude of normal forces, the relative variation is greater. This indicates that, on a normalized basis, tangential loading exhibits a higher degree of unsteadiness during roll motion across all phases.

An interesting contrast to the normal force is that an increase in TSR does not lead to a corresponding increase in the phase-averaged tangential load. In fact, the tangential load is slightly reduced at higher TSRs. This behavior can be attributed to the interplay between the resultant velocity and the angle of attack. At a higher TSR, the increased rotational speed leads to a larger resultant velocity but a smaller mean angle of attack. According to Equation 2.28, the significant reduction in the inflow angle diminishes this lift component more than the higher resultant velocity can compensate for. Thus, the net tangential force decreases at higher TSRs.

A second observation regarding the influence of TSR is that for TSR 9, the tangential load fluctuations remain entirely above the value of the bottom-fixed case. This suggests that for these specific high-TSR conditions, the roll motion consistently increases the tangential loading. This behavior can be explained by the operating aerodynamic regime. At a lower TSR, the larger fluctuations in the angle of attack may push the airfoil into regions of higher drag during parts of the roll cycle, causing the tangential load to drop below the baseline. At the higher TSR of 9, the operating angle of attack and its range of fluctuation are smaller, keeping the airfoil in a more aerodynamically efficient regime and preventing these significant, drag-induced drops in load. This suggests that roll motion almost consistently enhances the large-scale swirl within the wake for TSR 7 and always for TSR 9.

To determine if these trends are consistent along the blade's span, the tangential loads at the midspan location are examined in Figure 5.15.

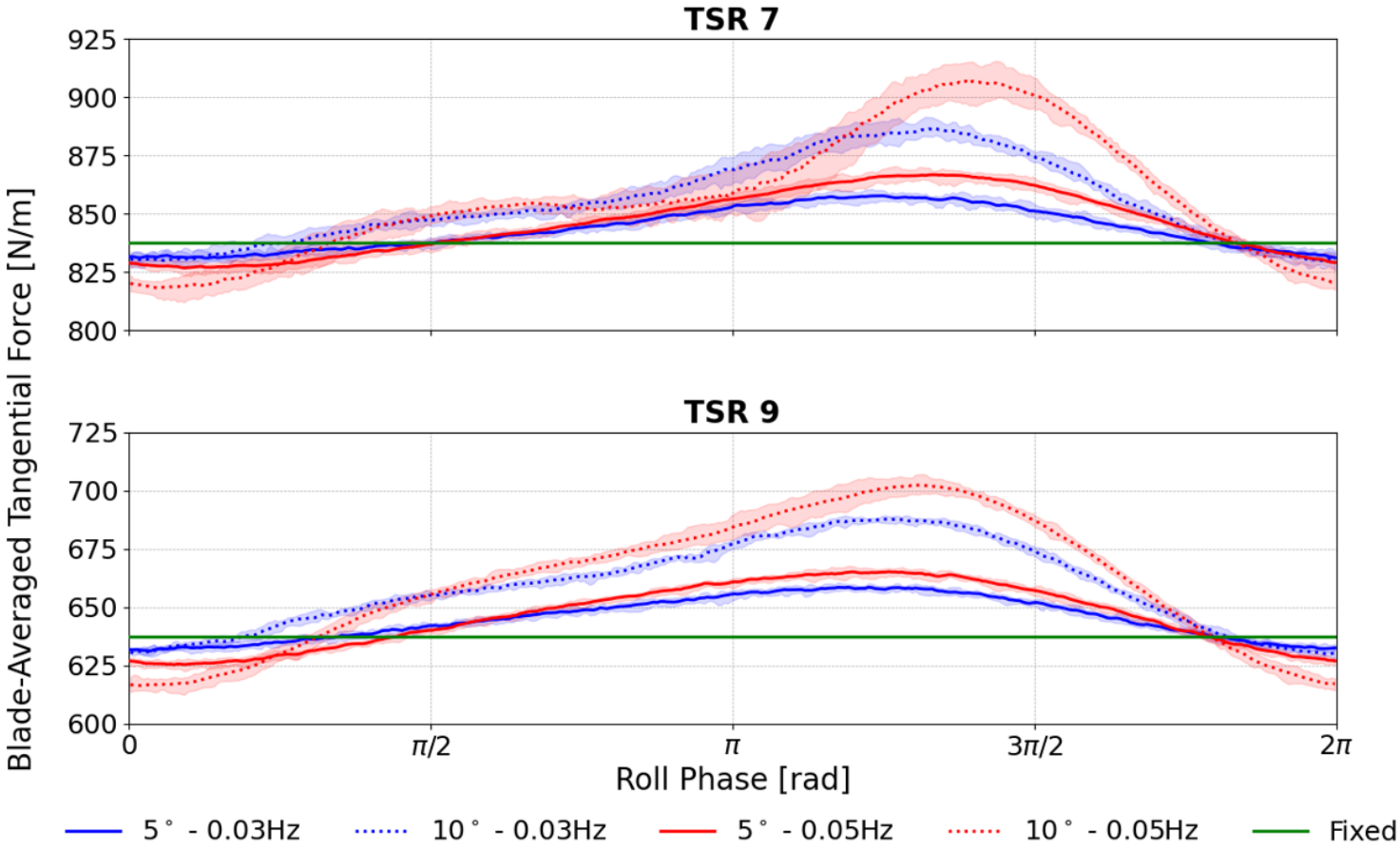

Figure 5.15: Phase-averaged blade-averaged tangential force variation at the mid-span (0.5 r/R) for all cases.

The results from the mid-span location, presented in Figure 5.15, confirm that whether the tangential load remains entirely above the bottom-fixed case baseline is indeed dependent on the spanwise position. Specifically, at locations closer to the hub, such as the mid-span, a greater portion of the load cycle dips below the bottom-fixed case value. This can be attributed to the lower rotational velocity at a smaller radius, which results in a higher mean angle of attack. This, in turn, can push the airfoil into regions of higher drag during certain phases of the roll cycle, causing a more pronounced reduction in tangential force.

Despite this, the plot clearly shows that the load remains above the baseline for the majority of the roll cycle. This highlights a fundamental asymmetry in the response, whereas the normal load fluctuates around the bottom-fixed value, the tangential load experiences a net average increase. The increase in tangential load during one phase of the roll cycle is consistently larger than the decrease in the other. Therefore, it is theorized that roll motion should lead to a higher mean power output and as mentioned previously, an increased swirl in the wake.

5.2.5 Power Spectral Density of Normal Loading

The PSD of the normal force at the mid-span of blade 1 is presented in Figure 5.16 for several selected cases. Similar to case 2 as was discussed in Subsection 5.2.1, for case 4 (Figure 5.16a), significant peaks are present at the roll and first sideband frequencies. The second sidebands are barely visible.

A comparison between case 4 and case 2, which differ only in roll frequency, reveals that a higher roll frequency consistently results in an increased peak power across all frequencies, as expected. This trend is also observed when comparing case 6 (Figure 5.16b) and case 8 (Figure 5.16c), which likewise differ only in their roll frequency.

Across all investigated roll motions, the same characteristics of power distribution are consistently replicated. These include the fact that the roll frequency is the dominant frequency, followed in power by the lower sideband frequency, and then the upper sideband frequency. While the second-order sideband frequencies are negligibly small in power, a consistent trend within a given order of sideband frequency persists: the power of the lower sideband frequency is always larger than that of its upper sideband counterpart.

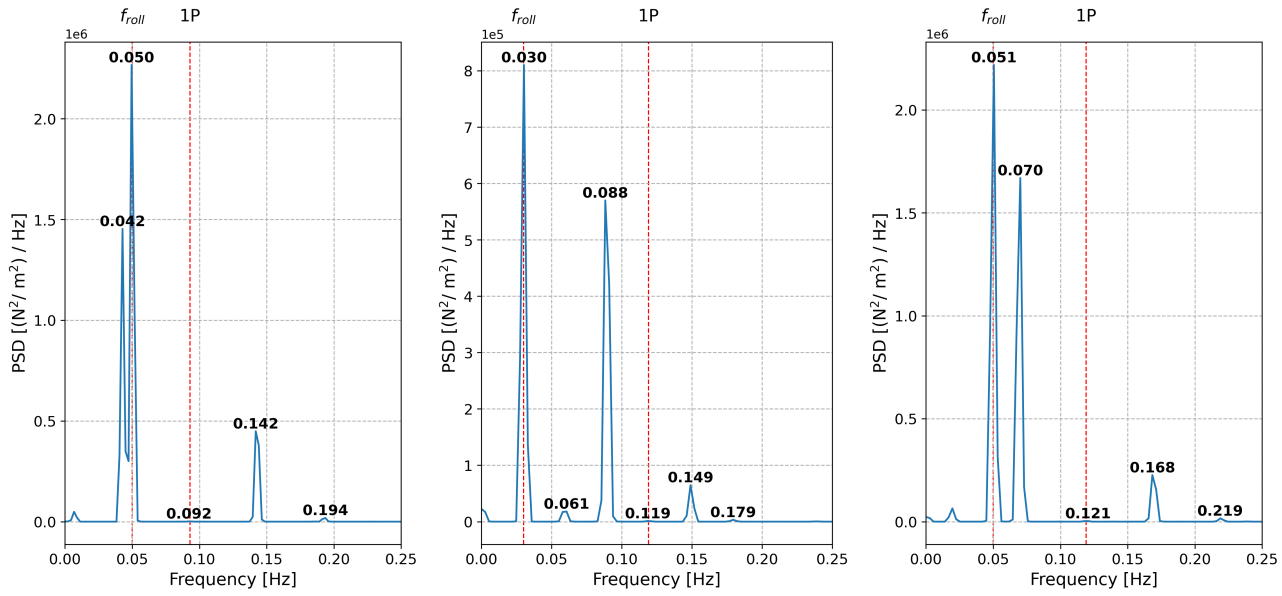

(a) Case 4 (5°, 0.05Hz, TSR 7). (b) Case 6 (5°, 0.03Hz, TSR 9). (c) Case 8 (5°, 0.05Hz, TSR 9).

Figure 5.16: Power Spectral Density of the normal force on blade 1 at mid-span for selected cases.

The effect of the TSR is examined through two distinct comparisons. First, comparing case 2 (Figure 5.7a) with case 6 reveals that an increase in TSR generally reduces the spectral power across all peaks.

However, an interesting and different trend emerges when comparing case 4 to case 8. These configurations involve higher roll frequencies compared to cases 2 and 6. In this scenario, a higher TSR leads to the amplification of all discernible frequency powers in the spectrum, with the exception of the roll frequency itself. This behavior is expected, as an increased TSR primarily influences the rotor frequency (1P) and its dependent sideband frequencies.

It is worth noting that while the comparison between case 2 and case 6 indicated a reduction in the roll frequency's power with increasing TSR, this decrease was very small. This consistent observation across comparisons suggests that the roll frequency's power is relatively insensitive to changes in TSR compared to the more pronounced effects on rotor-dependent frequencies.

The implications of these spectral characteristics are primarily relevant to structural and fatigue analysis. However, these blade loading variations also directly influence the turbine's wake. The energy injected at these specific frequencies is expected to manifest as coherent velocity fluctuations, particularly in the near-wake region where their influence is strongest.

5.2.6 Blade Spanwise Loading Distribution

To complement the loading analysis against phases of roll motion for a specific location on the span of the blade, this subsection examines the spanwise variation of phase-averaged loading at selected phases. This approach provides a comprehensive view of the loading across the entire blade at critical moments in the roll cycle.

However, a key limitation of the methodology must be noted. Given that this analysis is only studying a single blade rather than the blade-averaged data, the phase-averaging process disregards the azimuthal position of the blade. Consequently, certain results may be difficult to interpret. For example, at phase 0, the normal load is expected to increase for a blade in the upper half of the rotor but decrease for a blade in the lower half. While the net effect on the rotor is dominated by the upper blades due to the tangential velocity bias as was shown by Figure 5.3, the current averaging method combines these opposing effects. This can lead to an underestimation of the peak load variations and may obscure the underlying physics. Azimuthal angle dependent phase averaging was not implemented in the post-processing code used to generate the results herein.

The analysis begins with the steadiest condition, case 2, presented in Figure 5.17. The spanwise distribution of normal force reveals that the load increase at phase 0 is slightly smaller in magnitude than the load decrease at phase π. This is possibly caused by the limitation of this study as was explained above which produces falsely asymmetric load variation. Therefore this study should not focus on the minute variations in loading, but the larger more distinct variations which are large enough to be outside the margin of error.

The general shape of the normal force distribution is as expected. Near the blade root (r/R < 0.1), the load is nearly zero due to very high angles of attack, where the small drag force is the dominant contributor. Moving outboard, the load increases approximately linearly as the angle of attack decreases into the lift-dominated regime and the resultant velocity increases with radius. The magnitude of the load variation due to the roll motion is greatest near the blade tip, which aligns with the findings of Section 5.1 that the roll-induced velocity changes are largest at the maximum radius.

For this steady roll case, the variation in tangential load is negligible as was found to be the case in Figure 5.14 shown by very small fluctuation magnitude. The distribution itself shows a negative

tangential load near the blade root. This occurs because the low local TSR in this region results in very low tangential velocities and consequently very high inflow angles. Under these conditions, the drag component, which acts to oppose rotation, becomes the dominant contributor to the tangential force, resulting in a net negative value.

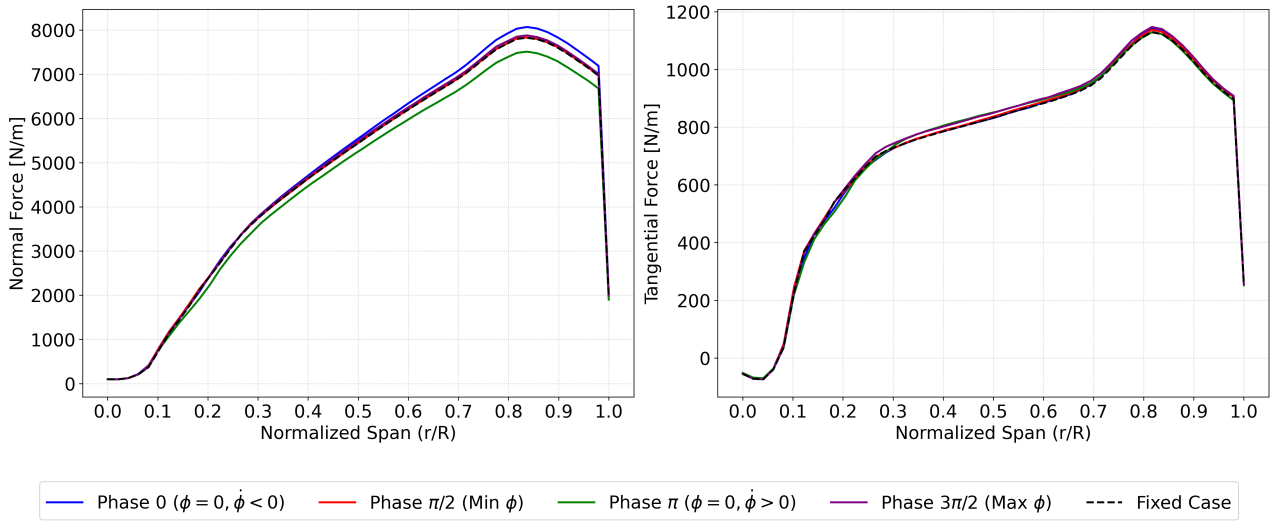

Figure 5.17: Phase-averaged spanwise distribution of normal and tangential loads of case 2 (5°, 0.03Hz, TSR 7).

A comparison between case 2 and case 3 (Figure 5.18), which differs only by a larger roll amplitude, reveals that the primary effect of the increased amplitude is a greater variation in load. The post-processing based asymmetry in the phase-averaged results is preserved. As expected for a high-amplitude case, the numerical artifact near the blade tip is also evident.

Furthermore, an examination of the general shape of the distribution and the location of the force peaks shows no significant inboard or outboard shift in the loading. This confirms that the radial velocities induced by the roll motion are too small to have a discernible impact on the spanwise load distribution, even at this higher roll amplitude.

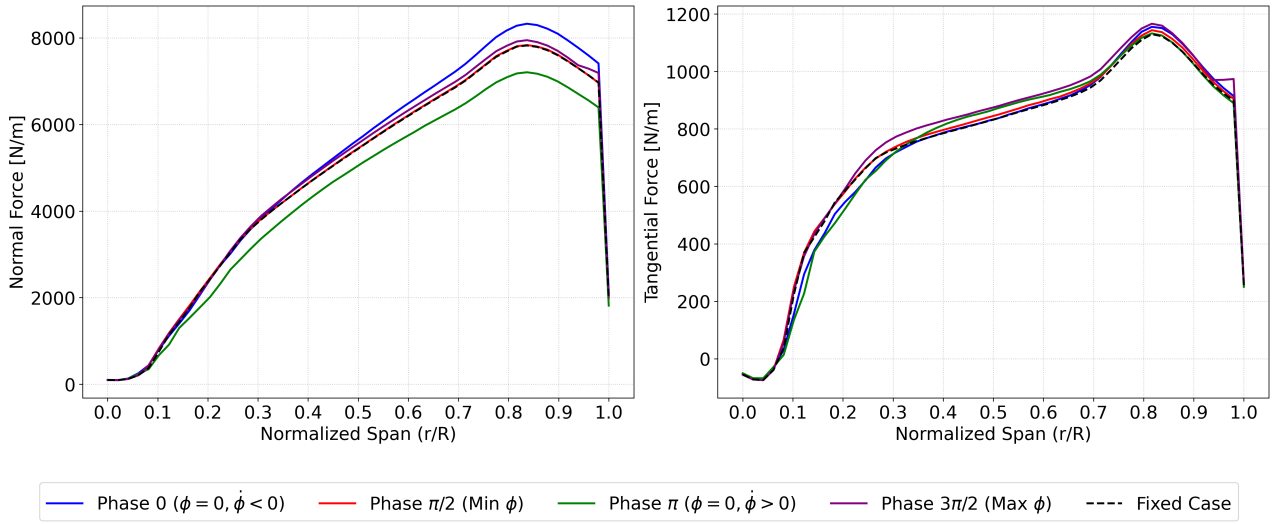

Figure 5.18: Phase-averaged spanwise distribution of normal and tangential loads of case 3 (10°, 0.03Hz, TSR 7).

An examination of case 4 in Figure 5.19 demonstrates that the asymmetry is gone, possibly because at this higher frequency of roll motion thanks to the harmonic interaction of the roll frequency and the rotor frequency, the data is collected more often when the blade is above the hub leading to the expected variation of loading with phase. A comparison with case 2 (Figure 5.17) confirms that a higher roll frequency leads to a larger fluctuation in the normal load. As previously explained, this is a direct result of the higher roll-induced velocities that are generated at a higher frequency for a given amplitude. The fundamental shape of the load distribution remains unchanged, again indicating that radial flow effects do not visibly alter the spanwise loading.

A comparison of the magnitude of these variations reveals that the normal load fluctuation in case 4 is greater than in case 2 but less than in case 3. This suggests that the tangential load variation is more sensitive to a change in roll amplitude than to a change in roll frequency at this TSR. For the normal force, however, this conclusion is less certain, as it shows comparable increases in fluctuation with an increase in either amplitude or frequency.

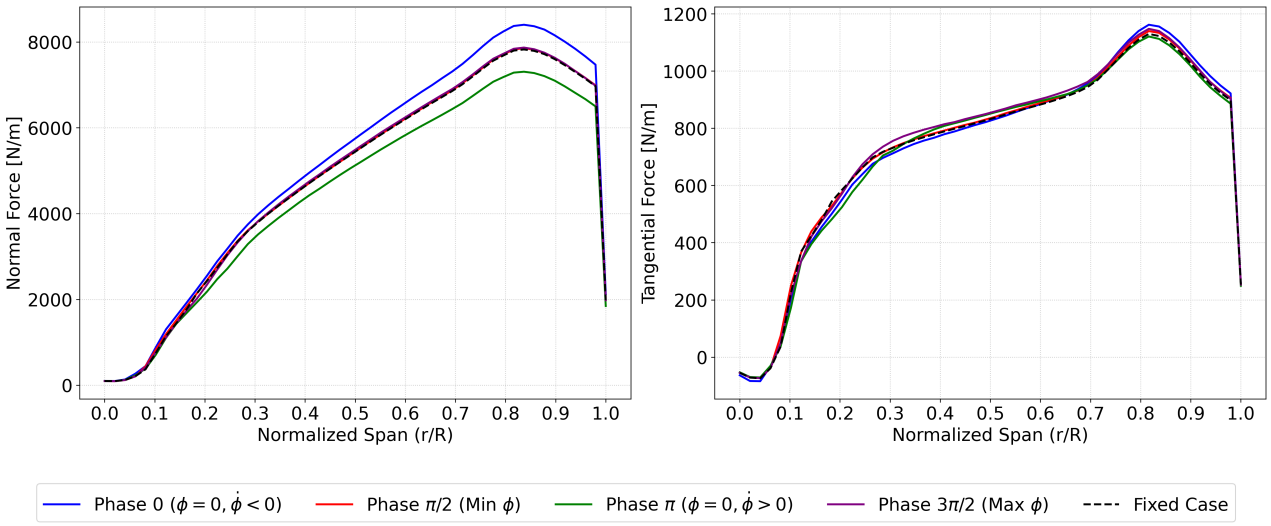

Figure 5.19: Phase-averaged spanwise distribution of normal and tangential loads of case 4 (5°, 0.05Hz, TSR 7).

As for the study of the effect of TSR on the shape of load distribution, case 7, which also showed the effect of numerical error most consistently, has been plotted in Figure 5.20.

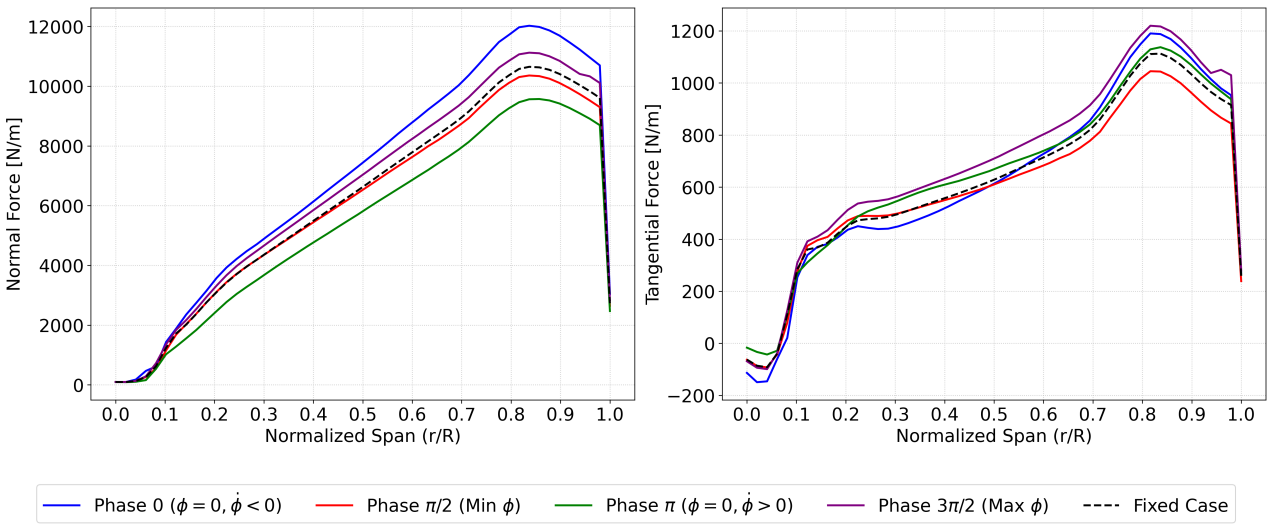

Figure 5.20: Phase-averaged spanwise distribution of normal and tangential loads of case 7 (10°, 0.03Hz, TSR 9).

A direct comparison with case 3 (Figure 5.18) allows for an analysis of the effects of an increased TSR. For the normal force, the overall shape of the distribution remains largely unchanged at the higher TSR. A notable difference, however, is the reduction of a kink previously observed near 0.2 r/R. This feature was likely attributable to the low local tangential velocities near the root at the lower TSR, a condition that is mitigated by the higher rotational speed. As established previously, the absolute magnitude of the load fluctuations is more pronounced at the higher TSR. Furthermore, at the zero roll velocity phases, the load distribution no longer converges to that of the bottom-fixed case, which is attributed to the more significant unsteady aerodynamic effects present at higher TSR.

At the higher TSR, the tangential force distribution shows a reduced load in the mid-span region. This can be explained by the smaller inflow angle at higher TSRs. According to Equation 2.28, this reduces the contribution of the lift vector to the propulsive tangential force, leading to a lower net load. Observing the differences per phase reveals that the distribution varies much more significantly within a roll cycle compared to the TSR 7 cases. This heightened sensitivity also explains the behavior at the blade root: at phase 0, where the local tangential velocity is highest, the drag component becomes more dominant, driving the tangential force strongly negative. This effect is less severe at phase π.

5.2.7 Standard Deviation Analysis of Unsteady Blade Loading

For a comprehensive roll analysis, it is essential to study not just the mean blade loading but also its variations. To quantify these unsteady load variations, the standard deviation (SDEV) is employed as a statistical measure to support the findings on blade loading.

The SDEV is calculated for a single blade over the entire simulation duration, yielding a metric for the overall loading fluctuation from the mean in a specific operational case. This metric facilitates the comparison of unsteadiness across different motion scenarios.

The SDEV plots for the normal and tangential forces are presented for all roll cases, with sub-figures for TSR 7 and TSR 9, in Figure 5.21 and Figure 5.22, respectively.

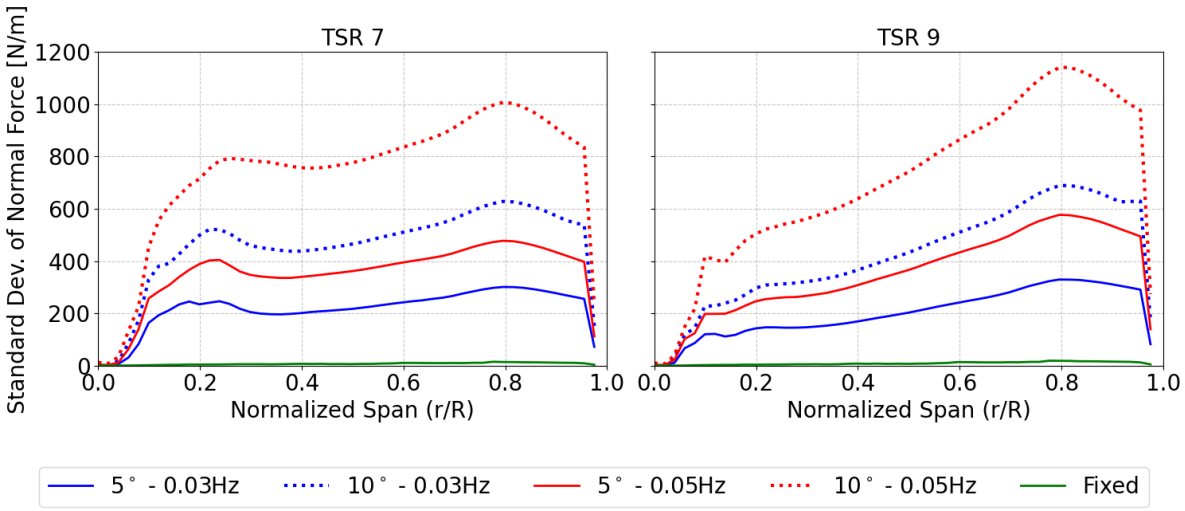

Figure 5.21: Distribution of standard deviation of normal force over the span of the blade for all test cases.

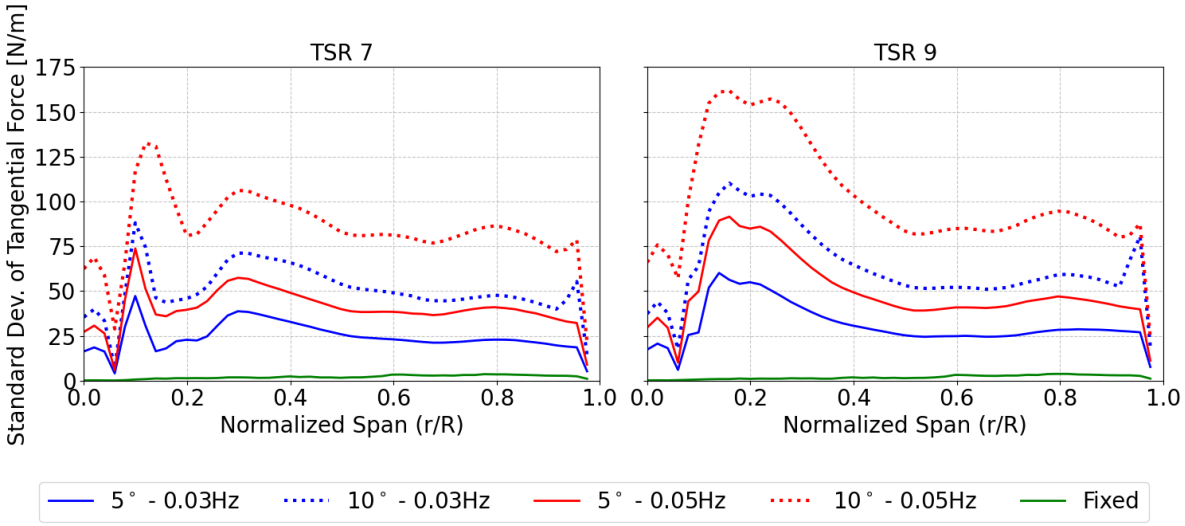

Figure 5.22: Distribution of standard deviation of tangential force over the span of the blade for all test cases.

The influence of roll amplitude and frequency on blade loading fluctuations is evident across all test conditions. An increase in roll amplitude from $5°$ to $10°$ consistently leads to a substantial rise in the SDEV of both normal and tangential blade loading, for both investigated TSRs. Similarly, increasing the roll frequency from 0.03Hz to 0.05Hz also elevates the SDEV of both force components at both TSRs. While both parameters increase loading fluctuations, the roll amplitude exerts a more pronounced impact on the absolute SDEV values than the roll frequency. This observation holds true despite the larger fractional increase in amplitude compared to frequency across the test cases.

A comparison of SDEV distributions between the two TSR conditions reveals distinct differences in their shape along the blade span. For the normal force, a higher TSR results in greater fluctuations outboard while reducing fluctuations inboard, leading to a steeper gradient of fluctuation towards the blade tip. These larger load fluctuations suggest that shed tip vortices will exhibit greater variation in

vorticity magnitude, potentially influencing the coherence of near-wake structures. Furthermore, observations from both Figure 5.21 and Figure 5.22 indicate that the more unsteady the roll motion, the more pronounced the increase in SDEV with TSR. For instance, the most stable case (represented by the solid blue line) exhibits the smallest variation in the overall SDEV distribution across TSRs, whereas the most unsteady case (dashed red line) shows the opposite behavior. This suggests that TSR not only magnifies the effects of roll motion on blade loading fluctuations (with noticeable implications for the wake), but also that the inherent unsteadiness of the roll motion further amplifies the TSR's influence.

Quantifying the percentage change in fluctuation for both normal and tangential loads at their respective maximum SDEV locations reveals a notable difference with increasing TSR. Specifically, the tangential load, as shown in Figure 5.22, experiences a 22.5% increase at its maximum SDEV location (0.15 r/R). In contrast, the normal load, presented in Figure 5.21, increases by 12.6% at its maximum SDEV location (0.8 r/R). This suggests, that relatively, the tangential load fluctuations are more sensitive to TSR but absolutely, the opposite is true.

Examining Figure 5.22 reveals that for the tangential load, the fluctuation distribution shape largely remains similar across the blade span for different TSRs. However, the primary differences in shape between the two TSRs are observed near the blade root (0.2 r/R), where a higher TSR corresponds to increased fluctuations. This phenomenon is attributed to the operating point of the blade section on the lift and drag curves of the local airfoil. This will be studied in detail subsequently and is illustrated by the comparison in Figure 5.23 and Figure 5.24 for Cases 3 and 6, which share identical roll motions but differ in TSR.

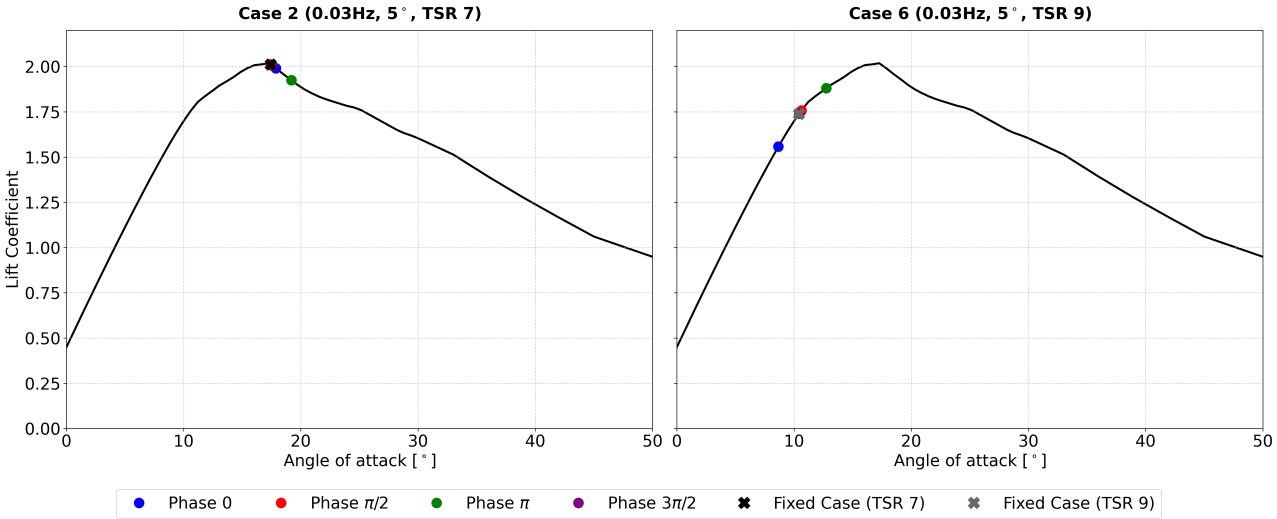

Figure 5.23: Operational points on the lift polar for case 2 (0.03 Hz, 5°, TSR 7) and case 6 (0.03 Hz, 5°, TSR 9) at location 0.2 r/R on the blade.

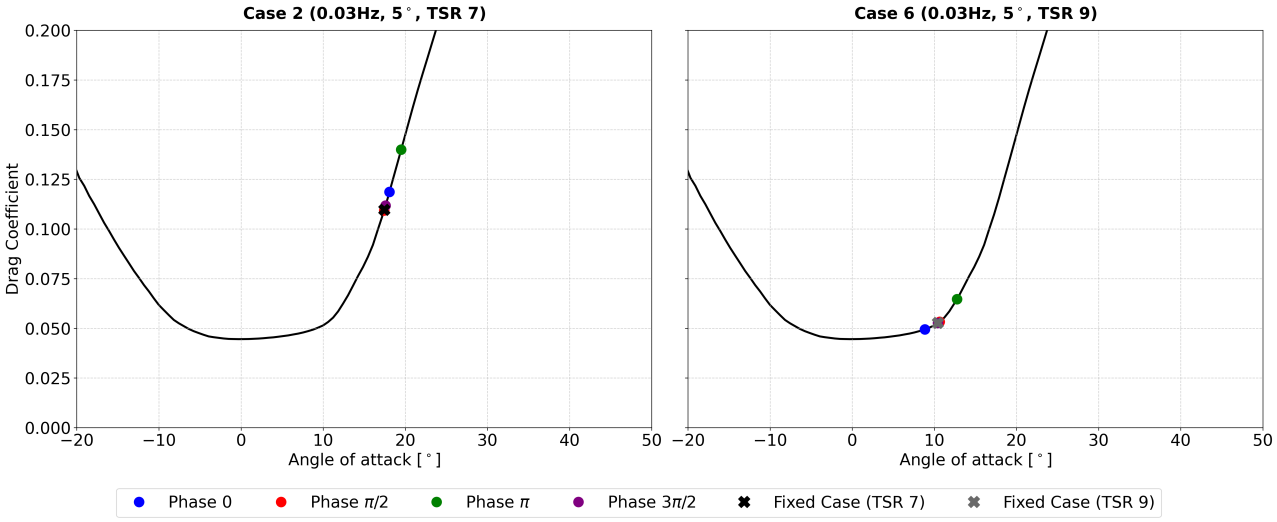

Figure 5.24: Operational points on the drag curve for case 2 (0.03 Hz, 5°, TSR 7) and case 6 (0.03 Hz, 5°, TSR 9) at location 0.2 r/R on the blade.

A simplified analysis confirms the reason for the significantly lower tangential load fluctuations observed near 0.2 r/R for the TSR 7 case. This analysis examines the tangential force coefficient at two extreme roll phases, 0 and π. Focusing on the tangential force coefficient isolates the aerodynamic behavior from the effects of varying tangential velocities.

At the selected blade location (0.2 r/R), the operational parameters differ notably between the two TSRs. The blade has a pitch angle of 1°. For TSR 7, the section operates at an angle of attack of 17.9° (inflow angle $\phi = 18.9°$) during phase 0, and 19.2° ($\phi = 20.2°$) during phase π. The corresponding lift and drag coefficients obtained from Figure 5.23 and Figure 5.24 are ($C_l = 1.991$, $C_d = 0.119$) for phase 0 and ($C_l = 1.925$, $C_d = 0.140$) for phase π. For TSR 9, the reduced angles of attack are 8.7° ($\phi = 9.7°$) at phase 0 and 12.8° ($\phi = 13.8°$) at phase π. This results in lift coefficients of 1.558 and 1.880, and drag coefficients of 0.0495 and 0.0647, for phases 0 and π respectively.

Given these results, the absolute change in the tangential force coefficient, ΔC_t, between the two phases can be computed using the following equation:

$$\Delta C_t = |C_{t_{\theta=0}} - C_{t_{\theta=\pi}}| = |[C_l \sin(\phi) - C_d \cos(\phi)]_{\theta=0} - [C_l \sin(\phi) - C_d \cos(\phi)]_{\theta=\pi}| \tag{5.13}$$

Substituting the values obtained from Figure 5.23 and Figure 5.24 for the TSR 7 case yields:

$$\begin{aligned}\Delta C_t &= |[1.991 \sin(18.9°) - 0.119 \cos(18.9°)] - [1.925 \sin(20.2°) - 0.140 \cos(20.2°)]| \\ &\approx 9.75 \times 10^{-4}\end{aligned}$$

Repeating the calculation for the TSR 9 case:

$$\begin{aligned}\Delta C_t &= |[1.558\sin(9.7^\circ) - 0.0495\cos(9.7^\circ)] - [1.880\sin(13.8^\circ) - 0.0647\cos(13.8^\circ)]| \\ &\approx 0.172\end{aligned}$$

The calculation shows that the variation in the tangential force coefficient at 0.2 r/R is significantly larger for the TSR 9 case. This larger coefficient variation directly accounts for the higher SDEV of the tangential force observed at 0.2 r/R, for TSR 9 cases in Figure 5.22. Regarding the normal force, these findings are consistent with the results presented in Subsection 5.2.2, where fluctuations were shown to increase significantly as the roll motion becomes more unsteady.

A notable feature in both the normal and tangential SDEV load distributions is a small kink at the blade tip, which is particularly evident in the 10° amplitude cases. This artifact is attributed to a peak in the angle of attack at the tip originating from the numerical effects discussed in Subsection 5.2.3. Consequently, this causes a slightly larger load fluctuation relative to adjacent spanwise locations.

This effect is most pronounced for the case with a 10° amplitude and a 0.03Hz frequency. This is because the specific conditions that trigger the numerical error, related to a harmonic interaction between the roll and rotor frequencies, are met during each roll cycle. Furthermore, the magnitude of this SDEV peak at the tip increases with TSR. At a higher TSR, the larger aerodynamic loads generated are prematurely truncated by the boundary of the ALM domain. This truncation leads to a greater variation in the blade tip circulation, manifesting as a higher SDEV value.

5.2.8 Study of Azimuthal Load Distribution

This subsection investigates the azimuthal variation of normal and tangential forces on the turbine blades during prescribed roll motions. The analysis concentrates the non-stationary phases; phase 0 and π, which correspond to the moments of maximum roll velocity. Conversely, at the stationary phases of $\pi/2$ and $3\pi/2$, when the roll velocity is zero, the azimuthal normal and tangential load variation is does not show significant localized increases of loads azimuthally, similar to the bottom-fixed cases. Consequently, these phases are omitted from the analysis. The influence of roll amplitude, roll frequency, and TSR on these load distributions is detailed below.

As a baseline for the roll cases, the azimuthal distributions of normal and tangential loads for the bottom-fixed turbines at TSR 7 and 9 are provided in Figure 5.25 and Figure 5.26, respectively.

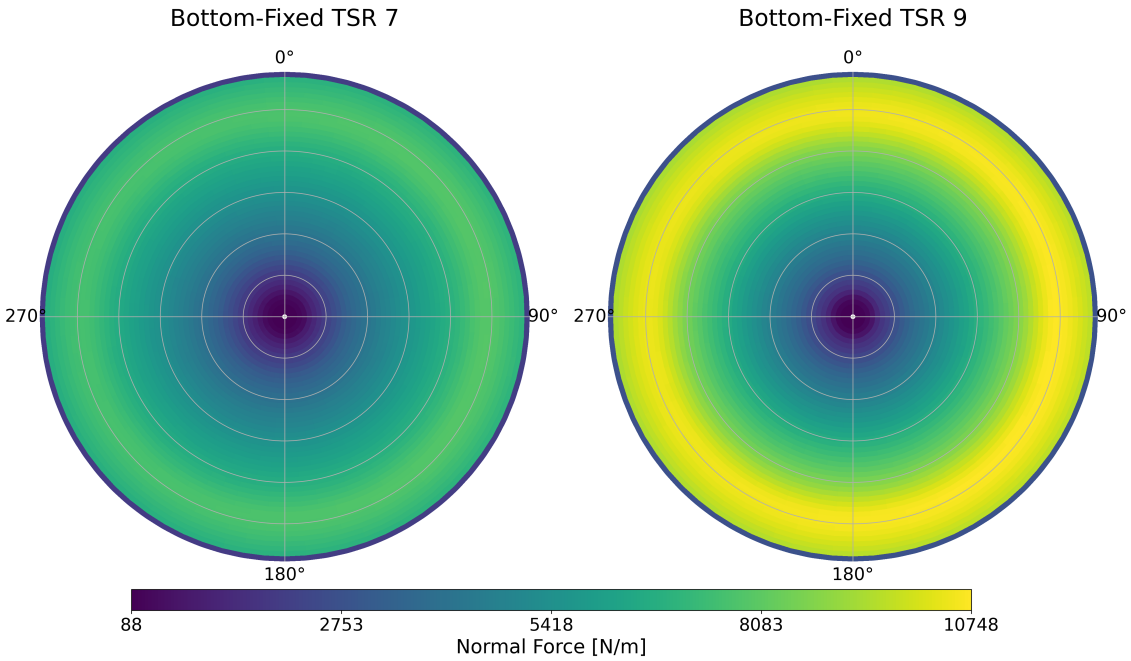

Figure 5.25: Azimuthal normal force distribution of bottom-fixed turbines operating at TSR 7 and 9.

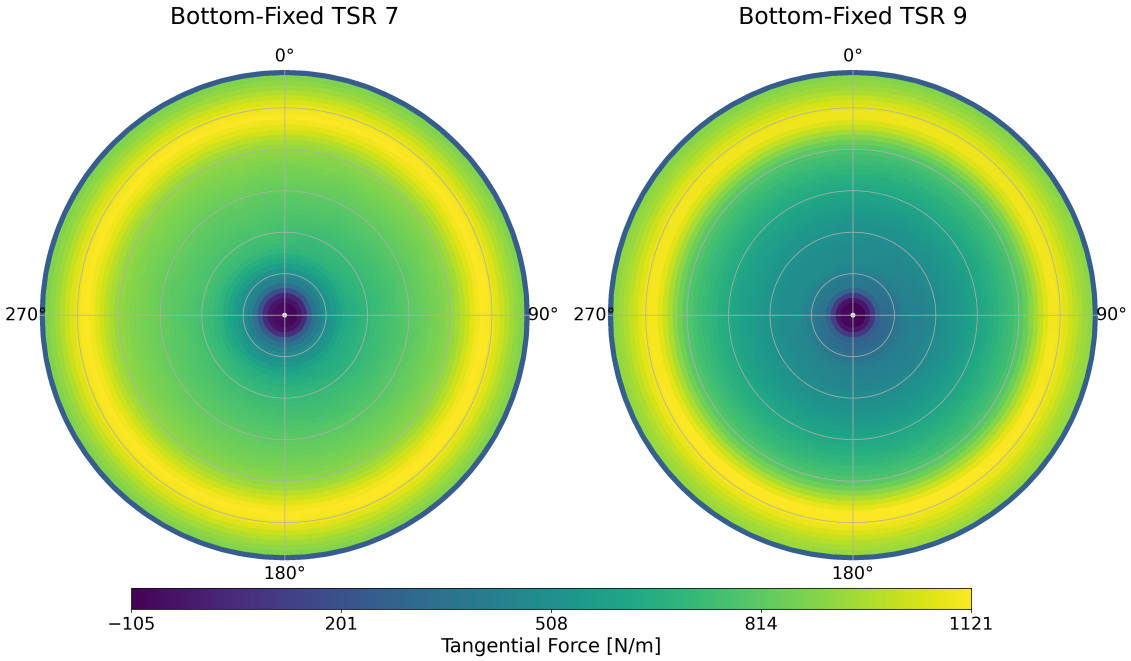

Figure 5.26: Azimuthal tangential force distribution of bottom-fixed turbines operating at TSR 7 and 9.

The bottom-fixed cases exhibit the expected load distribution, which remains constant across the blade azimuth. This lack of variation is anticipated, as the changing angle of attack that induces azimuthal load fluctuations is a direct consequence of roll motion. Furthermore, and consistent with previous findings, a higher TSR increases the magnitude of the normal force while the tangential force is reduced.

The analysis of the roll motion is conducted systematically. First, the normal force distribution at

phase 0 is examined across two amplitudes, two frequencies, and two TSRs. Next, the tangential load variation is analyzed. Finally, the analysis for phase π is presented shortly, as the observed trends are similar to those at phase 0.

For this analysis, cases 2, 4, 5, and 9 are selected as representative examples. This subset is chosen because the trends observed are consistent across all other roll scenarios, making a detailed analysis of every case redundant.

The influence of roll amplitude on the normal force azimuthal distribution at phase 0 is shown in Figure 5.27 by comparing case 4 and case 5.

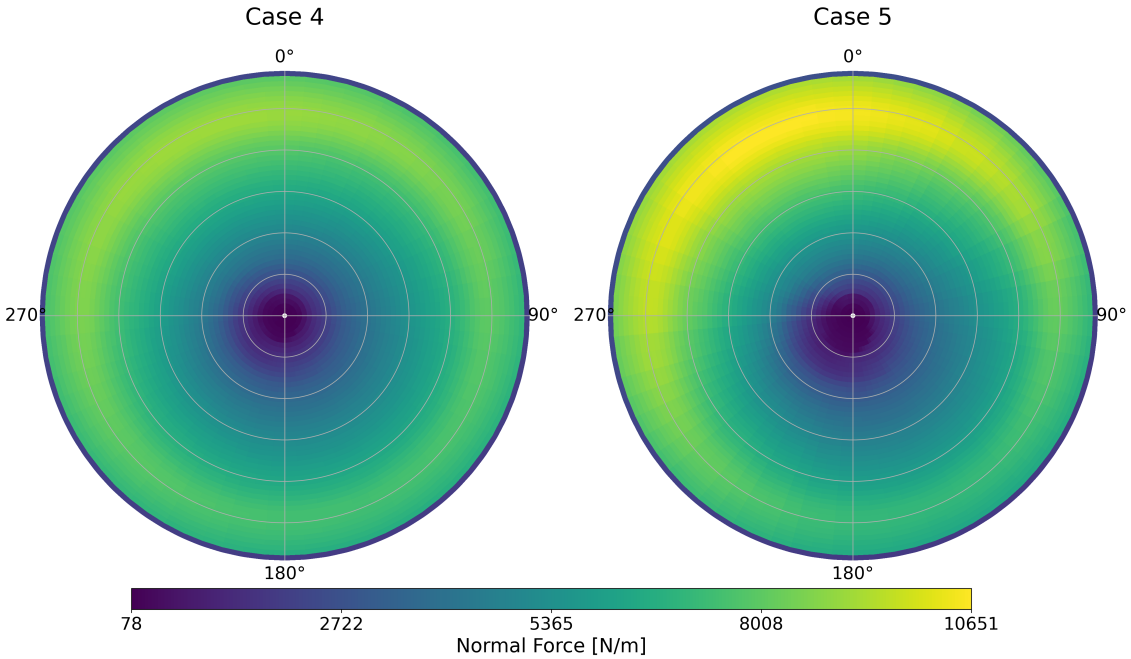

Figure 5.27: Azimuthal normal force distribution of case 4 (5°, 0.05Hz, TSR 7) and case 5 (10°, 0.05Hz, TSR 7) at phase 0.

A comparison between case 4 and case 5 shows that an increase in roll amplitude leads to a more azimuthally concentrated and intense load increase. This is visually represented by the significantly brighter upper-half region in the plot for case 5 relative to case 4, indicating a highly localized peak.

This increase in load due to the roll motion is observed primarily in the azimuthal range of 270° to 360°. The presence of a high-magnitude, cyclically applied load concentrated in a specific sector has significant implications for the fatigue life of the rotor blades.

Furthermore, a comparison of the rolling motion case presented in Figure 5.27 with the bottom-fixed case baseline at TSR 7 (Figure 5.25) reveals an asymmetric load response at phase 0. Specifically, the upper half of the rotor experiences a substantial increase in load, whereas the lower half shows a less pronounced decrease relative to the fixed case. This asymmetry is attributed to the varying distance of the blade sections from the roll center where regions farther from the center are subjected to larger roll-induced velocity fluctuations, which in turn generate larger load fluctuations.

The effects of amplitude and frequency can be summarized as follows. The primary effect of a higher roll amplitude is to intensify and concentrate the additional load within a specific azimuthal region. In contrast, while an increasing roll frequency also elevates the normal force, its impact on the peak magnitude is less significant than that of amplitude. Instead, a higher frequency tends to distribute the increased load more uniformly across the azimuth. This distinction is demonstrated by the comparison between case 2 and case 4 in Figure 5.28.

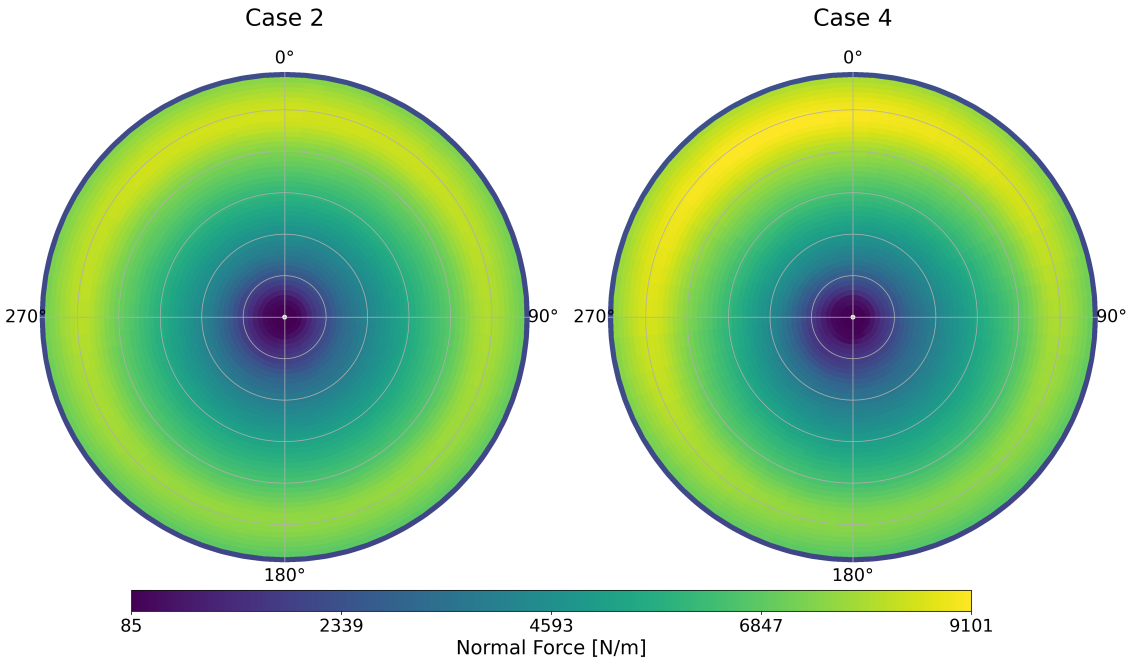

Figure 5.28: Azimuthal normal force distribution of case 2 (5°, 0.03Hz, TSR 7) and case 4 (5°, 0.05Hz, TSR 7) at phase 0.

In contrast to roll amplitude and frequency, the TSR does not significantly alter the azimuthal distribution of normal force. Its primary influence is to scale the overall load magnitude. This scaling effect is demonstrated in Figure 5.29 by a comparison between case 5 and case 9. These two cases represent the most unsteady roll conditions, with highest amplitude and frequency, tested for their respective TSRs, yet they exhibit a similar azimuthal normal load pattern that differs mainly in magnitude.

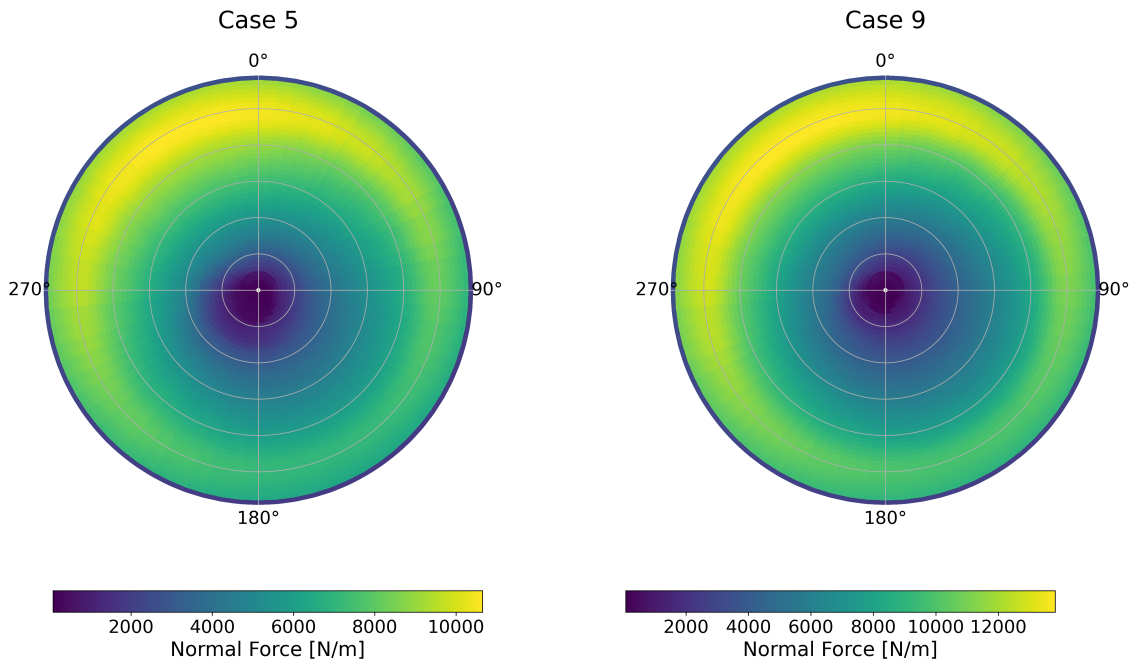

Figure 5.29: Azimuthal normal force distribution of case 5 (10°, 0.05Hz, TSR 7) and case 9 (10°, 0.05Hz, TSR 9) at phase 0.

A comparison between the rolling cases (Figure 5.29) and the bottom-fixed case baseline (Figure 5.25) reinforces a key finding. For both TSRs, the roll motion induces a significant increase in normal load on the upper side of the rotor, whereas the corresponding load reduction on the lower side is minimal. This top-bottom asymmetry is a direct consequence of the blade kinematics as was explained earlier.

An examination of the normal force in Figure 5.29 again reveals an asymmetry in the load increase at phase 0. The region of elevated load is not evenly centered on the upper half of the rotor but is shifted toward the top-left quadrant. A possible source of this asymmetry is the presence of the induction zone and its lag in adapting to the lateral motion of the turbine. As the turbine rolls from left to right when viewed from upstream, it interacts with its own evolving induction zone, particularly along the trailing boundary that lags behind the instantaneous turbine position. This interaction may cause the rotor to encounter a laterally non-uniform inflow velocity and, consequently, a lateral variation in loading. While it might be intuitive to expect higher axial velocities when the turbine moves out of the induction zone to lead to increased loading on the opposite horizontal side, the situation is complicated by the fact that higher axial velocity also results in a reduced angle of attack, which could conversely reduce loading outside the induction zone. This complex interplay between axial velocity and angle of attack within the evolving induction zone makes a definitive explanation for the observed asymmetry challenging.

Another possible explanation is related to the effects observed in the phase-averaged normal loading plots, for example in Figure 5.8, which exhibited a slight skew in load variation with phase compared to a perfectly sinusoidal trend. This skew was previously attributed to inertial effects in the flow, causing a lag in the loading response relative to the idealized case. This represents itself as a slightly azimuthally off peak on the rotor plane since the peak loading region rotates azimuthally around the

rotor plane with phase of roll, the maximum load at phase 0 does not align precisely with 0° azimuthal location but is instead shifted due to this lag.

The tangential load exhibits trends similar to those of the normal force, but its variation is predominantly lateral on the rotor plane. Consequently, the rotor disk is effectively divided into left and right halves with respect to load changes, in contrast to the upper and lower halves observed for the normal force. This lateral behavior is demonstrated in Figure 5.30, which compares the tangential load for case 4 and case 5 to illustrate the effect of roll amplitude.

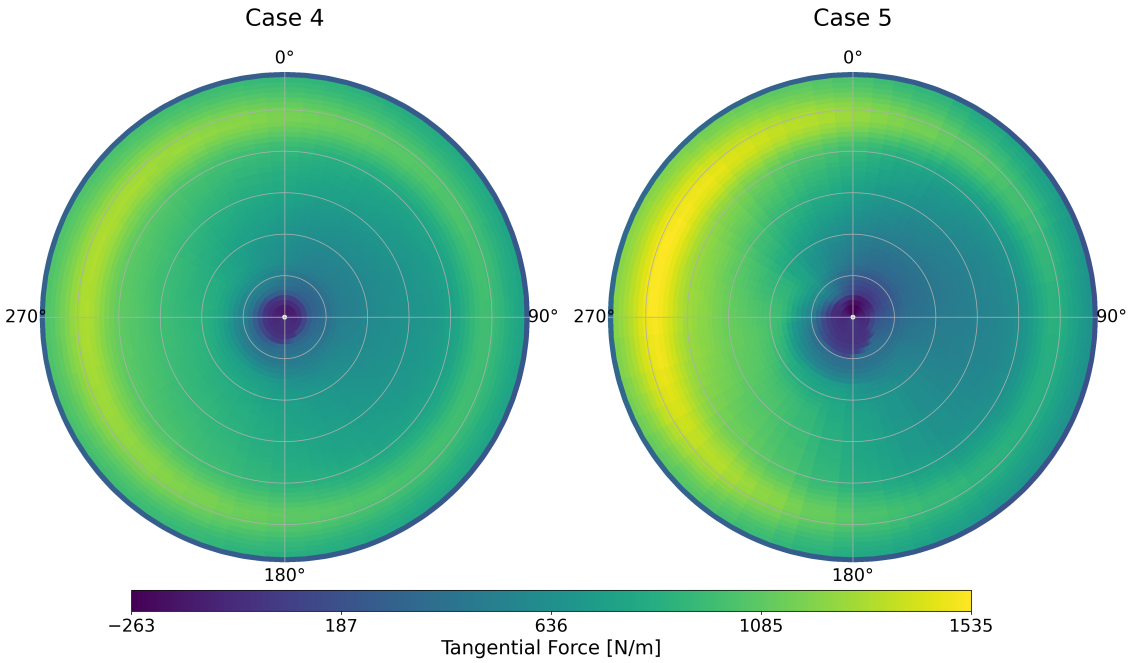

Figure 5.30: Azimuthal tangential force distribution of case 4 (5°, 0.05Hz, TSR 7) and case 5 (10°, 0.05Hz, TSR 7) at phase 0.

Consistent with the findings for the normal load, a higher roll amplitude leads to a larger and more azimuthally concentrated tangential load. Since the qualitative effects of roll frequency and TSR on the tangential load are also analogous to those observed for the normal force, a detailed repetition of that analysis of the tangential loading is omitted here. The key distinction lies in the azimuthal location of the increased loading, which is lateral (at 270° for phase 0) for the tangential force rather than vertical.

Finally, the analysis of the roll motion at phase π reveals two key findings. First, the azimuthal load distribution is a reflection of the pattern observed at phase 0. This holds true for both normal and tangential loads. This reflective behavior is illustrated in Figure 5.31, which shows the effect of roll frequency on the normal load distribution at phase π. A direct comparison with its counterpart for phase 0, Figure 5.28, confirms this mirrored relationship.

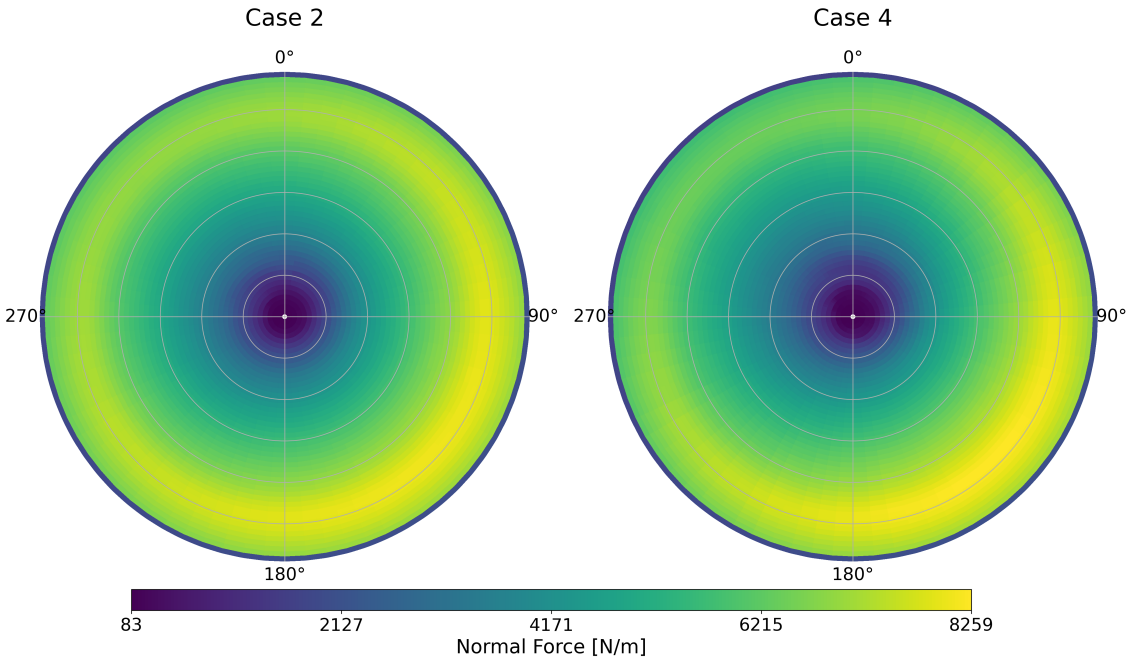

Figure 5.31: Azimuthal normal force distribution of case 2 (5°, 0.03Hz, TSR 7) and case 4 (5°, 0.05Hz, TSR 7) at phase π.

The second finding concerns the magnitude of the peak loads. A comparison between the magnitudes shown in Figure 5.31 and Figure 5.28 reveals that the maximum load is higher during phase 0.

The same reflective trend is also evident for the tangential load, as shown for phase π in Figure 5.32. A comparison with the tangential load distribution at phase 0, presented in Figure 5.30, confirms that the region of increased load is mirrored to the opposite side of the rotor. Notably, this principle of reflection holds true even though the specific roll cases presented in the two figures are different. Unlike the asymmetric behavior of the normal load, the tangential load variation is symmetric. The load pattern at one phase is simply a vertical mirror image of the pattern at the opposite phase, with the same magnitudes. This can be seen by comparing the magnitudes of case 4 tangential load plotted for phase 0 in Figure 5.30 with phase π in Figure 5.32.

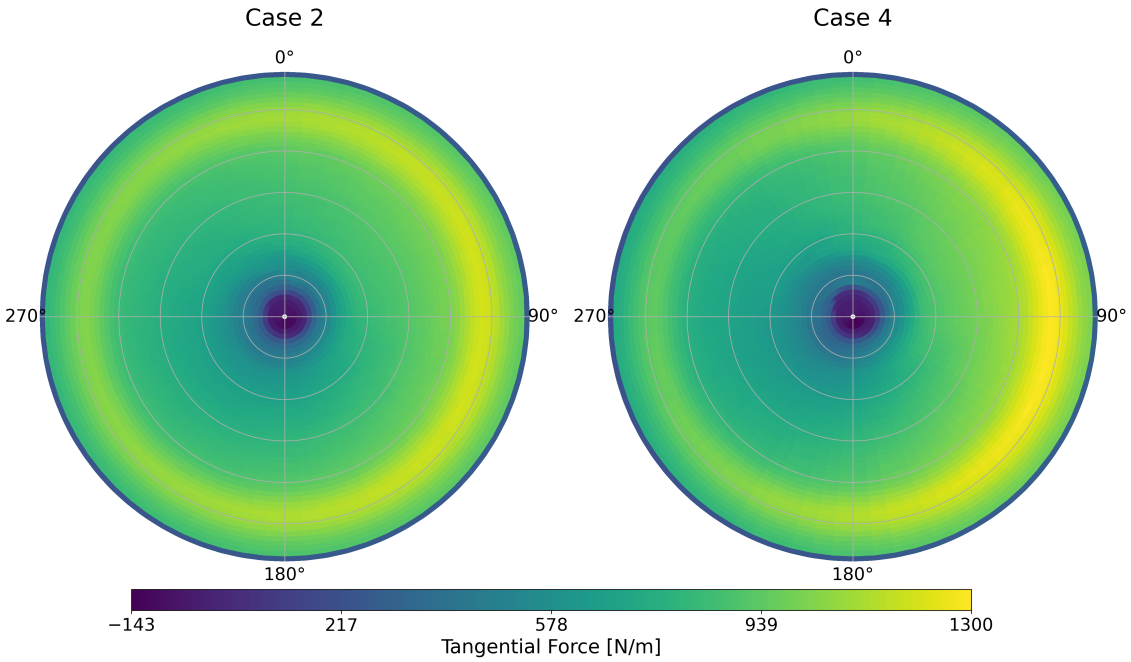

Figure 5.32: Azimuthal tangential force distribution of case 2 (5°, 0.03Hz, TSR 7) and case 4 (5°, 0.05Hz, TSR 7) at phase π.

The load variation across the rotor disk can be summarized as follows. For the normal force, the response is asymmetric with respect to the horizontal axis. At phase 0, the upper half of the rotor experiences a significant increase in load, while the lower half exhibits a comparatively minor decrease from the bottom-fixed case baseline. Conversely, at phase π, the load reduction in the upper half is more pronounced than the load increase in the lower half. The net result is that the upper half of the rotor is subjected to larger normal load fluctuations, a direct consequence of its greater distance from the roll axis.

For the tangential force, the variation is predominantly lateral. At phase 0, the load increases on the left side (270°) of the rotor, while the right side 90° shows minimal change. At phase π, the pattern is reflected, the right side experiences a load increase, while the left side remains relatively unaffected.

A key consequence of this asymmetric loading is that the maximum rotor-averaged load occurs during phase 0. At this critical phase, the peak normal force is concentrated in the fourth quadrant (270°–360°), while the peak tangential force is distributed across the third and fourth quadrants (180°–360°) This uneven blade loading vertically and laterally depending on the phase may have implications on the velocity deficit and other parameters in the wake which will be studied in Section 5.3.

5.3 Study of Near-Wake Aerodynamics

The study of the aerodynamics in the vicinity of the blade aims to understand the direct impacts of roll motion on the turbine's wake. The findings from the blade loading in Section 5.2 will be used to aid the explanation and understanding of the wake characteristics.

To comprehensively characterize the turbine wake and its relationship to blade loading, this chapter is organized into a series of focused analyses. The investigation begins in Subsection 5.3.1 by establishing the connection between blade loading and wake dynamics. Specifically, it examines how variations in the normal force, driven by the different phases of roll motion, influence the velocity deficit, utilizing data from discrete probes placed within the wake. Following this, Subsection 5.3.2 quantifies the magnitude of the unsteady fluctuations through a SDEV analysis of the velocity field. The velocity focused study is completed in Subsection 5.3.3 with a detailed examination of the streamwise (u), lateral (v), and vertical (w) velocity components across the different roll cases.

The focus then shifts from velocity statistics to the analysis of vorticity and coherent flow structures in the near-wake. Subsection 5.3.4 presents the vorticity distribution for all roll cases and investigates the influence of the TSR. The findings from the vorticity analysis are then supported by the summary of 3-dimensional Q-criterion study in Subsection 5.3.5. Finally, the chapter concludes in Subsection 5.3.6 with an investigation into the characteristic signals present in the wake. This analysis studies the spatial development of these signals, which originate from the combined effects of blade rotation and turbine roll motion.

5.3.1 Temporal Analysis of Near-Wake Velocity Deficit

This subsection connects the blade loading to the velocity deficit in the wake by analyzing data from selected probe points over time. The focus is on determining whether the effects of roll motion, which cause azimuthal variations in normal force loading as shown in Subsection 5.2.8, lead to temporal differences in the wake's velocity distribution.

The findings from Subsection 5.2.8 suggest a direct relationship. During a roll phase of 0, the normal force increases on the upper-left quadrant (270° to 360°) of the rotor. An increase in normal force results in greater thrust against the flow, enhancing its deceleration. Consequently, the velocity deficit in the wake is expected to be larger at the top of the turbine at this phase. Conversely, the load is reduced on the lower half due to kinematic effects, which should result in a lower velocity deficit. When the turbine rolls to a phase of π, the opposite behavior is expected. However, the asymmetry caused by the kinematics is preserved, meaning the increase in velocity deficit in the lower half of the rotor should be less pronounced than the decrease in the upper half at this phase.

To investigate these variations during roll motion, two points are probed in the wake at coordinates (X,Y,Z) P1(0.01D, 0D, 0.4D) and P2(0.01D, 0D, -0.4D) relative to the turbine. These points are positioned very close to the rotor in downstream to minimize delays from flow convection, allowing the effects of blade loading to be readily observed in the wake. The locations of these points are illustrated on the XZ velocity slice in Figure 5.33. The velocity data is pre-processed to plot the velocity deficit as a function of time for each location, as shown for case 9 in Figure 5.33.

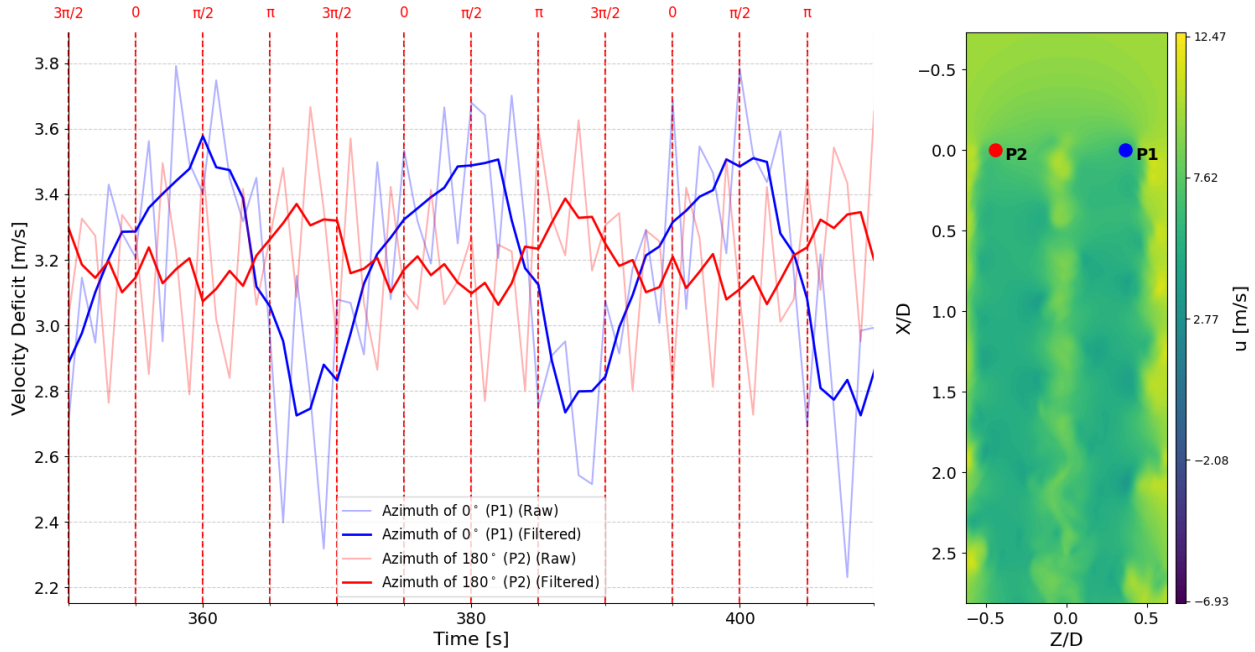

Figure 5.33: Temporal variation of raw and filtered velocity deficit at points P1 and P2 for case 9 (10°, 0.05Hz, TSR 9) (left), and locations of points annotated on the XZ velocity slice (right).

The raw velocity deficit data exhibits significant short-term fluctuations due to turbulence and the 1P frequency of the blades. The resolution of these fluctuations is limited by the data acquisition rate. To clarify the general trend and remove these short-term variations, a low-pass filter is applied with a filter window size of 5 seconds , represented by the brighter blue and red curves.

Case 9, being the most unsteady roll case with a TSR of 9, clearly demonstrates that the velocity fluctuation at the top of the rotor (P1) is much larger than at the bottom (P2). This is explained by the greater fluctuations in normal load on the upper half of the rotor compared to the lower half, as established in Subsection 5.2.8. The velocity distribution in Figure 5.3, which is the dominant influence on loading, also supports this observation.

The blue line indicates that the velocity deficit near the top of the wake begins to decrease at phase $\pi/2$ and stops decreasing at phase $3\pi/2$. This corresponds to the period between two stationary phases, during which the load is reduced on the top half of the rotor. Conversely, the deficit increases again as the turbine passes through phase 0, where the load at the top of the rotor substantially increases. This cyclical variation has implications for wake signals, which will be further studied through vorticity in Subsection 5.3.6.

A comparison of P2 to P1 shows that, as expected, the oscillations at P2 are significantly smaller in amplitude. This is due to P2's smaller distance from the roll axis, which results in a smaller roll-induced tangential velocity. The maximum velocity deficit at P2 occurs at a phase of π, where the lower half of the rotor experiences increased loads, though not as substantially. The load reduction at phase 0 is also far less pronounced at this location.

This analysis continues by examining the effect of roll motion on these fluctuations. The plot for case

9 in Figure 5.33 served as an introduction, displaying both raw and filtered data. For subsequent plots, only the filtered data will be shown, with an additional pre-processing step. Instead of plotting the velocity deficit for both points over time, the difference in velocity deficits between P1 and P2 is plotted. This approach simplifies the visualization while retaining the same essential information.

The effect of roll amplitude on the velocity deficit difference between the two selected points is investigated using case 4 and case 5. These are shown alongside the corresponding bottom-fixed case in Figure 5.34.

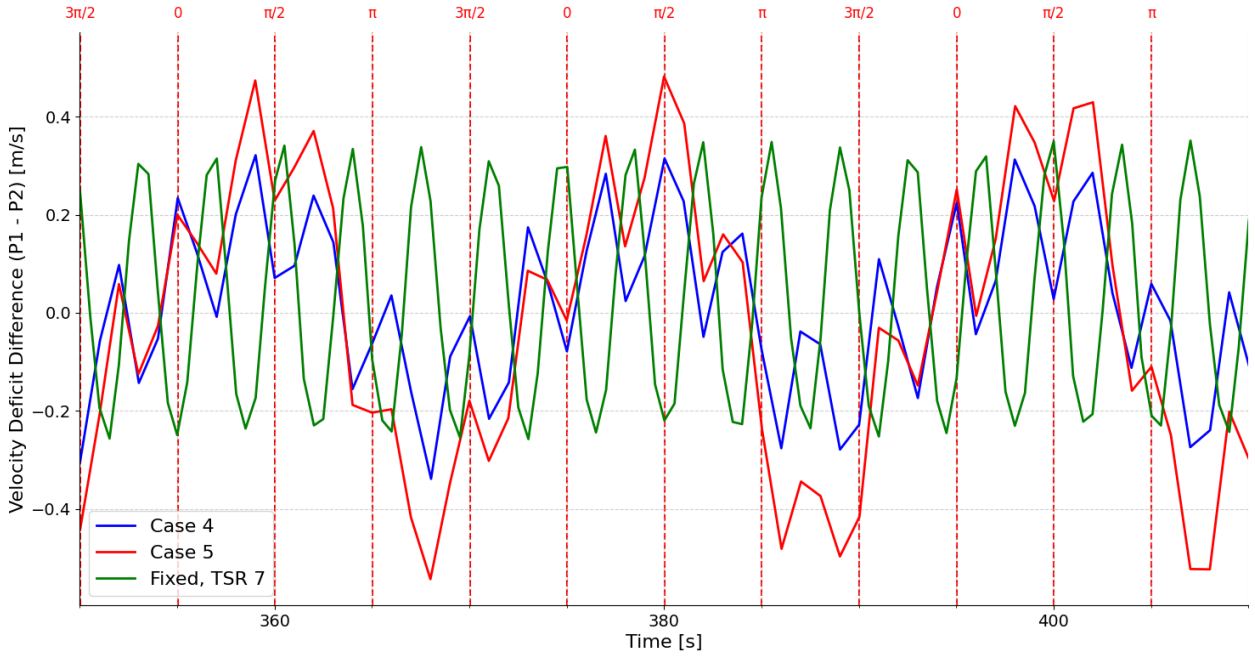

Figure 5.34: Roll amplitude comparison of temporal variation of filtered velocity deficit difference between points P1 and P2 for case 4 (5°, 0.05Hz, TSR 7), case 5 (10°, 0.05Hz, TSR 7), and the bottom-fixed case at TSR 7.

Figure 5.34 shows that the difference in velocity deficits between the upper and lower ends of the wake increases as the turbine crosses phase 0, reaching a maximum around $\pi/2$. While the maximum load difference between the upper and lower halves occurs at a phase of 0, the corresponding peak in the wake is observed slightly later due to convection delays. This difference diminishes as the turbine crosses phase π. The velocity deficit in the lower part of the wake is largest compared to the top part between the phases of π and $3\pi/2$.

The green curve, representing the bottom-fixed turbine, shows a steady oscillation caused by the periodic passage of the blades. The frequency of this oscillation is equal to 3 times the rotor's rotational frequency. The difference between P1 and P2 is maximized when a blade passes P1 (azimuthal angle 0°) because the local flow is decelerated only at the top-half of the wake at that instant and minimized when a blade passes P2 (azimuthal angle 180°).

Analyzing the effect of amplitude reveals that a larger roll amplitude amplifies the velocity deficit difference between the upper and lower ends of the wake. This can have implications for wake deflection.

Lastly, the effect of roll frequency on the velocity deficit difference between the top and bottom of the wake is shown by comparing case 2 and case 4 in Figure 5.35.

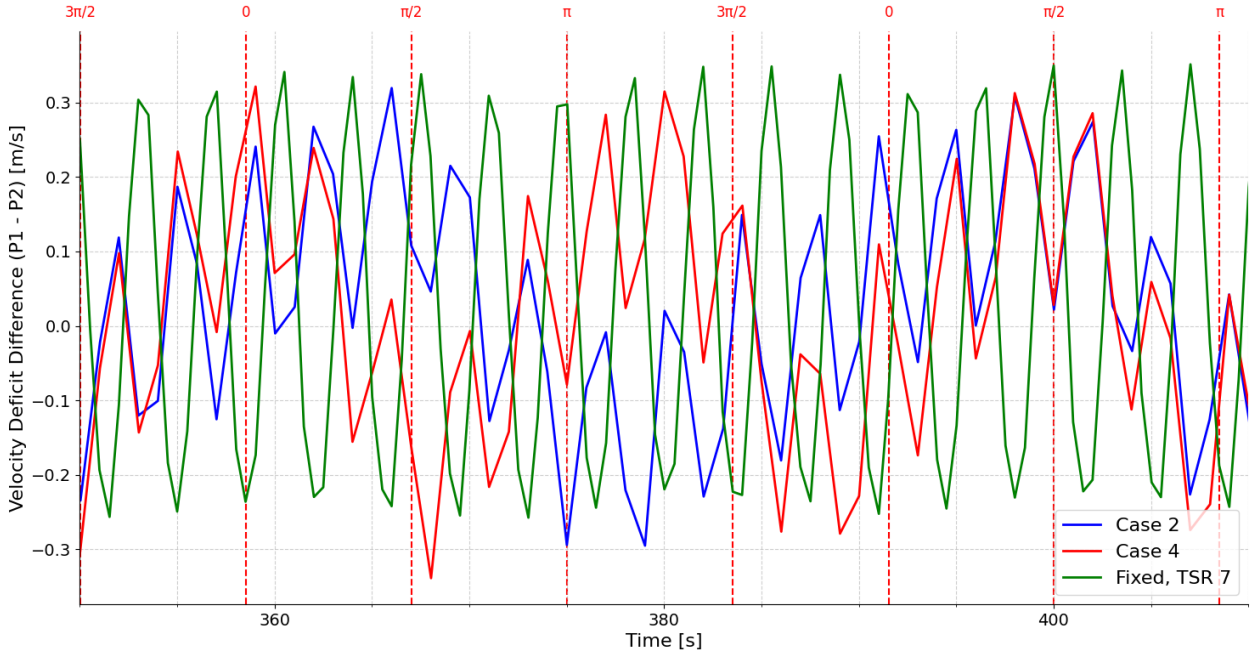

Figure 5.35: Roll frequency comparison of temporal variation of filtered velocity deficit difference between points P1 and P2 for case 2 (5°, 0.03Hz, TSR 7), case 4 (5°, 0.05Hz, TSR 7), and the bottom-fixed case at TSR 7.

As anticipated, the frequency of variation in the wake increases with the frequency of the roll motion. However, although a higher roll frequency induces larger velocities and thus larger loading fluctuations at the blades, the wake does not exhibit a noticeable change in the amplitude of the velocity deficit difference between P1 and P2. This observation aligns with the findings in Subsection 5.2.8, where higher roll frequencies were shown to increase the load, but this increase was more evenly distributed across the rotor compared to the concentrated load increase caused by a larger roll amplitude. The resulting effect on the wake is seen in Figure 5.35.

5.3.2 Standard Deviation Analysis of Near-Wake Velocity

The investigation of temporal velocity variations is extended by analyzing the SDEV of the streamwise velocity component. The preceding analysis in Subsection 5.3.1 examined the velocity deficit at discrete probe locations, establishing a link between blade loading and the phase-dependent behavior of the wake. This study, however, provides a more comprehensive view of the flow's unsteadiness.

This analysis focuses on quantifying the magnitude of these velocity fluctuations. The SDEV of the velocity at each point along a vertical profile provides a time-averaged measure of the flow's unsteadiness. This method condenses the temporal signal at each location into a single value, thereby creating a profile that highlights the regions with the most significant velocity variations.

Figure 5.36 presents the SDEV of the streamwise velocity plotted against the vertical Z-axis at a

downstream distance of 0.01D. The three subplots illustrate the respective effects of roll frequency, roll amplitude, and turbine TSR on the SDEV profile.

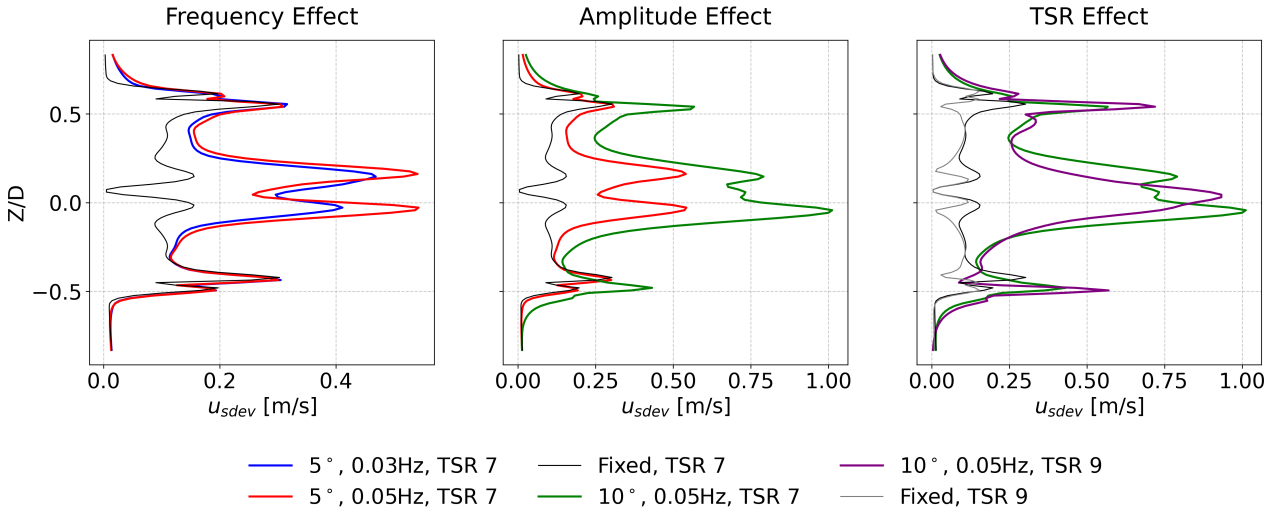

Figure 5.36: The effect of roll frequency (left), roll amplitude (center), and turbine TSR (right) on the standard deviation of the streamwise velocity component, plotted against the vertical Z-axis at 0.01D downstream of the rotor.

A limitation of this study is that the studied region is stationary while the turbine with it's wake is moving. When the turbine moves, the corresponding location on the blade to a fixed location in the wake shifts and so does the blade. This effect is not insignificant because laterally, the turbine at worst scenario (10° amplitude) shifts by 26m (H · sin(ϕ_0)). So the SDEV values seen are the result of combination of two factors; the asymmetric variation of load due to roll and the fixed location being sample in the wake.

This shortcoming is most noticeable for the amplitude comparison study in Figure 5.36 because the higher amplitude case exaggerates the asymmetry more than the lower amplitude due to a higher lateral shift of the rotor.

An analysis of the general shape of the profiles reveals several key characteristics. The edges of the wake (Z/D = ±0.5) and the center exhibit the largest SDEV fluctuations. The central peak is attributed to the absence of a hub model, which allows a jet of flow through the wake core. These regions experience large fluctuations due to the roll motion, as they alternate between velocity deficit and velocity surplus (due to blockage effects) depending on the turbine's roll phase. Consequently, the magnitude of these peaks increases as the roll motion becomes more unsteady, an effect clearly demonstrated in the amplitude and frequency plots.

A comparison with the bottom-fixed cases provides further insight. For a fixed turbine, the unsteady fluctuations and the corresponding SDEV values are, as expected, much smaller. Comparing the bottom-fixed cases (right plot), the TSR 7 profile exhibits larger velocity fluctuations near the root and tip compared to the TSR 9 profile. This is because the turbine operates sub-optimally at a lower TSR, which can lead to increased flow separation near the root and more complex tip effects, both of which are sources of unsteadiness.

It should be noted that numerical artifacts associated with the ALM could influence velocity fluctuations. The ALM can produce localized peaks in the normal force, leading to locally increased velocity deficits. However, these artifacts primarily occur on the horizontal plane. Since the current analysis is performed on the vertical plane, these effects are not a significant cause for concern here.

The primary characteristic in Figure 5.36 that reveals the asymmetric nature of the velocity fluctuations is that the SDEV values in the upper half of the wake (approximately 0.3D to 0.4D) are consistently larger than those in the lower half (-0.3D to -0.4D). While the aforementioned limitations of this study bring uncertainty to the conclusions, this aligns with the findings from both the blade loading analysis in Subsection 5.2.8 and the probe data in Figure 5.33. Observing the left plot, an increase in roll frequency does not cause a significant difference in SDEV between the upper and lower halves of the wake, which is consistent with the findings in Figure 5.35. In contrast, the center plot shows that increasing the roll amplitude has a much more significant impact, substantially increasing the SDEV in the upper half while the lower half remains less affected. This is however as mentioned previously due to the limitation of the study and should not be certainly taken as a conclusion. Lastly, the TSR plot on the right indicates that TSR does not influence the asymmetry in SDEV fluctuations caused by roll motion; instead, it primarily increases the velocity fluctuations near the tips. This is consistent with the higher SDEV of normal force loading at the tips for increasing TSR, as shown in Subsection 5.2.7.

The analysis is extended to the lateral Y-axis at the same downstream location (0.01D). These results are presented in Figure 5.37, which again compares the effects of roll frequency, amplitude, and TSR.

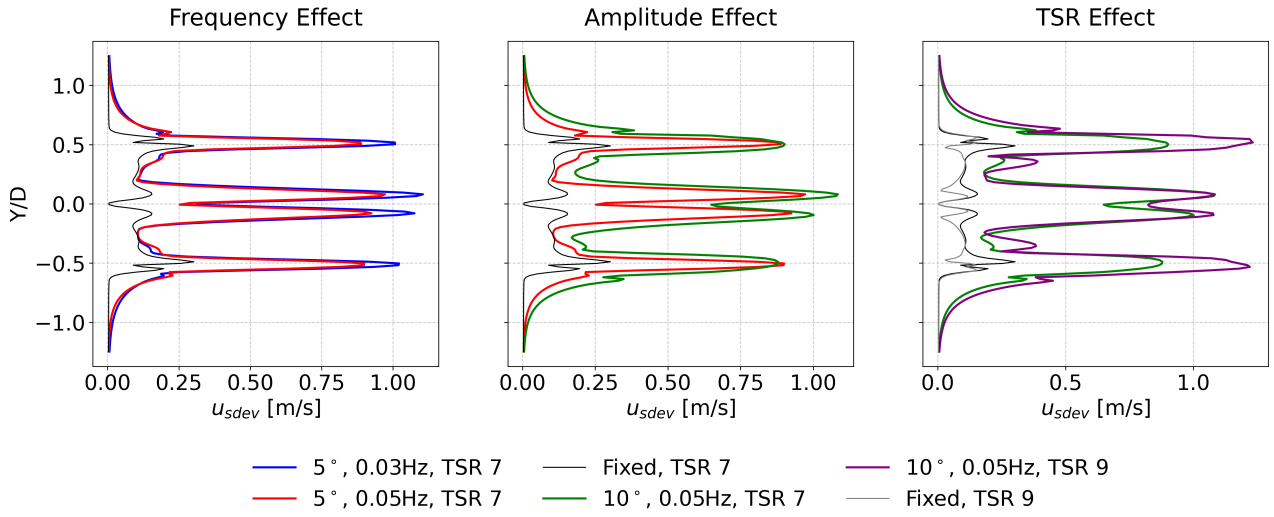

Figure 5.37: The effect of roll frequency (left), roll amplitude (center), and turbine TSR (right) on the standard deviation of the streamwise velocity component, plotted against the lateral Y-axis at 0.01D downstream of the rotor.

The limitation that was explained for Figure 5.36 does not apply here because the vertical shift of the rotor due to the roll motion is the limitation here which is negligibly small at 2.3m (H - H · cos(ϕ_0)). Figure 5.37 does not reveal significant trends related to the asymmetric nature of the rolling motion across the entire profile. The most notable effect of roll-induced asymmetry is observed near the hub, where the rolling cases exhibit a larger SDEV velocity on the positive Y-side compared to the negative

Y-side. The difference between these two peaks near the hub grows with increasing roll amplitude, which also widens the laterally disturbed region. Increasing the roll frequency increases the absolute magnitude of these peaks but does not significantly alter the relative difference between them.

Increasing TSR significantly raises the SDEV of velocity at these peaks, an effect attributed to the increased SDEV of the normal force, as studied in Subsection 5.2.7. Increasing TSR also appears to reduce the asymmetry between the peaks around the hub, potentially because asymmetric stall is more prevalent at the lower TSR.

5.3.3 Velocity Profile Analysis

This subsection presents a detailed analysis of the 2-dimensional velocity fields, examining the streamwise (u), lateral (v), and vertical (w) components. The objective is to investigate the effects of roll motion and TSR on the velocity distributions and to establish a direct connection with the blade loading characteristics identified in Subsection 5.2.8.

The analysis is based on the velocity maps on the XY-plane at hub height. The focus on 2-dimensional planar analysis, rather than 1-dimensional velocity profiles at multiple downstream locations, is intentional and addresses two significant methodological challenges. First, correlating downstream flow features with their causative blade loading events requires accurately tracking the advection of the wake. This is complicated by the variable advection speed, which makes it difficult to link a specific roll phase at the rotor to a corresponding flow structure observed further downstream.

Second, both instantaneous and phase-averaged 1-dimensional profiles are highly susceptible to the periodic influence of individual blade passages. As demonstrated in the bottom-fixed case velocity deficit oscillations (Subsection 5.3.1), the large, localized deficit created by a passing blade can obscure the more subtle, large-scale effects induced by the roll motion.

To perform a concise analysis, this section focuses on a few selected simulations. These cases were chosen because they are illustrative of the general trends observed across all roll conditions.

Study of TSR Effects on Velocity Profiles

A comparison between the bottom-fixed turbine cases at TSR 7 and 9 provides insight into the fundamental influence of TSR on the wake structure, absent of any platform motion. The velocity plots are given for these in Figure 5.38 and Figure 5.39, respectively.

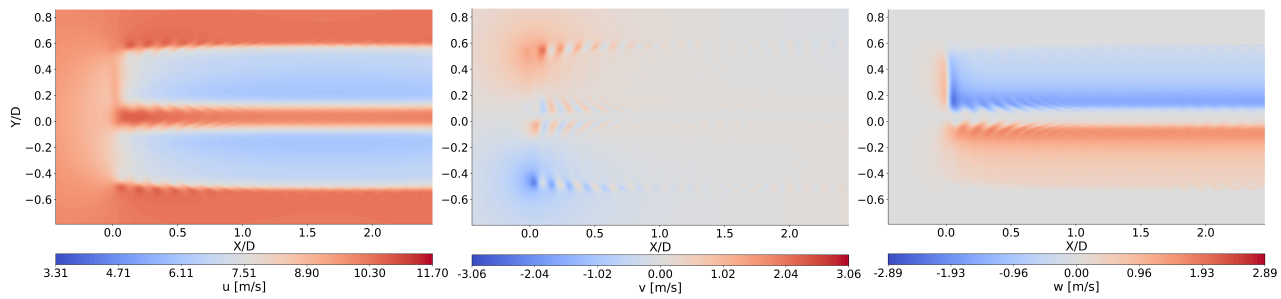

Figure 5.38: u, v, w velocities plotted on the XY-plane for bottom-fixed case at TSR 7.

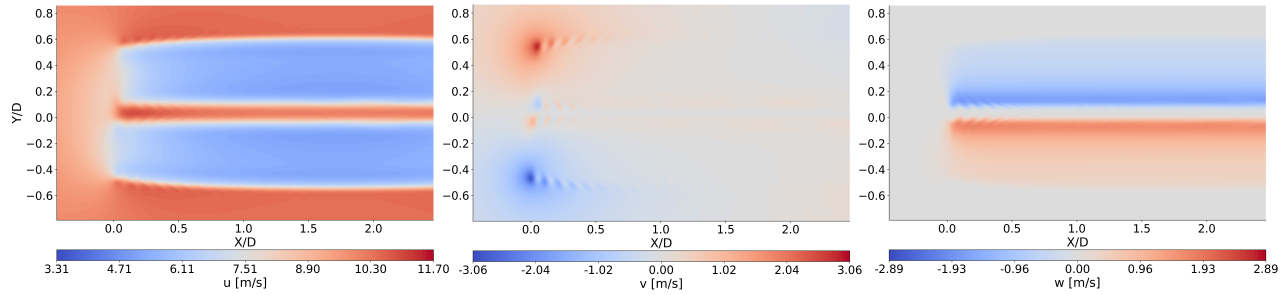

Figure 5.39: u, v, w velocities plotted on the XY-plane for bottom-fixed case at TSR 9.

The streamwise velocity (u) plots for both cases exhibit a steady wake characterized by a distinct velocity deficit region directly behind the rotor. The wake is symmetric as expected for a bottom-fixed turbine. The primary difference lies in the magnitude of this deficit. For the bottom-fixed TSR 7 case, the minimum velocity in the wake is approximately 6 m/s. In contrast, the TSR 9 case shows a much lower minimum velocity of about 5.1 m/s. This aligns well with the fact that a higher TSR leads to larger normal forces due to the higher tangential velocity component resulting in more momentum deficit. The induction zone in front of the turbine in the form of decelerated flow is also visible.

The lateral velocity (v) component for both bottom-fixed cases are mostly downstream close to zero, showing no lateral oscillation. However, near the rotor it reveals small-scale fluctuations which are represent the velocity induced of the vortical structures that reduce in strength downstream leading to lower magnitudes of lateral velocity. The vertical velocity (w) plot shows a region of positive (upward) velocity is present in the upper half of the rotor disc and a region of negative (downward) velocity in the lower half. This is a direct consequence of the blade rotation, where the blades moving through the horizontal plane induce vertical flow. Comparing the two cases, the magnitude of these induced velocities is slightly higher for the TSR 9 case, consistent with the generation of stronger tip and root vortices at higher operational rotor speeds.

The velocity profiles of TSR 9, particularly at the edges of the wake are more smooth compared to TSR 7 case. This is due to the reduced pitch in the vortex shed from each consecutive blade that leads to a more continuous velocity profile. The pitch refers to the streamwise distance between each consecutive vortex.

The influence of TSR on a turbine already undergoing rolling motion is examined by comparing case 4 and 8 which are plotted in Figure 5.40 and Figure 5.41, respectively.

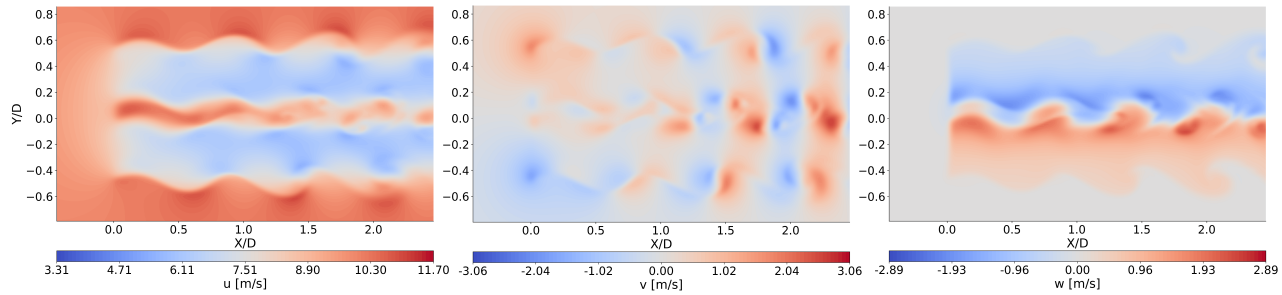

Figure 5.40: u, v, w velocities plotted on the XY-plane for case 4 (5°, 0.05Hz, TSR 7).

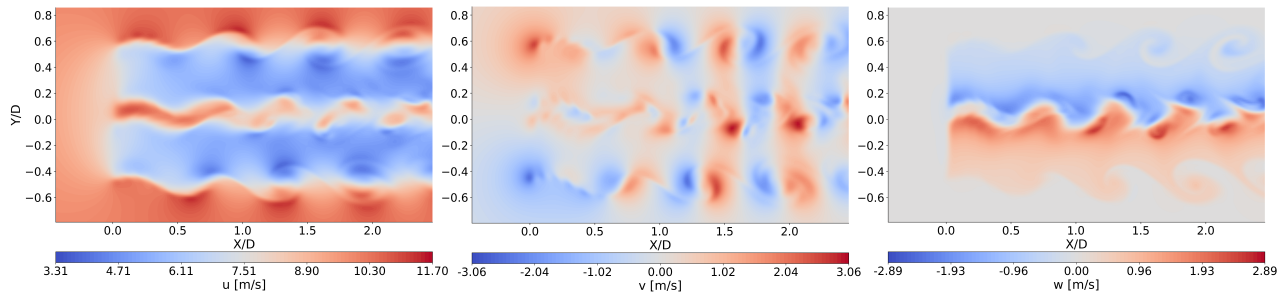

Figure 5.41: u, v, w velocities plotted on the XY-plane for case 8 (5°, 0.05Hz, TSR 9).

This comparison reveals two key effects. First, consistent with the findings from the bottom-fixed cases, increasing the TSR from 7 to 9 results in a larger wake deficit. The minimum streamwise velocity (u) drops from 5.73 m/s in case 4 to a lower 4.13 m/s in case 8. The rolling motion does not alter this fundamental relationship between TSR and wake momentum deficit.

An interesting finding here is that roll motion generates lateral velocities (v) that were non-existent in the bottom-fixed cases of Figure 5.38 and Figure 5.39 other than near the blades due to the shed vortices. The magnitudes of these velocities are not negligible either and they are similar to the lateral velocities that the turbine experiences with rolling motion formulated $H\phi_0 2\pi f_\phi \cos(2\pi f_\phi t)$. This suggests that the lateral movement of the turbine with roll drags a volume of air with itself, inducing lateral velocities in the wake. Another reason for this could be because while the horizontal plane of analysis is stationary, the wake slighlty moves vertically with the turbine. This is interesting phenomenon and requires a further analysis possible with a translational lateral motion, namely, sway to understand which of the two explanations are more suitable or if it is a combination of both.

Although the analysis is conducted on the horizontal plane at hub height, where the primary vertical loading asymmetry from roll motion is less direct, periodic variations are nonetheless observed. In the streamwise velocity (u) field, the wake exhibits a periodic intensification and weakening of the velocity deficit. This fluctuation becomes more pronounced at a higher TSR.

This behavior can be attributed to variations in the net normal force on the rotor. A higher TSR amplifies the influence of roll motion on blade loading, which consequently enhances the dynamic response of the wake. A key observation is that the regions of higher deficit appear out of phase on opposite sides of the wake centerline. This suggests that the roll motion induces a lateral alternation in blade loading, in addition to the dominant vertical one, which directly causes the observed fluctuations in the streamwise velocity (u).

TSR also influences the magnitude of the motion-induced velocities. The oscillation pattern is nearly identical in both cases, as the roll amplitude and frequency are held constant. However, the magnitudes of the lateral (v) and vertical (w) velocities are notably higher for the TSR 9 case. The peak lateral velocity increases from 1.9 m/s to 2.4 m/s, and the vertical velocity shows a similar amplification. The result is an amplification of the velocity fluctuations in the directions perpendicular to the main flow, leading to a more laterally and vertically active wake overall.

A more subtle effect is also visible in the spatial pattern of the wake. When comparing the lateral (v) and vertical (w) velocity fields, the alternating structures in case 8 appear more compressed in the streamwise direction than in case 4. For example, in the lateral velocity (v) plot for case 8, more alternating pockets of positive and negative velocity are visible within the same downstream distance compared to case 4. This indicates that a higher TSR leads to a shorter wavelength for the wake's oscillation pattern. This phenomenon can be explained by the difference in the wake's convection velocity. The higher normal force associated with TSR 9 results in a lower mean streamwise velocity (u) within the wake. Since the roll frequency is identical for both cases, the slower-moving wake of case 8 transports these time-periodic disturbances a shorter distance downstream in each cycle. This results in the observed compression of the wake features and a higher frequency of the velocity fluctuations.

Study of Roll Frequency Effects on Velocity Profiles

To study the impact of roll frequency, case 3 and case 5 are compared. Their plots are given below in Figure 5.42, and Figure 5.43 respectively.

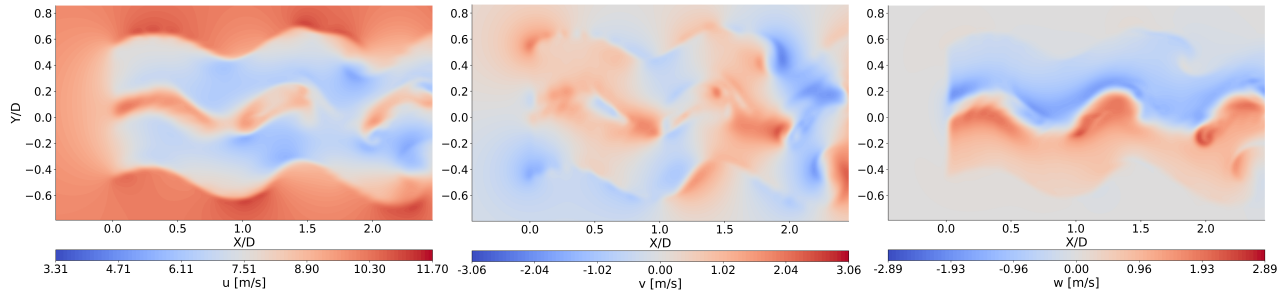

Figure 5.42: u, v, w velocities plotted on the XY-plane for case 3 (10°, 0.03Hz, TSR 7).

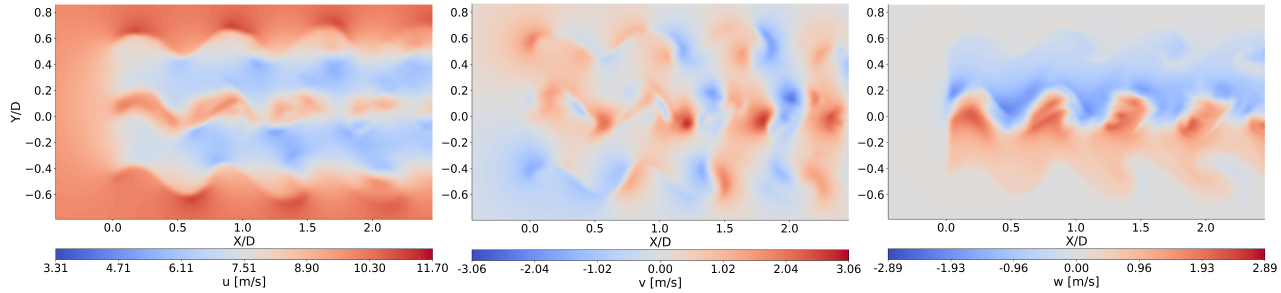

Figure 5.43: u, v, w velocities plotted on the XY-plane for case 5 (10°, 0.05Hz, TSR 7).

The primary effect of increasing the roll frequency from 0.03Hz to 0.05Hz is a reduction in the wavelength of the wake oscillation, an effect consistently observed across all velocity components. The peak velocity magnitudes are slightly different between the two cases, where the lateral velocity (v) is especially slightly larger for the higher roll frequency case.

It is observed that the maximum streamwise velocity (u) in some regions exceeds the freestream inflow velocity. This phenomenon is consistent with blockage effects, where flow accelerates as it is displaced around the rotor. Visually, these areas of accelerated flow correspond to instances where the turbine's motion presents the largest obstruction to the incoming flow.

Study of Roll Amplitude Effects on Velocity Profiles

To study the impact of roll frequency, case 8 and case 9 are compared. Their plots are given below in Figure 5.44, and Figure 5.45 respectively.

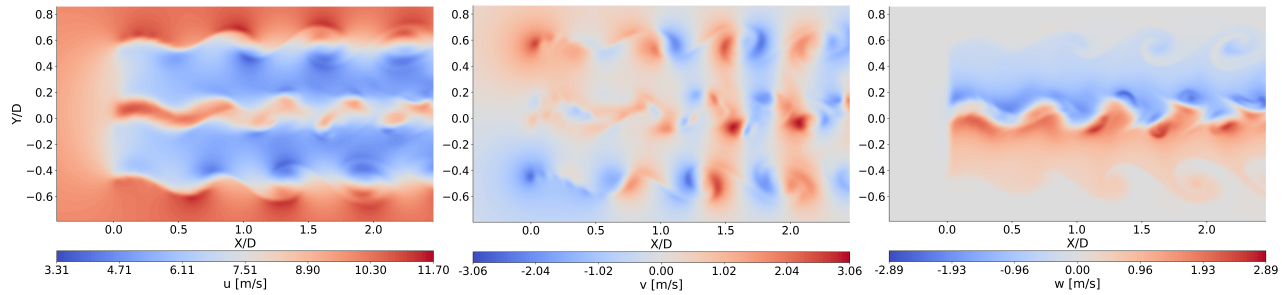

Figure 5.44: u, v, w velocities plotted on the XY-plane for case 8 (5°, 0.05Hz, TSR 9).

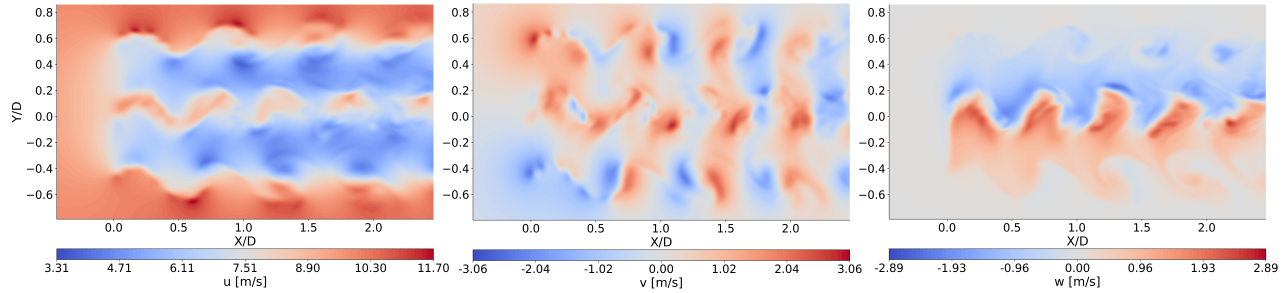

Figure 5.45: u, v, w velocities plotted on the XY-plane for case 9 (10°, 0.05Hz, TSR 9).

Increasing the roll amplitude from 5° to 10° directly influences the magnitude of the wake's lateral displacement. The streamwise velocity (u) field for case 9 shows a more pronounced oscillation, with the core of the deficit being displaced further from the centerline compared to case 8. This observation is corroborated by the lateral velocity (v) plots.

While the spatial pattern of the oscillation is similar between cases (as the roll frequency is constant), the velocity magnitudes present a mixed result. As expected, the minimum streamwise velocity (u) is lower for the higher amplitude case, a direct consequence of the larger roll-induced velocities at the rotor. However, the magnitude of the induced lateral velocity (v) is counter-intuitively larger for the smaller amplitude case, which exhibits both a greater maximum and smaller minimum value.

Despite the unexpected magnitudes observed in the lateral (v) and vertical (w) velocity components, their spatial distributions are physically intuitive. Overall, the distortion of all velocity components is more significant in the higher amplitude case, reflecting the greater dynamic forcing on the flow.

5.3.4 Study of Vorticity Distributions

This study extends the analysis beyond the influence of blade loads on the wake velocity deficit to also investigate their effect on the shed vorticity and its spatial and temporal evolution.

The wake of a turbine is characterized by regions of high vorticity, which are primarily concentrated in the helical tip vortices and the central root vortex system shed from the blades. The evolution,

interaction, and eventual breakdown of these vortex structures are critical, as they govern the wake's stability, recovery, and impact on downstream turbines.

The comparison between cases is based on an evaluation of the following key wake characteristics:

1. **Vortex Coherence:** The persistence of distinct, identifiable helical vortex cores as they travel downstream.
2. **Wake Breakdown:** The downstream location where coherent vortex structures transition into disorganized, chaotic distribution.
3. **Wake Oscillatory Motion:** The extent of the wake's lateral and vertical displacement from a steady trajectory.
4. **Vorticity Magnitude:** The magnitude of the shed vorticity, which indicates the strength of the vortex structures.

To systematically analyze the vorticity in the wake, the investigation is divided into two sections, each examining a different 2-dimensional plane. The first section focuses on the XY-plane. This perspective is ideal for observing the pronounced oscillatory and unsteady motion that results from the turbine's lateral movement during roll. This section analyzes the influence of roll motion by comparing a variety of selected cases.

The second section concentrates on the XZ-plane. This view facilitates an in-depth study of the vertical asymmetries in the wake, particularly the differences in vortex behavior between the upper and lower regions.

Top-View Study of TSR Effects on Vorticity

The analysis begins with the bottom-fixed cases, which serve as a baseline for comparison. The TSR 7 case, depicted in Figure 5.46a, exhibits a characteristic, well-ordered wake structure. Distinct helical vortex systems, corresponding to the root and tip of each of the three turbine blades, are clearly identifiable. In the near-wake, these vortices remain coherent and stable, contributing to an overall symmetrical wake profile.

It should be noted that the iso-vorticity visualization captures regions of high shear in addition to the vortex cores themselves, and these shear layers should not be mistaken for pure circulation. Such high-shear regions are particularly evident between the tip vortex cores, appearing as smudged regions in the figure between vortex cores.

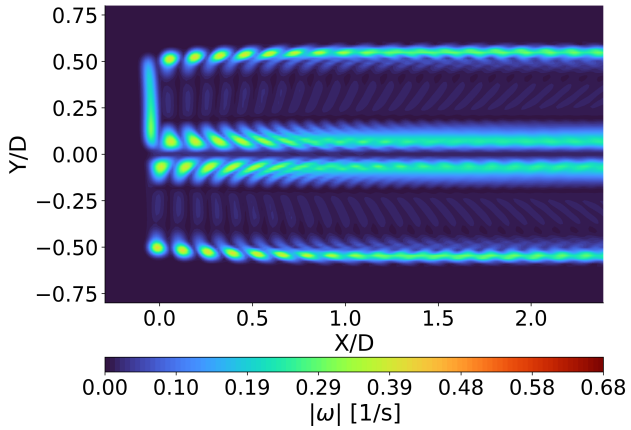

(a) Vorticity magnitude plotted on the XY-plane for bottom-fixed case at TSR 7.

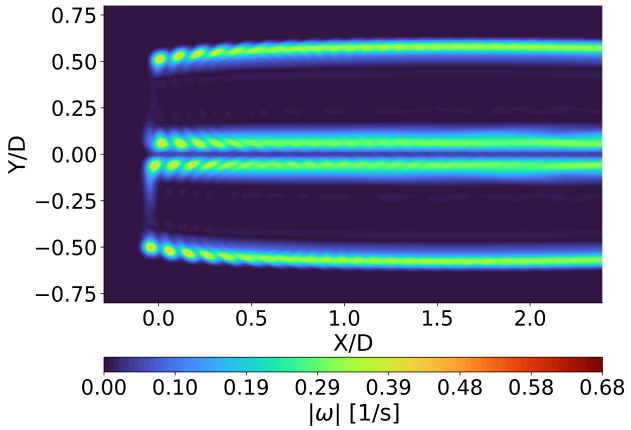

(b) Vorticity magnitude plotted on the XY-plane for bottom-fixed case at TSR 9.

Figure 5.46: Vorticity magnitude plotted on the XY-plane for bottom-fixed cases at TSR 7 and 9.

In case 11, as shown in Figure 5.46b, the wake structure at TSR 9 differs from the TSR 7 baseline. The helical vortices exhibit a smaller pitch to adjacent vortices, an expected consequence of the higher TSR, where the faster blade tip velocity relative to the freestream flow results in a more tightly wound helix. Furthermore, the magnitude of the shed tip vorticity is greater for the higher TSR case, indicating that stronger vortices are generated due to increased blade loading. Note that this conclusion is obtained from not only a snapshot of vorticity distribution but a time-averaged analysis that is not displayed here.

A direct consequence of this smaller pitch is that the shed vortex filaments begin to interact sooner in the wake for the TSR 9 case. Additionally, the vorticity originating from the mid-span of the blades is less prominent compared to the TSR 7 case. This observation correlates with the reduced tangential loads at the mid-span for higher TSRs, as shown previously in Figure 5.20. This suggests that the mid-span vorticity is primarily generated by shear in the wake, which are influenced by tangential loading, rather than by the shedding of distinct, coherent vortex structures.

A comparison between the bottom-fixed and rolling cases reveals the effect of TSR on the vorticity magnitude is less noticable when roll motion is involved in terms of the vorticity magnitude. Although the findings from Section 5.2 establish that an increased TSR leads to a substantial increase in normal force, resulting in stronger shed vorticity, this is not easily distinguishable here.

Furthermore, TSR also amplifies the fluctuations in normal loads across the blade span that are induced by the roll motion, an effect quantified by the SDEV analysis in Figure 5.21. In contrast, the tangential load fluctuation does not increase noticeably with TSR and therefore does not contribute to a corresponding increase in shear. These findings are illustrated in the plots for case 5 and case 9, shown in Figure 5.47a and Figure 5.47b, respectively.

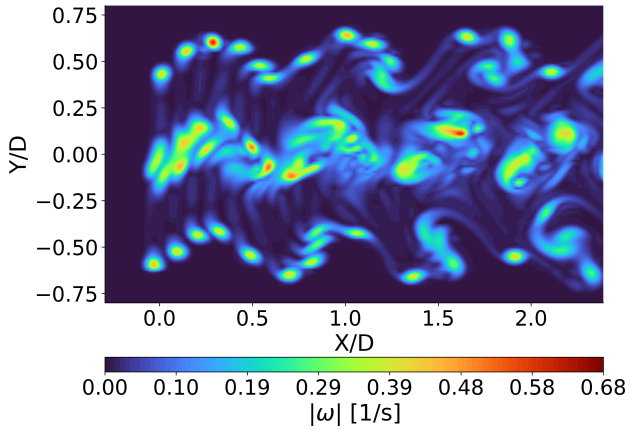

(a) Vorticity magnitude plotted on the XY-plane for case 5 (10°, 0.05Hz, TSR 7).

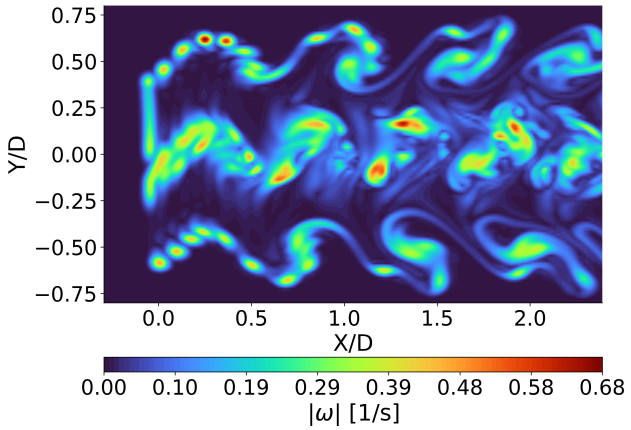

(b) Vorticity magnitude plotted on the XY-plane for case 9 (10°, 0.05 Hz, TSR 9).

Figure 5.47: Vorticity magnitude plotted on the XY-plane in the near-wake for varying TSR of 7 and 9 under roll motion of 0.05 Hz and 10°.

It is important to note that for the 10° roll amplitude cases, the maximum vorticity magnitudes shown in these plots can be influenced by the numerical error that has been explained in Subsection 5.2.3. An example of such a numerically-induced peak is visible at coordinates (X/D, Y/D) = (0.25, 0.63) in Figure 5.47a.

A second key finding is that a higher TSR promotes an earlier onset of the same wake phenomena. This can be seen by the fact that the clumping of the tip and root vortices occur earlier and more frequently in Figure 5.53d due to the smaller pitch between each consecutive vortex core. While this doesn't fully confirm it, but the acceleration of the wake development with higher TSR (as the wake is more compressed) suggests that the transition to the far-wake can happen earlier. As discussed by Goit and Meyers (2015)[24], a shortened near-wake is essential to faster overall wake recovery, as significant momentum entrainment from the freestream flow begins only after the breakdown of coherent structures. Additionally, the finding that a higher TSR amplifies the SDEV of normal force fluctuations suggests that a more unsteady wake is created potentially accelerating the wake breakdown, hence amplifying the influence of roll motion on wake recovery. The same trend has been observed by Farrugia et al. (2016)[16], where surge effects on the effect were amplified with increasing TSR.

The underlying mechanism for this behavior relates to vortex dynamics. The stronger, more tightly packed vortices at TSR 9 possess greater kinetic energy due to greater vorticity magnitude, rendering them more susceptible to instabilities such as vortex pairing. This process accelerates the dissipation of the ordered helical structures into disorganized turbulence. An example of this is evident when comparing a distinct vortex core in Figure 5.47a at coordinates (X/D, Y/D) = (1.75, -0.38) with the same region in Figure 5.47b. The vortex no longer exists as an independent structure; it has merged with adjacent filaments to form a larger, more diffuse structure. The rapid breakdown of the tip vortices weakens the "curtain" that encloses the wake, thereby enhancing mixing with the surrounding flow and promoting faster recovery.

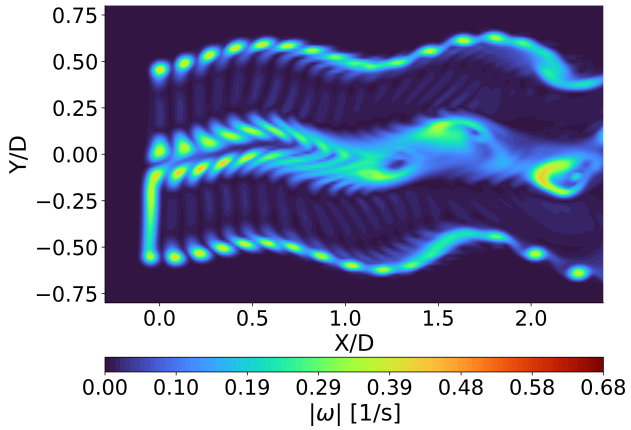

(a) Vorticity magnitude plotted on the XY-plane for case 2 (5°, 0.03 Hz, TSR 7).

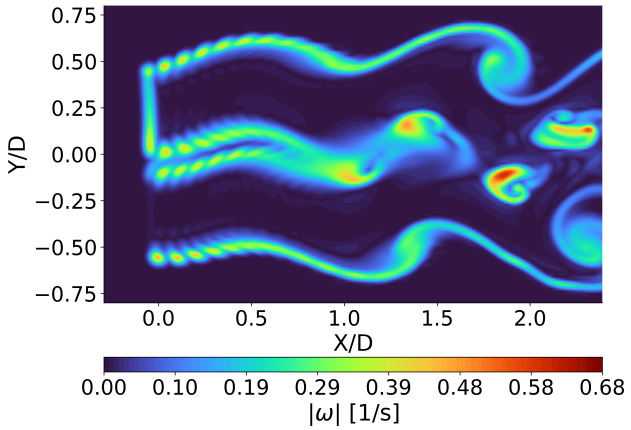

(b) Vorticity magnitude plotted on the XY-plane for case 6 (5°, 0.03 Hz, TSR 9).

Figure 5.48: Vorticity magnitude plotted on the XY-plane in the near-wake for varying TSR of 7 and 9 under roll motion of 0.03 Hz and 5°.

This same trend of TSR influence on the proximity of vortices in the wake is further confirmed by a comparison between case 2 and case 6, shown in Figure 5.48a and Figure 5.48b respectively. This proximity enhances vortex pairing, which leads to the formation of larger, coherent rotating structures and an overall increase in wake vortex clumping. This effect is particularly evident in Figure 5.48b near (X/D, Y/D) = (1.8, -0.5), where a pronounced region of high vortex clumping develops. This clumping seen especially at the tip vortices that is not observed for bottom-fixed cases is a product of the fluctuating loading with roll motion.

Top-View Study of Roll Amplitude Effects on Vorticity

The influence of roll amplitude on the wake vorticity is examined by comparing two pairs of cases. The first comparison is between case 2 and case 3, presented in Figure 5.49, and the second is between case 8 and case 9, presented in Figure 5.50.

An increased roll amplitude induces a more pronounced lateral oscillation of the wake, which is visually evident as an increased curvature in the trajectory of the tip vortices, as shown in Figure 5.49. In addition, the variation of vortex pitch increases due to a larger variation of the displacement of the turbine laterally. This variation occurs because the lateral velocity of the turbine alters the effective spacing between shed vortices. The vortex pitch increases when the turbine moves with high lateral velocity away from its previously shed vortex, effectively increasing the distance between them. Conversely, at the points of maximum roll displacement, where the turbine's velocity is momentarily zero, the instantaneous vortex pitch converges towards that of the corresponding bottom-fixed TSR case. However, even at these stationary moments, the wake is not identical to the bottom-fixed case. Inertial effects and residual lateral velocities from the oscillatory motion cause the vortices to interact and clump downstream, an effect particularly visible in the higher TSR case (Figure 5.48b).

This dynamic stretching of the wake is amplified by a larger roll amplitude. The increase in vortex pitch is most pronounced when the turbine rolls at maximum velocity, leading to larger gaps between the tip vortices, as exemplified at coordinates (X/D, Y/D) = (0.5, 0.63) in Figure 5.49b.

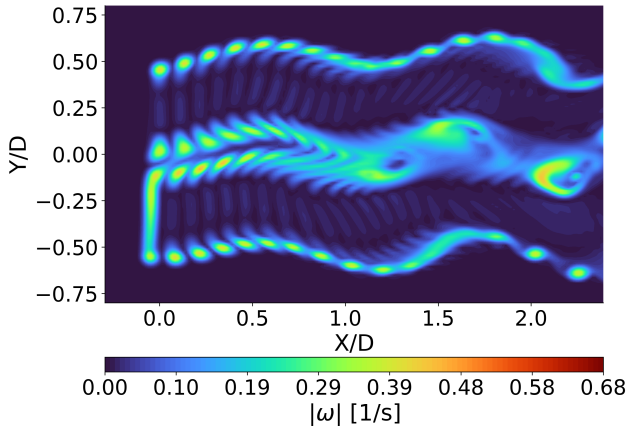

(a) Vorticity magnitude plotted on the XY-plane for case 2 (5°, 0.03 Hz, TSR 7).

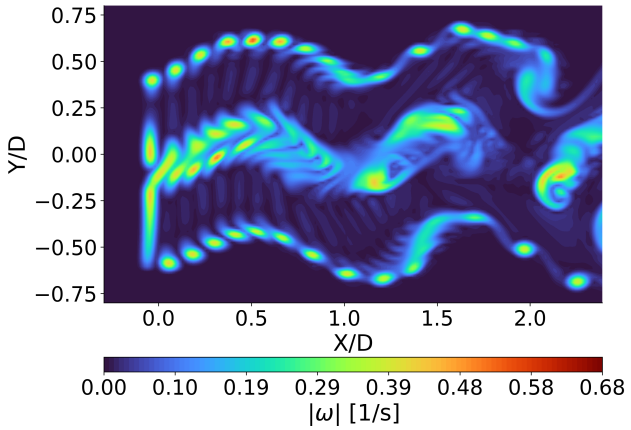

(b) Vorticity magnitude plotted on the XY-plane for case 3 (10°, 0.03 Hz, TSR 7).

Figure 5.49: Vorticity magnitude plotted on the XY-plane in the near-wake for varying roll amplitudes of 5° and 10° under roll motion of 0.03 Hz and operating TSR of 7.

Additionally, a larger roll amplitude accelerates the breakdown of the coherent structures originating from the turbine root. This breakdown is driven by a complex interaction between the root vortices shed during the roll cycle. The vortex shed from the side of the rotor moving in the same direction as the roll motion is imparted with a higher streamwise velocity, causing it to overtake the slower-moving vortex from the opposing side. This overtaking motion induces a clumping and mixing process between the root vortex filaments.

At smaller roll amplitudes, this interaction results in a high-vorticity region that is elongated along the streamwise direction and persists as a relatively continuous structure. In contrast, the greater lateral velocities associated with a higher roll amplitude cause this structure to fragment into more discrete, segregated pockets of high vorticity. Furthermore, the magnitude of the root vortices is also observed to slightly increase with a larger roll amplitude.

Finally, the large oscillatory motion associated with a 10° roll amplitude creates the potential for interactions between the tip and root vortex systems, which would further accelerate the overall wake breakdown. Although this phenomenon is not directly observed within the visualized downstream distance of $2D$, it is a consequence of the heightened unsteadiness. The increased amplitude of the wake's motion makes such complex vortex interactions more likely to occur at locations further downstream.

The comparison presented in Figure 5.50 reinforces these observations. In case 9 (Figure 5.50b), the higher roll amplitude leads to the shedding of more distinct and separated vortex structures, particularly those shed during moments of maximum roll velocity. The roll velocity in case 8 is insufficient to cause this same degree of fragmentation. As a result, the tip vortex filaments in Figure 5.50a appear more continuous.

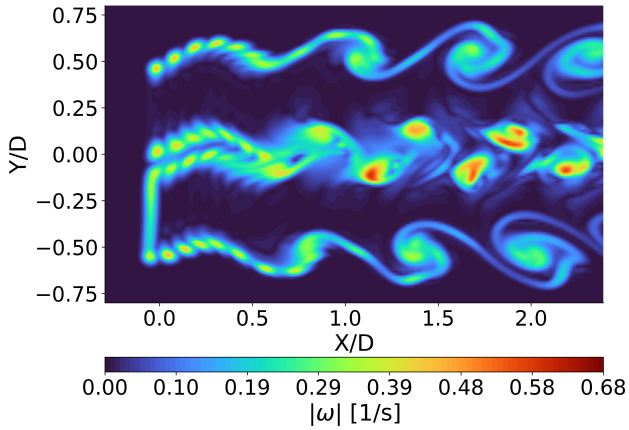

(a) Vorticity magnitude plotted on the XY-plane for case 8 (5°, 0.05 Hz, TSR 9).

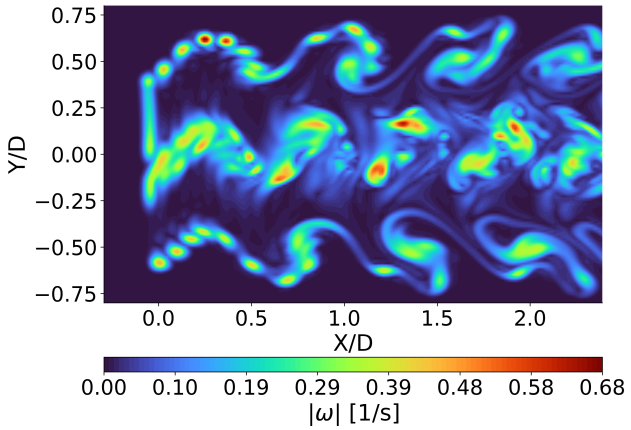

(b) Vorticity magnitude plotted on the XY-plane for case 9 (10°, 0.05 Hz, TSR 9).

Figure 5.50: Vorticity magnitude plotted on the XY-plane in the near-wake for varying roll amplitudes of 5° and 10° under roll motion of 0.05 Hz and operating TSR of 9.

A notable feature in these plots is the visible interaction between the root and tip vortex systems, which is more apparent here than in the comparison shown in Figure 5.49. This is attributed to the combined effects of a higher TSR and a higher roll frequency in these cases. Together, these parameters amplify the wake's unsteadiness and promote closer interactions between the different vortex structures.

Top-View Study of Roll Frequency Effects on Vorticity

An increased roll frequency also enhances wake instability, though its mechanism differs from that of roll amplitude. A higher frequency introduces perturbations with a shorter wavelength into the wake. A comparison between case 3 and case 5 in Figure 5.51 illustrates this. The wake in case 5 appears more perturbed, with more frequent oscillations and faster vortex interactions, leading to a more rapid breakdown.

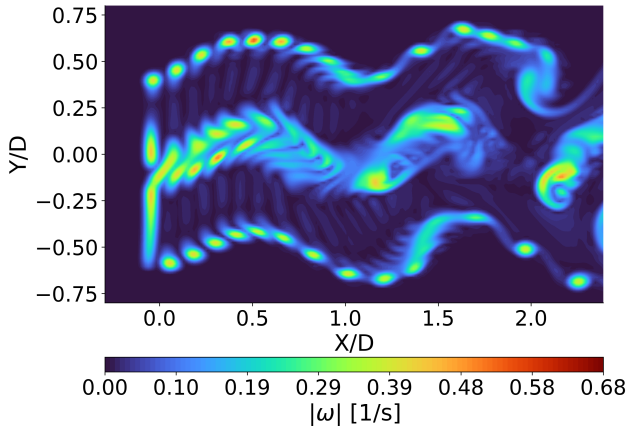

(a) Vorticity magnitude plotted on the XY-plane for case 3 (10°, 0.03 Hz, TSR 7).

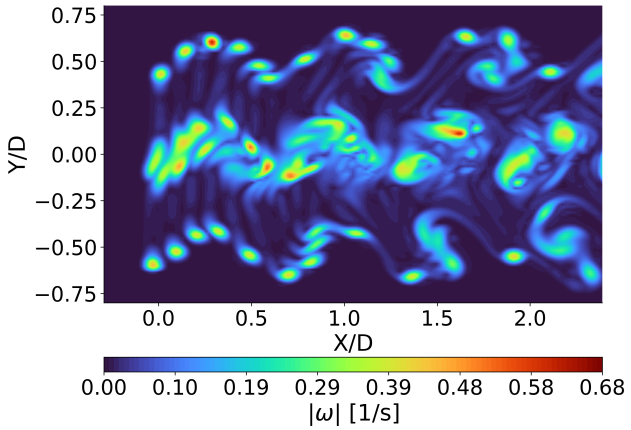

(b) Vorticity magnitude plotted on the XY-plane for case 5 (10°, 0.05 Hz, TSR 7).

Figure 5.51: Vorticity magnitude plotted on the XY-plane in the near-wake for varying roll frequencies of 0.03Hz and 0.05Hz under roll motion of 10° and operating TSR of 7.

Frequency has a more pronounced and consistent effect on the variation of pitch between the shed tip

vortices than amplitude. While a higher amplitude increases the spacing between vortices primarily when the turbine is at maximum roll velocity, a higher frequency leads to the formation of consistently distinct, separated tip vortices throughout each cycle. This is due to the combination of higher instantaneous roll velocities and the reduced time the turbine spends near its stationary roll positions with increasing roll frequency.

This behavior promotes more frequent vortex pairing, which is evident by the earlier onset of pairing at just $1D$ downstream in Figure 5.51b. This accelerated interaction has a shortening effect on the near-wake.

The root vortices in the higher frequency case (Figure 5.51b) are also significantly more fragmented and exhibit high magnitudes. Note that these comments are based on observations made when these plots are studied in time, but only the snapshots are provided here. The overall unsteadiness of the wake promotes the formation of these distinct vortex structures, which appear after the initial merging of the root vortex system at approximately $0.2D$ downstream, as seen in Figure 5.51b.

A general principle emerges where greater unsteadiness, whether from more aggressive roll motion or a higher TSR, leads to a larger maximum vorticity magnitude in the wake. As established in the blade loading analysis, more unsteady roll induces higher instantaneous velocities, which increase the effective tip speed and blade loads at certain phases of the cycle. However, more importantly, unsteadier motion also leads to greater temporal variation in the strength of the shed vorticity, corresponding to the larger SDEV load fluctuations. A wake composed of vortices with varying strengths is inherently more unstable and susceptible to breakdown, which can accelerate wake recovery.

The comparison in Figure 5.52, which examines the effect of frequency at a lower amplitude but a higher TSR, further substantiates these trends. The accelerated pairing of the tip vortices leads to the formation of larger vortex clumping structures. This process in turn weakens the shear layers between the individual clumped vortex regions, creating intermittent gaps in the wake structure that promote mixing and recovery. Consistent with previous observations, the root vortex system also demonstrates a more rapid breakdown into scattered pockets of high vorticity.

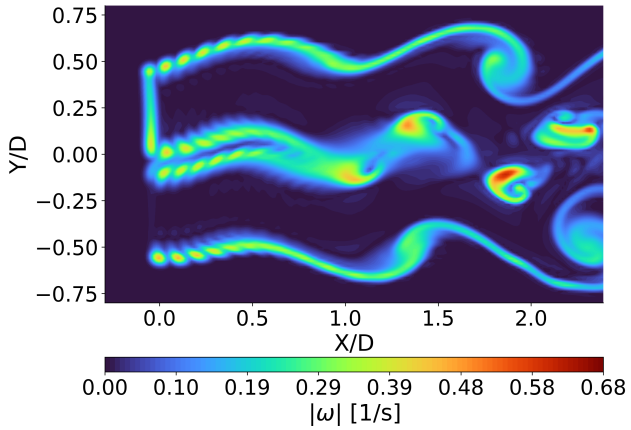

(a) Vorticity magnitude plotted on the XY-plane for case 6 (5°, 0.03 Hz, TSR 9).

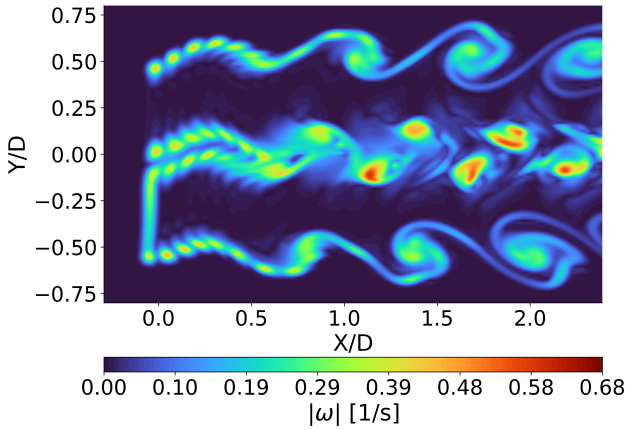

(b) Vorticity magnitude plotted on the XY-plane for case 8 (5°, 0.05 Hz, TSR 9).

Figure 5.52: Vorticity magnitude plotted on the XY-plane in the near-wake for varying roll frequencies of 0.03Hz and 0.05Hz under roll motion of 5° and operating TSR of 9.

As a final remark, this analysis reveals a mutually stimulating effect between TSR and roll motion on the wake's vorticity. The influence of TSR on the peak vorticity magnitude is substantially amplified as the roll motion becomes more unsteady. For the bottom-fixed and the most steady roll cases, increasing the TSR results in only a marginal increase in vorticity magnitude. In contrast, for the more aggressive roll motions, the same increase in TSR produces a much larger jump in peak vorticity.

Table 5.1: Summary of effects of roll motion and TSR on the top-view vorticity distribution in the wake.

Parameter	Wake Characteristic	Observed Effect
Increasing TSR	Vortex Coherence	Decreased, smaller pitch, leading to earlier interaction and clumping of vortices.
	Wake Breakdown	Accelerated, earlier onset due to reduced vortex pitch and increased vortex pairing.
	Wake Oscillatory Motion	Slightly increased unsteadiness, contributing to increased vortex clumping.
	Vorticity Magnitude	Increased, higher peak vorticity due to stronger blade loading, although less noticeable difference for rolling turbines compared to bottom-fixed cases.
Increasing Roll Amplitude	Vortex Coherence	Increased initially due to larger vortex pitch from higher turbine lateral velocities and more consistently distinct vortices. Reduced downstream due to increased vortex clumping.
	Wake Breakdown	Accelerated, enhanced fragmentation of root vortices, with potential for earlier tip-root vortex interactions downstream.
	Wake Oscillatory Motion	Increased, more pronounced lateral oscillation and curvature of the wake trajectory.
	Vorticity Magnitude	Marginally increased vorticity magnitude due to higher instantaneous velocities and greater temporal variation in shed vorticity strength.
Increasing Roll Frequency	Vortex Coherence	Increased initially due to larger vortex pitch from higher turbine lateral velocities and more consistently distinct vortices. Reduced downstream due to increased vortex clumping.
	Wake Breakdown	Accelerated, more rapid breakdown due to more frequent oscillations, faster vortex interactions, and enhanced vortex clumping.
	Wake Oscillatory Motion	Increased, more frequent oscillations and higher instantaneous roll velocities of the wake.
	Vorticity Magnitude	Marginally increased vorticity magnitude due to higher instantaneous velocities and greater temporal variation in shed vorticity strength.

Side-View Study of Roll Motion Effects on Vorticity

An analysis of the wake's side-view (XZ-plane) demonstrates the trends observed from the top-view regarding the influence of the roll parameters.

A comparison between case 2 (Figure 5.53a) and case 4 (Figure 5.53b) confirms that a higher roll frequency promotes earlier vortex pairing. This accelerates the transition to turbulence and shortens the near-wake. The effect is also visible in the root vortex system, which exhibits more frequent oscillations and a more rapid breakdown into fragmented structures.

Beyond the effect of frequency, a crucial observation in both cases is the pronounced vertical asym-

metry of the wake. The vorticity shed in the upper half of the wake deviates more significantly from a steady trajectory than its counterpart in the lower half. This asymmetry is a direct consequence of the higher SDEV load fluctuations experienced by the blades as they pass through the upper portion azimuthally. As established by the kinematic analysis in Section 5.1 and the blade loading results in Subsection 5.2.8, this phenomenon is an inherent characteristic of the roll motion.

Similarly, a comparison between case 4 (Figure 5.53b) and case 5 (Figure 5.53c) highlights the impact of roll amplitude. The larger amplitude in case 5 induces a more chaotic state in both the tip and root vortex systems, characterized by greater segregation of vortex pockets and vortex clumping regions formed by their pairing. The influence of a higher TSR is to amplify these effects.

Analyzing the magnitudes of vorticity, an increasing frequency shows only slight increase of magnitude in the vorticity comparing case 2 (Figure 5.53a) with case 4 (Figure 5.53b), however, there is a slightly more influence of roll amplitude on the increase in vorticity magnitude when case 5 is studied (Figure 5.53c). Although the larger amplitude is twice the smaller amplitude while the frequencies have a ratio less than that, the impact of amplitude still shows to be the greater one on the magnitude of vorticity in the wake. Comparing case 5 (Figure 5.53c) with the identical roll motion but with the higher TSR in case 9 (Figure 5.53d) shows that the maximum magnitude in the clumped vortices increase and become much more significant in size. The higher magnitudes in the higher amplitude cases must be studied cautiously with the numerical error described in Subsection 5.2.3 in mind.

A key mechanism, visible only in the high-amplitude cases regardless of TSR, is a multi-stage process of vortex assembly. Initially, individual vortex filaments shed from the blades align as they propagate downstream due to varying streamwise velocities of each vortex core. They then merge to form a larger, cohesive vortex clumping structure. This larger structure subsequently propagates downstream and interacts with similar structures from previous cycles, effectively stacking on top of one another. An example of this secondary merging is visible at (X/D, Z/D) = (2.4, -0.6) in Figure 5.53d.

This clumping phenomenon is particularly interesting as it suggests a mechanism for enhanced wake recovery. By consolidating the vorticity into large, discrete pockets, the roll motion creates significant gaps between them. These gaps could allow for more effective momentum entrainment from the surrounding flow.

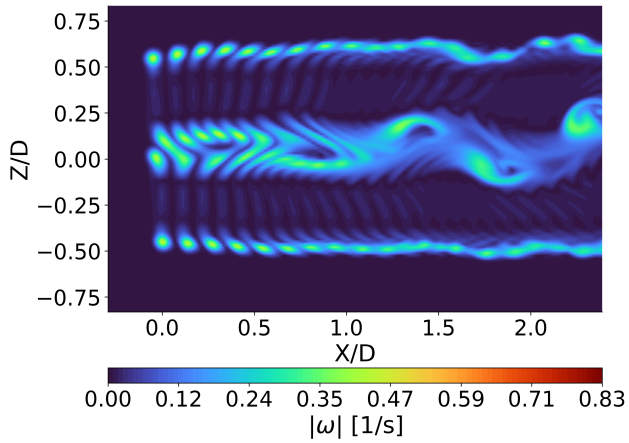

(a) Vorticity magnitude plotted on the XZ-plane for case 2 (5°, 0.03 Hz, TSR 7).

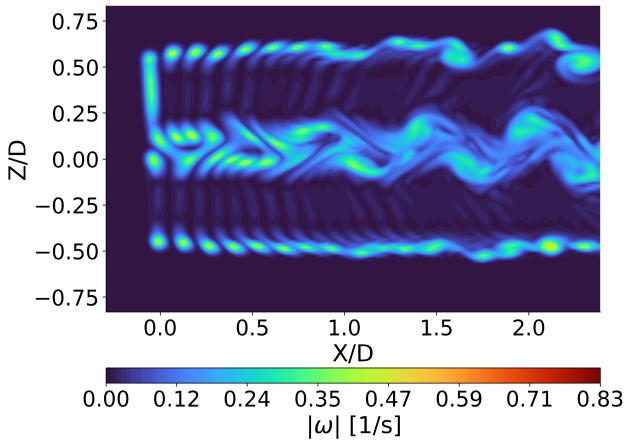

(b) Vorticity magnitude plotted on the XZ-plane for case 4 (5°, 0.05 Hz, TSR 7).

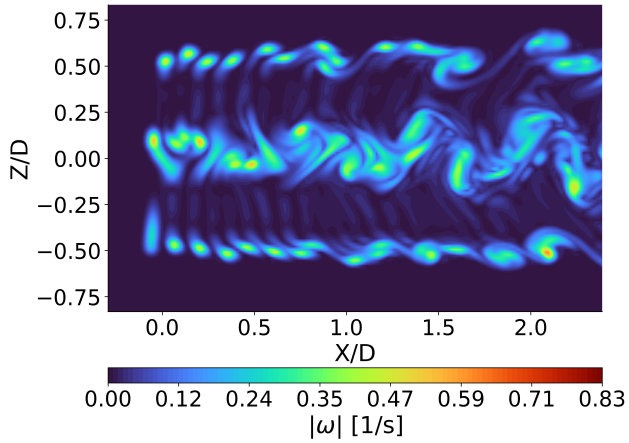

(c) Vorticity magnitude plotted on the XZ-plane for case 5 (10°, 0.05 Hz, TSR 7).

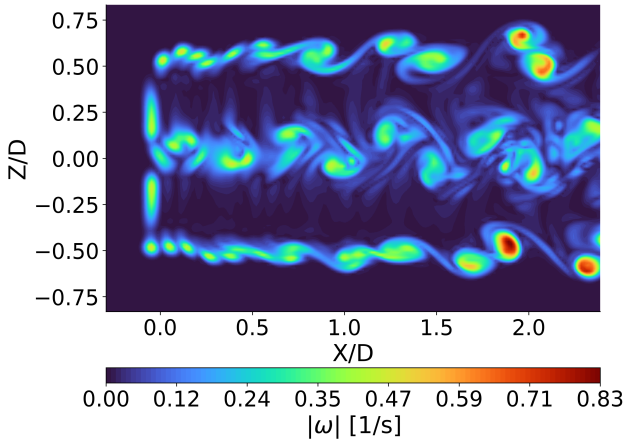

(d) Vorticity magnitude plotted on the XZ-plane for case 9 (10°, 0.05 Hz, TSR 9).

Figure 5.53: Vorticity magnitude plotted on the XZ-plane in the near-wake for cases 2, 4, 5, and 9.

5.3.5 Summary of Q-Criterion Analysis

The results of Q-criterion shows very similar results to the iso-vorticity subsection, Subsection subsubsection 5.3.4, therefore a summary is made rather than an extensive analysis. The plots referred in this subsection are given in Appendix B.

This section details a 3-dimensional analysis of turbine wakes using the Q-criterion to isolate coherent rotational structures from shear layers. This method visualizes regions where rotation dominates strain, providing a clear depiction of the vortex cores. The plots are colored to illustrate the distance from the viewer.

All Q-criterion plots were generated using an iso-Q value of 3.5×10^{-3} s^{-2}. This threshold fails to fully capture the downstream wake, particularly at the blade tips. This is because the chosen Q-value primarily visualizes the strong vorticity near the turbine. Further downstream, wake structures decay due to reduced circulation and viscous dissipation, causing their Q-values to fall below the visualization threshold. Consequently, this single iso-Q value does not fully represent the entire wake. Plotting with other Q-values did not yield improved overall visualizations.

Baseline Bottom-Fixed Cases

The analysis begins by establishing a baseline using the bottom-fixed turbine cases, plotted in Figure B.1a and Figure B.1b for TSR 7 and 9, respectively. The primary distinction observed is the pitch of the helical tip vortices. TSR 7 shows wider spacing, while TSR 9 exhibits a more tightly wound, smaller pitch helical system due to higher rotational speed.

The Influence of TSR on Rolling Turbine

- A higher TSR, as illustrated by comparing Figure B.2b to Figure B.2a, promotes the earlier formation of larger, paired vortex structures as the closer proximity of tip vortices facilitates their interaction and merging.
- This also leads to a greater overall wake oscillation and wider lateral excursion, as seen in Figure B.2b compared to Figure B.2a, indicating that higher TSR amplifies the unsteady motions induced by the platform's roll.
- The merger of tip vortices is observed to occur at the same downstream location where individual vortices ceased to be discernible in the fixed case. However, relying solely on the Q-criterion for this visualization carries a risk of over-interpretation. This is because the Q-criterion, by its nature as an iso-surface, presents vortices as either present or absent based on an arbitrary threshold. While the underlying vorticity field is continuous, this discrete visualization can artificially emphasize abrupt transitions across the chosen Q-value, potentially masking the gradual decay or evolution of structures.

The Influence of Roll Amplitude

- Increased roll amplitude significantly influences how quickly the wake loses its coherent structure. This is evident when comparing Figure B.3b with Figure B.3a.
- At lower amplitudes (Figure B.3a), the wake maintains a clear oscillatory pattern with largely intact helical vortices further downstream.
- At higher amplitudes (Figure B.3b), the wake becomes substantially more distorted, with vortex structures bending and interacting almost immediately behind the turbine.
- This trend persists at higher roll frequencies, as shown by comparing Figure B.4b to Figure B.4a.
- This destabilization is attributed to the amplified variation of tangential forces, inducing fluctuating swirl that promotes the chaotic evolution of coherent structures.

The Influence of Roll Frequency

- The frequency of the roll motion dictates the wavelength of the wake's oscillatory pattern.
- A comparison of cases with different frequencies, for example Figure B.4a with Figure B.3a or Figure B.4b with Figure B.3b, demonstrates this effect.
- Higher frequencies as in Figure B.4a and Figure B.4b) result in shorter wavelength lateral undulations, packing wake structures more closely together.

- This increased proximity accelerates the interaction between vortex filaments shed at different points in the roll cycle, leading to a more rapid decay of the coherent wake structure.

In summary, the Q-criterion analysis, despite its limitations in visualizing the full downstream wake, clearly demonstrates how TSR, roll amplitude, and roll frequency profoundly influence the stability, merging, and decay characteristics of the coherent vortical structures in the near-wake of a rolling turbine.

5.3.6 Power Spectral Density of Vorticity

A PSD analysis of the wake vorticity is also conducted. This method quantifies the distribution of energy within the vortical structures across a range of frequencies. Peaks in the resulting spectrum correspond to dominant periodic phenomena occurring within the flow. This analysis is therefore crucial for identifying the primary frequency signals present in the wake and tracking their spatial evolution.

Methodology of Vorticity Power Spectral Density Study

Probing vorticity for PSD analysis at discrete downstream locations is challenging due to the high sensitivity of the signal to the precise location of the probe relative to the vortex core. To mitigate this sensitivity, a methodology based on spatial averaging is employed. For each downstream location being analyzed (0.2D, 0.5D, 1.0D, 1.5D, and 2.0D), a rectangular zone is defined along the path of the tip vortices, as shown for case 2 in Figure 5.54. The PSD is then spatially averaged within this zone. This approach averages out localized fluctuations and provides a more robust and repeatable measure of the energy content within a given region.

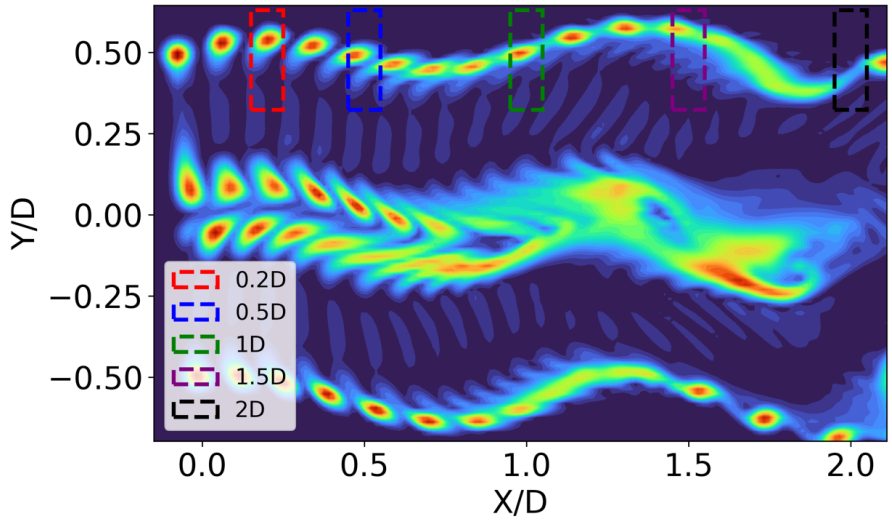

Figure 5.54: Selected PSD averaging zones at 0.2D, 0.5D, 1.0D, 1.5D, and 2.0D downstream.

Even with this spatial averaging, the resulting peak powers must be interpreted with caution, as some sensitivity to the zone selection may persist.

Frequency Spectra of Rolling Wind Turbine Wakes

The PSD of case 3, shown in Figure 5.55, reveals a complex spectrum with numerous frequency peaks, significantly more than were observed in the blade loading analysis. This case involves a roll frequency of 0.03Hz and a TSR of 7, corresponding to a rotor frequency (1P) of 0.093Hz. The complexity arises because the wake contains not only the primary roll and 1P frequencies, but also the blade-pass frequency (3P) and the sidebands of both the 1P and 3P signals. These sidebands are generated by the modulation of the primary frequencies by the roll motion, following the relationships $f_{\text{rotor}} \pm n \cdot f_{\text{roll}}$ and $3f_{\text{rotor}} \pm n \cdot f_{\text{roll}}$.

The 3P frequency appears at 0.279Hz, with adjacent peaks at 0.249Hz and 0.309Hz as the first sidebands. The 3P peak is dominant as it represents the direct passage of the three blades. Similar to the PSD analysis on blade normal loading in Subsection 5.2.5, the second sidebands of the 1P frequency are not prominent in the wake (0.153Hz or 0.033Hz). The second upper sideband of the 1P frequency coincides with the fourth lower sideband of the 3P oscillation; although both are small in the wake, their correspondence creates a noticeable but minor peak. The second lower sideband at 0.033Hz also coincides with the roll frequency, adding a small effect to its peak.

As established in Subsection 5.2.5, the most dominant frequencies were previously found to be the roll frequency, followed by the lower sideband of 1P, the upper sideband of 1P, and the 1P frequency, in decreasing order. A similar trend is observed here, with the roll frequency dominant, followed by the lower sideband at 0.06Hz. The difference lies in the order of the upper sideband and 1P frequencies, which switch in prominence.

Direct comparison of signal strength at different downstream locations is challenging, so a detailed spatial analysis is deferred to Figure 5.58. One clear trend is that the larger the signal power near the turbine, the faster it decays, since viscous effects and damping are stronger for stronger flow oscillations.

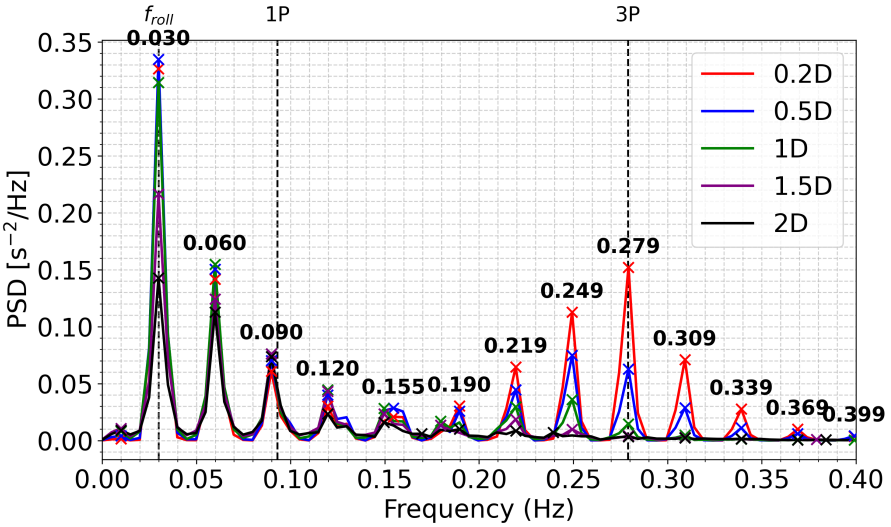

Figure 5.55: Spatially averaged PSD of vorticity at various downstream locations for case 3 (10°, 0.03 Hz, TSR 7).

Similar observations can be made for case 5 (Figure 5.56), which has a higher roll frequency of 0.05Hz. While the downstream trend in signal power is somewhat clearer, inconsistencies remain. It should be noted that the resolution of frequency is lowered by the fact that the usable-data time period being limited by the time of total simulation (500 seconds) and the threshold time for spin-up of simulation (250 seconds) which leaves a period of 250 seconds that is usable for frequency analysis. The shorter period results in lower frequency resolution (1/250 = 0.004 Hz) which can result in inaccurate peak locations and broadened peak bases, potentially obscuring closely spaced frequencies.

A comparison of case 3 in Figure 5.55 to case 5 in Figure 5.56 reveals the effects of roll frequency on the signals in the wake. Interestingly, and unlike the findings presented in Subsection 5.2.5, a higher roll frequency does not lead to an increase in power across all frequencies. Instead, a reduction in power is observed for all frequencies.

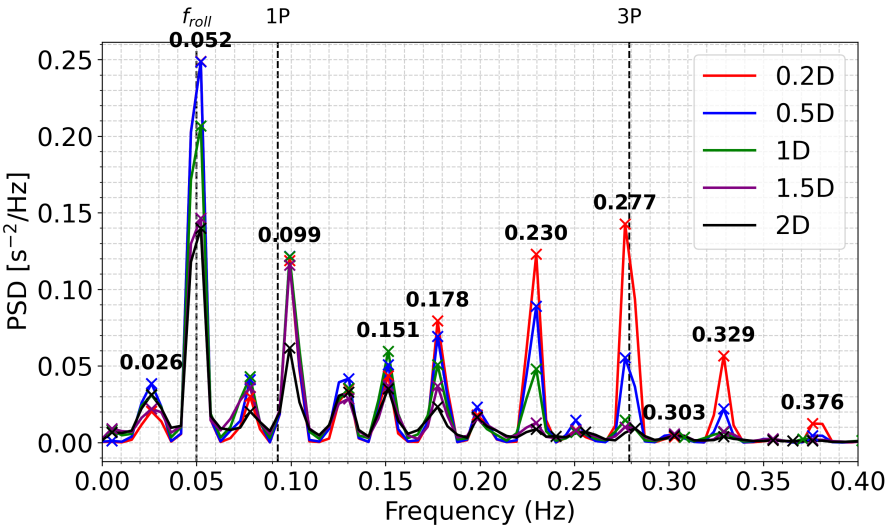

Figure 5.56: Spatially averaged PSD of vorticity at various downstream locations for case 5 (10°, 0.05 Hz, TSR 7).

The analysis of case 9 (Figure 5.57), representing the most unsteady motion with a TSR of 9, shows that the variation of signal power with downstream distance becomes more distinguishable. In general, the largest power is observed nearest to the rotor, and while some frequencies show minor increases further downstream, the signal does not significantly amplify. Lastly, the same frequency resolution issue is present, leading to broader peaks in the spectrum. To overcome this issue, it is recommended that the simulations are run for longer, which aids to increase the frequency resolution ($f = \frac{1}{T_{\text{total}}}$) where T_{total} is the total period of the simulation. This is also explained by the fact that the longer the simulation time is, more time is available to capture the small frequency differences among peaks (which correspond to high periods).

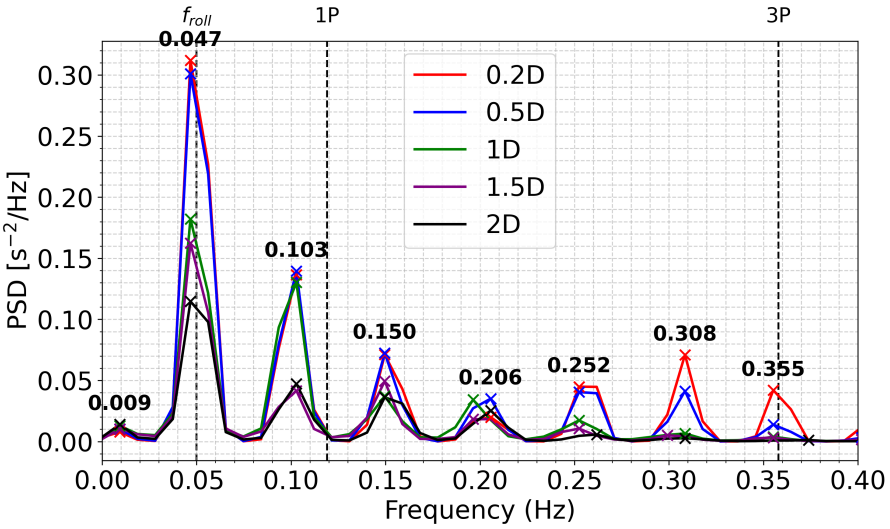

Figure 5.57: Spatially averaged PSD of vorticity at various downstream locations for case 9 (10°, 0.05 Hz, TSR 9).

The blade loading PSD analysis presented in Subsection 5.2.5 indicated that increasing the TSR leads to an amplification of power for signals related to the 1P frequency (1P and its sidebands), while the roll frequency power remained relatively unchanged.

Comparing Figure 5.56 with Figure 5.57 studies the effect of TSR on the signals within the wake. Interestingly, unlike in the blade loading, the power of the roll frequency in the wake increases with TSR. This could possibly be due to the fact that an increased TSR amplifies the influence of the roll motion within the wake. A direct comparison of the 1P frequencies is challenging due to the previously mentioned limitations. Furthermore, it is noteworthy that the 3P frequency and its sidebands show a reduction in power with increasing TSR.

Near-Wake Variation of Vorticity Signal

This section examines the streamwise evolution of signal power for key frequencies, which is critical for assessing potential fatigue impact on downstream turbines. Signal power is influenced by roll amplitude, TSR, the potential overlap of primary and sideband frequencies, and the sampling location. This analysis specifically concentrates on how signal power varies with downstream location.

The periodic rolling motion of the tower causes the entire system to oscillate. Consequently, wake vortex structures are periodically displaced at the roll frequency (f_{roll}). Conversely, the turbine's rotor speed dictates the shedding frequency of tip vortices, a phenomenon explained by the reduction in vortex pitch with increasing TSR in Subsection 5.3.4. When the roll frequency induces a periodic oscillation, it effectively modulates the characteristics of wake structures originating from the rotor frequency. This modulation results in the formation of sideband frequencies in the wake.

The downstream variation of baseline frequencies, including roll, 1P, and 3P frequencies, is presented for each roll case in Figure 5.58.

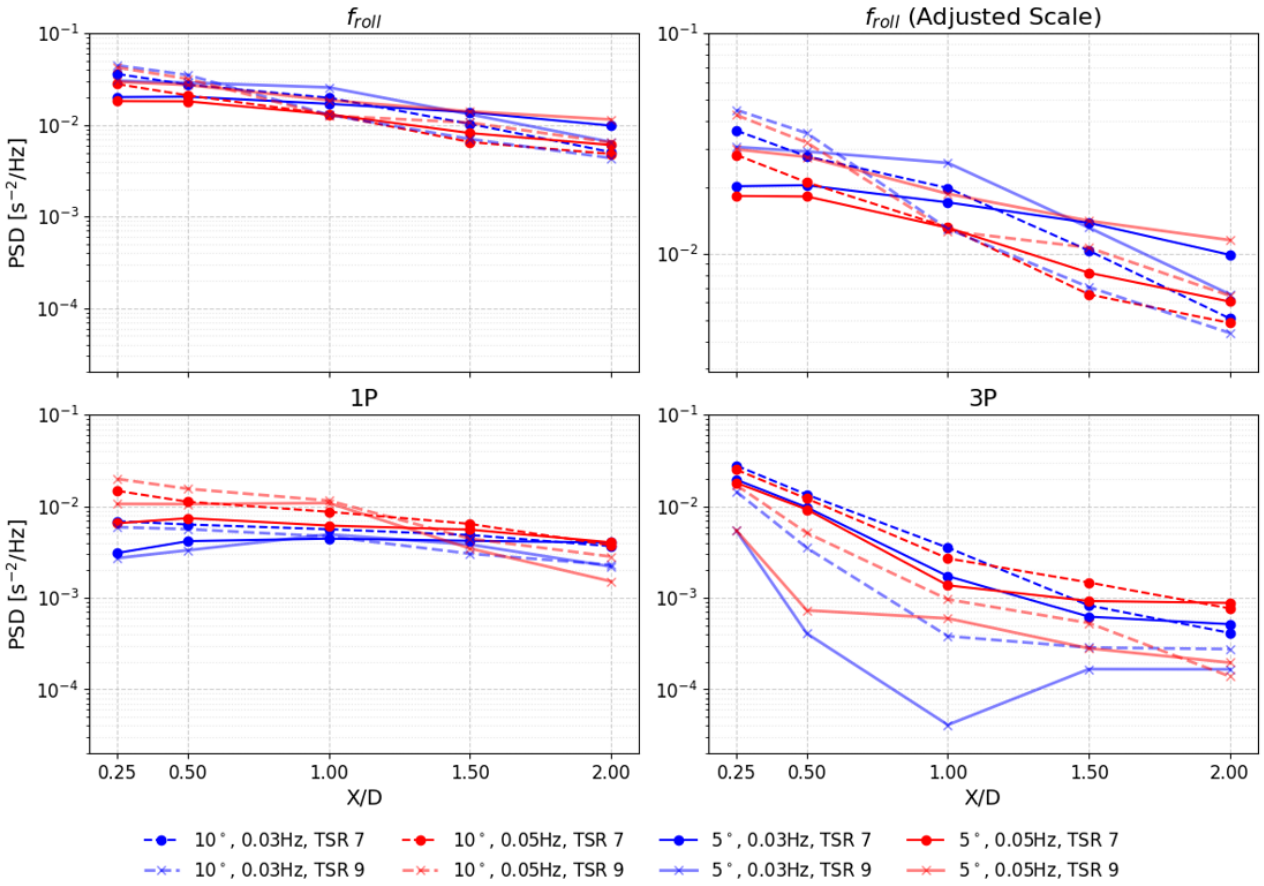

Figure 5.58: Downstream power variation of roll, 1P, and 3P frequencies of each roll case.

The downstream variation of the roll frequency is depicted in the top row of Figure 5.58. The top-right plot utilizes a distinct scale to enhance the clarity of the top-left plot. The results consistently indicate that the roll frequency power is highest in the immediate near-wake and exhibits a continuous decay with increasing downstream distance across all cases. Furthermore, the roll frequency maintains the largest power, a characteristic preserved even at more distant downstream locations. This finding aligns with observations made for blade loading in Subsection 5.2.5. While the 1P frequency in blade loading was found to have very low power, a similar relative insignificance is observed here compared to the roll frequency. However, a comprehensive comparison necessitates examining the 1P frequency alongside its sideband frequencies.

A key finding related to the impact of roll amplitude on the roll frequency is observed. For TSR 7 cases (non-faded lines), the $10°$ amplitude configurations (dashed lines) initially exhibit higher power but decay more rapidly, eventually falling below the $5°$ cases (solid lines). Conversely, for TSR 9 (faded lines) scenarios, the $5°$ cases consistently maintain higher signal power across all measured locations. TSR itself also exerts an influence on the downstream variation of roll frequency, a finding consistent with the observation that TSR amplifies roll effects in the wake, as previously detailed in Subsection 5.3.4.

The 1P frequency exhibits more complex behavior than a simple decay. For several cases, particularly at TSR 7 (non-faded), its PSD does not monotonically decrease but either remains high or slightly increases before eventually decaying. This suggests the persistence of large-scale coherent motions, characterized by the 1P frequency, within the near-wake region. Conversely, the 3P frequency plot reveals a rapid decay. This signal, associated with individual tip vortex structures, dissipates quickly as these small-scale vortices break down. Notably, TSR 7 cases (non-faded) demonstrate significantly higher 3P energy than TSR 9 (faded) cases, indicating that operation at a lower TSR generates stronger initial vortex structures. The effect of roll amplitude on the 3P signal is also evident, with lower amplitude cases generally possessing less power, though this trend may reverse further downstream.

Among the investigated variables, TSR emerges as the dominant factor influencing both the initial and downstream energy of these baseline frequencies. This dominance is anticipated for 1P and 3P frequencies, given their direct relationship with TSR. Specifically, TSR 7 cases demonstrate substantially higher 1P energy across the entire measured domain compared to TSR 9 cases. This implies that lower TSR operation, often associated with a higher thrust coefficient, generates a more dominant and persistent rotational signature within the wake.

Figure 5.59 presents the downstream variation of the first upper and lower sideband frequencies of both the 1P and 3P frequencies for each roll case.

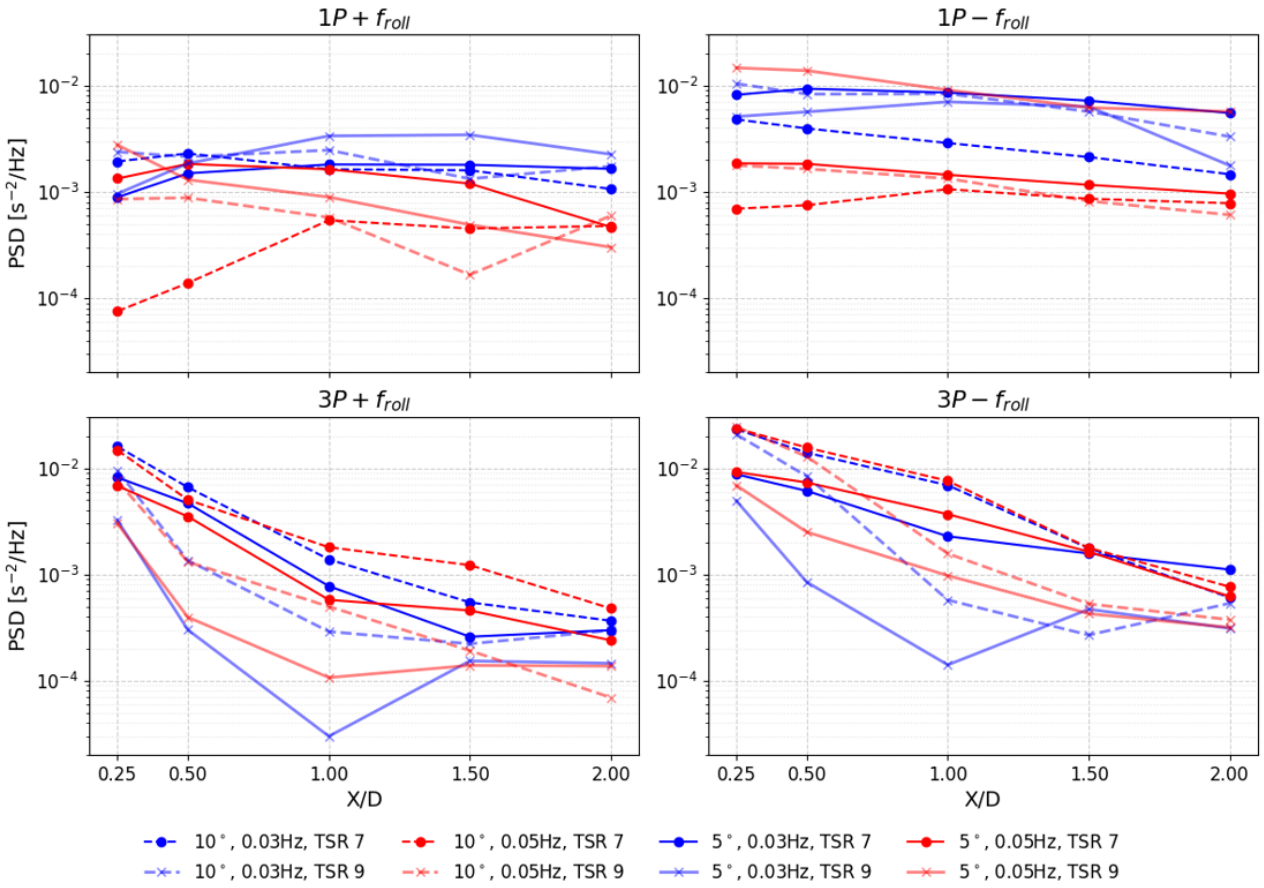

Figure 5.59: Downstream power variation of 1P and 3P first upper and lower sideband frequencies of each roll case.

Figure 5.59 indicates that the downstream variation of the sideband frequencies is largely determined by the variation of their respective parent rotor frequencies (1P or 3P). Consequently, the 1P sideband frequencies are preserved longer compared to the 3P sideband frequencies.

Studying the magnitudes of the upper and lower sideband frequencies of the 1P frequency (top-left and top-right of subsubsection 5.2.2, respectively), it is evident that the wake signals do not exhibit the same trend as the blade loading. In the wake, the sideband frequencies possess significantly lower power compared to their parent frequencies (1P and 3P), which was the opposite behavior observed at the blade for loading. What remains consistent, however, is that on average, the lower sideband frequency of 1P generally has a higher power than the upper sideband frequency of 1P, a finding also noted in Subsection 5.2.5.

Summarizing the important points; the roll frequency consistently exhibited the highest power, especially in the near-wake, decaying but remaining dominant downstream, with its behavior influenced by both roll amplitude and TSR. The 1P frequency displayed more complex decay patterns, sometimes persisting or even increasing, indicative of coherent large-scale motions, while the 3P frequency, linked to individual tip vortices, decayed rapidly. TSR emerged as the dominant factor, significantly influencing the energy of 1P and 3P frequencies, with lower TSR leading to stronger and more persistent wake signatures. Sideband frequencies' downstream behavior mirrored that of their parent rotor frequencies, with 1P sidebands persisting longer than 3P sidebands. Notably, unlike blade loading studied in Subsection 5.2.5, wake sideband frequencies possessed significantly less power than their parent frequencies, though the lower 1P sideband generally maintained higher power than its upper counterpart similar to the blade loading results.

6

Conclusions and Recommendations

This study presented a comprehensive numerical investigation into the blade loading and aerodynamic effects of imposed roll motion on a floating offshore wind turbine. Using the high-fidelity GPU-resident Large-Eddy Simulation code GRASP coupled with the aero-servo-hydro-elastic tool OpenFAST, the work examined the impact of varying roll amplitudes, roll frequencies, and turbine tip-speed ratios (TSRs) on the IEA 15 MW reference turbine. The objective was to establish a fundamental understanding of these phenomena, which remain underexplored compared to other platform motions.

This chapter begins by summarizing the study's key findings in Section 6.1, directly addressing the research questions posed in Section 2.3. Following this summary, Section 6.2 provides recommendations for guiding future research that builds upon this study's understanding of roll motion effects on blade loading and wake aerodynamics.

6.1 Conclusions

The results demonstrate that roll motion transforms the blade loading from the steady, azimuthally uniform state of a bottom-fixed turbine to an unsteady and azimuthally asymmetric condition. Unlike the constant loads experienced by a bottom-fixed turbine in uniform inflow, a rolling turbine is subjected to significant load fluctuations at both the roll frequency and the 1P frequency. These fluctuations produce a clear asymmetry in the rotor plane loading. For the normal force, the asymmetry occurs between the upper and lower halves of the rotor, with larger variations in the upper half due to the roll center being located at the tower base, which causes blades in the upper rotor disk to experience greater induced velocity. Tangential force asymmetry is lateral across the rotor plane, with loads increasing on one side and decreasing on the other depending on the roll direction. Power Spectral Density analysis further reveals that roll motion introduces powerful roll and 1P sideband frequencies at the blade loading spectrum. While the 1P frequency remains present, it is relatively weak compared to these signals. The sideband frequencies arise from the non-linear tangential velocity induced by rolling. The dominance of the roll frequency peak is attributed to a feedback loop between thrust variation and the upstream induction zone, which produces a velocity deficit oscillating at the same frequency as the roll.

The amplitude and frequency of roll motion influence the severity of these unsteady load fluctuations. Increasing roll amplitude consistently increases the magnitude of both normal and tangential load variations across the roll cycle, raising the standard deviation of the loads and concentrating load peaks in specific azimuthal regions of the rotor. Higher roll frequency also amplifies load fluctuations and increases their standard deviation, but tends to distribute them more uniformly around the

azimuth rather than concentrating them. Rotor speed, expressed as TSR, acts as an important modulator of these effects. Increasing TSR from 7 to 9 amplifies the absolute magnitude of roll-induced fluctuations, particularly in the outboard blade sections, and alters the mean loading trends by raising the mean normal force while slightly reducing the mean tangential force due to a smaller average angle of attack. At TSR 7, higher angles of attack make the blades more susceptible to drag-induced drops in tangential load during certain roll phases, while at TSR 9, tangential load fluctuations remain entirely above the bottom-fixed baseline.

These changes in blade loading have consequences on the near-wake. The stable, well-defined helical vortex system characteristic of a bottom-fixed turbine is replaced by a highly oscillatory, corkscrew-like wake with significant lateral and vertical motion that mirrors the turbine's own movement. The unsteady blade loading imprints directly onto the shed vorticity, accelerating wake breakdown. Variations in vortex strength and spacing promote instabilities, vortex pairing, and a faster transition to disorganized turbulence. Roll motion also appears to generate large-scale lateral and vertical induced velocity fields absent in the bottom-fixed case, possibly indicating that the turbine drags a volume of surrounding air as it moves. The streamwise velocity deficit varies more strongly in the upper half of the wake, consistent with the larger blade load variations occurring there. Spectral analysis of the wake shows that, unlike in blade loading, the 1P frequency is significant relative to the roll and sideband frequencies, and additional components such as 3P and its sidebands are also present.

The amplitude and frequency of roll motion influence the stability and breakdown of the near-wake. Larger amplitudes produce more pronounced lateral wake oscillations, accelerating the fragmentation of root vortices and intensifying tip–root vortex interactions. Higher roll frequencies lead to shorter-wavelength perturbations into the wake, compacting vortex structures and promoting more frequent vortex pairing, further hastening the decay of coherent wake patterns. Both higher amplitude and frequency result in a more disturbed wake, with the root vortex system breaking down into discrete pockets of high vorticity and tip vortices pairing earlier, weakening the structures enclosing the wake.

TSR amplifies the influence of roll motion on the near-wake in much the same way it amplifies blade loading variations. Higher TSR strengthens the shed helical vortices due to increased normal loads and reduces their spacing (pitch), bringing them into closer proximity and making them more prone to instability. This promotes earlier vortex pairing and wake breakdown compared to the same roll motion at lower TSR. Signals identified in the blade loading propagate downstream into the wake, with higher TSR increasing the power of the roll frequency component. While the 3P frequency, linked to individual blade passages, decays rapidly downstream, both the roll and 1P frequencies persist further, confirming that TSR intensifies the influence of roll motion on downstream flow dynamics.

6.2 Recommendations

The present work focused on the near-wake region. It is crucial to extend the computational domain to analyze how the asymmetric wake structures identified herein evolve into the far-wake. A far-wake study would enable an assessment of the impact on power production and fatigue loading for downstream turbines within a wind farm layout. Several wake characteristics remain to be explored, as they do not have sufficient time to manifest their influence within the near-wake. For example, the influence of roll motion on the wake expansion rate or wake deflection cannot be conclusively determined through a near-wake analysis, necessitating a far-wake study. These two characteristics of the wake are crucial for the understanding required for wind farm layout and operational optimization.

Furthermore, the current analysis primarily explained the observed phenomena with reference to the kinematics of the rolling turbine. A logical extension involves conducting a detailed acceleration analysis to investigate the inertial effects of roll on aerodynamic loading and the subsequent wake development. Discrepancies noted during this study between the kinematic results and those obtained from the numerical simulation have been attributed to the presence of inertial effects in the numerical setup, which the kinematic study ignored. An extension of the kinematic analysis to include accelerations would therefore serve to better understand the differences between the two methods. Similarly, the initial kinematics study identified a small but potentially significant axial velocity component induced by the roll motion. A more detailed investigation into this component is warranted to fully understand its implications for blade loading distribution and the resulting wake structure.

Regarding specifically the findings of the results, the lateral velocity component observed in Subsection 5.3.3 was an unpredicted finding of this study. Although an explanation has been put forward, suggesting that the turbine drags a volume of air as it rolls, thereby inducing lateral velocities in the wake, the reason for the persistence of this lateral velocity at a high magnitude over a significant duration has not yet been fully understood. An alternative explanation is that this effect may be due to the rotor moving out of the horizontal plane of reference. This can be tested with a near-wake analysis of a swaying turbine. If the same lateral velocities persist, then the explanation based on the dragging of air by the turbine would be confirmed as true. If this phenomenon is only observed for rolling motions, then the latter suggestion is supported. Another possible study that could aid in this understanding is an investigation of the near-wake of a floating turbine undergoing sway motions. Should the effect be related to the dragging of air, this phenomenon is not completely understood, and its implications for the far-wake, such as the lateral distortion of the wake, are yet to be further studied.

References

[1] Abkar, M., Sharifi, A., and Porté-Agel, F. (2016). Wake flow in a wind farm during a diurnal cycle. *Journal of Turbulence*, vol. 17:pp. 1–22. DOI:10.1080/14685248.2015.1127379.

[2] Angelou, N., Mann, J., and Dubreuil-Boisclair, C. (2023). Revealing inflow and wake conditions of a 6mw floating turbine. DOI:10.5194/wes-2023-37.

[3] Bastankhah, M. and Porté-Agel, F. (2014). A new analytical model for wind-turbine wakes. *Renewable Energy*, vol. 70:pp. 116–123. DOI:10.1016/j.renene.2014.01.002.

[4] Behrens de Luna, R., Marten, D., Barlas, T., Horcas, S. G., Ramos-García, N., Li, A., and Paschereit, C. (2022). Comparison of different fidelity aerodynamic solvers on the iea 10 mw turbine including novel tip extension geometries. *Journal of Physics Conference Series*, vol. 2265:pp. 032002.

[5] Belvasi, N., Conan, B., Schliffke, B., Perret, L., Desmond, C., Murphy, J., and Aubrun, S. (2022). Far-wake meandering of a wind turbine model with imposed motions: An experimental s-piv analysis. *Energies*. DOI:10.3390/en15207757.

[6] Blackmore, T., Batten, W. M. J., and Bahaj, A. S. (2014). Influence of turbulence on the wake of a marine current turbine simulator. *Proceedings. Mathematical, physical, and engineering sciences*, vol. 470. DOI:10.1098/rspa.2014.0331.

[7] Blazek, J. (2015). Chapter 7 - turbulence modeling. In *Computational Fluid Dynamics: Principles and Applications (Third Edition)*, pages 213–252. Butterworth-Heinemann, third edition edition. DOI:https://doi.org/10.1016/B978-0-08-099995-1.00007-5.

[8] Bouhelal, A., Hamlaoui, M. N., and Smaïli, A. (2024). Impact of surface roughness on the aerodynamic efficiency of wind turbines: A new cfd-based correlation. *Journal of Applied Fluid Mechanics*, pages pp. 438–449. DOI:10.47176/jafm.18.2.2830.

[9] Bouhelal, A., Smaïli, A., Guerri, O., and Masson, C. (2017). Comparison of bem and full navier-stokes cfd methods for prediction of aerodynamics performance of hawt rotors. DOI:10.1109/IRSEC.2017.8477247.

[10] Böing, S. J., Jonker, H. J. J., Siebesma, A. P., and Grabowski, W. W. (2012). Influence of the subcloud layer on the development of a deep convective ensemble. *Journal of the Atmospheric Sciences*, vol. 69(9):pp. 2682–2698. DOI:10.1175/JAS-D-11-0317.1.

[11] Combette, R. (2023). Large-eddy simulation of a floating offshore wind turbine with imposed motion. pages pp. 4–5. `https://resolver.tudelft.nl/uuid:c89f950b-22f6-4fb3-a390-8039237f15f8`.

[12] Davies, P. (1973). Structure of turbulence. *Journal of Sound and Vibration*, vol. 28(3):pp. 513–526. DOI:10.1016/S0022-460X(73)80038-0.

[13] Deardorff, J. W. (1970). A numerical study of three-dimensional turbulent channel flow at large reynolds numbers. *Journal of Fluid Mechanics*, vol. 41(2):pp. 453–480. DOI:10.1017/S0022112070000691.

[14] Duan, L., Sun, Q., He, Z., and Li, G. (2022). Wake topology and energy recovery in floating horizontal-axis wind turbines with harmonic surge motion. *Energy*, vol. 260(9). ISSN:0360-5442. 124907. DOI:10.1016/j.energy.2022.124907.

[15] en:former (2023). Floating offshore wind pipeline grows to 244 gw. Date accessed 06 February 2025.

[16] Farrugia, R., Sant, T., and Micallef, D. (2016). A study on the aerodynamics of a floating wind turbine rotor. *Renewable Energy*, vol. 86. ISSN:0960-1481.770-784.DOI:10.1016/j.renene.2015.08.063.

[17] Franke, J., Hirsch, C., Jensen, A., Krüs, H., Schatzmann, M., Westbury, P., Miles, S., Wisse, J., and Wright, N. (2004). Recommendations on the use of cfd in wind engineering. *Proceedings of the International Conference on Urban Wind Engineering and Building Aerodynamics*.

[18] Fu, S., Jin, Y., Zheng, Y., and Chamorro, L. P. (2019). Wake and power fluctuations of a model wind turbine subjected to pitch and roll oscillations. *Applied Energy*, vol. 253:pp. 113605. DOI:10.1016/j.apenergy.2019.113605.

[19] Gaertner, E., Rinker, J., Sethuraman, L., Zahle, F., Anderson, B., Barter, G., Abbas, N., Meng, F., Bortolotti, P., Skrzypinski, W., Scott, G., Feil, R., Bredmose, H., Dykes, K., Shields, M., Allen, C., and Viselli, A. (2020). Definition of the iea 15-megawatt offshore reference wind. National Renewable Energy Laboratory.

[20] Gambuzza, S. and Ganapathisubramani, B. (2023). The influence of free stream turbulence on the development of a wind turbine wake. *Journal of Fluid Mechanics*, vol. 963. DOI:10.1017/jfm.2023.302.

[21] Garcia, L., Conan, B., Aubrun, S., Perret, L., Piquet, T., Raibaudo, C., and Schliffke, B. (2022). Experimental analysis of the wake meandering of a floating wind turbine under imposed surge motion. *Journal of Physics: Conference Series*, vol. 2265:pp. 042003. DOI:10.1088/1742-6596/2265/4/042003.

[22] Gilbert, C., Messner, J., Pinson, P., Trombe, P.-J., Verzijlbergh, R., Dorp, P., and Jonker, H. (2019). Statistical post-processing of turbulence-resolving weather forecasts for offshore wind power forecasting. *Wind Energy*, vol. 23. DOI:10.1002/we.2456.

[23] Global Wind Energy Council (GWEC) (2022). Global offshore wind report 2022. Date accessed 06 February 2025.

[24] Goit, J. and Meyers, J. (2015). Optimal control of energy extraction in wind-farm boundary layers. *Journal of Fluid Mechanics*, vol. 768:pp. 5–50. DOI:10.1017/jfm.2015.70.

[25] Hansen, M. O. L. (2008). *Aerodynamics of Wind Turbines*. Routledge, 2nd edition.

[26] Haslum, H., Marley, M., Navalkar, S., Skaare, B., Maljaars, N., and Andersen, H. (2022). Roll–yaw lock: Aerodynamic motion instabilities of floating offshore wind turbines. *Journal of Offshore Mechanics and Arctic Engineering*, vol. 144:pp. 1–13. DOI:10.1115/1.4053697.

[27] Heus, T., van Heerwaarden, C., Jonker, H., Siebesma, A., Axelsen, S., Dries, K., Geoffroy, O., Moene, A., Pino Gonzalez, D., Roode, S., and Arellano, J. (2010a). Formulation of and numerical studies with the dutch atmospheric large-eddy simulation (dales). *Geoscientific Model Development Discussions*, vol. 3. DOI:10.5194/gmdd-3-99-2010.

[28] Heus, T., van Heerwaarden, C. C., Jonker, H. J. J., Pier Siebesma, A., Axelsen, S., van den Dries, K., Geoffroy, O., Moene, A. F., Pino, D., de Roode, S. R., and Vilà-Guerau de Arellano, J. (2010b). Formulation of the dutch atmospheric large-eddy simulation (dales) and overview of its applications. *Geoscientific Model Development*, vol. 3:pp. 415–444. DOI:10.5194/gmd-3-415-2010.

[29] Hintz, M. (2016). Theoretical analysis and large-eddy simulations of the propagation of land-surface heterogeneity in the atmosphere. `https://www.tr32db.uni-koeln.de/data.php?dataID=1320`.

[30] Hodgkin, A., Laizet, S., and Deskos, G. (2022). Numerical investigation of the influence of shear and thermal stratification on the wind turbine tip-vortex stability. *Wind Energy*, vol. 25. DOI:10.1002/we.2728.

[31] Hodgson, E., Madsen, M., Troldborg, N., and Andersen, S. (2022). Impact of turbulent time scales on wake recovery and operation. *Journal of Physics: Conference Series*, vol. 2265:pp. 022022. DOI:10.1088/1742-6596/2265/2/022022.

[32] Hodgson, E. L., Madsen, M. H. A., and Andersen, S. J. (2023a). Effects of turbulent inflow time scales on wind turbine wake behavior and recovery. *Physics of Fluids*, vol. 35(9):pp. 095125. DOI:10.1063/5.0162311.

[33] Hodgson, E. L., Madsen, M. H. A., and Andersen, S. J. (2023b). Effects of turbulent inflow time scales on wind turbine wake behavior and recovery. *Physics of Fluids*, vol. 35(9). ISSN:1070-6631. 095125. DOI:10.1063/5.0162311.

[34] Holtslag, M. (2016). Far offshore wind conditions in scope of wind energy. vol. 2767. DOI:10.4233/uuid:3c66f401-6cff-4273-aa49-df4274ba767f.

[35] International Renewable Energy Agency (IRENA) (2021). Tracking the impacts of innovation: Offshore wind as a case study. Date accessed 06 February 2025.

[36] International Renewable Energy Agency (IRENA) (2022). World energy transitions outlook. Date accessed 06 February 2025.

[37] International Renewable Energy Agency (IRENA) (2024). Floating offshore wind outlook. Date accessed 06 February 2025.

[38] Ivanell, S., Mikkelsen, R., Sørensen, J. N., and Henningson, D. (2010). Stability analysis of the tip vortices of a wind turbine. *Wind Energy*, vol. 13:pp. 705–715. DOI:10.1002/we.391.

[39] Janssen, M. (2023). On the influence of turbulent inflow conditions on the wakes of floating offshore wind turbines. pages pp. 2–8. `https://resolver.tudelft.nl/uuid:d428731d-896d-41d2-a291-2b17a4f55c34`.

[40] Jerôme, S., Griffith, E. J., Post, F. H., and Jonker, H. J. (2012). High-performance simulations of turbulent clouds on a desktop pc: Exploiting the gpu. *Bulletin of the American Meteorological Society*, vol. 93:pp. 307–314. DOI:10.1175/BAMS-D-11-00059.1.

[41] Jha, P. K., Churchfield, M. J., Moriarty, P. J., and Schmitz, S. (2014a). Guidelines for volume force distributions within actuator line modeling of wind turbines on large-eddy simulation-type grids. *Journal of Solar Energy Engineering*, vol. 136(3):pp. 031003. DOI:10.1115/1.4026252.

[42] Jha, P. K., Churchfield, M. J., Moriarty, P. J., and Schmitz, S. (2014b). Guidelines for volume force distributions within actuator line modeling of wind turbines on large-eddy simulation-type grids. *Journal of Solar Energy Engineering*, vol. 136(3):pp. 031003. DOI:10.1115/1.4026252.

[43] Jonkman, J., Hayman, G., Jonkman, B., Damiani, R., and Murray, R. (2017). Aerodyn v15 user's guide and theory manual.

[44] Khedr, A. and Castellani, F. (2025). Large eddy simulation of the effect of blade rotation on laminar separation bubbles in horizontal axis wind turbines. *Physics of Fluids*, vol. 37(4):pp. 044109. DOI:10.1063/5.0261925.

[45] Kopperstad, K., Kumar, R., and Shoele, K. (2020). Aerodynamic characterization of barge and spar type floating offshore wind turbines at different sea states. *Wind Energy*, vol. 23. DOI:10.1002/we.2547.

[46] Krishnendu, G. S. (2025). Understanding the cfl number: Physical significance and best practices. Date accessed 17 May 2025.

[47] Larsen, G., Madsen, H., Thomsen, K., and Larsen, T. (2008). Wake meandering: A pragmatic approach. *Wind Energy*, vol. 11:pp. 377–395. DOI:10.1002/we.267.

[48] Lee, S., Churchfield, M., Moriarty, P., Jonkman, J., and Michalakes, J. (2013). A numerical study of atmospheric and wake turbulence impacts on wind turbine fatigue loadings. *Journal of Solar Energy Engineering*, vol. 135. DOI:10.1115/1.4023319.

[49] Li, Z., Dong, G., and Yang, X. (2022). Onset of wake meandering for a floating offshore wind turbine under side-to-side motion. *Journal of Fluid Mechanics*, vol. 934. DOI:10.1017/jfm.2021.1147.

[50] Lilly, D. K. (1992). A proposed modification of the germano subgrid-scale closure method. *Physics of Fluids A: Fluid Dynamics*, vol. 4(3):pp. 633–635. DOI:10.1063/1.858280.

[51] Liu, M., Liang, Z., and Liu, H. (2022). Numerical investigations of wake expansion in the offshore wind farm using a large eddy simulation. *Energies*, vol. 15:pp. 2022. DOI:10.3390/en15062022.

[52] Lundquist, K., Chow, F., and Lundquist, J. (2010). An immersed boundary method for the weather research and forecasting model. *Monthly Weather Review*, vol. 138:pp. 796–817. DOI:10.1175/2009MWR2990.1.

[53] Martínez-Tossas, L., Churchfield, M., and Meneveau, C. (2017). Optimal smoothing length scale for actuator line models of wind turbine blades based on gaussian body force distribution: Wind energy, actuator line model. *Wind Energy*, vol. 20. DOI:10.1002/we.2081.

[54] Martínez-Tossas, L. A. and Meneveau, C. (2019). Filtered lifting line theory and application to the actuator line model. *Journal of Fluid Mechanics*, vol. 863:pp. 269–292. DOI:10.1017/jfm.2018.994.

[55] McKay, P., Carriveau, R., Ting, D. S., and Newson, T. (2012). *Turbine Wake Dynamics*. https://www.intechopen.com/chapters/40860#B5.

[56] Meneveau, C. (2016). Turbulence: Subgrid-scale modeling. Date accessed 23 May 2025.

[57] Messmer, T., Hölling, M., and Peinke, J. (2024). Enhanced recovery caused by nonlinear dynamics in the wake of a floating offshore wind turbine. *Journal of Fluid Mechanics*, vol. 984. DOI:10.1017/jfm.2024.175.

[58] Nanos, E. M., Bottasso, C. L., Tamaro, S., Manolas, D. I., and Riziotis, V. A. (2022). Vertical wake deflection for floating wind turbines by differential ballast control. *Wind Energy Science*, vol. 7(4):pp. 1641–1660. DOI:10.5194/wes-7-1641-2022.

[59] National Renewable Energy Laboratory (2024). Openfast. Date accessed 01 February 2025.

[60] Parinam, A., Bénard, P., Terzi, D., and Vire, A. (2024). Exploring the impact of different inflow conditions on wind turbine wakes using large-eddy simulations. *Journal of Physics: Conference Series*, vol. 2767:pp. 92–98. DOI:10.1088/1742-6596/2767/9/092098.

[61] Porchetta, S., Temel, O., Muñoz-Esparza, D., Reuder, J., Monbaliu, J., Beeck, J., and van Lipzig, N. (2019). A new roughness length parameterization accounting for wind–wave (mis)alignment. *Atmospheric Chemistry and Physics*, vol. 19:pp. 6681–6700. DOI:10.5194/acp-19-6681-2019.

[62] Raibaudo, C., Piquet, T., Schliffke, B., Conan, B., and Perret, L. (2022). Pod analysis of the wake dynamics of an offshore floating wind turbine model. *Journal of Physics: Conference Series*, vol. 2265:pp. 022085. DOI:10.1088/1742-6596/2265/2/022085.

[63] Ramos-García, N., Kontos, S., Pegalajar-Jurado, A., González Horcas, S., and Bredmose, H. (2022). Investigation of the floating iea wind 15 mw rwt using vortex methods part i: Flow regimes and wake recovery. *Wind Energy*, vol. 25(3):pp. 468–504. DOI:https://doi.org/10.1002/we.2682.

[64] Rozema, W., Bae, H. J., Moin, P., and Verstappen, R. (2015). Minimum-dissipation models for large-eddy simulation. *Physics of Fluids*, vol. 27(8):pp. 085107. DOI:10.1063/1.4928700.

[65] Santoni, C., García-Cartagena, E., Ciri, U., Zhan, L., Iungo, G., and Leonardi, S. (2020). One-way mesoscale-microscale coupling for simulating a wind farm in north texas: Assessment against scada and lidar data. *Wind Energy*, vol. 23. DOI:10.1002/we.2452.

[66] Schalkwijk, J., Jonker, H. J. J., Siebesma, A. P., and Bosveld, F. C. (2015). A year-long large-eddy simulation of the weather over cabauw: An overview. *Monthly Weather Review*, vol. 143:pp. 828–844. DOI:10.1175/MWR-D-14-00293.1.

[67] SCHEDMD (2024). Documentation. Date accessed 18 May 2025.

[68] Schepers, G., van Dorp, P., Verzijlbergh, R., Baas, P., and Jonker, H. (2021). Aeroelastic loads on a 10 mw turbine exposed to extreme events selected from a year-long large-eddy simulation over the north sea. *Wind Energy Science*, vol. 6:pp. 983–996. DOI:10.5194/wes-6-983-2021.

[69] Schliffke, B., Aubrun, S., and Conan, B. (2020). Wind tunnel study of a “floating” wind turbine’s wake in an atmospheric boundary layer with imposed characteristic surge motion. *Journal of Physics: Conference Series*, vol. 1618:pp. 062015. DOI: 10.1088/1742-6596/1618/6/062015.

[70] Schliffke, B., Conan, B., and Aubrun, S. (2024). Floating wind turbine motion signature in the far-wake spectral content – a wind tunnel experiment. *Wind Energy Science*, vol. 9:pp. 519–532. DOI:10.5194/wes-9-519-2024.

[71] Schmitt, F. G. (2007). About boussinesq’s turbulent viscosity hypothesis: historical remarks and a direct evaluation of its validity. *Comptes Rendus Mécanique*, vol. 335(9):pp. 617–627. DOI:https://doi.org/10.1016/j.crme.2007.08.004.

[72] Sheidani, A., Salavati, Dezfouli, S., Stabile, G., and Rozza, G. (2022). Assessment of urans and les methods in predicting wake shed behind a vertical axis wind turbine. DOI:10.48550/arXiv.2212.13076.

[73] Smagorinsky, J. (1963). General circulation experiments with the primitive equations: I. the basic experiment. *Monthly Weather Review*, vol. 91:pp. 99–164. DOI:10.1175/1520-0493(1963)091<0099:GCEWTP>2.3.CO;2.

[74] Sorensen, J. and Shen, W. Z. (2002). Numerical modeling of wind turbine wakes. *Journal of Fluids Engineering*, vol. 124:pp. 393. DOI:10.1115/1.1471361.

[75] Stanislawski, B. J., Thedin, R., Sharma, A., Branlard, E., Vijayakumar, G., and Sprague, M. A. (2023). Effect of the integral length scales of turbulent inflows on wind turbine loads. *Renewable Energy*, vol. 217:pp. 119218. DOI:10.1016/j.renene.2023.119218.

[76] Stanly, R., Martínez Tossas, L., Frankel, S., and Delorme, Y. (2022). Large-eddy simulation of a wind turbine using a filtered actuator line model. *Journal of Wind Engineering and Industrial Aerodynamics*, vol. 222:pp. 104868. DOI:10.1016/j.jweia.2021.104868.

[77] Stoevesandt, B., Schepers, G., Fuglsang, P., and Sun, Y. (2022). *Handbook of Wind Energy Aerodynamics*. `https://link.springer.com/referencework/10.1007/978-3-030-31307-4`.

[78] Stull, R. B. (1988). *An Introduction to Boundary Layer Meteorology*. Kluwer Academic Publishers. `https://www.academia.edu/41118210/An_Introduction_to_Boundary_Layer_Meteorology`.

[79] Taschner, E., Folkersma, M., A Martínez-Tossas, L., Verzijlbergh, R., and van Wingerden, J.-W. (2024). A new coupling of a gpu-resident large-eddy simulation code with a multiphysics wind turbine simulation tool. *Wind Energy*, vol. 27(11):pp. 1152–1172. DOI:https://doi.org/10.1002/we.2844.

[80] Thanh, T. T. and Kim, D.-H. (2016). A cfd study into the influence of unsteady aerodynamic interference on wind turbine surge motion. *Renewable Energy*, vol. 90:pp. 204–228. DOI:10.1016/j.renene.2015.12.013.

[81] The Intergovernmental Panel on Climate Change (IPCC) (2022). Climate change 2022: Mitigation of climate change. Date accessed 06 February 2025.

[82] Tran, T., Kim, D.-H., and Song, J. (2014). Computational fluid dynamic analysis of a floating offshore wind turbine experiencing platform pitching motion. *Energies*, vol. 7:pp. 5011–5026. DOI:10.3390/en7085011.

[83] Troldborg, N. (2009). Actuator line modeling of wind turbine wakes.

[84] TU Delft (2025). Delftblue documentation. Date accessed 09 May 2025.

[85] Uchida, T. (2020). Effects of inflow shear on wake characteristics of wind-turbines over flat terrain. *Energies*, vol. 13:pp. 3745. DOI:10.3390/en13143745.

[86] United Nations Framework Convention on Climate Change (UNFCCC) (2025). The paris agreement. Date accessed 06 February 2025.

[87] Vahidi, D. and Porté-Agel, F. (2024). Influence of incoming turbulent scales on the wind turbine wake: A large-eddy simulation study. *Physics of Fluids*, vol. 36. DOI:10.1063/5.0222372.

[88] van Bussel, G. and Bierbooms, W. (2004). Course offshore wind farm design oe 5662 - module 4 offshore wind climate. Date accessed 22 July 2025.

[89] Van Leeuwen, R. (2025). Tuning of a numerical model for a fowt with sinusoidal surge and pitch motion. (Unpublished master's thesis). Delft University of Technology.

[90] Vermeer, N.-J., Sørensen, J., and Crespo, A. (2003). Wind turbine wake aerodynamics. *Progress in Aerospace Sciences - PROG AEROSP SCI*, vol. 39:pp. 467–510. DOI:10.1016/S0376-0421(03)00078-2.

[91] Vollmer, L., Steinfeld, G., and Kühn, M. (2017). Transient les of an offshore wind turbine. *Wind Energy Science*, vol. 2:pp. 603–614. DOI:10.5194/wes-2-603-2017.

[92] Wei, N. J., El Makdah, A., Hu, J., Kaiser, F., Rival, D. E., and Dabiri, J. O. (2024). Wake dynamics of wind turbines in unsteady streamwise flow conditions. *Journal of Fluid Mechanics*, vol. 1000:pp. A66. DOI:10.1017/jfm.2024.999.

[93] Whiffle (2025). Aspire documentation, release 15.0.0.

[94] Wicker, L. and Skamarock, W. (2002). Time-splitting methods for elastic models using forward time schemes. *Monthly Weather Review - MON WEATHER REV*, vol. 130. DOI:10.1175/1520-0493(2002)130<2088:TSMFEM>2.0.CO;2.

[95] Wiegant, E. and Verzijlbergh, R. (2019). Grasp model description & validation report. `https://www.dutchoffshorewindatlas.nl/publications/reports/2019/12/05/whiffle-report---grasp-model-description-and-validation-report`.

[96] WindEurope (2024). Wind energy in europe: 2023 statistics and the outlook for 2024-2030. Date accessed 07 February 2025.

[97] Xie, S. and Archer, L. C. (2017). A numerical study of wind-turbine wakes for three atmospheric stability conditions. *Boundary-Layer Meteorology*, vol. 165. DOI:10.1007/s10546-017-0259-9.

[98] Xu, S., Zhuang, T., Zhao, W., and Wan, D.-C. (2023). Numerical investigation of aerodynamic responses and wake characteristics of a floating offshore wind turbine under atmospheric boundary layer inflows. *Ocean Engineering*, vol. 279:pp. 114527. DOI:10.1016/j.oceaneng.2023.114527.

[99] Yang, D., Meneveau, C., and Shen, L. (2014). Large-eddy simulation of offshore wind farm. *Physics of Fluids*, vol. 26. DOI:10.1063/1.4863096.

[100] Zhou, Y., Xiao, Q., Liu, Y., Incecik, A., Peyrard, C., Wan, D.-C., Pan, G., and Li, S. (2022). Exploring inflow wind condition on floating offshore wind turbine aerodynamic characterisation and platform motion prediction using blade resolved cfd simulation. *Renewable Energy*, vol. 182. DOI:10.1016/j.renene.2021.11.010.

Appendix A

Comparison of Kinematic and Numerical Blade Loading Parameters

The blade loading results obtained from the kinematic analysis and the numerical set-up are compared in Subsection 5.2.1. Complementary plots related to the parameters used in the computation of blade loading are provided in this Appendix. These plots have been used for the explanation of the differences and similarities in the two sources of blade loading.

While the reasoning for the differences observed in Figure A.1 and Figure A.2 have been explained thoroughly, more explanations are yet to be made.

Although the kinematic normal and tangential loading was found to be significantly larger than that of the loading obtained from the numerical set-up, the resultant velocity showed an opposite trend. This meant that significant part of the difference in loading was due to a larger angle of attack as seen by Figure A.1 which led to a shift in operational point of the blade that resulted in higher loading. Given that also the inflow axial velocity is over-estimated in the kinematic analysis due to the presence of the induction zone in the numerical set-up, this should result in a much larger resultant velocity for the kinematic analysis.

The reason for the opposite to be true is thought to be due to the way that the resultant velocity is computed and the presence of radial velocities induced by roll motion as was shown in Equation 5.10. The resultant velocity in the numerical set-up has been computed from the dynamic pressure which is influenced by any direction of velocity. An additional radial velocity simulated in the numerical set-up can lead to a higher dynamic pressure, which is simply not modeled by the kinematics. Given that the resultant velocity is directly obtained from the dynamic pressure, this component may also include the additional radial velocity causing it to be larger than the kinematic resultant velocity.

A solution to this may be subtracting the radial velocity obtained via kinematics from the resultant velocity of the numerical set-up which would not be ideal since the effects of kinematic assumptions would then be influencing the results of the numerical set-up. The second would be to find an OpenFAST parameter to output which filters the radial velocity from the net velocity at the blade, thus a 2-dimensional analysis can be made.

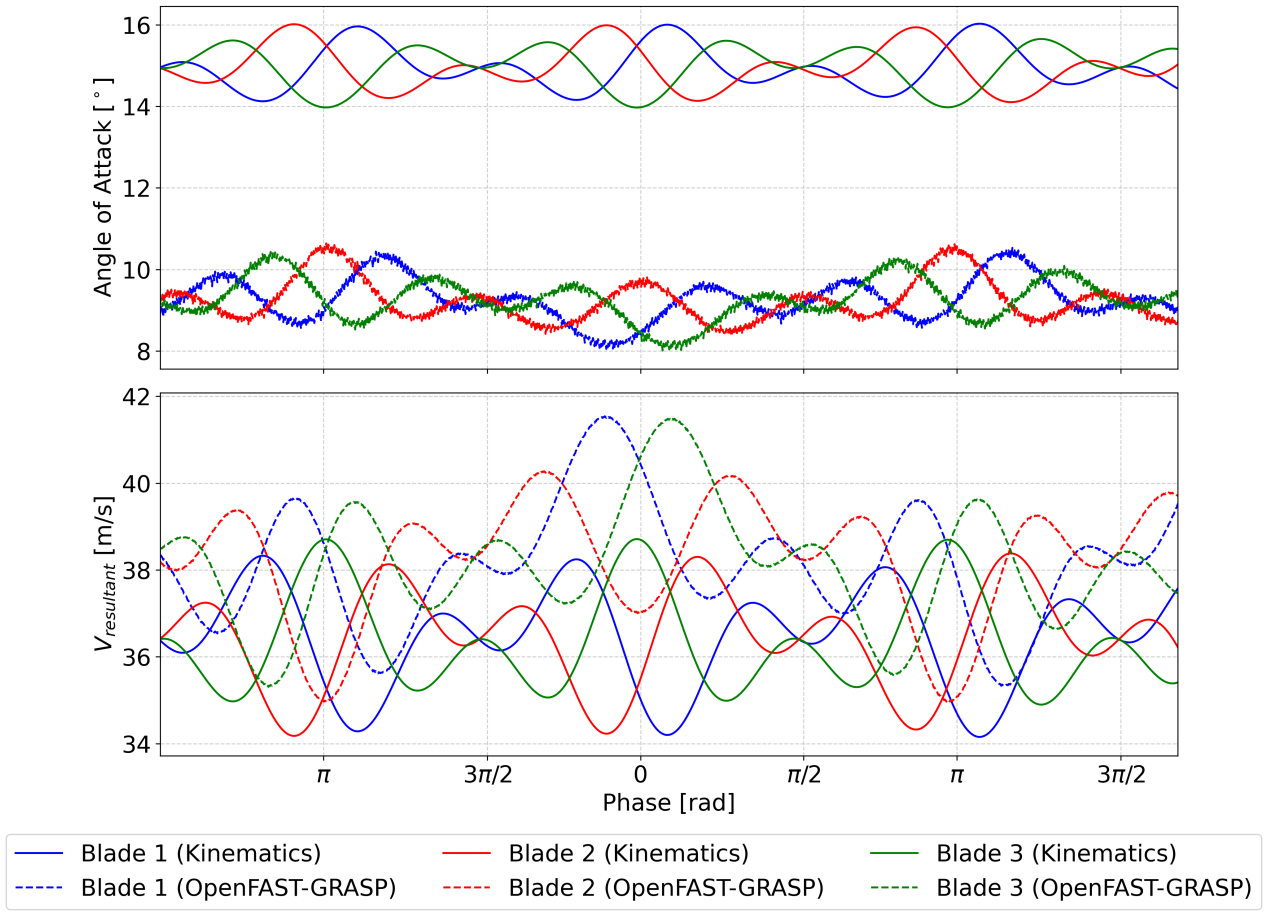

Figure A.1: Angle of attack and resultant velocity variation per blade in time at mid-span (0.5 r/R) for case 2 (5°, 0.03Hz, TSR 7).

Observing Figure A.2 shows that the peaks of the lift coefficient of the kinematic analysis are truncated. This is due to the airfoil operating at the maximum lift coefficient at that moment leading to a stagnation of this coefficient for a further increase in angle of attack.

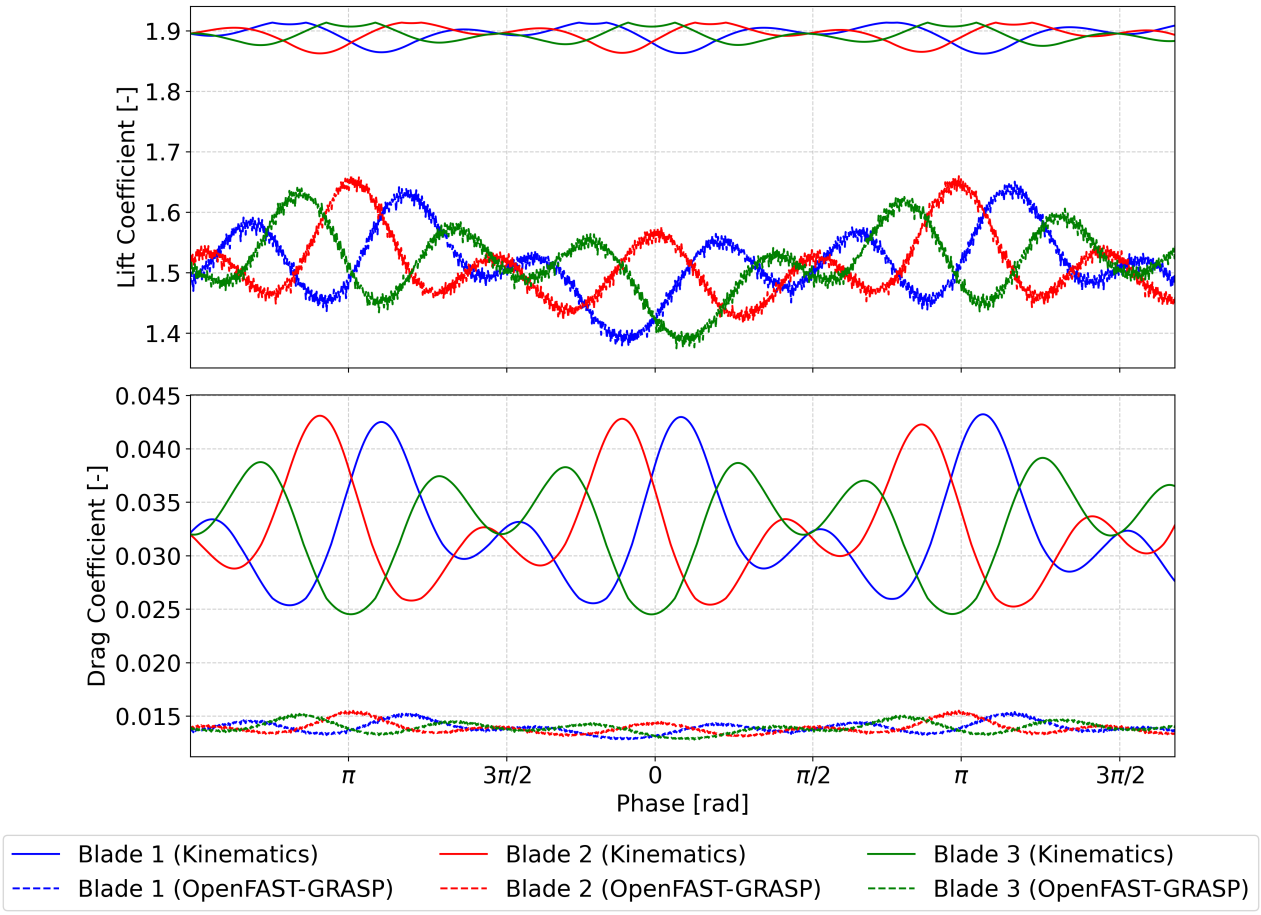

Figure A.2: Lift and drag coefficient variation per blade in time at mid-span (0.5 r/R) for case 2 (5°, 0.03Hz, TSR 7).

Appendix B

Q-Criterion Results

The plots of the Q-criterion study presented in Subsection 5.3.5 are given in this Appendix.

All Q-criterion plots were generated using a single iso-Q value of 3.5×10^{-3} s^{-2}. As discussed in Subsection 5.3.5 and reiterated here, this specific threshold primarily visualizes the strong vorticity near the turbine. Consequently, it fails to fully capture the entire downstream wake, particularly at the blade tips. This limitation arises because wake structures decay further downstream due to reduced circulation and viscous dissipation, causing their Q-values to fall below the selected visualization threshold. Attempts to plot with other Q-values did not yield improved overall visualizations of the complete wake structure. For visual clarity, the plots are colored to illustrate the distance from the viewer.

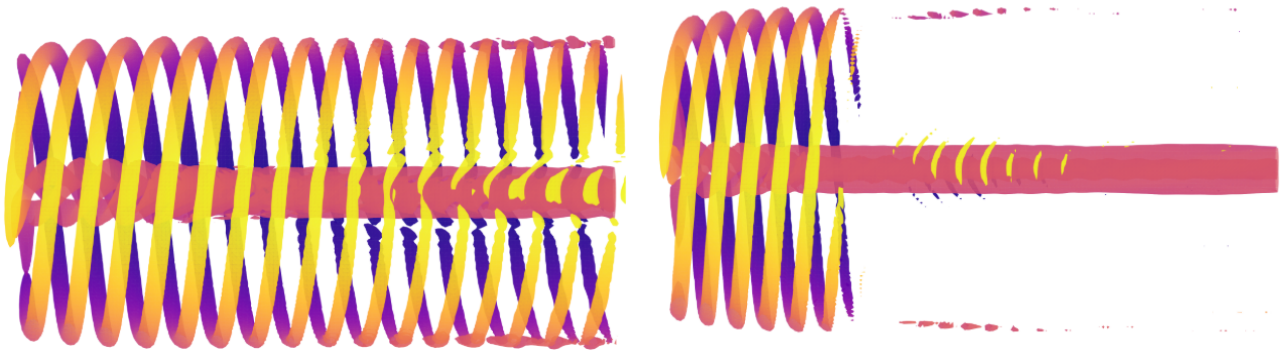

(a) Top-view Q-criterion (Q = 3.5×10^{-3} s^{-2}) of bottom-fixed case operating at TSR 7.

(b) Top-view Q-criterion (Q = 3.5×10^{-3} s^{-2}) of bottom-fixed case operating at TSR 9.

Figure B.1: Top-view Q-criterion (Q = 3.5×10^{-3} s^{-2}) of bottom-fixed cases operating at TSR 7 and 9.

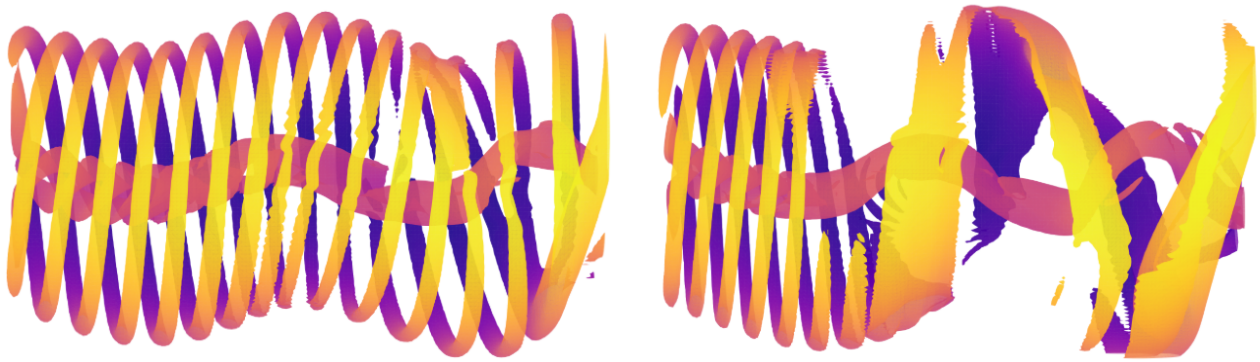

(a) Top-view Q-criterion (Q = 3.5×10^{-3} s^{-2}) of case 2 (5°, 0.03Hz, TSR 7).

(b) Top-view Q-criterion (Q = 3.5×10^{-3} s^{-2}) of case 6 (5°, 0.03Hz, TSR 9).

Figure B.2: Top-view Q-criterion (Q = 3.5×10^{-3} s^{-2}) in the near-wake for varying TSR of 7 and 9 under roll motion of 5° and 0.03Hz.

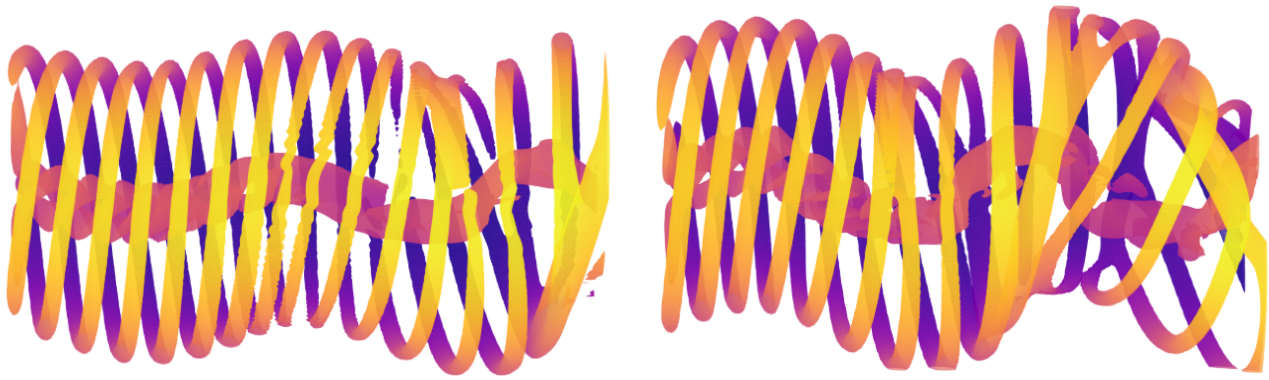

(a) Top-view Q-criterion (Q = 3.5×10^{-3} s^{-2}) of case 2 (5°, 0.03Hz, TSR 7).

(b) Top-view Q-criterion (Q = 3.5×10^{-3} s^{-2}) of case 3 (10°, 0.03Hz, TSR 7).

Figure B.3: Top-view Q-criterion (Q = 3.5×10^{-3} s^{-2}) in the near-wake for varying roll amplitudes of 5° and 10° under roll motion of 0.03Hz and operating TSR of 7.

(a) Top-view Q-criterion (Q = 3.5×10^{-3} s^{-2}) of case 4 (5°, 0.05Hz, TSR 7).

(b) Top-view Q-criterion (Q = 3.5×10^{-3} s^{-2}) of case 5 (10°, 0.05Hz, TSR 7).

Figure B.4: Top-view Q-criterion (Q = 3.5×10^{-3} s^{-2}) in the near-wake for varying roll amplitudes of 5° and 10° under roll motion of 0.05Hz and operating TSR of 7.